On the scaling and unsteadiness of shock induced separation
Louis J. Souverein

On the scaling and unsteadiness
of shock induced separation

THESIS

By

L.J. Souverein, M.Sc.

Front cover photo: RocketCam™ view of ground-lit solid-rocket booster separation during Delta II launch of the Mars Exploration Rover A ("Spirit") on 2003 June 10. Image from video courtesy Ecliptic Enterprises Corporation and NASA. Used with permission.
Monogram (LJS): design by the author.

On the scaling and unsteadiness
of shock induced separation

PROEFSCHRIFT

ter verkrijging van de graad van doctor
aan de Technische Universiteit Delft,
op gezag van de Rector Magnificus Prof. ir. K.C.A.M. Luyben,
voorzitter van het College voor Promoties
in het openbaar te verdedigen op maandag 15 maart 2010 om 10:00 uur

door

Louis Jacques SOUVEREIN

ingenieur Luchtvaart- en Ruimtevaart
geboren te Rotterdam

UNIVERSITÉ DE PROVENCE AIX-MARSEILLE I

THÈSE

présentée en vue de l'obtention du titre de

Docteur

de

L'Université de Provence

École Doctorale 353	:	Sciences pour l'Ingénieur
Spécialité	:	Mécanique Énergétique

Par

Louis Jacques SOUVEREIN

On the scaling and unsteadiness of shock induced separation

**Thèse soutenue publiquement le 15 mars 2010
devant le jury composé de :**

M. Denis Bertin	**Vice-Président** de l'Université de Provence, Professeur, F
M. Piotr Doerffer	**Rapporteur**, Polish Academy of Sciences, Professeur, PL
M. Alexander Smits	**Rapporteur**, Princeton University, Professeur, USA
M. Peter Bakker	**Directeur de Thèse**, TU Delft, Professeur, NL
M. Jean-Paul Dussauge	**Directeur de Thèse**, IUSTI, Directeur de Recherche, F
M. Jean Délery	**Examinateur**, Conseiller Emérite à l'ONERA, F
M. Fulvio Scarano	**Examinateur**, TU Delft, Professeur, NL
Mme. Brenda Timmerman	**Examinatrice**, University of Warwick, Professeur, UK

"Per aspera ad astra"

Contents

Preface

This thesis represents three and a half years of research work that was performed within the context of an international 'cotutelle', or double promotion, between the Delft University of Technology and the Université de Provence - Aix–Marseille I. An inherent risk of doing a research work at more than one institution is that one is given a lot of freedom and that it enlarges the bounds and scope of the research topic, which can make one feel left at large from time to time. On the other hand, the advantages are that one has access to a larger pool of information and expertise, and that the results are subject to a direct thorough and critical evaluation by multiple supervisors with different scientific backgrounds. The challenge was therefore to surmount the cultural (laboratory and country related) differences, to synthesise the scientific advise and opinions of the supervisors, to maintain the focus in the research, to bring harmony in the panoply of experimental results, and to distill out a single topic that serves as the central 'storyline'. For the current research, this storyline became the systematic geometrical and dynamical comparison of the phenomenon at hand (an interaction between a shock wave and a boundary layer), by virtue of the different available flow diagnostics techniques and the wide range of accessible flow conditions due to the use of two distinct experimental facilities. In this context, flow control experiments were also performed as a proof of concept for the conclusions drawn from the analysis of the baseline results. I hope that the reader will agree that this approach has increased the value of the scientific results and that it has lead to a coherent story.

The framework of this doctoral research went beyond the conventional bounds of a Ph.D. project, and it therefore required the commitment and support of a number of people, institutions and organisations, and it took quite some organisational effort to make it possible. First and foremost, I would like to acknowledge the cooperation between the TU Delft and the Université de Provence. More specifically, my gratitude goes out to prof. dr. ir. Peter Bakker, dr. ir. Bas van Oudheusden and prof. dr. Jean-Paul Dussauge for their sustained personal support and efforts in making this cotutelle possible. In addition, I would like to thank the French-Dutch Network for Higher Education ('Netwerk Frans-Nederlands Hoger Onderwijs - Réseau Franco-Néerlandais de l'Enseignement Supérieur') and prof. dr. ir. René de Borst for their advice and assistance in drawing up the contract for the cotutelle. Finally, I would like to render thanks to the French government in cooperation with KLM Royal Dutch Airlines, who provided me with a scholarship to cover the inherent additional expenses that such an international endeavour brings about.

This research project was also supported by the 6th Framework Programme of the European Commission through the STREP Specific Targeted Research Project UFAST "Unsteady Effects of Shock Wave Induced Separation", grant N° AST4-

CT-2005012226. An important part of this work was the contribution of results to an experimental database for cross–validation against numerical simulations. There was a close cooperation with a number of international partners within the project, notably the University of Southampton, the University of Rome "La Sapienza", the École Centrale de Lyon and the ONERA. I particularly enjoyed the six–monthly meetings with the people in the project. In addition, I would like to give credit to UFAST as an incubator for the next generation of researchers, and in this context I would like to thank dr. Alexandre Beer, dr. Paul Bruce and dr. Emile Touber for the good times that we spent together on the project and at the conferences.

Looking back at these last years, there is a number of people that accompanied me on this endeavour and to whom I would like to extend a special thanks. First of all, I would like to thank my supervisors, prof. dr. ir. Peter Bakker, prof.dr Jean-Paul Dussauge, dr. ir. Bas van Oudheusden, prof. dr. Fulvio Scarano, dr. Pierre Dupont and dr. Jean-François Debiève for giving me the opportunity to perform this Ph.D. research, and for their continuous support, inspiration and ideas. I would also like to thank Thibault Lang and ir. Alexander Jöbsis for the collaboration during their Master's thesis project and dr. ir. Jeroen Witteveen for the cooperation on the comparison between experimental and numerical results for the biconvex airfoil. I would also like to acknowledge ing. Frits Donker Duyvis, Peter Duyndam, ing. Eric de Keizer, Nico van Beek, Stéphane Mucini and Jean-Marie Félio for their involvement and assistance in the experiments and in making the equipment work. I would also like to render thanks to all my colleagues in Delft and in Marseille for making my stay in the respective laboratories a pleasant one, and for the good times we had at the different conferences and meetings. In particular, special credit goes to the 'Savants de Marseille' for enriching me with the subtleties of the French language, and to dr. Lionel Larchevêque for sharing his single malt collection with us.

I would like to thank Daniel & Marloes, Hugo, Joep, Joost, Merijn & Sabrine, Maarten, Mark, Marline, Martijn, Sam, Steven & Emilie and Veerle for staying in touch during my period in Marseille, and I appreciated very much the regular visits we received during these years. I am also very grateful for having made new friendships in Marseille with Chotiga, Lionel & Christel and Sebastien & Elise, and with Boris & Mylène, with whom it was a pleasure to share the experience of becoming parents during the many evenings spent together. Finally I would like to thank my family for their encouragements, interest and support during these years. And last, but not least, I would like to thank my wife Irène for her love and understanding during the sometimes stressful times, and my son Leen for making this life changing last year a truly unforgettable experience.

As a last remark, my time as a doctoral researcher has been a particularly interesting period, also from a personal point of view, changing countries, making French my second language, but also becoming a married man and founding a family. It was a period that I enjoyed a lot, and I would like to thank anyone in general who contributed to making it a pleasant one. I am proud that at its finale I can now become one of the 'Savants de Marseille'.

Louis Souverein
Marseille, January 27th, 2010

Résumé

Les interactions onde choc couche limite (IOCCL) constituent un phénomène courant dans les écoulements transsonique et supersonique. La présence des ondes des chocs provoque sur les parois une augmentation rapide de la pression, ce qui peut provoquer le décollement de la couche limite. Ces ondes de choc peuvent être provoquées par des configurations géométriques particulières. On trouve de nombreux exemples de ces interactions, à savoir dans les tuyères des moteurs fusées, sur des aerospikes, sur les corps de rentrée, dans les entrées d'air des moteurs supersoniques et hypersoniques, sur les extrémités des pales des compresseurs et des turbines dans les moteurs à réaction. Ces interactions sont donc des facteurs importants dans la conception d'un véhicule. Le décollement aussi bien que le choc induit sont très instationnaires, et provoquent des fluctuations de pression et des charges thermiques. Ceci dégrade la performance des moteurs et peut détériorer leur structure. Le travail ici décrit vise à améliorer la compréhension physique des mécanismes qui gouvernent les interactions, avec une attention particulière sur l'organisation de l'écoulement et les sources d'instationnarités dont le système de chocs est l'objet. On considère plus particulièrement des cas de réflexion d'ondes de choc obliques, mais les mécanismes mis en évidence dans ce cas particulier ont une généralité plus grande pour des configurations différentes. Par ailleurs, on vérifie si l'on peut contrôler l'interaction par une injection d'air dans la couche limite amont. Pour atteindre ces objectifs, des expériences ont été réalisées qui comparent systématiquement des interactions avec plusieurs intensités de choc (y compris des décollements naissants et des interactions décollées) et sous différentes conditions (nombres de Mach de 1,7 et 2,3 et nombres de Reynolds de 5.000 ('bas') et de 50.000 ('grand'). Les expériences ont été menées en prenant en compte les derniers développements dans le domaine des méthodes de mesure.

Un grand volume de données a été acquis, sur de multiples interactions en utilisant plusieurs méthodes de diagnostics de l'écoulement, et produisant des résultats très cohérents. Une détermination des échelles de temps dans tout le domaine de mesure a été effectué au moyen de la vélocimétrie d'image de particule en plan dual (Dual-PIV) ; cela a montré qu'il existe dans l'interaction naissante à grand nombre de Reynolds des fluctuations dont la gamme de fréquence porte sur de trois ordres de grandeur. En plus,

la dynamique à basses fréquences du choc réfléchi a été mise en évidence. L'effet du contrôle par générateurs de tourbillons par jets d'air (AJVG) a été caractérisé en détail. Ceci a mis en évidence la génération de paires de tourbillons contrarotatifs avec d'intensités différentes. Ces tourbillons induisent des zones de basse et forte vitesse près de la parois, qui modifient à leur tour le bulbe de décollement sans de le supprimer. La fréquence de choc dépend d'une manière inversement proportionnelle à la taille de bulbe. Une analyse des facteurs d'échelles caractéristiques a été effectuée, dans le but de réconcilier les différences apparentes entre les interactions documentées dans la littérature. Une partie de cette analyse est la formulation d'un critère de décollement qui dépend uniquement du nombre de Mach dans l'écoulement extérieur et de l'angle de déviation de l'écoulement. En outre, une adimensionnalisation a été déduite pour la longueur de l'interaction à partir de la conservation de masse et de la quantité de mouvement. Une analyse conditionnelle a été faite à partir de la taille instantanée du bulbe. La génération de grandes structures tourbillonnaires cohérentes a été mise en évidence, même en absence d'un décollement instantané. Pour les cas naissants, un lien a été mis en évidence entre la zone de décollement et la couche limite amont. Pour les cas décollés, ce lien n'existe pas et l'instationnarité du choc dépend principalement de la pulsation du bulbe.

Le critère de décollement utilisant la longueur d'interaction adimensionnelle présente une seule courbe qui regroupe un large ensemble d'interactions documentées dans la littérature avec une dispersion modérée. Cette courbe semble indiquer que le seul moyen de supprimer un bulbe de décollement fermé par du contrôle amont est de diminuer l'épaisseur de déplacement de la couche limite amont. Une normalisation a été définie pour la coordonnée perpendiculaire à la paroi, basée sur la longueur d'interaction et faisant intervenir une correction pour l'effet du nombre de Mach. Avec cette adimensionnalisation on obtient une large ressemblance géométrique des interactions considérées ici, indépendamment du nombre de Mach et de Reynolds. Il est proposé que l'importance relative de différents mécanismes change avec l'intensité imposée du choc. Il semble que les interactions faibles sans décollement instantané doivent être pilotées uniquement par des effets amont, avec des fréquences plutôt élevées. Pour les interactions naissantes, des effets aval commencent à apparatre ; la région avec des intensités de turbulence élevées montre une déviation de l'écoulement variable qui produit un pied de choc avec une intensité elle aussi variable, ainsi que des fréquences d'instationnarités qui peuvent varier sur trois ordres de grandeur. Les interactions avec un décollement significatif montrent surtout un mouvement de translation, ce qui est en accord avec un comportement d'interaction libre. En ce qui concerne les effets du nombre de Reynolds et de Mach, on en conclut que pour des couches limites turbulentes, le début du décollement est indépendant du nombre de Reynolds. La longueur d'interaction dépend par contre aussi bien du nombre de Reynolds que du nombre de Mach.

Samenvatting

Schokgolf grenslaag interacties (SGGLI) zijn een veelvoorkomend fenomeen in transsone en supersone stromingen. De aanwezigheid van schokgolven, opgewekt door bepaalde geometrische configuraties, zorgt voor een snelle druktoename op de wand, wat kan leiden tot stromingsloslating. Voorbeelden van dit type interacties zijn te vinden in raketmotorstraalpijpen en op aerospikes, op terugkeervoertuigen, in de luchtinlaat van supersone en hypersone motoren, en op de compressor- en turbinebladuiteinden in straalmotoren. De interacties zijn belangrijke factoren in de voertuigontwikkeling. Zowel de loslating als de geïnduceerde schok zijn zeer instationair, wat leidt tot fluctuerende drukken en warmtebelastingen. Deze hebben in het algemeen een verminderde prestatie tot gevolg en kunnen leiden tot het bezwijken van de structuur. Dit onderzoek heeft daarom tot doel om het fysische begrip van de mechanismen die de interactie beheersen te vergroten, met een speciale aandacht voor de stromingsorganisatie en de oorsprong van de instationariteit van de geïnduceerde schok. De aandacht gaat specifiek uit naar het geval van de gereflecteerde schok, maar de resultaten zijn ook van toepassing op andere configuraties. Daarnaast is geprobeerd de interactie te beïnvloeden door middel van stroomopwaartse luchtinspuiting. Om deze doelstellingen te bereiken zijn experimenten uitgevoerd, waarbij een systematische vergelijking is gemaakt tussen meerdere interacties voor een aantal schokintensiteiten (leidend tot beginnend losgelaten en sterk losgelaten stromingen) en onder verschillende stromingscondities (Machgetallen van 1,7 en 2,3 en Reynoldsgetallen van 5.000 ('laag') en 50.000 ('hoog')). Er is gebruik gemaakt van de meest recente meettechnieken.

De grote hoeveelheid gegevens, verkregen voor meerdere interacties en gebruikmakend van verschillende stromingsdiagnostiektechnieken, heeft zeer consistente resultaten opgeleverd. De karakteristieke tijdsschalen zijn bepaald voor de beginnend losgelaten interactie bij hoog Reynoldsgetal. Dit is gedaan voor het volledige stromingsveld door middel van 'dual-plane particle image velocimetry' (Dual-PIV). Zodoende is aangetoond dat de frequenties in de interactie een bereik bespannen van drie orde groottes en dat de schokgolf bovendien, ook in het geval van de beginnende loslating, een lagefrequentiedynamiek heeft. De mogelijkheid tot beïnvloeding van de interactie door middel van luchtstraalwervelopwekkers ('air jet vortex generators' - AJVGs)

is in detail gekarakteriseerd. Zo is het bestaan aangetoond van paren van in tegengestelde richting draaiende wervels die een partroon van lage- en hoge-snelheidsgebieden in de stroming induceren. Deze beïnvloeden op hun beurt de grootte van de loslaatblaas zonder deze te onderdrukken. Er bestaat een omgekeerd evenredig verband tussen de frequentie van de gereflecteerde schok en de blaasgrootte. Een schalingsanalyse is ondernomen met als doel het in overeenstemming brengen van de in de literatuur gedocumenteerde interacties. Deel van deze analyse was het definiëren van een loslaatkriterium dat afhangt van enkel het Machgetal en de opgelegde stromingsinvalshoek. Ook is een schaling afgeleid voor de interactielengte, gebaseerd op massa-en impulsbehoud. Een conditionele analyse is uitgevoerd, gebaseerd op de grootte van de instantane loslaatblaas. Dit heeft aangetoond dat er altijd, zelfs bij een instantaan aanliggende stroming, grootschalige samenhangende structuren gevormd worden die vervolgens in de stroomafwaartse grenslaag afgeschud worden. Voor de beginnend losgelaten gevallen is er een verband aangetoond tussen de stroming in het loslaatgebied en de toestand van de inkomende grenslaag. Voor de losgelaten interacties is deze link niet gevonden, en de instationariteit lijkt hoofdzakelijk gerelateerd te zijn aan de blaaspulsatie.

Als het loslaatkriterium gecombineerd wordt met de genormaliseerde interactielengte verkrijgt men een enkele kromme waarop een groot aantal in de literatuur gedocumenteerde interacties met een geringe spreiding samenvallen. Aan de hand van deze kromme kan voorspeld worden dat een gesloten loslaatblaas enkel onderdrukt kan worden door middel van stroomopwaartse beïnvloeding als daarbij de verdringingsdikte van de inkomende grenslaag verminderd wordt. Een schaling voor de coordinaat loodrecht op de wand is gedefinieerd, gebaseerd op de interactie lengte met een correctie voor de Macheffecten. Deze leidt tot een grote overeenkomst in de ruimtelijke organisatie van de gemiddelde en turbulente velden voor de beschouwde interacties. De resultaten duiden aan dat het relatieve belang van de verschillende mechanismen verschuift al naar gelang de opgelegde schokintensiteit. Zwakke interacties zonder instantane loslating lijken vooral gedreven te worden door stroomopwaartse effecten, met relatief hoge frequenties. Bij beginnende loslating observeert men voor het eerst stroomafwaartse effecten; het gebied met hoge turbulentie-intensiteiten geeft blijk van een hefbeweging, wat leidt tot een variatie in de schokvoetintensiteit en een schokdynamiek met tijdschalend die tenminste een orde-grootte kunnen verschillen. De dynamiek van interacties met aanzienlijke loslating bestaat uit een translerende beweging, wat leidt tot een lage frequentie-instationariteit en een constante schokvoetintensiteit, wat in overeenstemming is met een vrije-interactie-gedrag. Ten aanzien van Reynolds- en Machgetaleffecten kan geconcludeerd worden dat de aanvang van de loslating van turbulente grenslagen niet Reynoldsgetalafhankelijk is. De interactielengte daarentegen wordt bepaald door zowel het Reynolds- als het Machgetal.

Summary

Shock wave boundary layer interactions (SWBLI) are a common pheno-
menon in transonic and supersonic flows. The presence of shock waves,
induced by specific geometrical configurations, causes a rapid increase of
the pressure, which can lead to flow separation. Examples of such interac-
tions are found in amongst others rocket engine nozzles and on aerospikes,
on re-entry vehicles, in supersonic and hypersonic engine intakes, and at
the tips of compressor and turbine blades in jet engines. The interactions
are important factors in vehicle development. Both the separated flow and
the induced shock have been shown to be highly unsteady, causing pressure
fluctuations and thermal loading. This generally leads to a degraded per-
formance and possibly structural failure. The current work therefore aims
to improve the physical understanding of the mechanisms that govern the
interaction, with a special attention for the flow organisation and for the
sources of the unsteadiness of the induced shock. In particular, the case of a
reflecting incident shock is investigated, but the results find their application
more generally in other configurations. Additionally, it is verified whether
the interaction can be controlled by means of upstream fluid injection. To
attain these aims, experiments were performed, comparing systematically
several interactions for a range of shock intensities (producing incipiently
separated and well separated flows) and under a number of flow conditions
(Mach numbers of 1.7 and 2.3 and Reynolds numbers of 5,000 ('low') and
50,000 ('high')). This was done using the latest developments in the field of
measurement techniques.

   A large amount of data was obtained for multiple interactions by means
of a range of flow diagnostic techniques, yielding highly consistent results.
A full field determination of the characteristic time scales by means of dual-
plane particle image velocimetry (Dual-PIV) has shown that the unsteadi-
ness frequencies in the high Reynolds number incipient interaction span
almost three orders of magnitude, demonstrating additionally the existence
of low frequency dynamics of the reflected shock. The effect of control by
means of air jet vortex generators (AJVGs) was thoroughly characterised,
putting in evidence the generation of pairs of counter-rotating vortices of
unequal strength that induce streaks of low and high speed fluid. These in
their turn modify the separation bubble size without suppressing it. There

is an inversely proportional relation between the reflected shock frequency and the bubble size. A scaling analysis was made, aimed at reconciling the observed discrepancies between interactions documented in literature. As part of this analysis, a separation criterion has been formulated that depends on the free-stream Mach number and the flow deflection angle only. In addition, a scaling approach has been derived for the interaction length based on the mass and momentum conservation. A conditional analysis has been performed based on the instantaneous separation bubble size. The generation and successive shedding of large coherent structures was found to be present also in absence of instantaneous flow separation. For the incipient cases, a link has been put into evidence between the separation region and the state of the upstream boundary layer. For the separated interactions, this link was absent and the shock unsteadiness seems to be mainly related to the separation bubble pulsation.

The separation criterion in combination with the normalised interaction length represents a single trend line onto which all data for a large scope of documented interactions fall together with only a moderate scatter. This trend line predicts that the only way to effectively eliminate a separation bubble (without massive separation) by means of upstream control is by decreasing the displacement thickness of the incoming boundary layer. A scaling for the wall normal coordinate has been defined based on the interaction length with a correction for Mach number effects, producing a large resemblance in the geometric organisation of the mean and turbulent flow fields within the considered interactions. It can be concluded that multiple unsteadiness mechanisms are at work within the interaction, irrespective of the Mach number and the Reynolds number. It is proposed that the relative importance of the different mechanisms shifts with the imposed shock intensity. It seems that weak interactions without instantaneous flow separation should be governed by upstream effects only, with rather high shock frequencies. For incipient interactions, downstream effects start to occur; the region of high turbulence intensities displays mainly a lifting motion, producing a shock foot of varying strength and a shock unsteadiness that involves a time scales which can differ by at least one decade. Interactions with significant flow separation show mainly a translating motion, producing a low frequency unsteadiness and a shock foot of constant strength, which is in accordance with a free interaction behaviour. Concerning the Reynolds number and Mach number effects, it is concluded that for turbulent boundary layers, the onset of separation is Reynolds number independent. The interaction length is however governed by both the Reynolds number and the Mach number.

Nomenclature

Abbreviations

AJVG	Air Jet Vortex Generator
CTA	Constant Temperature Anemometry
DUAL	Dual plane Particle Image Velocimetry (DUAL-PIV)
TU Delft	Delft University of Technology (Delft)
IOCCL	Interaction Onde Choc Couche Limite
IUSTI	Institut Universitaire des Systèmes Thermiques Industriels (Marseille)
HWA	Hot Wire Anemometry
PIV	Particle Image Velocimetry
SGGLI	Schokgolf Grenslaag Interactie
SWBLI	Shock Wave Boundary Layer Interaction
UFAST	Unsteady Effects of Shock Wave Induced Separation
2C	Two component
3C	Three component
3D	Three dimensional

Greek symbols

β	Shock angle
δ	Boundary layer thickness
δ^*	Displacement thickness
φ	Deflection angle
ϕ	Diameter
γ	Specific heat ratio
μ	Viscosity
ν	Kinematic viscosity, μ/ρ
ψ	Jet inclination angle with respect to the tunnel wall
ρ	Density
θ	Momentum thickness
τ	Skin friction

Latin symbols

C_f	Skin friction coefficient
C_p	Pressure coefficient
f	Frequency; focal length
$f_\#$	F-number
H_{cv}	Control volume height
H	Shape factor
H_{int}	Interaction height
h	Height of the dividing streamline
h_0	Separation bubble height
L_{cv}	Control volume length
L	Interaction length
$\tilde{L}, \hat{L}$	Dimensionless interaction length
L_{sep}	Separation bubble length
M	Mach number
p	Pressure
Q	Iso-flux
r	Recovery factor
Re	Reynolds number
S_e	Dimensionless pressure, separation criterion
S_L	Strouhal number (based on the interaction length)
S_h	Strouhal number (based on the dividing streamline height)
T	Temperature
t	Time
U, u	Velocity (longitudinal component)
u_τ	Friction velocity
V, v	Velocity (wall-normal component)
W, w	Velocity (lateral component)
X, x	Longitudinal dimensional coordinate
X_0	Location of the reflected shock foot
X^*	Longitudinal dimensionless coordinate $X^* = \frac{X - X_0}{L}$
Y, y	Wall-normal dimensional coordinate
Z, z	Lateral dimensional coordinate

Subscripts

cv	Control volume
e	Value at free-stream condition, boundary layer edge
ic	Incompressible
in	Inflow condition
jet	Jet condition (AJVGs)
out	Outflow condition
pix	Pixel value
vd	Van Driest transformed
w	Value at wall
x	Value at position x
0	Value at stagnation condition
$1, 2, 3$	Value for interaction domain 1,2,3
99	Thickness at 99% of the mean free-stream velocity

Superscripts

$+$	Law-of-the-wall variable
$*$	Displacement thickness (δ)

Chapter 1

Introduction

Shock wave boundary layer interactions (SWBLI) are a common phenomenon in transonic and supersonic flows. They are observed on any object surface exposed to a high speed fluid that is experiencing a rapid increase in pressure. Such a pressure rise is notably induced by a change in surface geometry, or by a shock wave of external origin. These adverse pressure gradients are known to lead to a deceleration of the fluid near the wall, with the possible occurrence of flow separation. This causes the boundary layer on the object surface to thicken, imposing its own flow deflection on the external flow and hence inducing the formation of a shock discontinuity upstream of the disturbance that induces the pressure gradient. Both the separated flow and the induced shock have been shown to be highly unsteady, causing oscillating pressure fluctuations in the downstream flow field, generally leading to a degraded performance. In addition, the combination of a stagnating flow, separation and the shock oscillations expose the object surface to fluctuating pressure and thermal loads that can lead to vibrations and structural failure.

Due to their common occurrence in high speed flows and due to their generally adverse effects, shock wave boundary layer interactions have been the subject of extensive investigations since their first observation in the 1940s. This has lead to an understanding of the mean flow topology, the identification of several dynamical phenomena occurring within the interaction, and a demonstration of the low frequency nature of the shock unsteadiness. In addition, several mechanisms have been proposed to explain the origin of the shock dynamics, although no consensus has yet been achieved and the debate is ongoing. On the other hand, research has also been directed to the control of the interaction, attempting to negate the adverse effects by suppressing the separation bubble and the shock unsteadiness, so far with mixed success.

The aim of the current work is in the first place to improve the physical understanding of the mechanisms that govern the interaction unsteadiness.

This will be done experimentally, by systematically comparing several interactions for a range of shock intensities and under a number of flow conditions, making use of the latest developments in the field of measurement techniques. Secondly, it is attempted to define a scaling for the interaction length. Finally, an attempt has been made to control the interaction by means of upstream fluid injection.

1.1 Background

The interaction between a shock wave and a turbulent boundary layer establishes one of the classic phenomena in compressible viscous flow analysis. It has a direct technological relevance to the performance of aerospace vehicles. The first observation of a shock wave boundary layer has probably been made by Ferri (1940) during testing of an airfoil in a high speed tunnel, see Dolling (2001). However, examples of the occurrence of this form of interaction are found in a multitude of high speed applications. One may think of over-expanded rocket engine nozzles (figure 1.1), control surface deflections on re-entry vehicles (figure 1.2), engine intakes of supersonic and hypersonic vehicles and the internal flow of a scramjet (figure 1.3), and a barrel shock reflecting on a plug nozzle (figure 1.4), to name a few. They also occur on locations that would at first not have been intuited, such as within compressor cascades or on the tips of turbine blades in jet-engines due to the requirements for ever larger compression ratios (figure 1.5). This list of examples is far from exhaustive, but it gives an impression of the wide range of occurrences of the phenomenon.

That shock wave boundary layer interactions and their control are not just an academic problem, but that they can actually be seen in 'every day life' is demonstrated by figure 1.6. The figures shows the in-flight occurrences of shocks interacting with the boundary layer on the wing of a Boeing 737 and an Airbus A320 (figures 1.6(a) and (b) respectively). The first image was taken on a Czech Airlines flight from Prague to Bucharest, July 15th, 2007, and the second on an Air France flight from Paris to Marseille on June 28th, 2008. In both cases, the aircraft were in cruise condition and the flow over the wing may hence be expected to be low transonic. The shocks were found relatively stable, showing only mild large scale oscillations. The separation in figure 1.6(b) occurs downstream of the shock, indicating that the shock has not sufficiently depleted the boundary layer momentum to cause immediate large scale separation. No noteworthy vibrations were felt inside the aircraft. The wing airfoil has undoubtedly been shaped such as to limit the adverse pressure gradient and hence prevent large scale flow separation. Figure 1.6(a) also shows an example of flow control, where the boundary layer on the wing is re-energized by an array of vortex generators (generating a dark trace on the wing surface) in order to make it more

resistent to flow separation on the outer part of the wing. It appears hence that both manufacturers have optimised their wing designs, each in their own way, to negate the adverse effect of the shock wave boundary layer interactions.

(a)   (b)

(c)
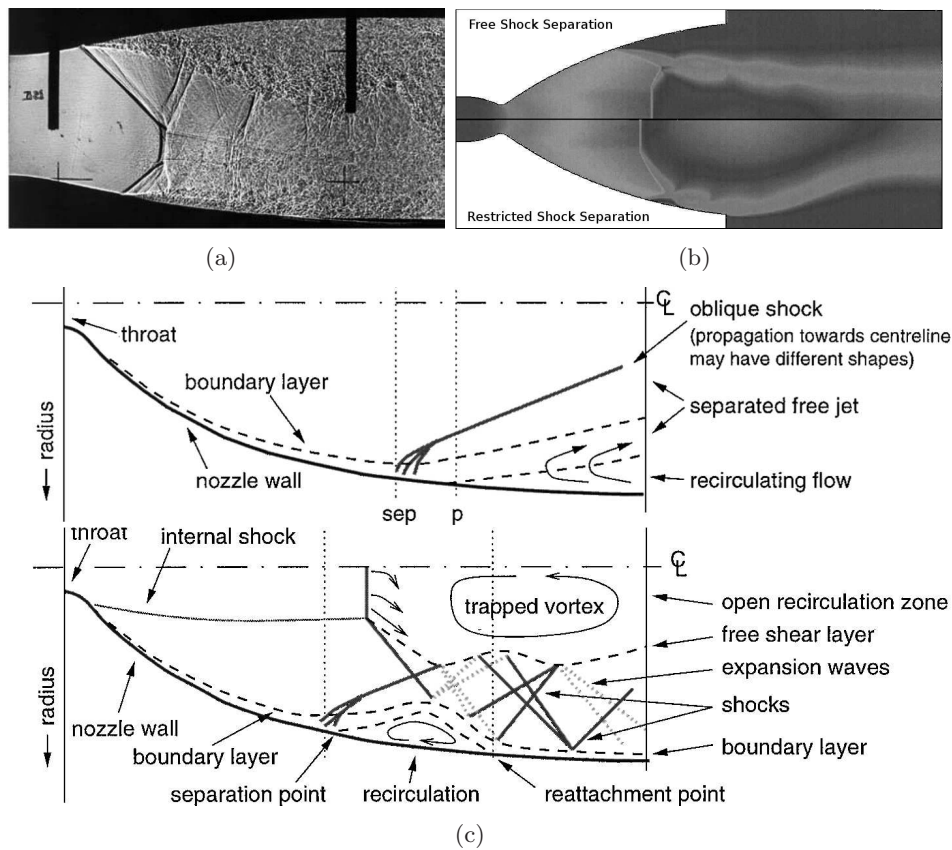
Figure 1.1: Shock wave boundary layer interactions within over-expanded rocket engine nozzles: (a) shadowgraphy of shock induced separation within the nozzle, from Bourgoing & Reijasse (2005); (b) numerical simulation of the Vulcain engine nozzle flow with free shock separation (FSS) and restricted shock separation (RSS), from Frey & Hagemann (2000); (c) schematic of the flow topology for FSS and RSS, from Frey & Hagemann (1998).

(a)   (b)
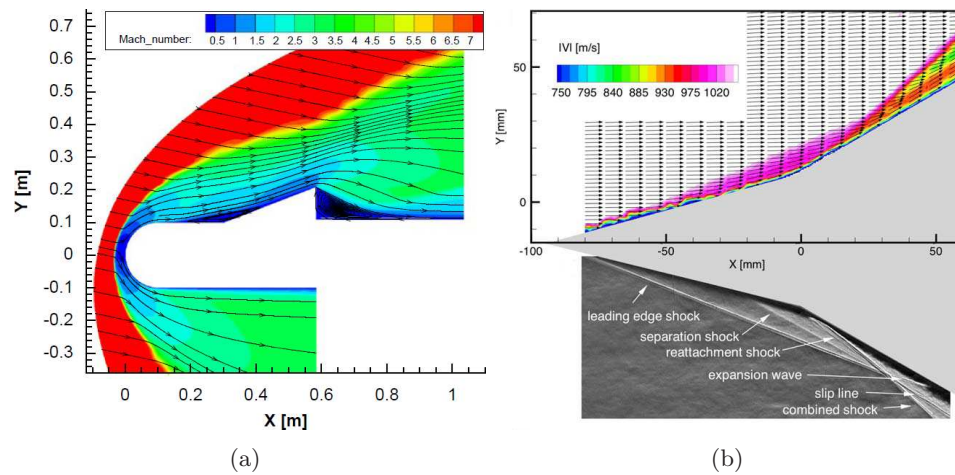
Figure 1.2: Shock wave boundary layer interaction occurrences on re-entry
vehicle body flaps: (a) numerical simulation of a wind tunnel model for
the EXPERT vehicle control surface, representing a 20° flap deflection at
Mach=7; (b) future experiments are to be performed to characterise the
shock wave boundary layer interaction under high enthalpy conditions, from
Di Clemente *et al.* (2009); particle image velocimetry measurement and a
Schlieren visualisation of the flow field induced by a double ramp at Mach=7,
representative of a flap deflection, from Schrijer *et al.* (2006).

(a)   (b)
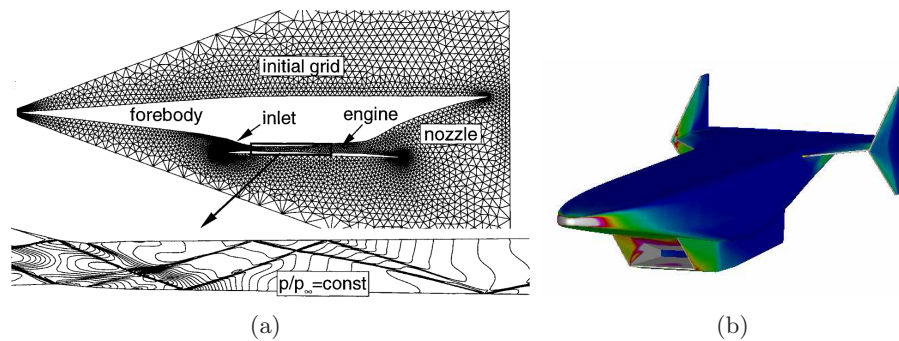
Figure 1.3: Shock wave boundary layer interactions within scramjets: (a)
inviscid simulation of the flow around the JAPHAR hypersonic vehicle,
putting in evidence the shock train through the engine, showing multiple
wall reflections, from Eggers *et al.* (2001); (b) pressure distribution around
the engine intake of the LEA hypersonic vehicle, putting in evidence pres-
sure jumps within the intake caused by shock reflections, from Felempin &
Serre (2006).
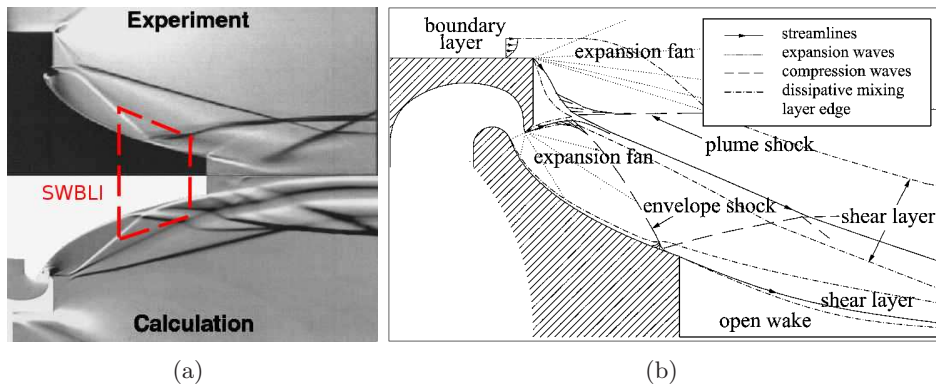
Figure 1.4: Shock wave boundary layer interaction on a plug nozzle: (a) Schlieren visualisation and numerical computation showing a barrel shock reflecting on the aero-spike contour, causing the flow on the nozzle surface to separate; (b) schematic representation of the flow topology. From Wisse & Bannink (2001).
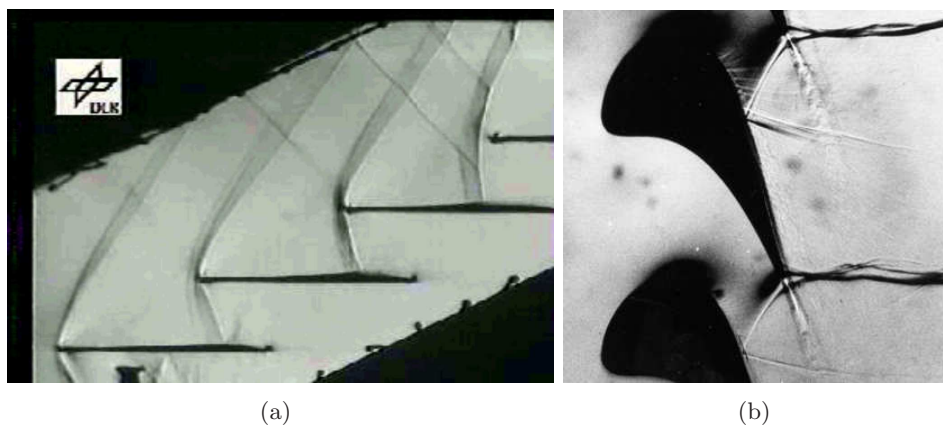
Figure 1.5: Shock wave boundary layer interactions within jet engines: (a) Schlieren visualisation of a compressor cascade at Mach=1.2, courtesy of Rolls-Royce Deutschland and DLR Cologne; (b) Schlieren visualisation of a turbine blade at Mach=1.2, courtesy of Rolls-Royce Deutschland and DLR Göttingen.
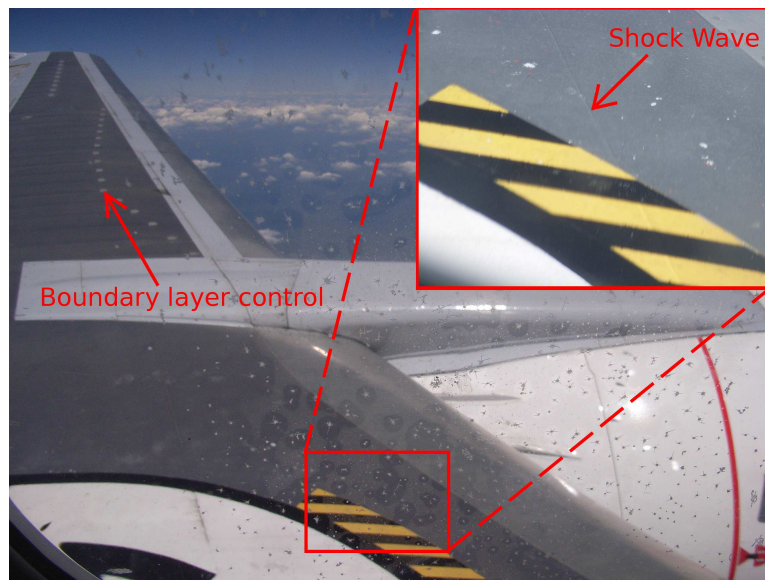
(a)
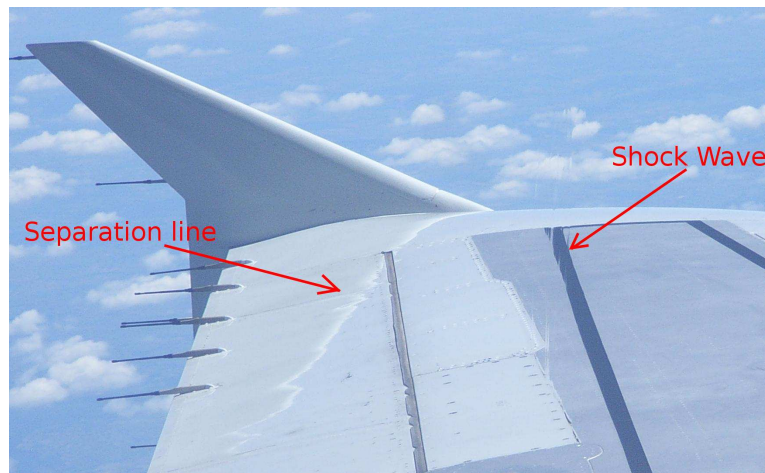
(b)

Figure 1.6: Shock wave boundary layer interactions and boundary layer control in real flight situations: (a) shadowgraphy of a shock wave on the inboard part of a Boeing 737 wing (the black and white line running across the insert image), and separation control by means of vortex generators on the outer part of the wing; (b) shock wave and boundary layer separation near the wing tip of an Airbus A320 aircraft, the shock is visible through refraction of the background image (wing and clouds), the separation line is visualised by the accumulation of the white deposit on the aileron. Photos by the author.

The occurrence of unexpected fluid dynamic effects can lead to disaster, as is shown in Peebles (2008), chapter 5. For the first X-43 test flight, the Pegasus based HXLV launch vehicle was purposely operated outside its original design envelope, inducing higher dynamic pressures than foreseen in the vehicle design. Unexpected non-linear effects on the control surfaces, which were not noticed due to a too sparse wind tunnel measurement matrix, were the major reason for the loss of the vehicle. Shock wave boundary layer interactions, an inherently non-linear phenomenon, induce several inconvenient effects. In the first place, they lead to pressure fluctuations within the flow field and to oscillating surface loads, often detrimental to vehicle performance. In addition, maximum mean and fluctuating pressure and thermal loads on a structure are most often found in regions of shock wave boundary layer interactions. They are hence important factors in vehicle development. Negating or controling adverse effects requires a rigorous physical understanding of the mechanisms behind the flow phenomenon as well as improved simulation capabilities, both of which cannot be attained without fundamental experimental investigation and validation.

The renewed attention for the feasibility of sustainable supersonic transport has revived the interest in SWBLI in the moderate supersonic regime. In this context the European sixth framework program UFAST "Unsteady effects of shock wave induced separation" was initiated, in which the shock reflection interaction is one of the flow cases of interest, with an emphasis on closely coupled and mutually validated numerical and experimental investigations, see Doerffer (2007).

1.2 Flow description

The previous section shows that shock wave boundary layer interactions are omnipresent in high speed flows. As hinted earlier, different types of interactions exist. In general, any geometrical change or external pressure gradient is susceptible to generate a shock wave that could interact with the boundary layer on the object surface. However, several basic types are generally recognised. Among these academic cases we may count the *normal shock interaction* (Atkin & Squire (1992); Bruce & Babinsky (2008b); Bur *et al.* (2008)), the *blunt fin interaction* (Brusniak & Dolling (1994); Ünalmis & Dolling (1996); Bueno (2006)), the *compression ramp interaction* (Thomke & Roshko (1969); Spaid & Frishett (1972); Settles *et al.* (1979); Debiève (1983); Ardonceau (1984); Dolling & Or (1985); Smits & Muck (1987); Kuntz *et al.* (1987); Selig *et al.* (1989); Erengil & Dolling (1991b); Thomas *et al.* (1994); Beresh *et al.* (2002); Hou (2003); Ganapathisubramani *et al.* (2007b); Wu & Martin (2008); Ringuette *et al.* (2008)) and the *incident reflecting shock interaction* (Green (1970); Dupont *et al.* (2006); Pirozzoli & Grasso (2006); Touber & Sandham (2008); Piponniau *et al.* (2009); Humble
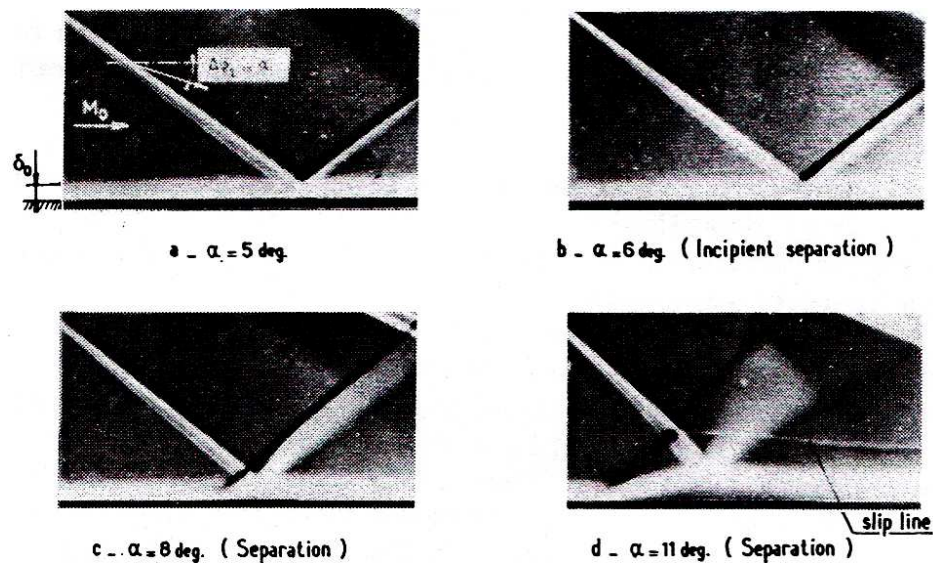
Figure 1.7: Schlieren visualisations of incident reflecting shock interactions at Mach=1.93 for increasing flow deflection angle (shock intensity) ranging from attached (a) to strongly separated (d), from Délery & Marvin (1986).

et al. (2009a); Souverein *et al.* (2009b,a); Polivanov *et al.* (2009); Garnier (2009); Touber & Sandham (2009); Pirozzoli *et al.* (2009). More examples of interaction types are given in for instance Smits & Dussauge (2006). This list is evidently not exhaustive. The most commonly considered interactions concern those with a turbulent boundary layer, although laminar or transitional interactions have also been investigated (see for example Délery & Marvin (1986)). A detailed treatment of shock wave boundary layer interactions and a survey of the research field can be found in amongst others Délery & Marvin (1986); Dolling (2001); Smits & Dussauge (2006); Clemens & Narayanaswamy (2009); ?. This section will go in more detail into some relevant issues concerning the interaction that is investigated in this thesis, notably the interaction between a planar shock wave impinging on a turbulent boundary layer.

1.2.1   Flow characterisation

The two dimensional inviscid flow solution for a shock reflecting on a wall is well known and can easily be obtained from perfect fluid theory, see for example Anderson Jr. (1991). In a viscous flow, a boundary layer is present, and the solution deviates from this inviscid case, see figure 1.7. One can clearly recognise the flow topology that also appeared in figures 1.1, 1.3, 1.4 and 1.5. An incident shock of external origin impacts on the wall boundary

layer, causing a thickening thereof. For small flow deflection angles (in other words, shock intensities), the boundary layer is only mildly affected, and the flow remains attached. The shock reflects almost as in the inviscid case. For increasing deflection angle, the thickening of the boundary layer becomes more important, and the flow starts to separate at least part of the time, but without forming a mean separation bubble. The reflected shock is now directly followed by an expansion fan and a gradual recompression farther downstream. The expansion and recompression waves interact with the reflected shock, and in the far field the flow will hence approach the inviscid solution. For the largest flow deflections, the flow is separated on the mean. The reflected shock is displaced significantly upstream with respect to the extrapolated wall-impact point of the incident shock. The expansion fan can clearly be distinguished, and an entropy slip line may be observed emanating from the shock crossing point.

The difference between the flow organisation for an interaction that is attached on the mean and an interaction with mean separation is shown in figure 1.8. The combined pressure gradient imposed by the incident and the reflected shock cause the fluid near the wall to decelerate. If the pressure gradient is weak enough, the flow does not separate, see figure 1.8(a). However, it does induce a region of slow moving fluid within the interaction, and instantaneous flow reversal may occur. The deceleration of the fluid causes the sonic line to be lifted away from the wall, and hence a significant portion of the boundary layer to become subsonic. The incident shock itself curves due to the Mach number gradient and it consecutively forms the expansion fan before vanishing on the sonic line. The thickening of the boundary layer imposes its own flow deflection upstream of the impact point of the incident shock, inducing compression waves that coalesce into what is known as the reflected shock.

For larger pressure gradients, the flow will separate, see figure 1.8(b). A mean separation bubble occurs within the interaction and the reflected shock is displaced further upstream. The boundary layer thickness is significantly increased and the expansion fan becomes clearly distinguished from the reflected shock, turning the separated flow back to the wall. Recompression waves may occur downstream of reattachment to bring the flow direction back to the horizontal. These waves could coalesce to form a reattachment shock. An entropy slip line could emanate from the shock crossing point since the shocks above and below this point need not necessarily be of identical intensity.

For reference, the flow organisation for the compression ramp case is also shown in figure 1.8(c), representing the flow at the ramp corner in figure 1.2. The incident shock is evidently absent in this case, and hence no expansion fan occurs. The pressure gradient is imposed by a single shock, which is analogous to the reflected shock in the previous case. The retarded fluid zone imposes an equivalent 'curved wall' geometry, causing the formation of

(a)

(b)

(c)
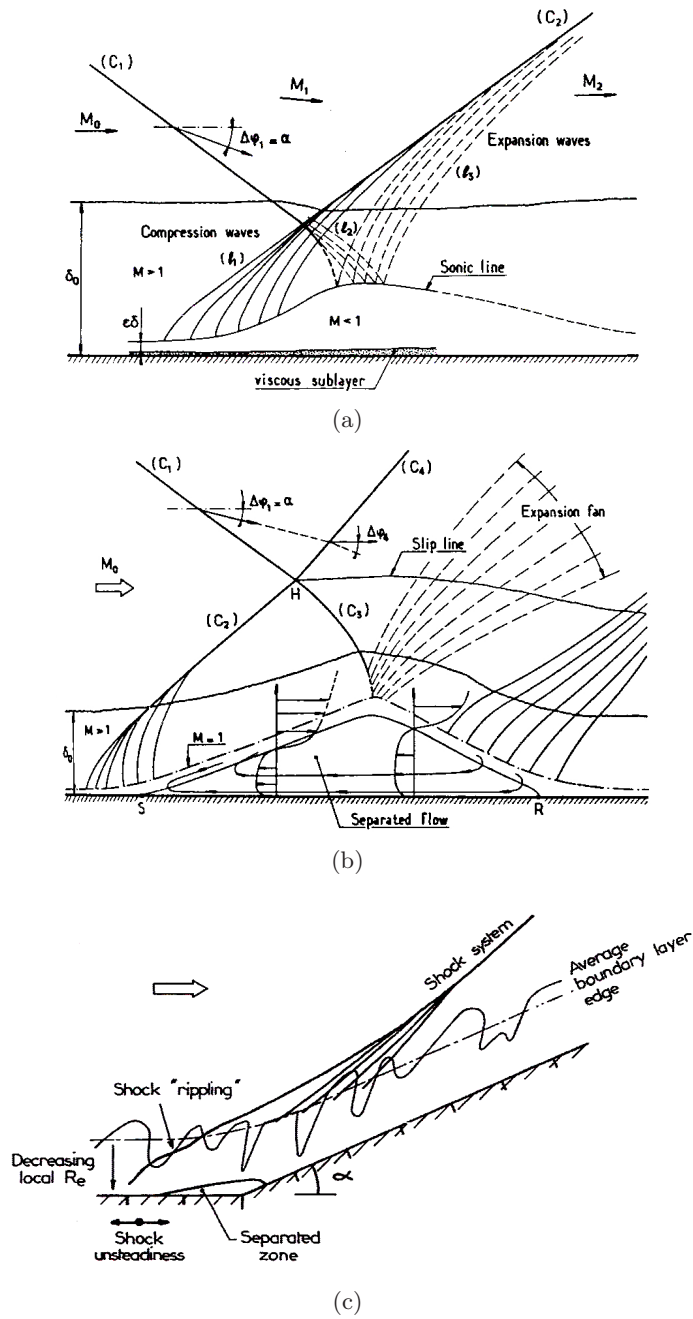
Figure 1.8: Schematic representation of the interaction topology: (a) incident reflecting shock without flow separation; (b) incident reflecting shock with flow separation; from Délery & Marvin (1986); (c) Compression ramp, from Smits & Dussauge (2006).
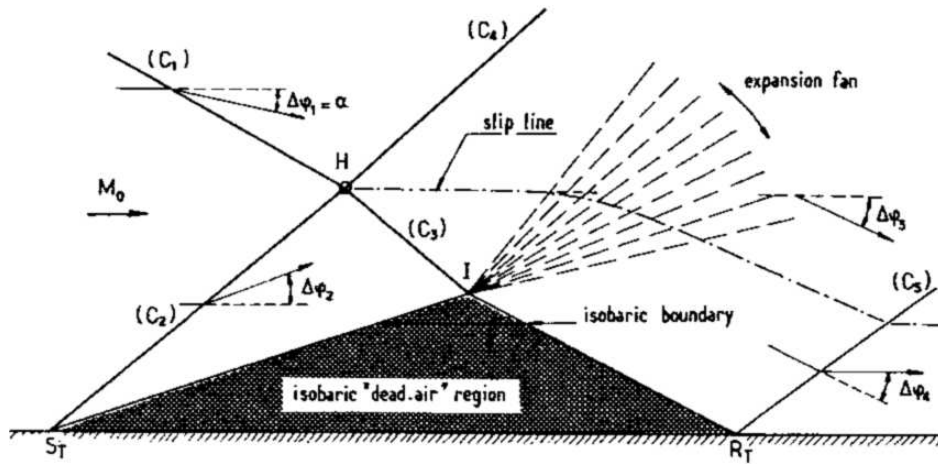
Figure 1.9: Inviscid flow model for the shock-reflection interaction with separation, from Délery & Marvin (1986).

a leading shock, followed by a fan of compression waves. The shock and the compression waves meet, tending towards the perfect fluid solution.

An inviscid flow model has been proposed for the separated incident reflecting shock interaction, see for example Délery & Marvin (1986). It omits the boundary layer and models the separation region as a 'solid prism', see figure 1.9. This purely non-viscous model is a useful tool for the interpretation of the flow organisation that results for a given separation bubble (prism) geometry. It can however not give a prediction of the interaction topology, since it is imposed *a priori* by the prism shape.

Concerning the dynamical organisation, different known flow features can be identified that have their significance for the interpretation of the interaction behaviour. For instance, the existence of hairpin vortices and their organisation into coherent packets has been demonstrated in turbulent boundary layers (see Head & Bandyopadhyay (1981); Robinson (1991); Zhou *et al.* (1999); Adrian *et al.* (2000); Christensen & Adrian (2001)). It has been shown that these packets induce a streamwise elongated organisation of the flow into low and high speed streaks with lengths of the order of ten boundary layer thicknesses or more (see Adrian *et al.* (2000); Ganapathisubramani *et al.* (2006a)). In addition, the concave curvature of the wind tunnel nozzle could lead to the formation of Taylor-Görler vortices, inducing a streamwise coherent organisation within the upstream boundary layer (see Smits & Dussauge (2006); Ünalmis & Dolling (1996); Dussauge & Piponniau (2008)). Both phenomena could exert an influence on the shock motion and the separation bubble dynamics within the interaction. Concerning the separation region, it is furthermore classical to relate the existence of mean separation
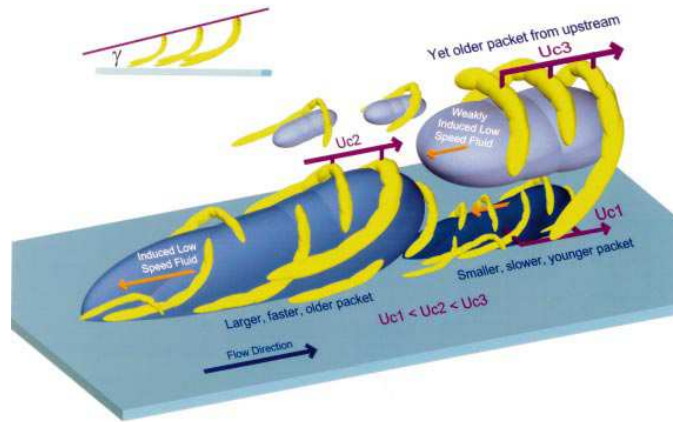
Figure 1.10: Schematic representation of coherently aligned hairpin packets, inducing streamwise elongated low speed streaks, from Adrian *et al.* (2000).

to the development of a mixing layer (see Mabey (1972); Eaton & Johnston (1981); Driver *et al.* (1987); Simpson (1989)). This is illustrated for a back ward facing step in figure 1.11. The separated flow displays unsteadiness with frequencies much lower than the incoming turbulence boundary layer characteristic frequency. In addition, the mixing layer has been shown to display a flapping motion at a low frequency that was found to scale on the free-stream velocity and the separation length. The vortical structures that are formed within the shear layer are shed into the downstream redeveloping boundary layer. Driver *et al.* (1987) intuited that the flapping motion is caused by this shedding, causing a mass imbalance that induces a pulsation of the separation bubble. Such a pulsation could be at the source of the large scale shock oscillations within the interaction. As can be seen from figure 1.11(a), the development of the new shear layer takes place under the original boundary layer. It is known that after reattachment, the boundary layer remains perturbed for large distances downstream (see Bradshaw & Wong (1972); Jović (1998)). The internal boundary layer structure recovers rather rapidly to a turbulent boundary layer state ($O(10h)$, where h is the height of the disturbance, see figure 1.11(a)). The turbulent quantities in the outer layer appear to take more than $100h$ to recover, indicating a long life time of the coherent structures generated in the mixing layer. Assuming that h is of the order of the boundary layer thickness δ_0 for a shock wave boundary layer interaction with significant flow separation, it can be concluded that the effect of the interaction is felt over an important downstream distance, the extent of which largely exceeds the measurement domains within most of the investigations.

(a)

(b)
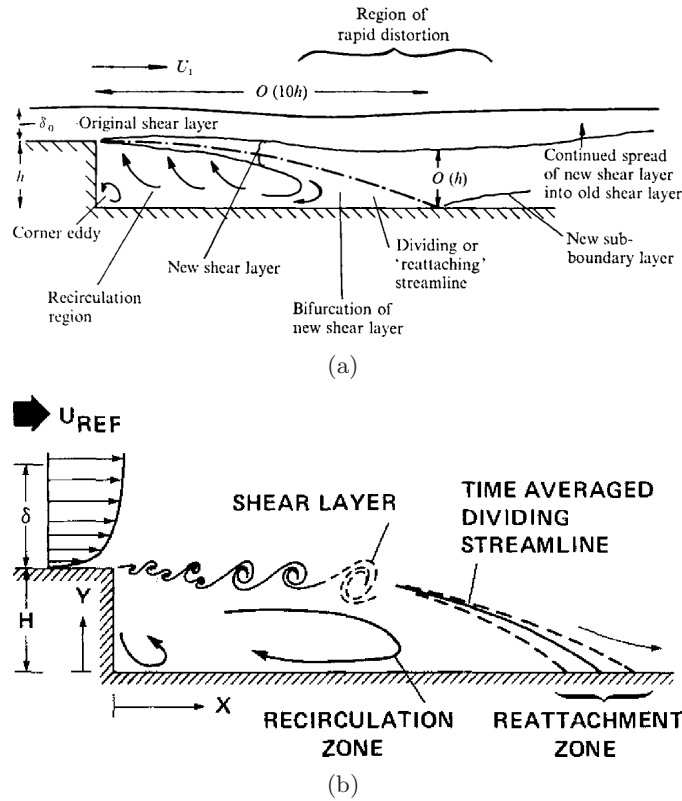
Figure 1.11: Schematic of the flow topology around the reattachment zone (a), from Bradshaw & Wong (1972); illustration of the development of a mixing layer over a separation region (b), from Driver *et al.* (1987).

1.2.2 Flow unsteadiness

One of the key issues in shock wave boundary layer interaction research is the origin of the low frequency of the large scale motion of the shock. Frequency spectra of the shock unsteadiness display a development from broadband for mild interaction strength to a frequency band clearly distinct from the turbulence frequencies, with a clear low frequency bump for well separated flows (Piponniau *et al.* (2009)), see figure 1.12. The three spectra correspond globally to the cases (b)-(d) reported in figure 1.7.

There is a debate over the sources of this unsteadiness. On the one hand, it has been proposed that the shock dynamics are governed by the upstream boundary layer. For instance, a statistical model relating shock excursions to random turbulence fluctuations has been proposed by Plotkin (1975). In addition, a correlation has been observed in literature between fluctuations in the upstream boundary layer and the shock foot motion (see Beresh *et al.* (2002); Ganapathisubramani *et al.* (2006b, 2007a); Humble *et al.* (2009a)).
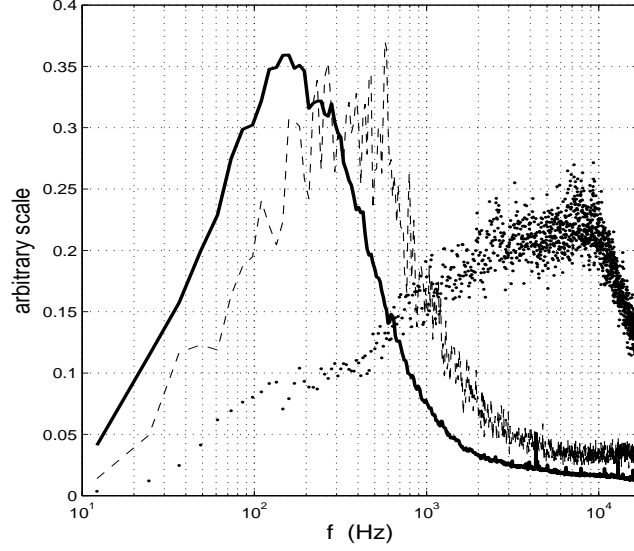
Figure 1.12: Power spectral density of the unsteady reflected shock for increasing flow deflection; $(\cdots)$ $\theta = 5.5°$, (---) $\theta = 8°$, (——) $\theta = 9.5°$, from Piponniau *et al.* (2009).

This mechanism is illustrated in figure 1.13(a). The organisation of the boundary layer into streamwise elongated low and high speed streaks, induced by the aforementioned hairpin packets and/or Taylor-Görtler vortices (see section 1.2.1), leads to the supposition that the low frequency shock dynamics are governed by the state of the upstream boundary layer. It is noted that due to the inherent lateral modulation of these flow features, they cannot be expected to induce a full span coherent shock motion; their spanwise effect can only be local. In addition, their characteristic time scales are fixed for a given boundary layer, and they can by consequence not explain the change in shock frequency with the interaction strength as observed in figure 1.12. On the other hand, a mechanism has been proposed for separation bubble dynamics based on the entrainment of mass by the mixing layer and subsequent vortex shedding (see Piponniau *et al.* (2009)), as illustrated in figure 1.13(b). The resulting time scales for the collapse of the mean separation bubble based on the entrainment rate are of the same order as those observed for the low frequency shock excursions. Moreover, the model explains the change in shock frequency with interaction strength observed in figure 1.12, leading to the supposition that it is the downstream separation bubble that governs the shock unsteadiness. This dependence on the separation bubble dynamics has also been observed in other literature (see

(a)

(b)
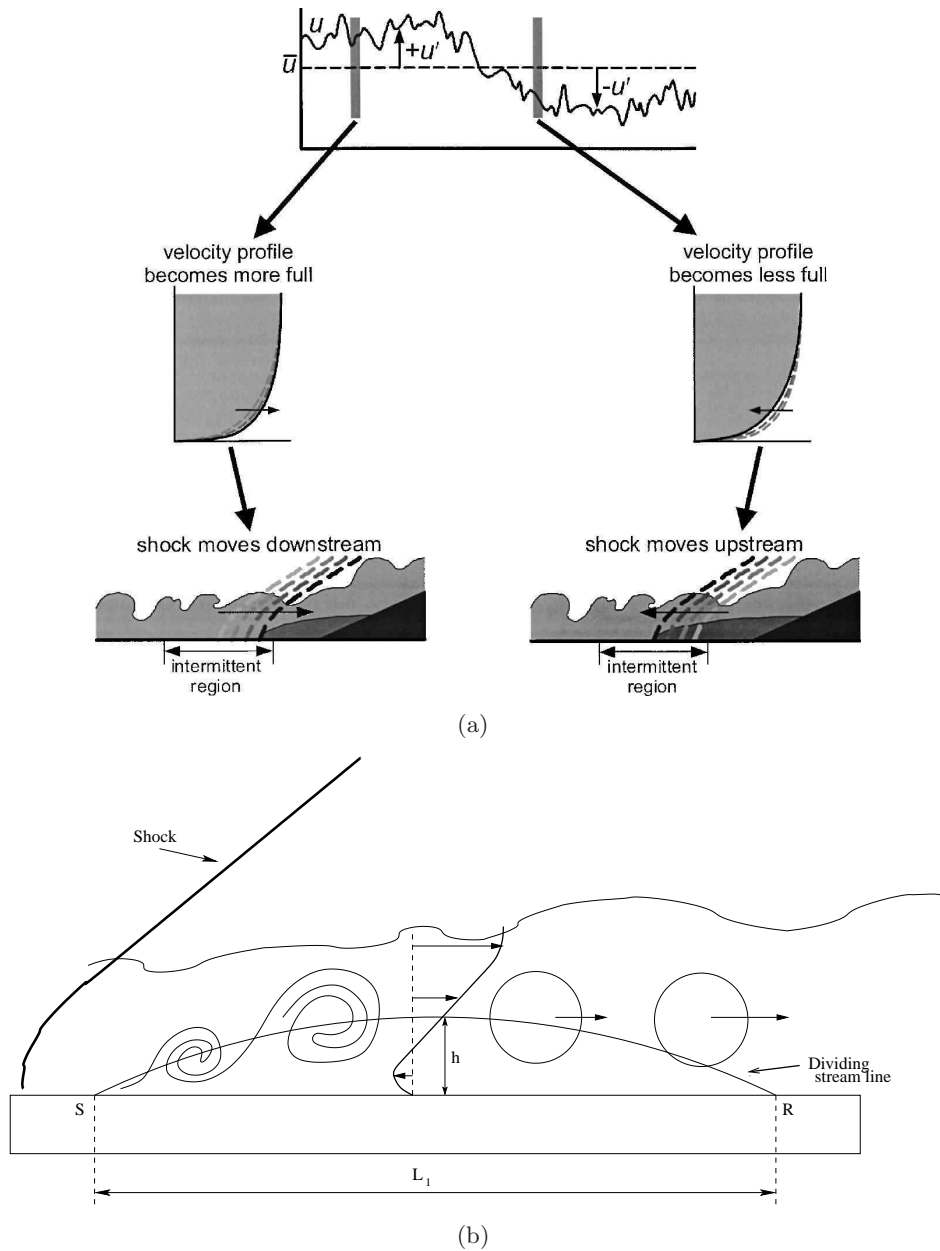
Figure 1.13: Proposed mechanisms for the unsteady shock motion: (a) upstream mechanism, governed by fluctuations in the boundary layer, from Beresh *et al.* (2002); (b) downstream mechanism, governed by a separation bubble pulsation induced by mass entrainment by the mixing layer, from Piponniau *et al.* (2009).

Erengil & Dolling (1991b); Thomas *et al.* (1994); Dupont *et al.* (2006); Wu
& Martin (2007, 2008); Touber & Sandham (2008)), putting in evidence a
statistical link between the bubble size and the shock motion, at least when
the flow is significantly separated. Computational results for well separated
interactions have also demonstrated that there is no significant dependence
of the large scale low frequency shock dynamics on the properties of the in-
coming boundary layer (see Wu & Martin (2007, 2008); Touber & Sandham
(2008)). In particular, Touber & Sandham (2008) have shown that the low
frequency unsteadiness is present even in absence of streamwise elongated
streaks in the inflow conditions. Furthermore, Pirozzoli & Grasso (2006)
argue that an acoustic resonance mechanism in the separation bubble might
be at the origin of the low frequency bubble dynamics. Evidence for an
acoustic feedback has also been found by Touber & Sandham (2008). A low
frequency bubble pulsation is also in agreement with the observations for the
backward facing step presented above (see section 1.2.1). In addition, this
mechanism provides an explanation for a full span coherent motion of the
shock front. Finally, there are indications for the existence of an inherent
instability of the mean separation bubble leading to pulsations, which would
be in further support of a downstream dependence (see Alizard & Robinet
(2008); Ehrenstein & Gallaire (2008); Touber & Sandham (2008)).

1.2.3   Mean field scaling

Concerning the mean flow organisation, there are several directly observable
effects of the Mach number and the Reynolds number. A first known effect
of the Reynolds number concerns the shock focalisation within the bound-
ary layer. For small Reynolds numbers, the shock foot constitutes a fan of
compression waves rather than a well focalised shock wave. Such a depen-
dence of the separation shock on the Reynolds number has been observed
in the case of compression ramps, both from experiments and DNS (see
Ringuette & Smits (2007); Wu & Martin (2008); Ringuette *et al.* (2008)). A
Mach number effect is the change in interaction geometry, as a direct conse-
quence of oblique shock wave theory. Considering the more indirect effects,
the Mach number has a documented influence on the spreading rate of the
mixing layer, see Papamoschou & Roshko (1988). This has its relevance
for the shock unsteadiness (see section 1.2.2), as has been demonstrated by
Piponniau *et al.* (2009).

   Considering the interaction length, it has been attempted in the past to
define a scaling of the length as a function of the shock intensity that takes
into account the effects of changes in the Reynolds number and the Mach
number. An example can be found in figure 1.14. The idea of relating the
interaction length to the normalised shock intensity in this manner finds
its origins in the Free-Interaction concept from Chapman *et al.* (1957), see
Délery & Marvin (1986). It proposes that $\frac{L}{\delta^*} \sim \frac{\Delta p}{\tau_w}$. The scaling incorpo-

rates the idea that the separation length is determined by the ratio of the pressure jump over the wall shear stress, which is interpreted as the ability of the boundary layer to resist to the pressure jump. The wall shear stress is hence seen as a shape parameter for the boundary layer, at least for low Reynolds number flows. This scaling has been found to successfully collapse data from multiple experiments under similar conditions, including measurements with heated walls (Laurent (1996); Benkemoun & Salaun (1988)). It is noted that Spaid & Frishett (1972) also investigated the effect of heat transfer, showing that wall cooling reduces the interaction length and the separation length for a given shock intensity. The generality of the scaling $\frac{\Delta p}{\tau_w}$ with respect to other Mach and Reynolds numbers, independent of the effect of flow geometry (for example compression ramp or incident reflecting shock), has not been confirmed. Other authors (see Ginoux (1973)) have considered with some success the ratio $\frac{\Delta p}{\frac{1}{2}\rho_e U_e}$ to scale the shock intensity, see figure 1.15. They remark that for turbulent boundary layers at sufficient Reynolds numbers, the occurrence of flow separation is Reynolds number independent. The effect of the Reynolds number seems indeed to depend on its magnitude and consequently the flow regime (laminar, transitional, turbulent), see figure 1.16. Several investigations have been performed concerning the Mach and Reynolds number effects on the interaction length (see for example Thomke & Roshko (1969); Spaid & Frishett (1972); Settles *et al.* (1976)), putting in evidence a dependence on the Reynolds number. On the contrary, some of the commonly use separation criteria (see Summerfield *et al.* (1954); Zukoski (1967); Schmucker (1973)) are a function of the Mach number and the flow deflection only, implying that the occurrence of separation is Reynolds number independent, at least for high Reynolds numbers, which is in accordance with Ginoux (1973). Considering these elements, the precise Mach number and Reynolds number effects on the interaction therefore seem to remain rather elusive.

1.3   Flow control

Flow control is seen as an important issue in future vehicle design, see Dolling (2001). The purpose of such control is either to reduce the shock strength with the aim of reducing the drag or to reduce the extent of the flow separation in order to suppress the unsteadiness, or both, see Délery (2000). Considering the first approach, examples are found in Bur *et al.* (1997) and Doerffer & Szluc (2002). Considering the second objective, various systems have been imagined. The most sophisticated concern the dynamic control using actuators in a feedback loop, some time dependent actuation, or a combination of multiple control methods (see for example Selig & Smits (1991); Bueno (2006); Bueno *et al.* (2006); Valdivia *et al.* (2009)). More crude solutions consists of static systems based on the generation of vortices
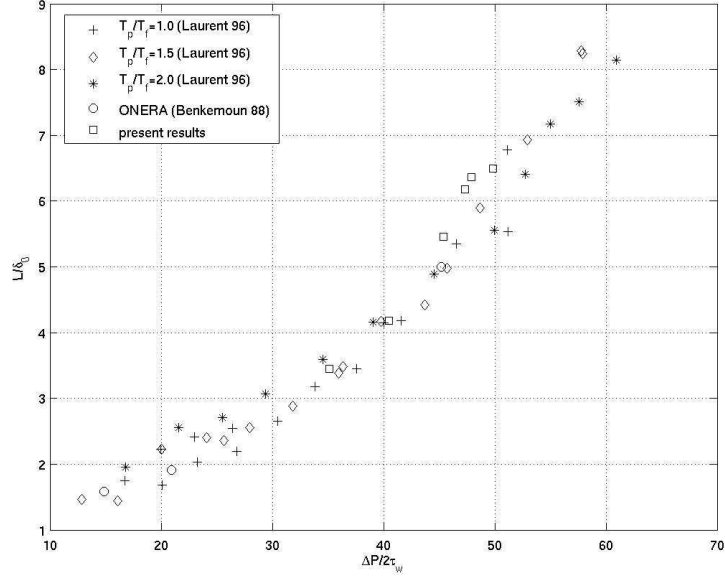
Figure 1.14: Interaction length dependence on the pressure jump over the incident shock normalised by the viscous shear stress at the wall for the incident reflecting shock interaction, from Dupont *et al.* (2006).

near the wall upstream of the interaction. One can think of sub-boundary layer vortex generators, consisting of mechanical devices fixed at the wall (see for example Ashill *et al.* (2001); Bueno *et al.* (2006); Holden & Babinksy (2007); Bruce & Babinsky (2008a); Blinde *et al.* (2009a); Lee *et al.* (2009); Lee & Loth (2009); Bur *et al.* (2009)). A review of different types of such mechanical control devices and their effectiveness is given by Lin (2006). An alternative is based on the injection of fluid by means of an array of continuous Air Jet Vortex Generators (AJVGs) in the upstream boundary layer. An approach that combines fluid injection with separation control is of particular interest due to the potential of integrating flow control with transpiration cooling, see Reijasse & Boccaletto (2008). This case has been studied principally in the transonic or low supersonic flows (see for example Yamagata *et al.* (2009); Yang & Wang (2005)). Therefore, the current work examines this problem in the fully supersonic flow domain, where only limited data is available, one of the few examples being Doerffer & Szwaba (2004). In addition, this investigation provides the possibility of evaluating the influence of the upstream boundary layer on the shock unsteadiness.

The documentation concerning upstream control with inclined air jet vortex generators is rather sparse. However, quite abundant literature is
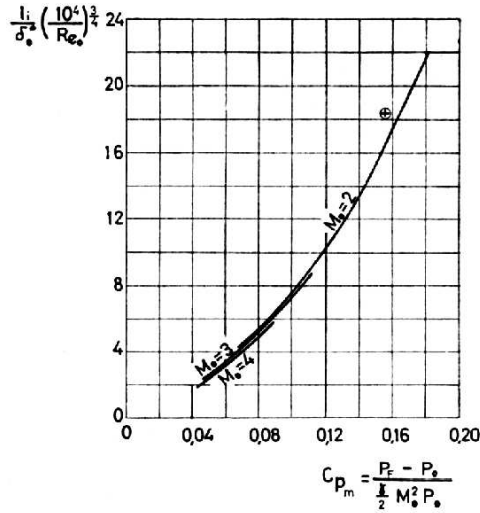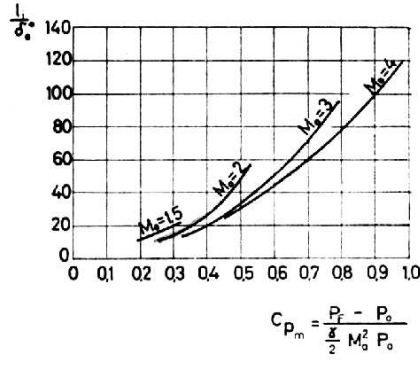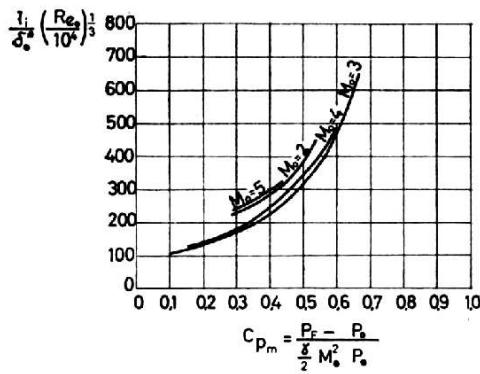
Figure 1.15: Interaction length dependence on pressure jump over the complete shock system normalised by the inertial forces in the free-stream for the incident reflecting shock interaction; (a) laminar regime; (b) transitional regime; (c) turbulent regime; from Ginoux (1973).

available in the field of jets in crossflows, particularly in the subsonic regime (see Kamotani & Greber (1972); Andreopoulos & Rodi (1984); Fric & Roshko (1994); Smith & Mungal (1998); Cortelezzi & Karagozian (2001)). The near field vortical structure is illustrated in figure 1.17. Fric & Roshko (1994) have made a detailed investigation of the wake generated by the jet. This wake is not unlike a classical cylinder wake, with the distinction that the wake vortices have their termination points both on the wall and on the jet itself. The development of the jet and the wake are hence linked and the
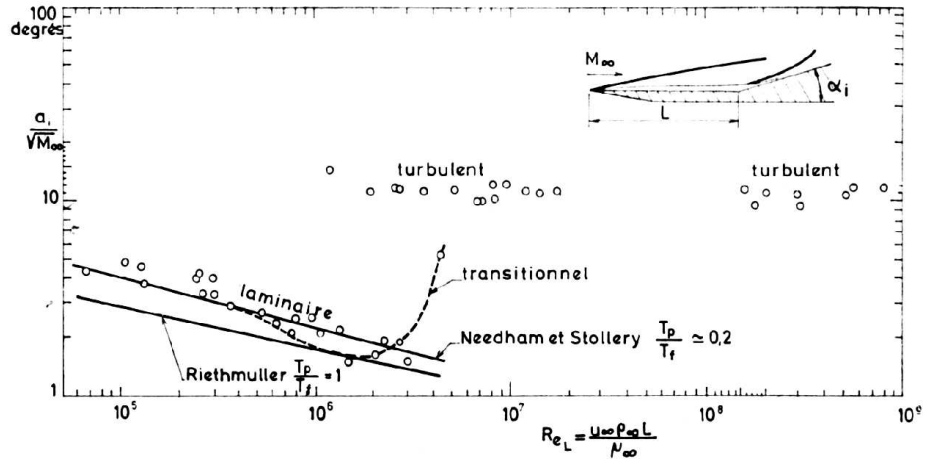
Figure 1.16: Dependence of the occurrence of flow separation on the development length based Reynolds number for different flow regimes (laminar, transitional, turbulent); note that the onset of separation becomes Reynolds number independent for turbulent flows; from Ginoux (1973).

formation mechanism was found to be different and distinct from the shedding of vortices in a solid cylinder wake. In the far field, the jet generates a pair of counter rotative vortices of equal strength. The generation of the vortex pair has been explained theoretically by Broadwell & Breidenthal (1984). They find their origin in the jet momentum that is injected into the crossflow, which can be interpreted as a transverse force, in other words 'lift'. As in the case of an airplane wing, it is this lift force that generates the vortex pair.

It may hence be expected that for an inclined jet in crossflow, as used in the current work, these two main components (the wake and the co-rotative vortex pair) are still present. However, it would be reasonable to expect that the vortices will no longer be of equal strength. This is confirmed by the results from Yamagata *et al.* (2009); Yang & Wang (2005). Concerning the effect of the vortices on the separation bubble, Yamagata *et al.* (2009), considering the control of the reattachment of a separated shear layer behind a backwards facing step at low subsonic conditions, shows that the reattachment line remains quasi-two dimensional in spanwise direction. This is explained by the fact that the vortex pair affects only the upper portion of the detached shear layer, while the lower portion remains unaffected. Such a behaviour appears to be confirmed by the numerical results from Lee & Loth (2009), which indicate that the longitudinal vortex pairs generated by mechanical vortex generators are also lifted over the separation region. On the other hand, Doerffer & Szwaba (2004) and Bur *et al.* (2009) show by
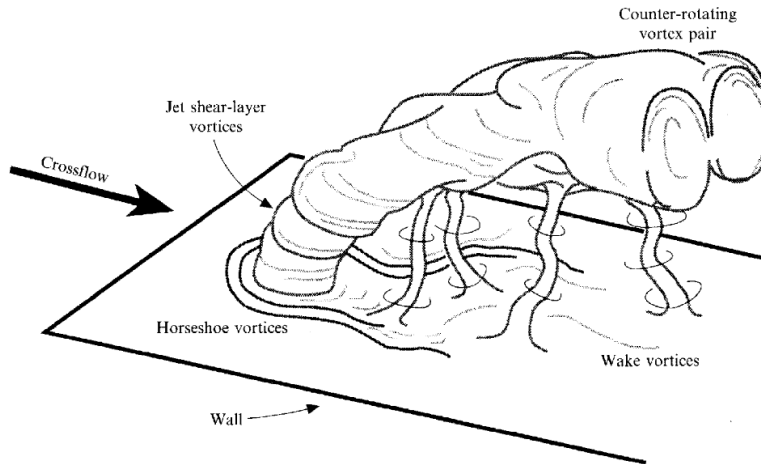
Figure 1.17: Near field vortical structures generated by a jet in crossflow, from Fric & Roshko (1994).

means of wall flow visualisation that the vortices leave traces within the separation zone, but without suppression of the flow separation. The vortices cause the separation line to become highly corrugated with a reduction of the separation bubble size for Doerffer & Szwaba (2004). In the case of Bur *et al.* (2009), the separation bubble topology is completely altered, inducing a spanwise modulated organisation of cells with strong separation interrupted by streaks of attached flow.

1.4 Problem statement

The aim of the current research is to characterise the mean flow topology and the sources for the unsteady behaviour of the incident reflecting shock interaction as a function of the incident shock intensity, the Reynolds number and the Mach number. To achieve this aim, a number of objectives have been set:

- Evaluate the potential of the application of the Dual-PIV measurement technique for the analysis of high speed flows incorporating a large range of time scales (at least two orders of magnitude).

- Investigate the effect of the imposed shock intensity and the influence of the Reynolds number on the interaction unsteadiness. It is verified which mechanisms are present in different interactions by systematically varying the interaction strength. Furthermore, the universality of these mechanisms with respect to an order of magnitude variation

in the Reynolds number is evaluated for weak shock intensities (incipient separation). This is done with a special attention to upstream and downstream effects.

- Characterise of the effect of flow control by means of upstream air jet vortex generators. This enables the evaluation of the influence of upstream disturbances on the interaction unsteadiness.

- Define a scaling that takes into account the observed effects of the Reynolds number and the Mach number. The validity of this scaling is verified with respect to interactions documented in literature, considering both compression ramp and incident shock interactions. It is evaluated whether this scaling enables to make prediction with respect to the separation state and whether it can be linked to the dependence of the unsteadiness on upstream and downstream mechanisms.

1.5 Thesis outline

This thesis consists of two parts: The first part contains the experimental methods and results, and the second part concerns the analyses that have been performed. The first part treats in the first place the two flow facilities that have been used, the different experimental techniques that were employed during the investigation, and the validation of the measurement data. Furthermore, the inflow conditions, the mean and fluctuating statistics, and the instantaneous results are presented for all interactions. In addition, the temporal characterisation through Dual-PIV and the results from the investigation of the effect of upstream control are detailed. In the second part, a new spatial scaling is derived for the interaction and the sources of the reflected shock unsteadiness are investigated.

Part I

Experimental methods and results

Chapter 2

Experimental facilities

During the investigation, experiments were performed in two facilities: the TST-27 transonic supersonic wind tunnel of the High-Speed Aerodynamics Laboratory at Delft University of Technology and the S8 Supersonic wind tunnel at the Institut Universitaire des Systèmes Thermiques Industriels in Marseille. The most important parameter distinguishing both facilities is the momentum thickness based Reynolds number, which is a factor 10 higher for the TST-27 as compared to the S8. Another specificity of the TST-27 as opposed to the S8 is that it operates over a range of Mach numbers. On the other hand, the S8 is equipped with a shock generator with continuously variable angle, enabling the investigation of a large range of shock strengths. In addition, the S8 was equipped with an array of upstream air jet vortex generators for interaction control experiments. It is also a continuously running facility, making long data runs possible for conditional analysis. The current investigation has taken advantage of the combined use of both facilities to obtain measurements of the same flow phenomenon over a range of measurement conditions (Reynolds number, Mach number, shock strength, interaction control) and using of different measurement systems, enabling a thorough comparison and validation of the observations.

The subsequent sections give a detailed description of both installations and the experimental set-up for the shock wave boundary layer interaction experiments, including an overview of the relevant measurement conditions.

2.1 TST-27 Transonic Supersonic Tunnel Delft

The high Reynolds number experiments were performed in the TST-27 transonic supersonic wind tunnel of the High-Speed Aerodynamics Laboratory at Delft University of Technology, see figure 2.1, with test section dimensions of $280mm$ (width) $\times$ $255mm$ (height). It is a blow-down facility that can operate at Mach numbers ranging from 0.5 to 0.85 and from 1.15 to 4.2 and a unit Reynolds number in the range of 30×10^6 to $130 \times 10^6 m^{-1}$, with

a run time of up to 300 seconds. The Mach number is set by means of a continuously variable throat and flexible upper and lower nozzle walls. The stagnation pressure can be set independently with typical values ranging from 2.0 to 3.0bar, the stagnation temperature is determined by the ambi-
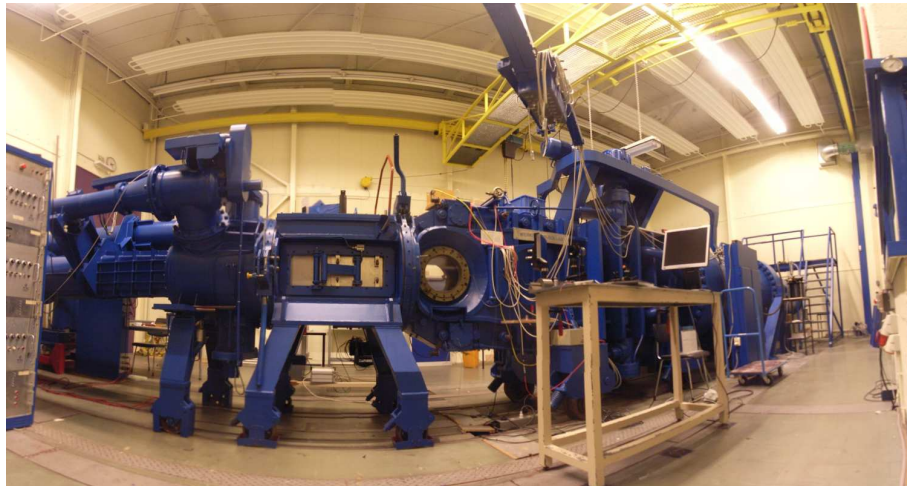
(a)
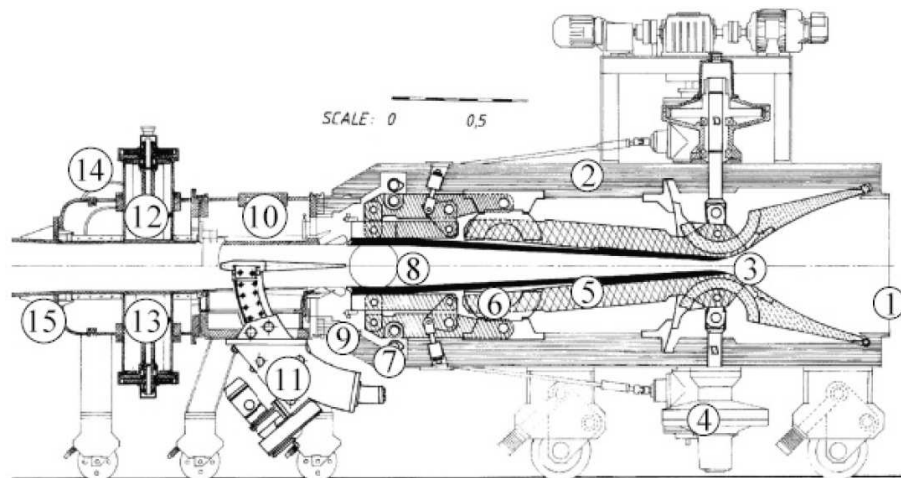
(b)

1.	Settling chamber	6.	Node bearing	11.	Angle of attack mech.
2.	Nozzle section	7.	Boundary layer mech.	12.	Choke section
3.	Variable nozzle	8.	Supersonic test section	13.	Choke body
4.	Adjustable screw mech.	9.	Rapid clamp coupling	14.	Bleed-off device
5.	Semi-flexible wall	10.	Model support section	15.	Outlet diffuser

Figure 2.1: TST-27 facility of the TU Delft; (a) photo of the wind tunnel; (b) schematic representation (courtesy TU Delft); the flow is from right to left.

ent temperature of the air storage vessel. The velocity drift inherent to blow down operation has been determined to be approximately $5 \times 10^{-2} ms^{-2}$ corresponding to a total temperature transient of $6 \times 10^{-2} K s^{-1}$, see appendix A.1.2. The effect on the mean velocity is less than 1% of the free-stream velocity over a complete run duration of 60 seconds, approximately equal to the free-stream turbulence level as measured by HWA (see Van Oudheusden & Scarano (2008)).

During the current experimental investigation, the measurement conditions were a nominal free-stream Mach number of $M_e = 1.69$ ($U_e = 448 ms^{-1}$), a total temperature of $T_0 = 273K$ and a total pressure of $p_0 = 2.3bar$ resulting in a free-stream unit Reynolds number of $36 \times 10^6 m^{-1}$. A nominally two-dimensional supersonic boundary layer develops on the wind tunnel nozzle wall with transition to turbulence occurring naturally. The test section wall is a flat plate forming an integral part of the nozzle wall. Its distance to the nozzle throat is approximately two meters yielding a Reynolds number of $Re_x = 7.2 \times 10^7$ at the location of the inlet conditions for the interaction. At this point, the turbulent equilibrium boundary layer has a thickness of $\delta_{99} = 17.2mm$, a Reynolds number based on momentum thickness of approximately $Re_\theta = 50,000$ and a friction coefficient of $C_f = 1.5 \times 10^{-3}$ (obtained from a log-law of the wall fit). Further details are provided in the table 2.1. See appendix 4.1 for details on the incoming boundary layer characterisation.
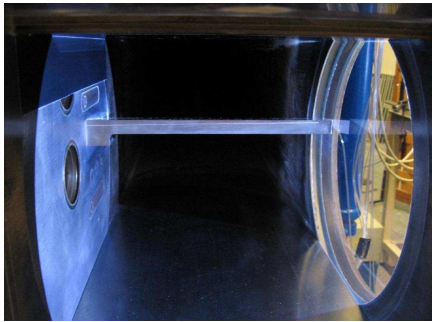
Figure 2.2: Experimental configuration: the test section with the sidewall mounted shock generator as viewed from downstream. The viewing window is on the right.

The boundary layer on the tunnel ceiling is subjected to a shock wave produced by a rigid side-wall mounted wedge ($100mm$ chord, 96% span of the test-section, leaving a gap of $10mm$ between the tip of the wedge and the Schlieren window to prevent damage to the latter) placed in the external flow at a vertical distance to the wall of $150mm$, see figure 2.1. The generator incidence angle was corrected for the wall inclination angle of $\varepsilon = 0.22°$ to obtain an imposed flow deflection of $\varphi = 6.0°$, corresponding to an interaction of the incipient type. The deflection angle measured with respect to the tunnel axis will hence be slightly larger ($\varphi = 6.2°$). The shock generator was mounted such as to induce an interaction in the centre of the optical access window. Simultaneously it was assured that the point of impact of the expansion fan emanating from the shoulder of the wedge on the recovering boundary layer was positioned as

far downstream as possible (approximately 3δ behind the interaction). A
stable and reproducible flow was achieved over both sides of the wedge even
at this relatively low Mach number, which is a condition where the wind
tunnel is sensitive to choking (see also section A.1.1).

2.2   S8 Supersonic wind tunnel Marseille

The low Reynolds number experiments were performed in the S8 Supersonic
wind tunnel at the Institut Universitaire des Systèmes Thermiques Indus-
triels (IUSTI) in Marseille, see figure 2.3, with test section dimensions of
$120mm$ (width) $\times$ $170mm$ (height). It is a closed-loop continously running
hypoturbulent facility with a Mach number of 2.3 determined by the fixed
throat, and a free-stream unit Reynolds number of $5.5 \times 10^6 m^{-1}$, with a
run time of up to four hours, limited by the cooling water supply. The stag-
nation pressure can be set independently with typical values ranging from
0.15 to $0.9atm$. The stagnation temperature is determined by the ambient
air temperature and is kept constant to within $0.2K/hour$. The tunnel has
a particularly low free-stream turbulence level of approximately 0.1% of the
free-stream velocity.

During the current experimental investigation, the measurement con-
ditions were a nominal free-stream Mach number of $M_e = 2.28$ ($U_e =
550ms^{-2}$), a total temperature of $T_0 = 295K$ and a total pressure of $p_0 =
0.507bar$ ($0.5atm$). A nominally two-dimensional supersonic boundary layer
develops on the wind tunnel nozzle wall with transition to turbulence being
ensured by straight turbulator strips slightly upstream of the throat. The
test section wall is a flat plate which is aligned flush to the nozzle insert
wall. The start of the test section is at $350.6mm$ downstream from the
nozzle throat. The inlet conditions for the interaction are taken at a dis-
tance of approximately $650mm$ from the throat, yielding a Reynolds number
of $Re_x = 3.6 \times 10^6$. At this location, the turbulent equilibrium boundary
layer has a thickness of $\delta_{99} = 10mm$, a Reynolds number based on momen-
tum thickness of approximately $Re_\theta = 5,000$ and a friction coefficient of
$C_f = 2.1 \times 10^{-3}$ (obtained from a log-law of the wall fit). Further details
are provided in the table 2.1. See section 4.2 for details on the incoming
boundary layer characterisation. It is remarked for completion that the lon-
gitudinal dimensional coordinates, X, for the Marseille dataset are measured
with respect to the start of the original tunnel measurement section, which
was $388.6mm$ downstream of the nozzle throat. The start of the current
measurement section is $38mm$ farther upstream.

The boundary layer on the tunnel floor is subjected to a shock wave
produced by a full-span sharp edge plate ($160mm$ chord, 99% span of the
test-section) placed in the external flow. The imposed flow deflection angles
in the current investigation ($\varphi = 5.5°$, $8.0°$ and $9.5°$) range from incipient

separation to well developed separation. The angle of incidence of the shock generator is actuated by a mechanism conceived to obtain an approximately fixed impact point of the incident shock on the tunnel floor (located at $X = 337mm$). The generator has been calibrated to obtain the prescribed

(a)
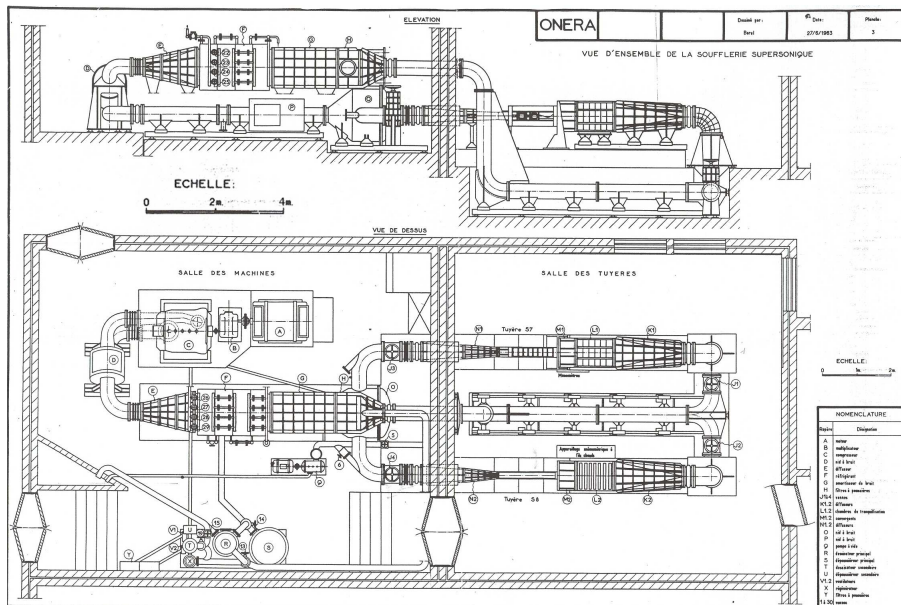
(b)

Figure 2.3: S8 facility of the IUSTI; (a) photo of the wind tunnel, with the S8 test section on the left hand side (courtesy S. Piponniau); (b) schematic representation, side-view and top-view respectively, with the S8 test section in the lower half of the top-view drawing (courtesy ONERA).
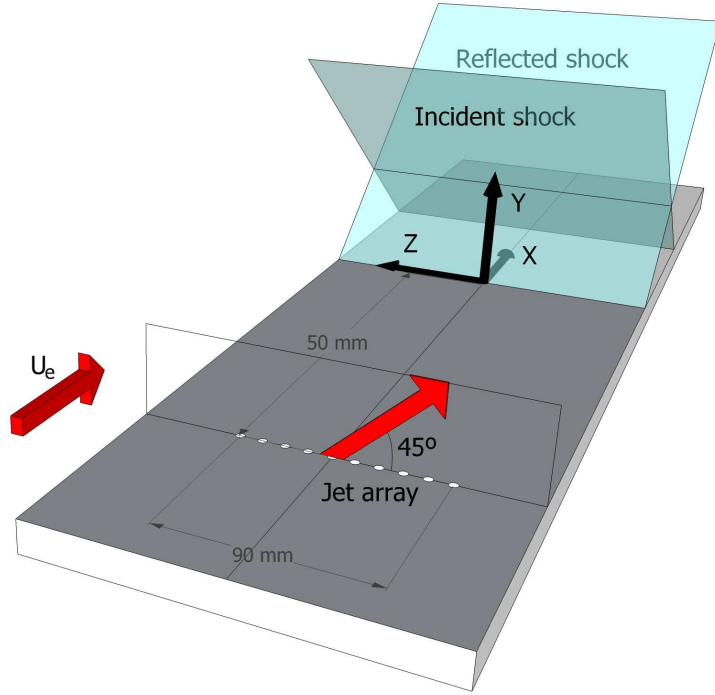
Figure 2.4: Schematic representation of the AJVG experiment.

flow deflection angle with respect to the tunnel axis. The opening angle of
the test section wall with respect to the tunnel centre line was determined to
be approximately $\varepsilon = 0.16°$. The estimated impact point on the boundary
layer of the expansion fan emanating from the shock generator shoulder is
11δ behind the extrapolated impact point of the incident shock.

2.3   Interaction control experiment set-up

A row of Air Jet Vortex Generators (AJVGs) was installed in the S8 Super-
sonic wind tunnel to study the effect of upstream disturbances on the mean
and unsteady flow characteristics for the control of a shock wave boundary
layer interaction, see figure 2.4 for a schematic representation of the experi-
ment. The vortex generators are made of a row of ten holes, with a spanwise
pitch of $d = 10mm$ (about one boundary layer thickness). The spanwise ex-
tent of the row of AJVGs is $90mm$ for a channel span width of $170mm$. One
orifice is placed on the axis and the others are disposed in an asymmetric way
on each side (looking in downstream direction, 4 jets are located on the left
side of the tunnel centre line and 5 on the right). The diameter of the holes is
$\phi = 0.8mm$ ($\phi < d/10$). The row is oriented perpendicular to the flow. The
axis of the holes is inclined within the spanwise-wall-normal-plane under an

(a)   (b)

(c)
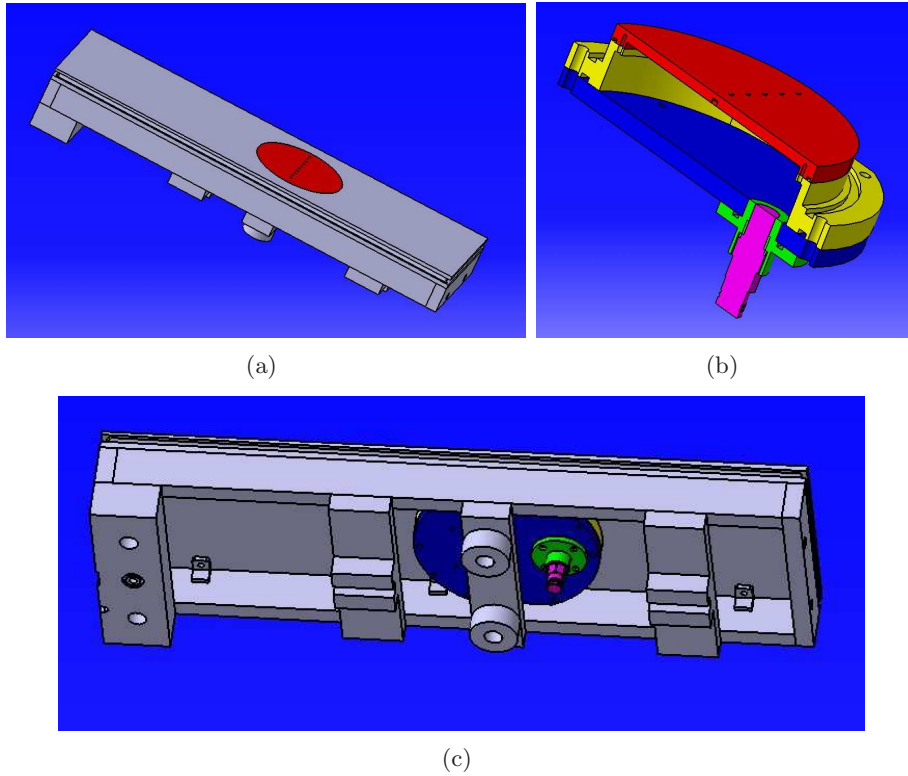
Figure 2.5: AJVG array: (a) top view; (b) settling chamber cavity with the mounting for the pressure transducer, cut through view; (c) bottom view.

angle of $\psi = 45°$, with the jets blowing towards the right when looking in downstream direction. The design of the AJVG set-up is such that the jet row is placed on a removable cover, it can be replaced by a dummy cover or by another upstream control experiment. The AJVG array is located at $X = 212.5mm$, approximately $50mm$ (5δ) upstream of the reflected shock foot and $124.5mm$ upstream of the extrapolated wall impact point of the incident shock (the dimensional coordinates for the AJVG-experiment are defined with respect to the tunnel reference frame, see section 2.2). Ambient air is fed to the jets orifices from outside by means of natural suction due to the under pressure in the test section (approximately $0.04bar$).

A settling chamber is installed underneath the array of AJVGs to assure a homogeneous and stable air injection along full the span of the jets. It consists of a circular box containing a porous medium. Air temperature and pressure in this chamber are measured by respectively a thermocouple and a unsteady pressure sensor. The temperature in the chamber is $T_{0_{jets}} \approx 290K$, which roughly equals the stagnation temperature of the wind tunnel or the ambient temperature in the room of the experiments. It was verified that the

pressure spectrum in the chamber filled with the porous medium does not presents any resonant peaks. The stagnation pressure in the chamber can be adjusted manually by fixing the volume flux injected by the jet array, yielding pressures in the range of $p_{0_{jets}} = [0.04 - 0.50]\, bar$. The setting $0.04 bar$ corresponds to 'jets off' since the pressure is in equilibrium with the static pressure in the test section.

The AJVG array design is shown in figure 2.5, with a 3D top view showing the removable cover with the AJVG array as installed in the test section wall (figure 2.5(a)), a 3D bottom view of the ensemble (figure 2.5(c)), and cut through view of the AJVG settling chamber cavity without porous medium and with the mounting for the pressure transducer (figure 2.5(b)).

2.4　Overview of measurement conditions

The following inlet measurement conditions have been obtained during the current SWBLI investigation, see table 2.1. The directly measured quantities are the Mach number (through a static pressure orifice in the test section wall in the TST-27 and by means of a pitot-tube in the free-stream in the S8), the total pressure, the total temperature (S8 only), and the free-stream velocity (by means of PIV). The boundary layer thickness corresponds to $\delta_0 = \delta_{99}$, the thickness where 99% of the free-stream velocity is attained. The required density profile for the determination of the compressible boundary layer length scales (δ^* and θ, with $H = \frac{\delta^*}{\theta}$) was estimated from the velocity data using the modified Crocco-Busemann relation, see White (1991), assuming adiabatic wall conditions and a recovery factor $r = 0.89$. The incompressible values are also specified (δ^*_{ic} and θ_{ic}, with $H_{ic} = \frac{\delta^*_{ic}}{\theta_{ic}}$). The friction velocity u_τ, and hence the friction coefficient C_f, have been obtained from the slope fit to the log-law of the wall. The required value of the viscosity coefficient has been obtained using Sutherland's law, see White (1991). For reference, the value of y^+ at $1mm$ from the wall is given ($y^+_{unit} = \frac{u_\tau}{\nu_w}$ in mm). The approximate development length based Reynolds number Re_x is defined at the interaction location, see sections 2.1 and 2.2. For more details, reference is made to chapter 4.

Table 2.1: Measurement conditions.

Facility	TST-27	S8	−
Variable	High Reynolds number	Low Reynolds number	Units
M_e	1.69	2.28	−
U_e	448	550	ms^{-1}
T_0	273	295	K
p_0	230	50.7	kPa
φ	6.0	5.5; 8.0; 9.5	$degrees$
δ_0	17.2	10.2	mm
δ^*	3.3	3.0	mm
θ	1.4	0.9	mm
H	2.4	3.5	−
δ_{ic}^*	2.0	1.7	mm
θ_{ic}	1.6	1.2	mm
H_{ic}	1.3	1.4	−
C_f	1.5×10^{-3}	2.1×10^{-3}	−
u_τ	15.1	24.7	ms^{-1}
y_{unit}^+	562.4	73.89	mm^{-1}
Re_{unit}	3.6×10^7	5.5×10^6	m^{-1}
Re_x	7.2×10^7	3.6×10^6	−
Re_θ	$50,000$	$5,000$	−

Chapter 3

Flow diagnostics methods

During the course of the investigation, different flow diagnostics methods have been employed. The most extensive use has been made of Particle Image Velocimetry (PIV), in different implementations. However, also other techniques have been employed to obtain qualitative or quantitative flow data, such as Schlieren visualisations and Hot Wire Anemometry (HWA). The following chapters describe the principle measurement techniques that have been implemented.

3.1 Schlieren visualisation

3.1.1 Working principles

Schlieren visualisation is a qualitative flow visualisation method based on the propagation of light through a medium of varying refractive index. The technique is sensitive to the gradient of density and hence regions of varying density within the flow domain will appear either darker or brighter on the resulting image, depending on the direction of the gradient. Zones of constant density will have a uniform light intensity. The sensitivity and directivity can be adjusted by means of a knife edge filter in the focal point of the optical set-up. The resulting flow visualisations are recorded by a camera. With the standard implementation, only time averaged realisations can be obtained. Depending on the shutter time, the visualisations are more or less time-averaged and the flow will appear more or less smooth. The technique cannot distinguish between flow unsteadiness or spanwise three-dimensionalities. One can obtain instantaneous measurements by means of spark Schlieren, but Schlieren visualisations will however always represent the integrated density gradient along the optical path. Hence spanwise flow variations cannot be distinguished. Further details on qualitative optical flow visualisation techniques can be found in Settles (2006).

3.1.2   Experiment set-up

The implementation used during the current investigation consists of a light source, a planar mirror, a parabolic mirror and imaging optics, yielding a very compact set-up. The light source generates a slightly conical beam which is directed into the test section by the plane mirror. Care is taken that the axis of the light beam is perpendicular to the optical access window of the wind tunnel. After traversing the test section, the beam is redirected towards the source by a parabolic mirror. It therefore traverses the section a second time, reflecting again on the planar mirror and forming a focal point just next to the light source before entering the imaging optics. The beam then is transformed into an image on the image plane of the camera. A Schlieren knife is located in the focal point. It was oriented parallel to the flow direction in the current investigation to visualise the shocks, expansion fan and density gradients within the boundary layer and the separation bubble. The image was recorded using a shutter time of $1/125s$ on a *IL-FORD FP4 Plus* black and white film, which was developed in house. The scanned digital images were processed using the *GIMP*-software to extract length-scales and shock angles.

3.2   Hot wire anemometry

3.2.1   Working principles

Hot wire anemometry (HWA) is a method for obtaining single point, time resolved, fluid velocity measurements (or mass flux (ρu) in the case of compressible flows). The hot wire probe consists of a tungsten wire supported by two prongs and the operating principle is based on the Joule effect. The wire probe is heated by a current passing through it (hence the name) while being cooled at the same time by the fluid flowing around the wire. The implementation of the technique used in the current investigation is the constant temperature anemometer (CTA). In this form of HWA, a feed back control maintains a constant wire temperature by varying the voltage over the wire. The required voltage can be directly related to the mass flux by means of an *a priori* determined calibration curve (King's Law). The disadvantage of this measurement technique is that it is a single point technique, hence not providing full field flow data. In addition, it is not directionally sensitive and can only measure the absolute velocity. The advantage however is that it has a high frequency response, which enables the acquisition of time resolved continuous data for a wide range of time scales, even in supersonic flows. More information, particularly on measurements in high speed flows, can be found in (amongst others) Smits & Dussauge (2006), Dupont & Debiève (1992) and Smits *et al.* (1983).

3.2.2 Experiment set-up

During the current investigation, measurements have been made with a constant temperature anemometer, *Streamline* manufactured by *Dantec Dynamics*, operated in a symmetric bridge configuration. The diameter of the hot wire is $5\mu m$ and its length is $0.75mm$. It was operated at an overheat ratio of $a_w = 0.6$. In such conditions, the bandwidth of the CTA system is about 80 kHz. For the shock unsteadiness measurements, the analog signal was sampled and acquired at a rate of 100 kHz using a National Instrument converter (NI6133). The bandwidth of the applied filter is about 30 kHz. The size of the acquired blocks is 1×10^6 samples.

A calibration of the hot wire was made in the external flow upstream of the interaction by varying the stagnation pressure of the wind tunnel facility, which leads to a variation in the mass flow for a fixed Mach number. This enabled the determination of the constants in King's Law (which specifies the output voltage E delivered by the hot wire as a function of the mass flux ρu) by means of a least square fit. The obtained values are given by equation 3.1. These calibration constants correspond to the expected values for this type of wire in supersonic conditions.

$$
\begin{aligned}
E^2 \quad &= \quad A\rho u^n + B \\
\text{with:} \quad &A = 0.25 \\
&B = 0.73 \\
&n = 0.58
\end{aligned}
\tag{3.1}
$$

The King's Law was inverted to derive ρu from the measured wire voltage. Some narrow peaks in the spectra of the signal appeared, which can be associated with classical strain gauge effects. The signal variance was corrected of such effects.

3.2.3 Measurement programme

Hot wire anemometry has been employed for the low Reynolds number case with three specific aims: for the characterisation of the shock unsteadiness, to quantify the noise radiated by the interaction, and in combined PIV-HWA measurements as a preliminary study for the potential of such an approach for a conditional analysis. The noise measurement method and results, as well as the full unsteadiness characterisation, are described in Souverein *et al.* (2008a). Table 3.1 shows the hot wire measurement programme for the shock unsteadiness characterisation at $\varphi = 9.5°$ that has been carried out for the AJVG experiment. All measurements were made at $M_e = 2.3$, $p_0 = 0.5atm$, $T_0 = 297K$ and $T_{0_{jets}} = 289K$.

Table 3.1: HWA measurement programme.

Angle	HWA position		Range	AJVG settings	
$\theta[deg]$	$Y[mm]$	$X[mm]$	$\Delta X[mm]$	on/off	$p_{0_{jets}}[bar]$
9.5°	18	292.0	$[-6:2:6]$	off	0.04
9.5°	18	296.0	$[-6:2:6]$	on	0.4

3.3 Particle image velocimetry

3.3.1 Working principles

Particle Image Velocimetry is a quantitative flow visualisation technique that provides full field velocity information. The working principle is based on the suspension of tracer particles in a fluid flow. Quantitative velocity field data can be obtained through the illumination of these particles in rapid succession using light sheets created by means of a pulsed laser. The resulting particle images are then recorded, allowing the evaluation of the motion of groups of particles by comparing their displacement from one image frame to the other. Since the interval between both recordings is known, the velocity of the particle group can be computed, enabling the reconstruction of the complete velocity field. An example of the set-up of a PIV arrangement can be found in figure 3.1.

The recording of the different image patterns is nowadays generally done digitally by means of a CCD sensor. The individual recordings are stored on the hard disk of a computer. The evaluation of the displacement from the images is done by means of statistical techniques, notably cross-correlation for double frame/single exposure images. To this purpose, the images are divided into small regions, so called interrogation windows. Each interrogation window in the first exposure is cross-correlated with a region in the second exposure. The best estimate for the displacement of the particle images contained inside the interrogation window is obtained at the location where the highest correlation occurs. The interrogation window size is limited by the maximum particle displacement, the general rule of thumb being that the displacement should be $\frac{1}{4}$ of the window size. The displacement estimate can be improved by implementing an interative procedure, using the estimate from the preceding step as an off-set for the next. This way, a significant reduction in the final window size can be obtained (and hence an increased resolution), since it is no longer limited by the $\frac{1}{4}$-rule. A lower limit for the window size is however imposed by the seeding density, since sufficient tracer particles should be present to allow for a *statistical* displacement estimate. Another extension is the implementation of deforming windows to compensate for the rotation and shear of the particle group within the interrogation window between the two exposures, hence improv-
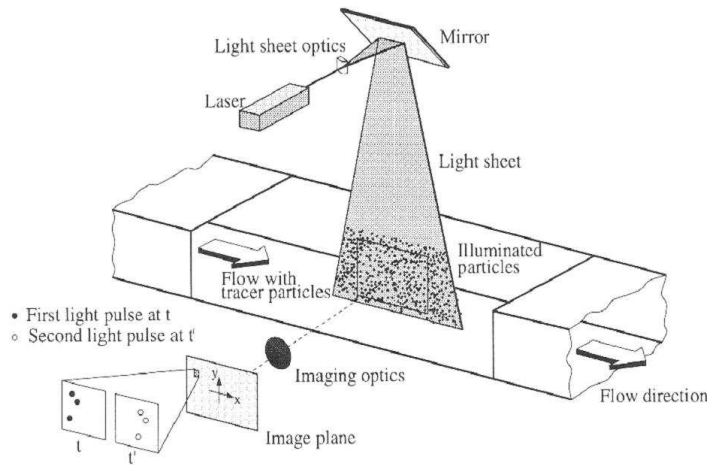
Figure 3.1: PIV operating principle, from Raffel *et al.* (2007).

ing the statistical correlation between the particle images.

Different implementations of this measurement technique are in use today. Some examples of extensions of the bacic operating principle are Pano-PIV, 3C-PIV, Tomo-PIV and Dual-PIV. Starting from the conventional two component PIV (2C-PIV) set-up with a single camera and a single double-pulsed laser, on can augmented the system with a second camera, also in two-component mode, to create a panoramic field of view (panoramic PIV, or Pano-PIV). The acquired images from each camera can subsequently be stitched together (provided that there is an overlap between the images and that the cameras were correctly aligned) and treated as a single image. This creates data fields with a large aspect ratio, ideal for elongated flow domains. Another implementation is three-component PIV (3C-PIV), also called stereoscopic PIV (or Stereo-PIV). In this case, two cameras are put under an angle with respect to eachother and with respect to the laser plane, enabling the observation of the out-of-plane displacement of the tracer particles within the light sheet. The third velocity component (perpendicular to the measurement plane) can hence be retrieved from the two-component velocity fields obtained from each camera by means of a parallelogram reconstruction. This procedure requires knowledge of the geometry of the set-up, which is obtained in practice by means of a geometric calibration procedure. An extension of this technique is tomographic PIV (Tomo-PIV), see Elsinga (2008) and Elsinga *et al.* (2006). While Stereo-PIV still assumes that measurements are made in an infinitely thin plane, operating on two-dimensional projections of the velocity field, Tomo-PIV abandons this assumption. In the case of Tomo-PIV, the third velocity component is determined directly from displacement of the tracer particles in the volume illuminated by the

laser. The thickness of the light sheet is increased and stereoscopic vision is used to reconstruct the three dimensional particle distribution. More than two cameras are used, typically four, to increase the fidelity of the reconstruction. The three-dimensional three-component velocity field is obtained directly by means of a cross-correlation technique which operates on interrogation volumes rather than on interrogation windows. Finally, a variation of the 2C-PIV principle can be obtained by adding not only a second camera but also a second laser. This implementation is called dual plane PIV, Dual-PIV for short. Aligning both cameras to view the same domain of interest, four particles images can be taken, one pair for each double-pulse illumination. Two velocity fields can hence be acquired with an arbitrarily small time delay between them, depending on the time separation between two laser systems and independent of the pulse delay between the image pairs from each camera. This enables making time correlated acquisitions, even for the very high frequency phenomena in high speed flows (order $100kHz$). Note that the regular PIV acquisition frequency is around 10Hz and that even high repetition rate PIV systems currently are limited to acquisition rates of the order of 10kHz, generally at degraded resolution and laser power.

The procedure for the determination of velocity fields by means of PIV comes with a number of inherent advantages and limitations. It will appear that certain characteristics will have a particularly important influence on the accuracy of the velocity determination, as well as on the accuracy of the higher order statistical moments. In addition, certain characteristics impose limits on the achievable spatial and temporal resolution. A number of these properties especially relevant to the current research are summarized below.

- **Whole field technique.** PIV measurements yield instantaneous full field velocity data. Mean and turbulence statistics can be obtained over an ensemble of instantaneous realisations. The full field quality of the technique enables the direct deduction and tracking of coherent structures and flow features. In addition, spatial correlations between different regions of the flow can be investigated. This can be done either point wise by means of correlation coefficients or globally by means of conditional statistics, yielding the dependence of the full flow field on a single conditioning parameter. Finally, PIV data lends itself particularly well for analysis using proper orthogonal decomposition (POD).

- **Non-intrusiveness of the velocity measurement.** The inherent principle of this technique is based completely on optical measurements of particle displacements. The only requirement for the observation is the dispersion of tracer particles, which are assumed not to alter the flow characteristics due to their low concentration. The laser probe for the light sheet generation (implementation depending on the measurement set-up) is placed sufficiently far downstream to avoid any

perturbance within the domain of interest. A possible source of disturbances is the seeding array for the dispersion of the particles, being placed upstream of the measurement domain. It was evaluated that the seeding rake, as used in the TST-27 (see section 3.3.3), has no significant effect on the free-stream turbulence level, although effects of the seeding injection at the wall could persist over larger distances. Nonetheless, the fact that no probes need to be inserted locally to perform the in-situ measurements makes that PIV is generally considered to be non-intrusive.

- **Spatial resolution.** The data field resolution is determined by the size of the interrogations windows in combination with the overlap factor. The velocity vector obtained for each interrogation area is an average of the velocities of the individual particles contained within the window. The size of the interrogation area is therefore especially relevant in the presence large gradients (shocks, shear layers, regions of high vortical activity). Larger windows will lead to more smoothing of the velocity field and a reduced fidelity of the displacement estimate. A related issue is the minimal flow structure size that can be resolved, and hence the minimum time scale based on a Taylor's hypothesis. Naturally, all flow features smaller than the interrogation window size and all time scales smaller that the convection time through the window are not resolved. As an indication, given a mean flow velocity of $500ms^{-1}$ and a window size of $1mm$, a characteristic time scale of $2\mu s$ is obtained.

- **Temporal resolution: pulse delay.** Apart from spatial averaging, the technique also introduces a temporal averaging due to the finite differencing scheme used for the velocity determination. Since PIV is an inherently Lagrangian method being applied to determine a Eulerian velocity field (it tracks particles rather than determining local flow velocities), the approximation of the velocity field becomes less accurate with growing time separation. A certain smoothing of the velocity field is therefore introduced. This imposes a lower limit on the resolved time scales of the flow, determined by the pulse delay of the laser system. This time separation is the result of an optimisation with respect to a number of parameters. On one hand it has to be large enough to allow for a sufficient displacement of the particles. The longer the pulse separation, the larger the particle travel, and thus the larger the dynamic range in the velocity determination. However, the time delay should also be small enough to prevent out-of-plane loss of particle pairs. Typical values of the pulse delay are in the order of half a microsecond to a few microseconds in high speed flows.

- **Temporal resolution: acquisition rate.** Another aspect of the temporal resolution of the PIV measurements is the repetition rate of the instantaneous (image pair) measurements. This resolution depends on the maximum double pulse frequency of the laser as well as the frame rate of the CCD sensor. Most common PIV systems allow for a double frame acquisition rate in the range of 1-10Hz. Acquisitions from these systems are hence uncorrelated in high speed flows. Faster systems (kHz range) currently exist as well. Neither of these systems is (fully) time resolved for high speed flows where frequencies up to 100kHz may appear, for example in the boundary layer. A way to circumvent this would be the use of a Dual-PIV system, as described above, see also Souverein *et al.* (2009b) and Souverein *et al.* (2008b).

- **Tracer fidelity.** The accuracy of the velocity determination depends on the faithfulness with which the tracer particles follow the flow, since the tracer particle velocity is measured rather than the true flow velocity. The particle velocity is only identical to the fluid velocity if either the density of the fluid and the particles is identical, or in the case of vanishing particle size, or in absence of accelerations. In general, these conditions are not satisfied in at least part of the flow domain (or there would be no need to perform measurements). Therefore, the particles need time to adapt to changes in flow velocity, determined by the response time (see Elena *et al.* (1999); Schrijer & Scarano (2007); Ragni *et al.* (2009)). This time response can be predicted from a shock test (representing an impulse response of the particle) using Stokes drag law. Typical values are in the order of a few microseconds in high speed flows. This imposes another limitation on the smallest observable time and space scales in the flow.

- **Two-Dimensionality.** PIV is commonly employed as a planar technique, yielding only two-dimensional velocity field data. If the flow is three-dimensional, then a projection of the flow field within the imaging plane is obtained. If strong deviations from two-dimensionality exist, then this out-of-plane velocity information will be lost. In addition, the measurement quality may be reduced due to out-of-plane loss of particle pairs. A way to include the third velocity component information and/or the three-dimensional aspect of the flow is to implement a Stereo-PIV system or a Tomo-PIV system, as described above.

- **Imaging through density gradients.** Since large density gradients may occur in supersonic flows, an effect may be expected on the imaging of the tracer particles due to aero-optical aberrations (see Elsinga *et al.* (2005b)). This effect is especially significant for the imaging of shocks under a certain angle. In addition, any other strong density

gradient within the optical path (like interactions of shock waves with the side wall boundary layers) can cause refractions. This may cause geometrical deformation of the recorded particle patterns as well as blurring and shifting of the individual particle images, hence introducing uncertainties in the displacement estimates. This reduces the fidelity of the velocity determination close to a shock wave.

- **Peak-locking.** An inherent characteristic of imaging with a CCD system is that the resolution is limited by the size of the pixels. This leads to a limitation in the discretisation of the estimated displacements. A way to circumvent this limitation is by fitting a gaussian distribution to the particle images, hence enabling a sub-pixel estimate of the particle location (the typical resolution is 0.1 pixels). This procedure is only possible if the particle image is spread out over multiple pixels. This can be achieved through diffraction limited imaging, where the image size is determined by the Airy disk. However, since this procedure incorporates a reduction of the aperture of the objective of the camera, it also implies a reduction in recorded light intensity, reducing the dynamic range of the image. Hence, sufficient laser power should be available to compensate, in combination with a careful choice of the camera set-up to take maximum advantage of the Mie scattering.

Peak-locking will occur if the particle images cannot be discretised using multiple pixels. It appears as characteristic peaks for integer pixel values in the histogram of the displacement, and consequently as a non-continuous stepwise discretisation of the mean velocity. However, an effect will also transpire on the estimation of the statistical moments. If the velocity fluctuations drop below the level of a single pixel displacement they can no longer be resolved, leading to an underestimation of the Reynolds shear stress. This has an especially strong effect when approaching the wall on the vertical fluctuation component (which has the smallest magnitude and hence is the most sensitive). This is due to the fact that the velocity vanishes when approaching the wall. Since the vertical velocity is close to (and approaching) zero, the fluctuations will be 'locked' to the zero velocity in the case of insufficient pixel displacement dynamics. This in turn will lead to an under-estimated V-fluctuation and hence an under-estimated Reynolds stress. The horizontal U-component is less sensitive to this effect due to the inherently larger fluctuation value. To remedy this problem (apart from increasing laser power and decreasing the aperture) one may opt for a larger pulse delay and higher image magnification, both yielding an improved displacement discretisation and hence an increased dynamic range of the velocity measurement. See Piponniau (2009) for experimental evidence of this phenomenon and the effectiveness of the proposed solution on the Reynolds stress measurements.

- **Effect of validation settings.** Different validation procedures and criteria are applied in the treatment of PIV results, notably during the iterative correlation procedure and consecutively in the computation of the velocity statistics. Regarding firstly the iterative correlation procedure, the most common validation criteria are the peak height and width, both a measure of the fidelity of the obtained correlation result for the particle displacement. This criteria may break down in regions of strong density gradients, where particle images are naturally blurred, leading to a lower validation rate, especially near shocks. Another common criterion is based on a neighbourhood validation, in other words, implying a local smoothness of the velocity field. The filter bounds must be carefully optimised since too strict values will unnaturally restrict the velocity fluctuation, to the detriment of the Reynolds stress estimates. Considering the statistical validation, a common criterion is based on the rejection of outliers using a filter based on the standard deviation, or alternatively on a median filter. Like for the local neighbourhood filter, the bounds must be carefully optimised or the fluctuation estimates will be too restrictive, to the detriment of the Reynolds shear stress estimates, as is demonstrated in appendix A.2.

The techniques employed in this research are 2C-PIV, Pano-PIV, 3C-PIV, and Dual-PIV. Details of the experimental set-up are described in the following sections. It is noteworthy that in another research, Tomo-PIV has been applied to the high Reynolds number flow case for the instantaneous spatial characterisation of the interaction under conditions similar to those described here, see Humble (2009) and Humble *et al.* (2009a). More information on Particle Image Velocimetry and its applications can be found in Raffel *et al.* (2007).

3.3.2 Dual-PIV measurement technique

Conventional two-component and three-component particle image velocimetry (PIV) measurements have been reported that document both the statistical and instantaneous behaviour of shock wave boundary layer interactions (see for example Dussauge *et al.* (2006), Dupont *et al.* (2008), Humble (2009) and Piponniau (2009)). Indeed, such techniques have also been employed in the current work. Although these PIV measurements provide a good idea of the overall flow organisation, information is lacking on its temporal development, as characterised by quantities such as time scales, characteristic frequencies and the local acceleration, information that is normally only accessible with unsteady single point probes such as hot wires and unsteady pressure sensors. Given the three dimensional (see Humble *et al.* (2009a) and Dussauge *et al.* (2006)) multi-timescale (see Dupont *et al.* (2006)) nature of

the phenomenon, full field knowledge of these quantities would profoundly increase the understanding of the flow, especially considering the correlation between events in different regions of the flow domain. In particular, for the flow under consideration, one can think of the relation between the motion of the reflected shock and upstream and downstream events (respectively the passage of turbulent structures through the interaction and the expansion and contraction of the separation bubble), as discussed in section 1.2.2. Furthermore, the local acceleration field has an interest in its own right (see Perret *et al.* (2006); Christensen & Adrian (2002a,b)), for example for the modelling of the structure of wall turbulence in the context of the improvement of subgrid-scale models for large-eddy simulations (LES). It may tentatively also enable compressible loads determination methods (as discussed in Souverein *et al.* (2006, 2007b); Van Oudheusden *et al.* (2007); Van Oudheusden & Souverein (2007)) to be extended to include instantaneous loads and pressures (see Liu & Katz (2006)). However, due to the technical restrictions on both the double pulse repetition rate of the laser system and the acquisition rate of the cameras, the recording frequency is limited to the order of $10Hz$ for conventional CCD-based PIV systems, and still to typically $1-10kHz$ for currently available CMOS based high-speed PIV systems (at a significant reduction of image quality in terms of illumination power and spatial resolution). This is by far insufficient to obtain accurate time-resolved data for the high-speed flow case under investigation. The time scales in the shock wave turbulent boundary layer interaction typically span three orders of magnitude (see for example Dupont et al (2006)): $O(10kHz)$ for the incoming boundary layer, $O(1kHz)$ for the mixing layer developing inside the interaction and $O(100Hz)$ for the reflected shock motion. For example, for the flow under consideration, the integral time scales in the incoming boundary layer are estimated at $24\mu s$, the associated frequency being $42kHz$, as will be shown in section 6.2.

A dual-system PIV-approach was therefore applied to study the interaction with sufficient temporal resolution. Two independent CCD-based PIV systems are combined to obtain instantaneously time-resolved whole field measurements, where the time delay between the acquisitions from both PIV systems could be set to arbitrarily small values, not limited by the repetition-rate restrictions of a single system. This way, time correlated data could be obtained as well as acceleration data. The advantage of this approach with respect to the available high-speed PIV systems is in the first place that it benefits from the higher laser power and image resolution of the low rep-rate CCD systems. Secondly, it allows setting the delay time between the two PIV systems independent of the pulse separation of the individual systems, decoupling the temporal resolution of the time-resolved velocity fields from the time separation between the PIV image pairs, this being without consequence for the illumination power. A large range of time delays is therefore accessible, including very small delay times (below $100\mu s$

Table 3.2: Overview of the high Reynolds number datasets.

short name	dataset	description
BLZoom	Boundary layer zoom	High resolution zoom of the upstream boundary layer
Pano	Panoramic PIV	Global overview of the interaction with upstream and recovering boundary layers
IntZoom	Interaction Zoom	High resolution zoom of the interaction region between reflected and incident shock
Dual	Dual-PIV	Interaction with part of upstream and recovering boundary layers, time resolved acquisitions

or less). This gives the Dual-PIV system the advantage of a quasi-infinite dynamic range, as opposed to the limited time interval between the high-repetition rate acquisitions. In addition, since the time delay is uncoupled from the image resolution, it is possible to obtain compatible values for both the spatial and temporal resolution (for example, using Taylor's hypothesis, $5\mu s$ corresponds to $2.5mm$ at $500ms^{-1}$). The smallest time separation employed in the current investigation was $5\mu s$, corresponding to an effective frequency of $200kHz$ (as opposed to acquisition rates in the order of $10kHz$ for available high-speed PIV systems). This allows temporally resolving the time scales within the boundary layer and within the interaction region.

Examples of equivalent systems can be found in Christensen & Adrian (2002a), Christensen & Adrian (2002b), Liu & Katz (2006) and Kähler (2004), the latter using two non-overlapping light sheets in a stereoscopic implementation. Other dual plane PIV systems are described in Guibert & Lemoyne (2002), and Perret *et al.* (2006), the latter being again a stereoscopic implementation. The applications range from the investigation of the spatio-temporal flow structure of turbulence, the determination of accelerations and the deduction of instantaneous pressure fields, notably in subsonic and stationary flows. Furthermore, Hou (2003) has implemented an equivalent system for the study of a shock wave boundary layer interaction in a compression ramp configuration at Mach 2. This to attempt to correlate acceleration fluctuations in the upstream boundary layer with the shock foot motion.

3.3.3   Experiment set-up: high Reynolds number case

Four different, complementary, datasets have been acquired during the high Reynolds number campaigns, summarised in table 3.2. All dataset have been acquired in two-component mode and constitute vertical plane measurements in the streamwise-wall normal plane on the centre line of the test section. The short names in the table will serve for future reference in figures and tables.

Each experiment (Boundary layer zoom, Panoramic, Interaction zoom,
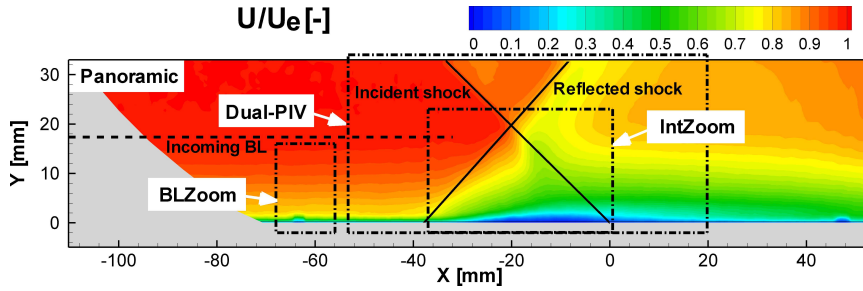
Figure 3.2: Overview of the fields of view of the high Reynolds number datasets with respect to the Panoramic domain of interest.
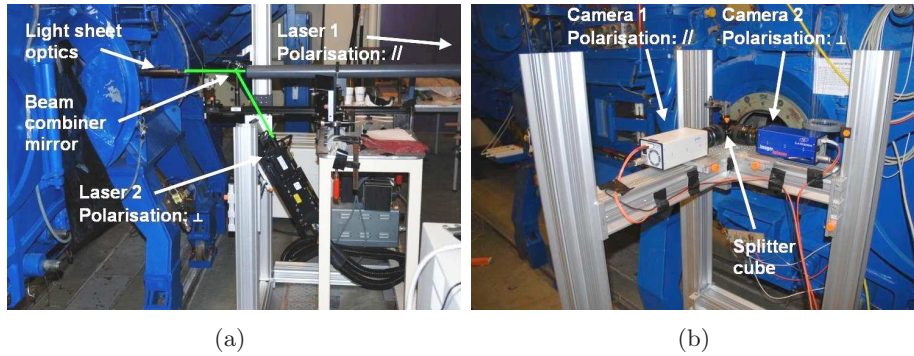
Figure 3.3: High Reynolds number Dual-PIV experimental arrangement: (a) set-up of the lasers with the beam combiner; (b) set-up of the cameras with the splitter cube.

Dual-PIV) was performed with a different field of view, as depicted in figure 3.2, superimposed onto the mean U-component velocity field from the panoramic dataset. Note that the FOV of the Dual-PIV dataset extends to $Y = 45mm$, which is beyond the FOV of the panoramic dataset. The grey area indicates the tunnel wall and the tunnel window edge. The boundary layer edge is indicated by the horizontal dashed line, the incident and reflected shocks by the solid inclined lines.

The Dual-PIV system was set up to acquire locally time resolved PIV data to obtain time correlated velocity field information. Illumination is provided from downstream of the test section while the observation is performed through a large window in the sidewall (see figure 2.1). The principle of Dual-PIV depends on the mutually independent operation of two 2C PIV systems. Both systems are aligned to provide illumination in the same measurement plane while observing identical fields of view, see figure 3.3. The laser light of the two systems was optically distinguished by means of polar-
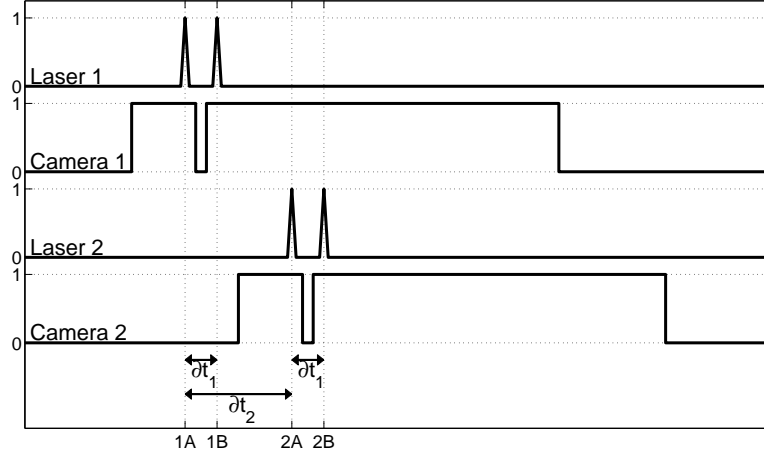
Figure 3.4: Dual-PIV timing diagram.

isation and the beams of the two lasers were combined and aligned before entering into the light sheet optics. The overlap of the field of view of both cameras was guaranteed by means of a polarising beam splitter cube, which also assured the independence of the two PIV systems by separating the images based on the polarisation. Both cameras were equipped with an additional polarising filter with the aim of further improving the independence.

Care was taken that the total of four laser sheets generated by both lasers overlapped in space. Furthermore, special attention was dedicated to the temporal alignment of the laser pulses. The triggering was calibrated such that both lasers flashed simultaneously for a zero time delay between both systems ($\partial t_2 = 0s$), see figure 3.4 for the timing diagram. This was done by means of a calibration run, determining the temporal off-set in the Q-switch trigger between both lasers through a correlation of the images corresponding to the same respective laser pulse (in other words image 1A with image 2A, see figure 3.4).

The potential of the current set-up becomes evident from the timing-schematic in figure 3.4, since for a given pulse-delay ∂t_1, the time separation ∂t_2 can be set arbitrarily (and indeed even ∂t_1 for each PIV system individually, if desired). This allows obtaining time correlated data at different time scales. In principle, measurements can be made with an unlimited temporal dynamic range, since ∂t_2 can be set to any value between zero and infinity. In the current experiment, a sweep of ∂t_2 was performed in the range of $5\mu s$ to $2000\mu s$ (corresponding to equivalent frequencies of $200kHz$ down to $0.5kHz$) with a reference measurement at $0\mu s$ to check the consistency between the two PIV systems. A minimum of 200 acquisitions (400 image pairs) were made per time delay. The illumination was provided by a *Spectra-Physics Quanta Ray* laser ($400mJ/pulse$ energy and a $6ns$ pulse du-

ration) and a *Quantel* laser ($300mJ/pulse$ energy and a $9ns$ pulse duration), installed as lasers 1 and 2 respectively. Both are double-pulsed Nd:Yag lasers with a wavelength of $532nm$. The light sheet thickness was approximately $2mm$. The flow was seeded with liquid DEHS (Di(2-ethylhexyl)sebacate) droplets, dispersed in the settling chamber of the wind tunnel by means of a seeding rake using a *PIVTEC* aerosol generation device. It was evaluated that the seeding rake has no significant effect on the free-stream turbulence levels (which are increased by 0.2% for a nominal value of 1% of the free-stream velocity (see Scarano & Van Oudheusden (2003); Van Oudheusden & Scarano (2008)). The estimated effective particle size is about $1\mu m$. The particle images were recorded at 12-bit with a resolution of 1376×1040 pixel using a *PCO Sensicam QE* (camera 1) and a *LaVision Imager Intense QE* (camera 2), both equipped with a Nikon $f = 60mm$ lens, diffracting with $f_\# = 8$. Of the CDDs only 992 pixels were used in the vertical direction given the aspect ratio of the interaction region of interest. The flow was imaged over a FOV of $76mm \times 45mm$ (approximately $4\delta \times 3\delta$) in streamwise and wall-normal direction respectively, at a digital resolution of $55.1\mu m/pixel$, yielding a field of 168×120 vectors. The timing and data acquisition was performed by *LaVision Davis 7.2* in combination with a *PTU 9* timing unit.

Recordings were made at an acquisition rate of $5Hz$. The pulse separation ∂t_1 was kept constant at $1.5\mu s$ for both laser systems, producing particle displacements of approximately $0.7mm$ (corresponding to 12 pixels) in the free-stream flow. The image pairs were interrogated using the WIDIM algorithm (Scarano & Riethmuller (1999)), employing correlation window deformation with an iterative multi-grid scheme, at 31×31 pixels window size ($1.7mm \times 1.7mm$) and an overlap factor of 75%. The resulting measurement grid resolution is $0.43mm/vect$ in both the X and Y direction. A wall boundary condition was implemented to mask the unseeded area. This is a procedure in the *WIDIM* software that also provides a boundary condition for the displacement estimate (zero displacement in the wall) which is used during the iterative procedure to replace non-valid data. A local minimum background intensity has been subtracted for each run individually to suppress the CCD measurement noise and to eliminate the wall reflections.

The boundary layer zoom, Panoramic PIV and interaction zoom datasets were acquired to support the interpretation of the Dual-PIV dataset. They have been obtained using essentially the same PIV system as discussed above for the Dual-PIV measurements and the acquisitions were processed in a similar way. Only a single laser (the *Spectra-Physics Quanta Ray* laser) was used for the illumination. The *PCO Sensicam QE* was used as the main camera for the acquisitions, and the *LaVision Imager Intense QE* was installed as the second camera for the panoramic PIV runs. The timing and data acquisition was performed by *LaVision Davis* in combination with a *PTU 8* timing unit.

Table 3.3: High Reynolds number datasets: PIV acquisition parameters.

Dataset			BLZoom	Panoramic	IntZoom	Dual-PIV
Camera type	cam1	$[-]$	PCO QE	PCO QE	PCO QE	PCO QE
	cam2	$[-]$	$-$	LaVision QE	$-$	LaVision QE
Focal length	f	$[mm]$	105	50	105	50
F-number	$f_\#$	$[-]$	11	8	8	8
Sheet thickness	d	$[mm]$	1	2	1	2
Ensemble size		$[-]$	1200	700	870	4220
Runs		$[-]$	4	3	3	15
FOV		$[mm^2]$	12×16	170×34	37×23	76×45
Sensor size		$[pix^2]$	1376×1040	1376×576	1376×1040	1376×992
Pulse delay	∂t_1	$[\mu s]$	0.6	2	1	1.5
Time delay	∂t_2	$[\mu s]$	$-$	$-$	$-$	$5 - 2000$
Resolution		$[\mu m/pix]$	11.7	70.1	29.0	55.1
		$[pix/mm]$	85.6	14.3	34.5	18.2
		$[mm/vect]$	0.091	0.543	0.225	0.427
Window size	ws	$[mm^2]$	0.36×0.36	2.17×2.17	0.90×0.90	1.71×1.71
Pix displ.	X_{pix}	$[pix]$	20.5	12.4	14.6	12.2
Pix vel.	V_{pix}	$[m/s/pix]$	21.9	36.1	30.7	36.7

All recording parameters for each dataset are summarised in table 3.3. The PIV processing parameters are summarised in table 3.4. It is noted that in order to enhance the statistical convergence of the data, the measurements from all the runs have been combined to come to the final ensemble size mentioned in table 3.3. The Dual-PIV dataset also encompasses the data from both cameras combined. This approach is justified by the fact that the flow conditions are highly repeatable (see appendix A.1.3) and that there is a good agreement between the results from all datasets (see appendix A.3.1 and section 4.1) and from both cameras for the Dual-PIV data (see appendix A.4).

3.3.4   Experiment set-up: low Reynolds number case

Four distinct datasets have been acquired during the low Reynolds number campaign, each with their own specificities. In additions, data from previous investigations have been used for the interpretation of the current results. The datasets were acquired in the horizontal as well as in the vertical plane, using both 2C-PIV and 3C-PIV. This was done for a range of measurement conditions, both with and without control. The dataset used during the current research are summarised in table 3.5. This section discusses in the first place the characteristics of the PIV arrangement that are common to all low Reynolds number experiments. Secondly, an overview will be given of the particularities of each individual set-up.

The PIV investigation was made using a *Dantec Dynamics* system and software. The light sheets are generated by a double pulse ND:YAG *New wave Solo II* laser, which delivers $30mJ$ per pulse, with a pulse delay set in the range of $1 - 2\mu s$. The light sheet thickness is $1mm$. Incense smoke

Table 3.4: High Reynolds number datasets: PIV processing parameters.

Dataset	BLZoom	Panoramic	IntZoom	Dual-PIV
Cross-correlation				
Software	WIDIM9.3	WIDIM9.3	WIDIM9.3	WIDIM9.3
Interrogation window[pix^2]	31×31	31×31	31×31	31×31
Overlap factor [%]	75	75	75	75
Wall boundary condition	on	on	on	on
SN threshold	1.1	1.1	1.1	1.1
Median threshold	2	2	2	2
Corrector threshold	2	2	2	2
Predictor scheme	local	local	local	local
Smooth	on	on	on	on
Multi grid iterations	3	3	3	3
Max iterations	5	5	5	5
Statistical validation				
SN threshold	1.5	1.5	1.5	2.0
Median threshold	0	0	0	0
INFO threshold	0	0	0	0

was used to seed the boundary layer. After decantation of the smoke, the particles were injected from the wall, upstream of the sonic section. For all measurements, 4 to 6 injector holes were used, placed symmetrically with respect to the wind tunnel axis with a spacing of $20mm$. As the wind tunnel stagnation pressure is subatmospheric, the particles are naturally sucked into the flow. The time constant of the particles was estimated with PIV measurements of the mean velocity across the incident shock outside the boundary layer. A time constant of $4.55\mu s$ has been deduced, which corresponds to diameters of $0.5\mu m$ (see Elena *et al.* (1999)). The particle images are recorded by *Flowsense* 10-bit cameras with a CDD size of 1600×1200 pixels, equipped with *Nikon Macro Nikkor* $f = 60mm$ objectives with the diaphragm set to $f_\# = 2.8$. Images were recorded at 8-bit with an effective sensor size adapted to the field of view under consideration. The acquisitions were made using *Flowmanager 4.71* software via the *Dantec Flowmap System Hub*. A peculiarity of this system is an internal storage, and therefore long data acquisitions at a high rate are possible ($12Hz$ using the two cameras in half frame mode). A maximum of 10,000 image pairs were acquired with two cameras (5000 per camera), which corresponds to about 7 minutes of acquisition. The images were processed with *DynamicStudio2.00* (or *DS2.00* for short), statistics and post-processing were done with in-house Matlab routines.

Referring to table 3.5, an overview will now be given of each specific experiment and its distinctiveness. In the first place, the flow was characterised in multiple wall parallel planes by means of stereoscopic PIV, yielding 3C-velocity information. These measurements were made for two overlapping domains of interest: the upstream boundary layer with AJVG array, and the interaction region. Secondly, measurements were made in multiple

Table 3.5: Overview of the low Reynolds number datasets.

short name	dataset	description
HorAJVG	Horizontal plane AJVG	3C-PIV measurements in the wall parallel plane with AJVG control (on/off) at 4 heights for two domains (upstream boundary layer and interaction).
VerAJVG	Vertical plane AJVG	Panoramic 2C-PIV measurements in the streamwise-wall-normal plane with AJVG control (on/off) at 4 spanwise locations for a domain covering the upstream boundary layer and the interaction.
VerZoom	Vertical plane Zoom	Zoomed 2C-PIV measurements in the streamwise-wall-normal plane on the tunnel axis, interaction only, no control.
VerPIV-HWA	Vertical plane PIV-HWA	2C-PIV measurements in the streamwise-wall-normal plane on the tunnel axis, interaction only, no control, simultaneous HWA measurements on the shock for conditional analysis.

streamwise-wall-normal planes with two side-by side cameras in a panoramic two-component PIV set-up. The domain of interest spans the full flow domain from the AJVG array to the recovering boundary layer. Both experiments were done specifically at a flow deflection angle of $\varphi = 9.5°$, with and without control. Further acquisitions were made in the streamwise-wall-normal plane on the tunnel axis, but with a single camera and at a higher magnification factor. This was done at a deflection angle of $\varphi = 5.5°$, without control only. Finally, vertical plane acquisitions were also made in combination with hot wire measurements to evaluate the possibilities to perform conditional statistics, at deflection angles of $\varphi = 5.5°$ and $9.5°$, again on the tunnel axis and without control. The characteristics of all set-ups will now be treated in detail.

The horizontal plane stereo-PIV measurements (*HorAJVG*) were made using the full CDD size. A maximum number of 3500 acquisitions (7000 image pairs) was made per run at a flow deflection angle of $\varphi = 9.5°$, consisting of 500 reference measurements without AJVGs and 3000 measurements with AJVGs. The final FOV was approximately $100 \times 100mm^2$ ($\approx 10\delta \times 10\delta$) and the magnification factor in the dewarped images was $10pix/mm$ (note that in the actual acquisitions, the scale factor depends on the location within the image due to perspective effects, the value is hence indicative). A pulse separation of $2\mu s$ was employed, yielding a free-stream displacement of 11 pixels and a displacement of 7.2 pixels at $1mm$ height from the wall. The final PIV data resolution is $0.61 \times 0.63mm/vect$, yielding a field of 250×249 vectors.

The vertical plane panoramic 2C-PIV measurements (*VerAJVG*) were made using two cameras mounted side by side to obtain a panoramic field of view. Each CCD was cropped to a size of 1600×595 pixels. The number

Table 3.6: Low Reynolds number datasets: PIV acquisition parameters.

Dataset			HorAJVG	VerAJVG	VerZoom	VerPIV-HWA
Camera type	cam1	$[-]$	Flowsense	Flowsense	Flowsense	Flowsense
	cam2	$[-]$	Flowsense	Flowsense	$-$	$-$
Focal length	f	$[mm]$	60	60	60	60
F-number	$f_\#$	$[-]$	2.8	2.8	2.8	2.8
Sheet thickness	d	$[mm]$	1	1	1	1
FOV		$[mm^2]$	100×100	224×20	44×15	100×20
Sensor size		$[pix^2]$	1600×1186	1600×595	1600×800	1600×800
Pulse delay	∂t_1	$[\mu s]$	2	1	1	1
Resolution		$[\mu m/pix]$	100.0	74.0	26.7	62.8
		$[pix/mm]$	10.0	13.5	37.4	15.9
	ΔX	$[mm/vect]$	0.61	0.59	0.43	0.50
	ΔY	$[mm/vect]$	0.63	0.30	0.21	0.25
Window size	ws	$[mm^2]$	3.20×1.60	2.37×1.18	1.71×0.85	2.01×1.00
Pix displ.	X_{pix}	$[pix]$	11.0	7.4	20.6	8.8
Pix vel.	V_{pix}	$[m/s/pix]$	50.0	74.0	26.7	62.8

of acquisitions was between 2000 and 5500 per run at a flow deflection angle of $\varphi = 9.5°$, of which 500 reference measurements without AJVGs, and the rest with AJVGs. The images from each camera were stitched together to obtain an effective sensor size of 3018×595 pixels. The final field of view was $224 \times 44mm^2$ with a magnification factor of $13.5pix/mm$. A pulse separation of $1\mu s$ was employed, yielding a free-stream displacement of 7.4 pixels. The final PIV data resolution is $0.59 \times 0.30mm/vect$, yielding a field of 374×77 vectors. The useful data range is $224 \times 20mm^2$ ($\approx 22.4\delta \times 2\delta$).

The vertical plane 2C-PIV zoom measurements (*VerZoom*) were made using a single camera. The CCD was cropped to a size of 1600×800 pixels. A single run was made to obtain 5000 acquisitions without AJVGs at a flow deflection of $\varphi = 5.5°$. The field of view was $44 \times 22mm^2$ with a magnification factor of $37.4pix/mm$. A pulse separation of $1\mu s$ was employed, yielding a free-stream displacement of 20.6 pixels. The final PIV data resolution is $0.43 \times 0.21mm/vect$, yielding a field of 97×78 vectors. The useful data range is $44 \times 15mm^2$ ($\approx 4.4\delta \times 1.5\delta$).

The vertical plane 2C-PIV-HWA measurements (*VerPIV-HWA*) were made using a single camera. The CCD was cropped to a size of 1600×800 pixels. Four runs were made yielding 3200 acquisitions each (12800 in total), without AJVGs at flow deflections of $\varphi = 5.5°$ and $9.5°$. The runs were subdivided in bursts of 800 realisations for the different investigated hot wire positions. The field of view was $100 \times 50mm^2$ with a magnification factor of $15.9pix/mm$. A pulse separation of $1\mu s$ was employed, yielding a free-stream displacement of 8.8 pixels. The final PIV data resolution is $0.50 \times 0.25mm/vect$, yielding a field of 197×97 vectors. The useful data range is $100 \times 20mm^2$ ($\approx 10\delta \times 2\delta$).

Before analysing the images, a minimum background intensity was subtracted. The background was obtained per batch of 500 images to compen-

sate for possible variations in image intensity during the course of the run. The wall reflections for the vertical plane acquisitions were masked using a uniform zero intensity background substitution. This wall masking does not incorporate a boundary condition which sets the displacement estimates at the wall to zero. Hence, also velocity estimates inside the wall are obtained for interrogations windows that overlap with the wall. To correct for this, the velocity vectors near the wall have been shifted from the geometric centre of the interrogation window to the geometric centre of the actual seeded part of the window. This wall correction reduces the vector spacing by a factor two for the last four data points at the wall.

For all cases (horizontal and vertical plane), an iterative cross-correlation of the image pairs was performed using an initial interrogation window size of 64×32 pixels and a single iteration step giving a final size of 32×16 pixels (cross-correlation was performed on both cameras separately for the Stereo-PIV acquisitions and on the final stitched panoramic image pairs for the 2C-PIV acquisitions). This with the exception of the zoom dataset (*VerZoom*), where the initial window size was 128×64 and the final window size 64×32. A Gaussian weighting function was applied to the iteration windows, giving a final effective window size of 16×8 pixels (32×16 for the *VerZoom* dataset). Three iterations were performed on the final window size to refine the result. An overlap factor of 75% was employed. It was verified that sufficient particle images were present within the final effective iteration windows. Within the iterative process, the data was validated employing several criteria (peak width, peak height, local neighbourhood median filter). The correlation and validation settings were optimised to obtain consistent results in combination with a high validation rate within regions of large velocity gradients (notably the reflected shock foot). The stereo-PIV results had to be processed further to obtain the three-component velocity fields. This was done by projecting the obtained data from the two cameras into physical coordinates using a direct linear transformation. A range validation was applied before the 3D processing.

All recording parameters for each dataset are summarised in table 3.6. The PIV processing parameters are summarised in table 3.7. As remarked, use is made in this research of previous measurements of the same low Reynolds number interaction at flow deflection angles of $\varphi = 8.0°$ and $9.5°$ (without control). Details on these datasets can be found in Piponniau (2009) and Piponniau *et al.* (2009).

3.3.5   Measurement programme

In the following, a combined overview will be given of the measurement programs for the high Reynolds number case and the low Reynolds number case, see table 3.8. Most notably, the respective grid resolution ($mm/vector$) will be compared in non-dimensional terms. All vertical plane dataset from the

low Reynolds number case have a very similar non-dimensional wall normal resolution as compared to the Dual-PIV dataset from the high Reynolds number case: $\frac{\Delta y}{\delta_0} \approx 2 - 2.9 \times 10^{-2}$. The data resolution in wall units for the high Reynolds number is a factor ten lower for the low Reynolds number, at comparable resolution in outer scaling. It is therefore more demanding in terms of the magnification factor to obtain points within the viscous sub-layer for the high Reynolds number case.

Table 3.7: Low Reynolds number datasets: PIV processing parameters.

Dataset		HorAJVG	VerAJVG	VerZoom	VerPIV-HWA
Cross-correlation					
Software		DS2.00	DS2.00	DS2.00	DS2.00
Interrogation window	$[pix^2]$	32×16	32×16	64×32	32×16
Overlap factor	$[\%]$	75	75	75	75
Gaussian weighting function		0.75	0.75	0.75	0.75
Wall boundary condition		−	mask	mask	mask
SN threshold		1	1	1	1
Peakwidth min		2.8	2.0	2.2	2.0
Peakwidth max		7.2	5.0	5.5	5.0
Local median filter	size	3×3	3×3	3×3	3×3
	acc.factor	0.2	0.2	0.2	0.2
	iterations	no	no	no	no
Intermediate iterations		1	1	1	1
Initial iterations		1	1	1	1
Intermediate iterations		0	0	0	0
Final iterations		3	3	3	3
High accuracy		on	on	on	on
Deforming windows		off	off	off	off
Statistical validation					
Range filter		on	on	on	on
Median threshold		10	10	10	10
INFO threshold		0	0	0	0

Table 3.8: PIV measurement programme.

Dataset	φ	h ; z	AJVG	$\frac{\Delta X}{\delta}$	$\frac{\Delta Y}{\delta}$;$\frac{\Delta Z}{\delta}$	ΔX^+	ΔY^+;ΔZ^+
	$[deg]$	$[mm]$	$[-]$	$[10^{-3}]$	$[10^{-3}]$	$[-]$	$[-]$
High Reynolds number case: $Re_\theta = 50,000$, $M_e = 1.7$							
BLZoom	$6.0°$	0	−	5.3	5.3	51	51
Pano	$6.0°$	0	−	31.6	31.6	305	305
IntZoom	$6.0°$	0	−	13.1	13.1	127	127
Dual	$6.0°$	0	−	24.8	24.8	240	240
Low Reynolds number case: $Re_\theta = 5,000$, $M_e = 2.3$							
HorAJVG	$9.5°$	$1, 2, 4, 6$	on/off	59.8	61.8	45	47
VerAJVG	$9.5°$	$-5, -2.5, 0, 2.5$	on/off	57.8	29.4	44	22
VerZoom	$5.5°$	0	off	42.2	20.6	32	16
VerPIV-HWA	$5.5°, 9.5°$	0	off	49.0	24.5	37	19

Chapter 4

Boundary layer characterisation

The incoming boundary layer has been characterised for both the high and low Reynolds number datasets. This with the aim to verify whether the inflow conditions are repeatable, consistent with previous measurements made in the same facilities, and in accordance with classical boundary layer data and semi-empirical relations. In short, it is verified that boundary layer state corresponds to that of a canonical turbulent boundary layer.

4.1 High Reynolds number flow case

The incoming boundary layer profiles are compared for all high Reynolds number datasets containing sufficient undisturbed upstream information (*BLZoom*, *Pano* and *Dual-PIV*, see tables 3.2 and 3.3). The validation is performed for the complete Dual-PIV data ensemble, encompassing all acquisitions for both cameras combined (in total 4000 realisations). For the boundary layer profiles, the ensemble size has been augmented by taking statistics in the flow direction (over $0.7\delta_0$ for the boundary layer zoom experiments, $0.6\delta_0$ for the Dual-PIV data, and $1.5\delta_0$ for the panoramic measurements) to increase the convergence and to attenuate measurement noise. It has been verified that this does not bias the results.

4.1.1 Boundary layer profiles

The incoming boundary layer profiles are shown in figure 4.1. The U-component profiles are in good agreement, see figure 4.1(a). It is noted that the discrepancy close to the wall is due to the fact that the last four data points are less well resolved as an inherent consequence of the measurement technique. The velocity is underestimated for these points, as can be observed from figure 4.1(b). None of the datasets resolves the log-law down
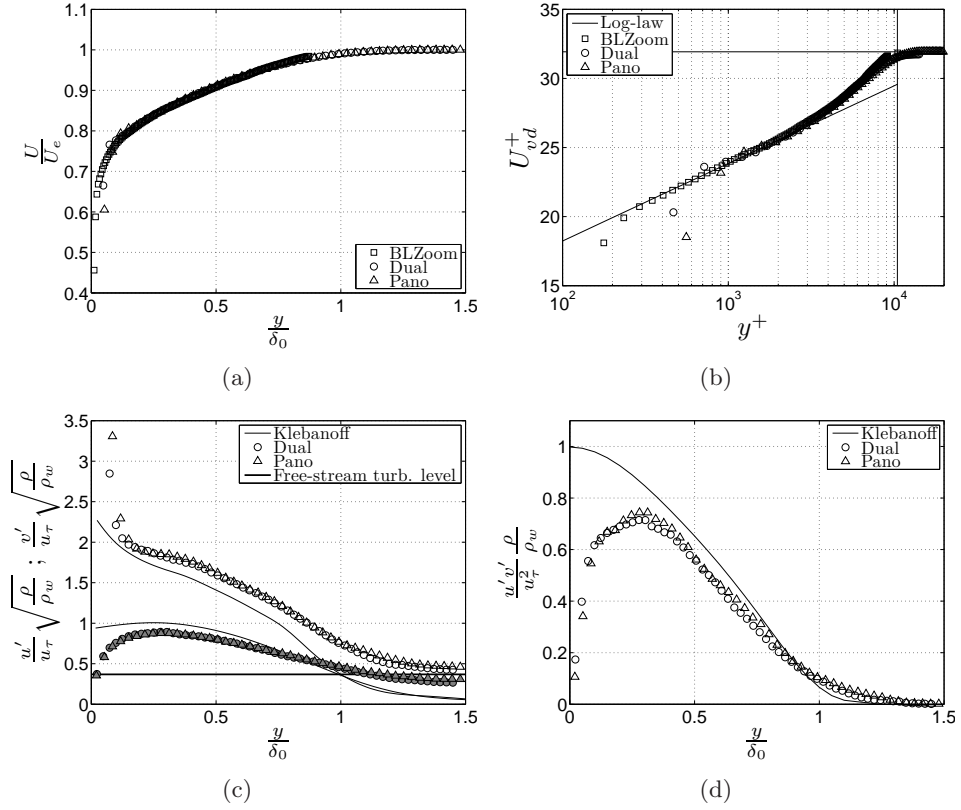
Figure 4.1: Boundary layer profiles, high Reynolds number datasets: (a) mean horizontal velocity component; (b) log-law of the wall (solid vertical and horizontal lines indicate the approximate boundary layer thickness and free-stream velocity respectively); (c) velocity fluctuations in Morkovin scaling (open symbols: u', closed symbols: v'); (d) Reynolds shear stress in Morkovin scaling.

to the viscous sub-layer. This a consequence of the limited PIV-resolution in combination with the high Reynolds number: $y^+ = 30$ corresponds to $53\mu m$, which equals one pixel at the Dual-PIV magnification (see table 3.3). In addition, a wall boundary condition has been applied, see section 3.3.3, which tends to bias the measurement towards lower velocities for the last four data points. The first reliable velocity measurement in the current experiment is at about $y/\delta_0 = 0.1$, or $y^+ = 1000$ for the *Dual-PIV* and *Panoramic* datasets, and at about $y/\delta_0 = 0.02$, or $y^+ = 200$ for the *BLZoom* dataset (each corresponding to approximately one interrogation window size). The log-law region extends to approximately $y^+ = 3000$. This corresponds to $y/\delta_0 \approx 0.3$ in outer scaling, which is identical to the low Reynolds number dataset (see section 4.2).

The velocity fluctuations in Morkovin scaling (Smits & Dussauge (2006)) are in good agreement with the Klebanoff (1955) reference data (note that the horizontal line in figure 4.1(c) indicates a 1% turbulence intensity in the free-stream). It can be concluded that the velocity fluctuations show a satisfactory behaviour. The U-component fluctuations seem to be slightly overestimated, whereas the V-component fluctuations are slightly underestimated. It should be remarked that, contrary to the Reynolds shear stress (which inherently represents only correlated velocity fluctuations, measurement noise is uncorrelated), the velocity fluctuations also include a contribution from the measurement noise. This would explain the overestimation of the U-fluctuations, indicating that the estimation of the V-fluctuations distribution could be too optimistic with respect to the adherence to the Klebanoff curve. The Reynolds shear stress follows the Klebanoff reference curve accurately in most of the boundary layer, see figure 4.1(d). However, for both datasets the distribution levels off and attains a plateau value too soon. Theoretically, a peak value of '1' should be attained due to the Morkovin scaling, which expresses the ratio of the turbulent shear stress over the viscous shear stress.

Based on these considerations, it can be concluded that the Reynolds shear stress is resolved with sufficient accuracy (maximum error of approximately 15%) down to $y/\delta_0 = 0.3$. Below this height the stresses are underestimated, which may imply that the Reynolds shear stress near the wall suffers from a systematic measurement error. The source of this error is thought to be mostly in the underestimation of the V-component fluctuations, as explained in section 3.3.1. This could be due to an increased sensitivity to peak-locking of the V-component fluctuations, both due to the small magnitude of the quantity under consideration and the small magnitude of the V-component itself. This mechanism and its effect on the Reynolds shear stress was demonstrated by Piponniau (2009). Another suspected source of uncertainty, also mentioned in sections 3.3.1 and appendix A.2, concerns the validation settings within the iterative PIV correlation procedure. When these are set too strict, the measured velocity dynamics are unnaturally restricted, hence yielding underestimated Reynolds shear stresses. The U-component fluctuations are thought to be more accurately resolved in general due to their larger magnitude. A comparison to the Klebanoff reference data in figure 4.1(c) indicates that the U-component fluctuations are resolved with good confidence down to $y/\delta_0 = 0.1$. The V-component fluctuations and the Reynolds shear stress seem to be the most difficult quantities to measure with PIV in high speed flows.

Special attention is drawn to the fact that the Dual-PIV data compare very well to the the boundary layer zoom data acquired at a five times higher spatial resolution (see table 3.3), confirming that the same flow physics are captured. The Dual-PIV measurements, obtained by combining data from multiple runs and two cameras, are consistent with both other datasets.

4.1.2   Length scales

The displacement thickness δ^*, momentum thickness θ, and shape factor H, were obtained by integration of the velocity profiles in figure 4.1(a). The results are summarised in table 4.1. The required temperature and density profiles were estimated using the modified Crocco-Busemann relation, see White (1991), assuming adiabatic wall conditions and a recovery factor of $r = 0.89$. The accuracy of the integration was increased by means of an extension of the velocity profile towards the wall by using a power law extrapolation, see Smits & Dussauge (2006). In the results, the exponent of the power law fit n is also stated. Furthermore, the 'incompressible' values (density ratio = 1) of the displacement thickness δ^*_{ic}, momentum thickness θ_{ic}, and shape factor H_{ic}, are given. As can be observed, the differences between the values obtained for both datasets are negligible. Unless specified otherwise, the Dual-PIV values are taken as reference values in all analyses.

Using the power law relations, an estimate can be made of the incompressible length scales by following the approach in Smits & Dussauge (2006). In the first place it is noted that the value of the exponent of the power law fit n depends weakly on the Reynolds number and is expected to vary from 7 for $5 \times 10^5 < Re_x < 10^7$ to a value of 9 for $10^6 < Re_x < 10^8$. The estimated value is in good agreement with the specified range ($Re_x = 7.2 \times 10^7$, see table 4.2). Using this value of n, the following length scales are obtained by means of equation 4.1: $\delta^*_{ic} = 1.93$, $\theta_{ic} = 1.54$ and $H_{ic} = 1.25$. The experimental values correspond well to these estimates; the shape factor is indeed identical. In addition, it agrees well with the experimental data and the Coles' correlation in figure 7.18 from Smits & Dussauge (2006) for $Re_\theta = 50,000$. The value of the shape factor is in very good agreement with the relation from Cousteix (1989), see equation 4.2, with $T_w = T_{aw}$ for an adiabatic wall, yielding $H = 2.39$ for $M_e = 1.69$ and $H_{ic} = 1.25$.

$$H_{ic} \quad = \quad \frac{\delta^*_{ic}}{\theta_{ic}} = \frac{(2+n)}{n} \tag{4.1}$$

with:
$$\delta^*_{ic} = \frac{1}{1+n}\delta_0$$
$$\theta_{ic} = \frac{n}{(1+n)(2+n)}\delta_0$$

$$H = H_{ic} + 0.4M_e^2 + 1.222\frac{T_w - T_{aw}}{T_e} \tag{4.2}$$

Table 4.1: Length scales, high Reynolds case.

dataset	$n[-]$	$\delta^*[mm]$	$\theta[mm]$	$H[-]$	$\delta_{ic}^*[mm]$	$\theta_{ic}[mm]$	$H_{ic}[-]$
Dual	7.90	3.31	1.39	2.38	2.00	1.60	1.25
Pano	7.91	3.33	1.40	2.38	2.01	1.61	1.25

4.1.3 Reynolds numbers

Using the quantities determined above, the following Reynolds numbers have been computed based on the different reference flow conditions, see table 4.2. The Reynolds numbers are defined according to equation 4.3, where Re_θ is the reference Reynolds number that will be used to characterise the boundary layer. The Reynolds number Re_x was computed based on the development length of $x = 2m$, as specified in section 2.1. The required value of the viscosity coefficient has been obtained using Sutherland's law, see for example White (1991).

$$Re_{unit} = \frac{U_e \rho_e}{\mu_e} \quad Re_{\delta_0} = \frac{U_e \rho_e \delta_0}{\mu_e} \quad Re_{\delta^*} = \frac{U_e \rho_e \delta^*}{\mu_e}$$
$$Re_\theta = \frac{U_e \rho_e \theta}{\mu_e} \quad Re_{\theta_w} = \frac{U_e \rho_e \theta}{\mu_w} \quad Re_x = \frac{U_e \rho_e x}{\mu_e} \tag{4.3}$$

Table 4.2: Reynolds numbers, high Reynolds case.

Re_{unit}	Re_{δ_0}	Re_{δ^*}	Re_θ	Re_{θ_w}	Re_x
35.9×10^6	61.7×10^4	119.0×10^3	50.0×10^3	35.2×10^3	71.8×10^6

4.1.4 Friction coefficient

The friction velocity u_τ has been obtained by fitting equation 4.4 to the slope of the log-law region of the mean velocity profile, taking the compressibility effects into account by means of the Van Driest transformation, see Smits & Dussauge (2006).

$$\frac{U_{vd}}{u_\tau} = \frac{1}{k} \ln\left(\frac{y u_\tau}{\nu_w}\right) + C \quad \text{with: } U_{vd}^+ = \frac{U_{vd}}{u_\tau}; \quad y^+ = \frac{y u_\tau}{\nu_w} \tag{4.4}$$

Where U_{vd} is the Van Driest transformed velocity, k is Von Kaŕmań's constant ($k = 0.41$), and C is the log-law constant. The log-law fit was made without *a priori* fixing the second constant C. The best fit was obtained for $C = 7$ and $u_\tau = 15m/s$, see table 4.3. As can be observed, there is again a good agreement between the results from all datasets. The obtained slope-fit is also shown in figure 4.1(b).

A consistency check has been performed of the friction coefficient and friction velocity obtained from a log-law fit with respect to results from two semi-empirical relations (Cousteix (1989) and Fernholz (1971)), see equations 4.5 and 4.6 respectively. For the Cousteix relation, $f(M_e) = 0.83$ for $M_e = 1.69$. For the Fernholz equation, it is assumed that the wall temperature T_w equals the adiabatic wall temperature T_{aw}. Furthermore, the typical values are used for the specific heat ratio ($\gamma = 1.4$) and the recovery factor ($r = 0.89$). A good agreement was found between the log-law fit results and the semi-empirical correlations, see table 4.3. As can be observed, Cousteix gives slightly overestimated results, whereas the Fernholz result is slightly below the experimental values.

In summary, the boundary layer measurements for all datasets are found to be mutually consistent and the obtained boundary layer length scales, friction coefficient and friction velocity are in good agreement with the results obtained with the semi-empirical relations. The incoming boundary layer under consideration is a canonical turbulent boundary layer and the flow conditions are repeatable.

- Cousteix (1989):

$$C_f = \frac{0.172}{Re_\theta^{0.2}} f^{6/5} \quad \text{with: } f(M_e) = \frac{C_f}{C_{f_i}} \tag{4.5}$$

- Fernholz (1971):

$$C_f = 2\frac{\rho_w}{\rho_e} \left\{ \frac{U_e^* - U_1^*}{U_e} \left[\left(\frac{1}{k} - M\right) \ln\left(\frac{y}{\Delta^*}\right)_p - N - \frac{1}{k} \ln\left(\frac{y_1}{\Delta^*}\right) \right]^{-1} \right\}^2$$

$$\tag{4.6}$$

where:

$M = 4.70, N = 6.74$ for: $1.5 \times 10^3 \leq Re_{\theta_w} \leq 10^5$

$\ln\left(\frac{y}{\Delta^*}\right)_p = 2.70$ for: $Re_{\theta_w} \geq 2 \times 10^3$

$\frac{1}{k} \ln\left(\frac{y_1}{\Delta^*}\right) = -2.57 - \ln(Re_{\theta_w})$

$\frac{U_1}{U_e} = 0.60 + 0.0233 M_e$ for: $Re_{\theta_w} \geq 2 \times 10^3$ and: $M_e \leq 4.5$

$\frac{U^*}{U_e} = \phi^{-\frac{1}{2}} \sin^{-1}\left(\frac{2\phi\frac{U}{U_e} - \psi}{\psi^2 + 4\phi^{\frac{1}{2}}}\right)$

with:

$\phi = r\frac{T_e}{T_w}\frac{\gamma - 1}{2}M_e^2$

$\psi = \frac{T_{aw} - T_w}{T_w} = 0$

Table 4.3: Friction coefficient, high Reynolds case.

dataset	$C_f[-]$	$u_\tau[m/s]$
BLZoom	1.48×10^{-3}	14.99
Dual	1.49×10^{-3}	15.07
Pano	1.49×10^{-3}	15.06
Cousteix	1.58×10^{-3}	15.50
Fernholz	1.46×10^{-3}	14.89

4.2 Low Reynolds number flow case

The incoming boundary layer profiles are compared for the low Reynolds number *VerAJVG* and *VerZoom* datasets (see tables 3.5 and 3.6). The validation is performed for the undisturbed boundary layer (AJVGs off) and for the complete data ensemble. Only a single profile has been taken (no statistics in flow direction). The state of the boundary layer is compared with the previous measurements taken from the 'PIV zoom pano 9.5° 2007' dataset, see section 3.1.2 in Piponniau (2009).

4.2.1 Boundary layer profiles

The incoming boundary layer profiles are shown in figure 4.2. The U-component profiles are in good agreement, see figure 4.1(a). A good agreement is also achieved for the velocity profiles in Van Driest scaling, see figure 4.1(b). The law-of-the-wake is slightly stronger for the *VerZoom* datasets in comparison to all other datasets. This is due to a slightly smaller value of the friction velocity u_τ, see table 4.6. The log-law is completely resolved down to the viscous sub-layer for all datasets. The velocity profile continues to follow the log-law even within the viscous sub-layer. This is attributed to the measurement uncertainties for the last four points close to the wall: $y^+ = 30$ corresponds to $406\mu m$, which equals approximately half an interrogation window size (see table 3.6), or four data points after the wall correction which was implemented to take into account the shift in the geometric centre (see section 3.3.4). The last four vectors are likely biased towards the higher velocities, contrary to the high Reynolds dataset, where a wall boundary condition was implemented (see section 4.1). The first reliable velocity measurement in the current experiment is therefore at about $y/\delta_0 = 0.04$, or $y^+ = 30$ (corresponding to approximately one interrogation window size before wall correction). The log-law region extends to approximately $y^+ = 200$, corresponding to $y/\delta \approx 0.3$, which is identical to the high Reynolds number dataset (see section 4.1).

The velocity fluctuations in Morkovin scaling (Smits & Dussauge (2006)) are in good agreement with the Klebanoff (1955) reference data, see figure

Figure 4.2: Boundary layer profiles, low Reynolds number datasets: (a) mean horizontal velocity component; (b) log-law of the wall (solid vertical and horizontal lines indicate the approximate boundary layer thickness and free-stream velocity respectively); (c) velocity fluctuations in Morkovin scaling (open symbols: u', closed symbols: v'); (d) Reynolds shear stress in Morkovin scaling.

4.2(c). It can be concluded that the velocity fluctuations show a satisfactory behaviour. In the first place, it is remarked that the measurement noise increases towards the boundary layer edge, particularly for the non-zoomed datasets. This is due to the fact that only the boundary layer is seeded (there is no seeding in the potential flow). The Reynolds shear stress, see figure 4.2(d) shows a more physical behaviour here since it contains only the correlated part of the velocity fluctuations. Considering the complete profile, the U-component fluctuations again seem to be slightly overestimated, whereas the V-component fluctuations are slightly underestimated

with respect to the Klebanoff reference profiles. Looking at figure 4.2(d), it is evident that the Reynolds shear stress is only correctly measured for the zoom-datasets (*Piponniau* and *VerZoom*), with a peak value approaching the theoretical value of '1' within the log-law region. The fact that the other data (which are large field measurements) under-resolve the Reynolds shear stress has been documented in Piponniau (2009). This has been attributed to an underestimation of the V-component fluctuation due to peak-locking, see section 3.3.1. The large field datasets do indeed suffer from underestimated V-fluctuations, see figure 4.2(c). The validation settings, which were proposed as the suspected source of the underestimated $\overline{u'v'}$-levels for the high Reynolds case, see section 4.1, have been optimised to avoid underestimating the Reynolds shear stress and should therefore not be the cause of this measurement bias.

4.2.2 Length scales

The displacement thickness δ^*, momentum thickness θ, and shape factor H, were obtained by integration of the velocity profiles in figure 4.2(a). The same approach was followed as in section 4.1. The results are summarised in table 4.4. For the *VerAJVG* dataset, the measurement plane on the wind tunnel centre line was taken for reference. It is noted that the values for the other planes are the same to within second digit accuracy for all length scales. It can be concluded that there is a very good agreement between the results for the reference profile from Piponniau (2009) and the current results from the *VerAJVG* and the *VerPIV-HWA* datasets. Since the variation within the *VerAJVG* dataset is of the same order as the difference with the *Piponniau* reference data, it may be concluded that all results are identical to within the measurement uncertainty. Unless specified otherwise, the *VerAJVG* values are taken as reference values in all analyses.

Following the approach from Smits & Dussauge (2006), an estimate can be made of the incompressible length scales using the power law relations. Unlike for the high Reynolds case, the value of the exponent of the power law fit n does not correspond to the expected range of 7 for $5 \times 10^5 < Re_x < 10^7$ to 9 for $10^6 < Re_x < 10^8$. The value is underestimated considering the current Reynolds number ($Re_x = 3.6 \times 10^6$, see table 4.5). Using the experimental value of $n = 5.6$, the following length scales are obtained by means of equation 4.1: $\delta_{ic}^* = 1.51$, $\theta_{ic} = 1.11$ and $H_{ic} = 1.36$. Hence, even though the power law exponent falls outside the expected range, the experimental values show an excellent agreement with these estimates. In addition, it agrees well with the experimental data and the Coles' correlation in figure 7.18 from Smits & Dussauge (2006) for $Re_\theta = 5,000$. The value of the shape factor is in good agreement with the relation from Cousteix (1989), see equation 4.2, with $T_w = T_{aw}$ for an adiabatic wall, yielding $H = 3.44$ for $M_e = 2.28$ and $H_{ic} = 1.36$.

Table 4.4: Length scales, low Reynolds case.

dataset	$n[-]$	$\delta^*[mm]$	$\theta[mm]$	$H[-]$	$\delta^*_{ic}[mm]$	$\theta_{ic}[mm]$	$H_{ic}[-]$
VerAJVG	5.6	2.93	0.84	3.47	1.50	1.12	1.34
VerZoom	5.2	3.17	0.90	3.52	1.70	1.23	1.38
VerPIV-HWA	5.5	2.80	0.80	3.51	1.49	1.09	1.37
Piponniau	5.8	2.92	0.85	3.43	1.51	1.13	1.33

4.2.3   Reynolds numbers

Using the quantities determined above, the following Reynolds numbers have been computed based on the different reference flow conditions, see table 4.5. The Reynolds numbers are defined according to equation 4.3, where Re_θ is the reference Reynolds number that will be used to characterise the boundary layer. The Reynolds number Re_x was computed based on the development length of $x = 650mm$, as specified in chapter 2.2. The required value of the viscosity coefficient has been obtained using Sutherland's law, see for example White (1991).

Table 4.5: Reynolds numbers, low Reynolds case.

Re_{unit}	Re_{δ_0}	Re_{δ^*}	Re_θ	Re_{θ_w}	Re_x
55.6×10^5	55.0×10^3	163×10^2	46.8×10^2	26.7×10^2	36.1×10^5

4.2.4   Friction coefficient

The friction velocity u_τ has been obtained by fitting equation 4.4 to the slope of the log-law region of the mean velocity profile, taking the compressibility effects into account by means of the Van Driest transformation, see Smits & Dussauge (2006). The best fit was obtained using a fixed value of $C = 5.25$ for the second constant. The obtained slope-fit is also shown in figure 4.1(b). As can be observed, there is again a good agreement between the results from all datasets.

A consistency check has been performed of the friction coefficient and friction velocity obtained from a log-law fit with respect to results from two semi-empirical relations (Cousteix (1989) and Fernholz (1971)), as has been done in section 4.1. For the Cousteix relation, $f(M_e) = 0.75$ due to the different Mach number ($M_e = 2.28$), see equation 4.5. The same conditions apply for the Fernholz equation 4.6 as for the high Reynolds case. A good agreement was found between the log-law fit results and the semi-empirical correlations, see table 4.6. As in the high Reynolds case, Cousteix again

Table 4.6: Friction coefficient, low Reynolds case.

dataset	$C_f[-]$	$u_\tau[m/s]$
VerAJVG	2.09×10^{-3}	24.68
VerZoom	1.99×10^{-3}	24.06
VerPIV-HWA	2.10×10^{-3}	24.76
Piponniau	2.15×10^{-3}	25.06
Cousteix	2.24×10^{-3}	25.58
Fernholz	1.96×10^{-3}	23.91

gives a slightly overestimated results, whereas the Fernholz result is slightly below the experimental values. This tendency of the experimental results to fall consistently within the range indicated by the semi-emperical relations increases the confidence in the correctness of the experimental friction coefficient estimates for both the high and the low Reynolds number cases. It is noted that, notwithstanding the fact that the values for the *VerZoom* data are slightly lower with respect to the other datasets, they still agree well with the semi-empirical estimates.

In summary, the boundary layer measurements for all datasets are found to be in good agreement with previous data from the same facility. The obtained length scales, friction coefficient and friction velocity are in good agreement with the results obtained with the semi-empirical relations. The incoming boundary layer under consideration is a canonical turbulent boundary layer.

Chapter 5

Mean and instantaneous flow organisation

Before commencing a detailed analysis of the interactions under considerations, a direct comparison will be made between the high Reynolds number case and the low Reynolds number case concerning the inflow conditions and corresponding flow organisation. First, the flow characteristics will be compared based on the incoming boundary layer properties and the general flow organisation. Then, the mean and fluctuating flow fields will be compared. Finally, the last section is dedicated to the instantaneous realisations. The PIV-data for the $\varphi = 8.0°$ and $9.5°$ low Reynolds number interactions presented here are taken from the 'PIV champs larges 2006' dataset, see section 3.1.2 in Piponniau (2009). They are incorporated to facilitate a consistent comparison between all interactions. Unless stated otherwise, the dimensionless longitudinal coordinate is defined as $X^* = (x - X_0)/L$, where X_0 is the mean position of the reflected shock foot and L the interaction length. All data will be analysed in detail in part II. The validation of the data presented here (concerning both the flow conditions and the data quality) is treated in detail in appendix A.

5.1 Flow characterisation

The upstream boundary layer profiles under consideration are compared using the classical scaling approaches. In addition, the flow topology of the interactions for the investigated flow deflection angles is considered by means of flow visualisations.

The incoming boundary layer profiles for both Reynolds number cases are shown in figure 5.1. Considering the mean velocity profile, the first evident effect of a higher Reynolds number is to increase the fullness, as can be appreciated from figure 5.1(a). A second consequence of an increase in Reynolds number is the larger extent of the log-law region, going up to

(a)

(b)

(c)
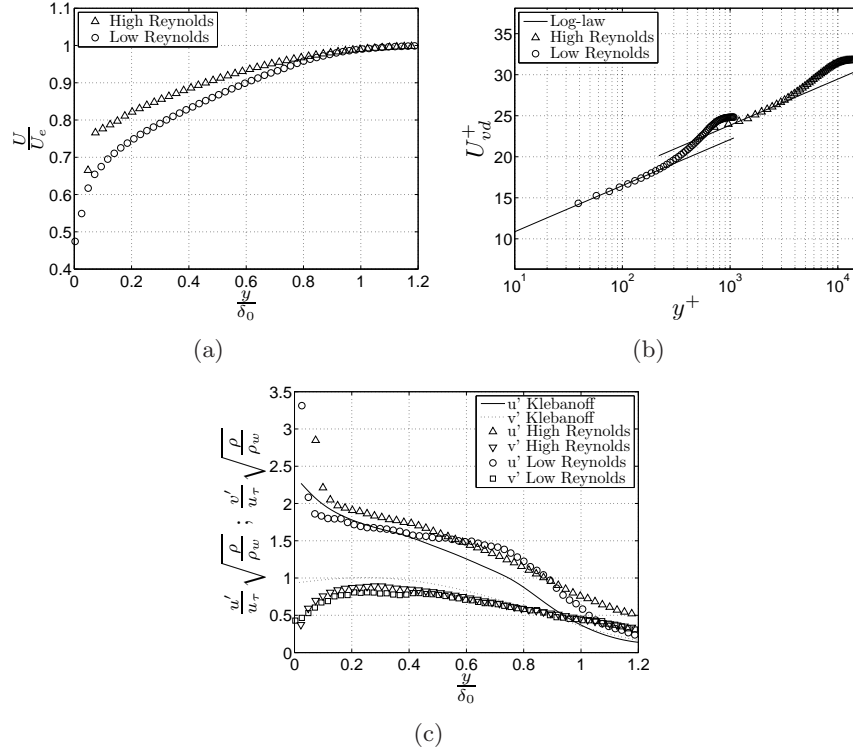
Figure 5.1: Incoming boundary layer characterisation: (a) non-dimensional mean streamwise velocity; (b) mean velocity profile in Van Driest scaling with the log-law fit; (c) non-dimensional velocity fluctuations with Klebanoff reference profile, see Klebanoff (1954).

$y^+ = 3000$ for the high Reynolds number in comparison to $y^+ = 200$ for the low Reynolds number, see figure 5.1(b). Note that the vertical shift in the log–law is due to the difference in the second constant that yields optimal fit ($C = 7$ for the high Reynolds number case versus $C = 5.25$ for the low Reynolds number case, see chapter 4). It is verified that for both Reynolds number cases, the log-law extends to about the same height in external scaling ($y/\delta_0 = 0.3$). No significant differences are observed between both flows with regard to the velocity fluctuations in the boundary layer, which are shown in Morkovin scaling (see Smits & Dussauge (2006)) in figure 5.1(c). This confirms that in both cases the inflow conditions comprise a canonical zero pressure gradient supersonic ($M < 5$) turbulent boundary layer.

Turning the attention to the general flow topology of the different interactions, it can be seen in figure 5.2 that the interactions display a large qualitative resemblance. The high Reynolds number interaction is shown in figure 5.2(a), displaying contours of the mean vertical velocity component
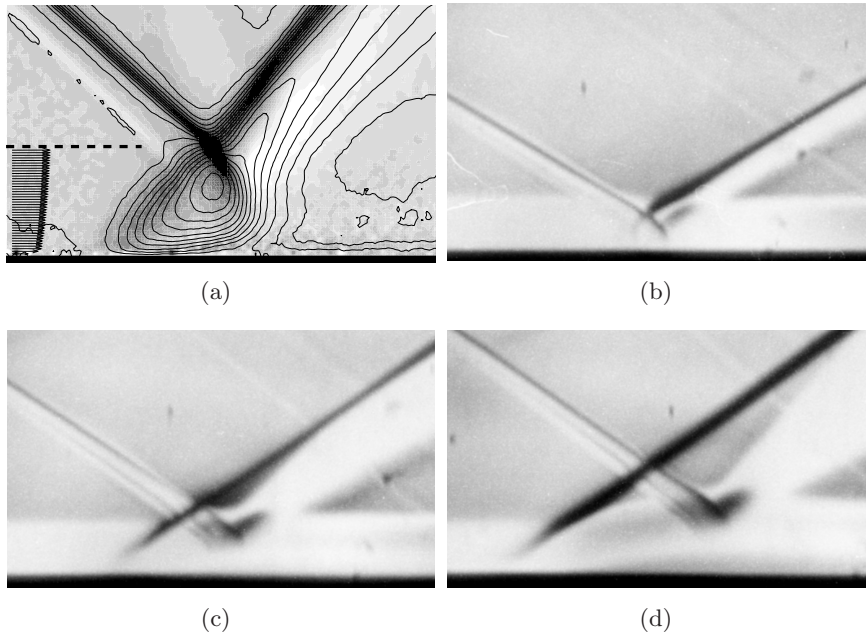
Figure 5.2: Interaction topology for the four flow cases: high Reynolds number (a) $\varphi = 6.0°$; low Reynolds number (b) $\varphi = 5.5°$; (c) $\varphi = 8.0°$; (d) $\varphi = 9.5°$.

superimposed on the divergence of the velocity field. The boundary layer profile and the boundary layer edge are also shown for reference. The figures for the low Reynolds number case, figures 5.2(b)-(d), represent Schlieren visualisations. In all cases, the incident shock wave impacts on the boundary layer, causing a thickening thereof. A reflected shock forms upstream of the the extrapolated impact point of the incident shock. The incident shock on the contrary reflects as an expansion fan, which in turn interacts with the reflected shock in the potential flow region. A classical evolution of the interaction is observed from the incipient to the separated cases, see figure 1.7 in chapter 1, taken from Délery & Marvin (1986). In particular, the expansion fan becomes attached to the reflected shock for the incipient interactions and the shock crossing point becomes immersed in the boundary layer. It is remarked that the low Reynolds interaction at $\varphi = 5.5°$ shows a large topological similarity to the high Reynolds number $\varphi = 6.0°$ case.

Tables 5.1 and 5.2 give an overview of the upstream and downstream flow conditions, including the boundary layer length scales. The values are reported from chapter 4 and section 3.3.5. The free-stream thermodynamic quantities have been obtained through the isentropic relations, for the values at the wall, an adiabatic wall temperature is assumed using a recovery factor of $r = 0.89$. The viscosity coefficients have been estimated using

Sutherland's law, see for example White (1991). It has been verified that the upstream and downstream value of the wall temperature is identical to within a few degrees. The inviscid quantities in table 5.2 represent the respective theoretical values derived from the oblique shock relations, see for example Anderson Jr. (1991).

Table 5.3 gives an overview of the interaction characteristics: the interaction length (dimensional and normalised by the boundary layer thickness), the theoretical height of the interaction (defined as the shock crossing point, given by $\frac{H}{L} = \frac{1}{2}\tan(\beta)$ with β the incident shock angle). Also reported are the height of the dividing streamline, h, and the height of the zero velocity contour, h_0. It can be remarked that the interaction height increases by 50% for the Mach=1.7 high Reynolds number case as compared to the Mach=2.3 low Reynolds number case. This is a purely geometrical effect, the shock wave being steeper for the lower Mach number. This can be inferred from figure 5.2: the shock angle is larger at Mach=1.7 (see figure 5.2(a)) than at Mach=2.3 (see for example figure 5.2(b)).

5.2   Mean flow fields

Figures 5.3 and 5.4 compare the mean U and V-velocity fields for all interactions under consideration. Both the horizontal and vertical coordinate are scaled by δ_0 and all figures use the same scale. This makes a direct visual evaluation of the effect of the shock intensity on the flow organisation possible. Figures 5.3 also shows the evolution of the fullness of the boundary layer profiles and the local flow direction, visualised using mean velocity vectors. Figure 5.4 also indicates the location of the sonic line (the dashed contour line) and the height of the dividing streamline (the dashed-dotted line). Both figures show the height of the reversed flow region (the black solid line).

The flow organisation from figure 5.2 is easily recognised in both figures. The low Reynolds interaction at $\varphi = 5.5°$ again shows a large similarity to the high Reynolds number case. Considering the external flow outside the boundary layer, the flow is initially parallel to the wall and consecutively decelerated by the shock system. The first (impinging) shock causes a downward deflection resulting in a negative vertical velocity in the order of $0.1 - 0.2U_e$, see figure 5.4. The second (reflected) shock causes an upward deflection, which is followed by an acceleration caused by the expansion fan (which is the actual physical reflection of the incident shock wave). The expansion fan was observed to be attached to the reflected shock for the small flow deflection angles and it is detached for the large shock intensities, see figure 5.2. It deflects the flow back to the horizontal or to a small negative vertical velocity component (approximately 3% of the free-stream velocity) for the weak shock intensities. The interactions with a larger shock intensity

Table 5.1: Overview of the upstream conditions.

Experiment		**High Re**	**Low Re**
M_e		1.69	2.28
U_e	$[ms^{-1}]$	448	550
T_0	$[K]$	273	295
p_0	$[kPa]$	230	50.7
Re_θ		$50,000$	$5,000$
$Re_{\delta_w^*}$		$84,000$	$10,000$
Re_{θ_w}		$35,000$	$3,000$
δ_{99}	$[mm]$	17.2	10.2
δ^*	$[mm]$	3.31	2.98
θ	$[mm]$	1.39	0.86
H		2.38	3.46
δ_{ic}^*	$[mm]$	2.00	1.70
θ_{ic}	$[mm]$	1.60	1.23
H_{ic}		1.25	1.38
n		7.90	5.2
C_f		1.5×10^{-3}	2.1×10^{-3}
u_τ	$[ms^{-1}]$	15.07	24.68
y_{unit}^+	$[mm^{-1}]$	562.4	73.89
p_e	$[kPa]$	46.6	4.18
T_e	$[K]$	173.0	144.8
T_w	$[K]$	262.0	278.8
ρ_e	$[kgm^{-3}]$	0.9384	0.1006
ρ_w	$[kgm^{-3}]$	0.6197	0.0522
μ_e	$[kgm^{-1}s^{-1}]$	1.1704×10^{-5}	0.9951×10^{-5}
μ_w	$[kgm^{-1}s^{-1}]$	1.6608×10^{-5}	1.7446×10^{-5}
ν_e	$[m^2s^{-1}]$	1.2472×10^{-5}	9.8939×10^{-5}
ν_w	$[m^2s^{-1}]$	2.6802×10^{-5}	33.396×10^{-5}

Table 5.2: Overview of the downstream conditions.

Experiment		**High Re**	**Low Re**		
Flow deflection		6.0°	5.5°	8.0°	9.5°
M_e		1.27	1.87	1.69	1.58
U_e	$[ms^{-1}]$	366.0	494.0	464.1	444.3
p_e	$[kPa]$	85.9	7.90	10.3	12.0
T_e	$[K]$	206.3	174.1	188.4	197.3
ρ_e	$[kgm^{-3}]$	1.4496	0.1580	0.1901	0.2111

Table 5.3: Overview of the interaction parameters.

Experiment		High Re	Low Re		
Flow deflection		6.0°	5.5°	8.0°	9.5°
L	[mm]	37	25	46	71
L/δ_0		2.2	2.3	4.2	6.5
H/L		0.45	0.30	0.32	0.34
h	[mm]	0	0	5.5	10.2
h_0	[mm]	0	0	3.2	5.7

show a more significant overshoot towards negative velocities. These will be compensated further downstream by a gradual recompression, as stated in Délery & Marvin (1986). It is noted that the mean velocity measurements around the shocks are subdued to smoothing effects due to a combination of particle inertia, optical refraction effects (see Elsinga *et al.* (2005b,a)) and the limited PIV spatial and temporal resolution (due to central differencing over the time separation between the image pairs).

Considering the boundary layer, the strong adverse pressure gradient imposed by the shocks causes it to thicken, driving it towards separation. A large body of retarded fluid is observed downstream of the interaction in all cases. The sonic line is lifted away from the wall to a height of $0.5 - 1\delta_0$. Downstream of the interaction, the sonic line coincides with the streamlines. It recovers only very slowly and seems to level off, becoming parallel to the wall in conjunction with the flow direction. An important part of the boundary layer remains subsonic for a large distance downstream of the interaction, making it likely that the displacement thickness is significantly increased with respect to the upstream state. The effect of a thickening of the boundary layer is not included in the inviscid flow model in Délery & Marvin (1986), see figure 1.9 in section 1.2.1, since only the shape of the separation bubble is modeled.

The interaction length increases considerably with the imposed flow deflection and the consecutive growth of the retarded fluid region. It is approximately $2\delta_0$ for small flow deflections (5.3(a) and 5.3(b)) and increases up to $7\delta_0$ for the largest shock intensity (5.3(d)). At the same time, a significant region of mean reversed flow can be seen to develop within the interaction for the two largest flow deflections, delineated by the solid black contour line. The mean negative velocity attains values superior to $0.1U_e$ for the largest flow deflection, with the height of the reversed flow region attaining a value of $\frac{y}{\delta_0} = 0.5$. No mean flow reversal is observed for the two small flow deflections, though flow separation is observed instantaneously, as will be shown in section 5.4. The dividing stream line attains a height of $\frac{y}{\delta_0} = 1$ for the largest flow deflection.
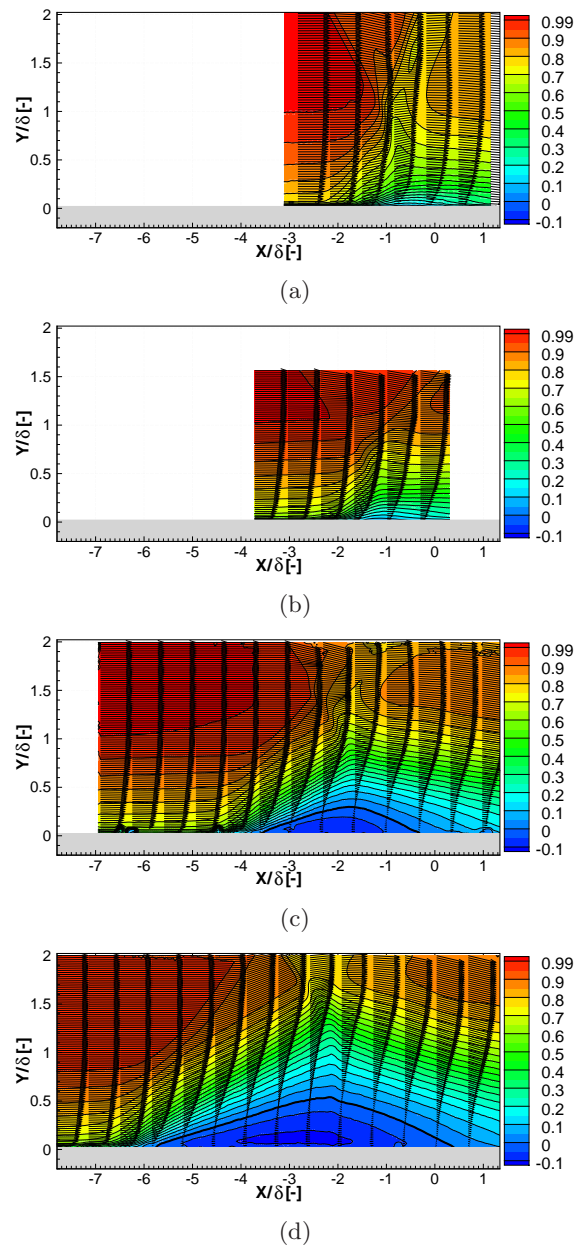
Figure 5.3: Mean streamwise velocity component U normalised by free-stream value U_e with the mean velocity vectors superposed: high Reynolds number (a) 6.0°; low Reynolds number (b) 5.5°; low Reynolds number separated cases (c) 8.0° and (d) 9.5°, from Piponniau (2009). The black solid line indicates the zero velocity contour.

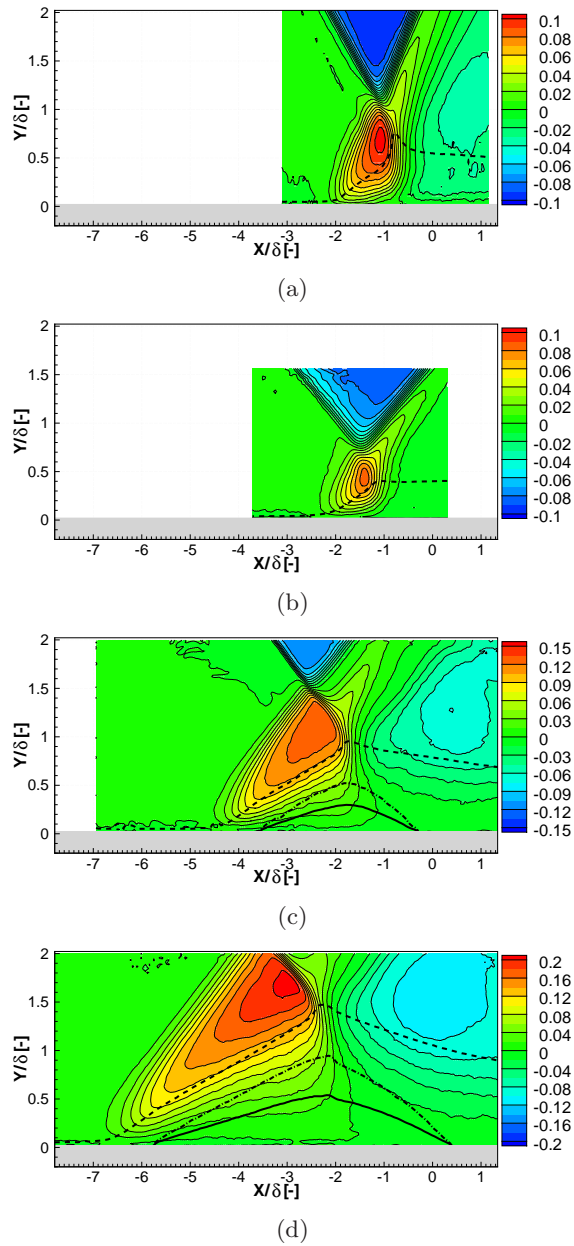Figure 5.4: Mean wall normal velocity component V normalised by free-stream value U_e: high Reynolds number (a) 6.0°; low Reynolds number (b) 5.5°; low Reynolds number separated cases (c) 8.0° and (d) 9.5°, from Piponniau (2009). The black solid line indicates the zero velocity contour, the dashed contour represents the sonic line and the dashed-dotted contour indicates the dividing streamline.

5.3 Fluctuating flow fields

In analogy to the previous section, figures 5.5, 5.6 and 5.7 compare the turbulence intensity for both velocity components and the Reynolds shear stress for all interactions under consideration.

The reflected shock shows strong velocity fluctuations as a consequence of pronounced variations in the shock positions for all interactions. The incident shock wave was observed to be stationary and local velocity fluctuations (particularly for the high Reynolds case, where the potential flow is seeded) are mainly attributed to PIV measurement uncertainties in the direct vicinity of the shock. The increase in V-component fluctuations observed just upstream of the incident shock in the high Reynolds case is also due to optical refraction effects (as mentioned in the previous section), probably due to density gradients within the optical path caused by the interaction of the shock with the boundary layer on the tunnel side window. The particle images in this region are blurred with no physical change in the flow velocity.

An increase in the velocity fluctuations and the Reynolds shear stress throughout the interaction region can be observed. The large increase in the U-component fluctuations directly behind the reflected shock foot is associated to the development of a shear layer, generating large scale coherent structures. It can be seen to occur for all interactions, even for the small flow deflections. In the latter case, it occurs close to the wall, while for the large flow deflection interactions, this region is clearly detached from the wall. The path of the peak horizontal turbulence intensity seems to be enclosed by the sonic line and the dividing streamline (or the wall, in absence of the latter). This could just be an evidence caused by the presence of the shear layer itself, and it is not known whether this fact has a particular significance. The peak levels coincide with neither the zero velocity contour, nor with the dividing streamline. The structures generated by the mixing layer are shed at the approximate impact point of the incident shock on the shear layer, see Dupont *et al.* (2006) and Dupont *et al.* (2008). They induce elevated levels of the turbulence intensity and the Reynolds shear stress in the recovering boundary layer downstream of the interaction. The Reynolds shear stress has been found to be susceptible to yielding underestimated values in the upstream boundary layer (see chapter 4 and Piponniau (2009)). However, due to the larger velocity dynamics inside the interaction, the value is still expected to give a good indication of the development of vortical structures. A decrease in Reynolds shear stress occurs behind the reflected shock foot for all interactions, attaining even slightly negative values in three of the cases. This decrease appears to coincide with the location of the shear layer.
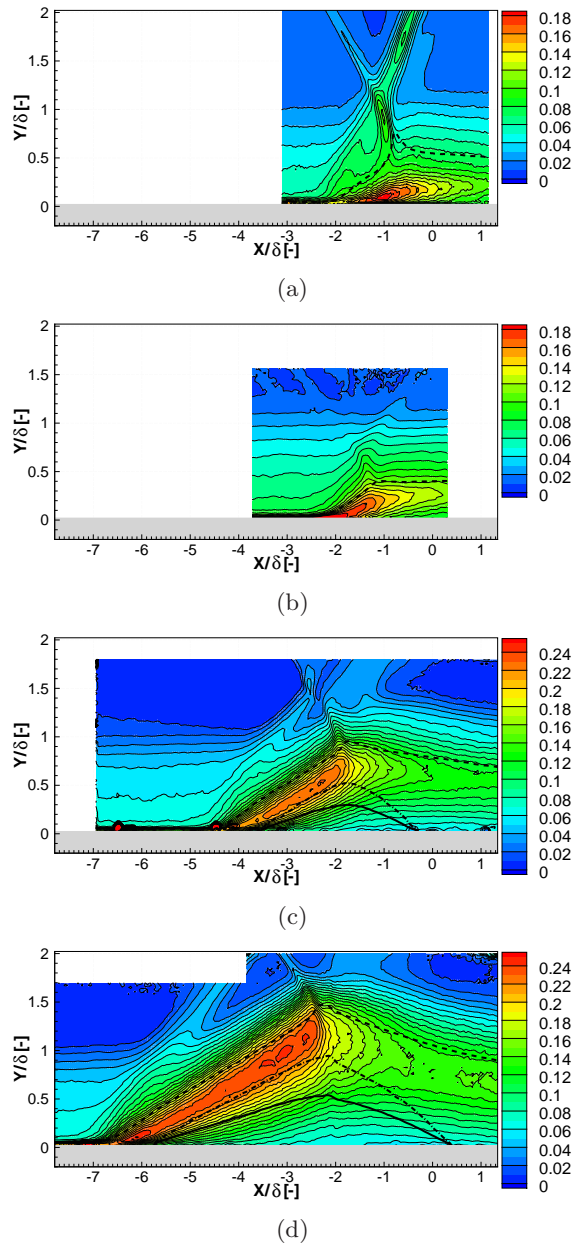
Figure 5.5: Streamwise turbulence intensity: high Reynolds number (a) 6.0°; low Reynolds number (b) 5.5°; low Reynolds number separated cases (c) 8.0° and (d) 9.5°, from Piponniau (2009). The black solid line indicates the zero velocity contour, the dashed contour represents the sonic line and the dashed-dotted contour indicates the dividing streamline.
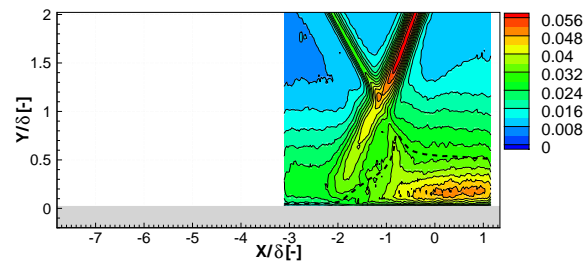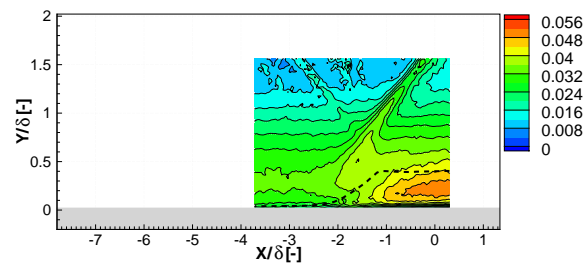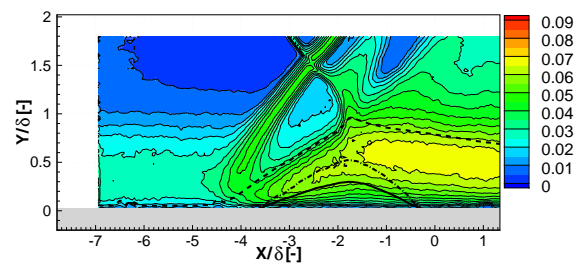
Figure 5.6: Wall normal turbulence intensity: high Reynolds number (a) 6.0°; low Reynolds number (b) 5.5°; low Reynolds number separated cases (c) 8.0° and (d) 9.5°, from Piponniau (2009). The black solid line indicates the zero velocity contour, the dashed contour represents the sonic line and the dashed-dotted contour indicates the dividing streamline.
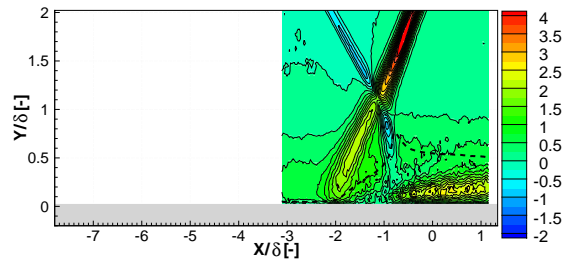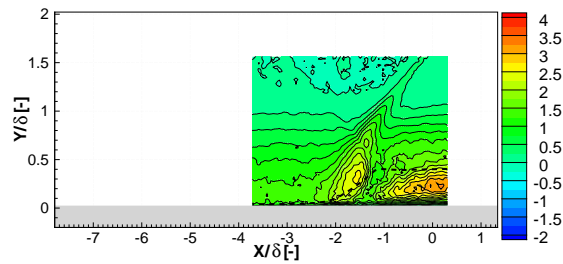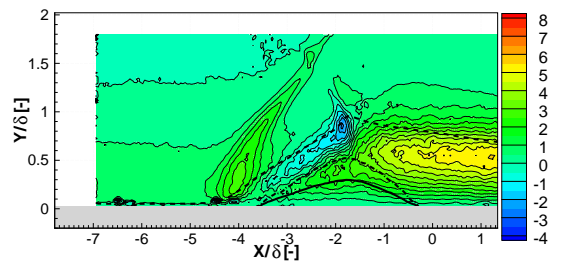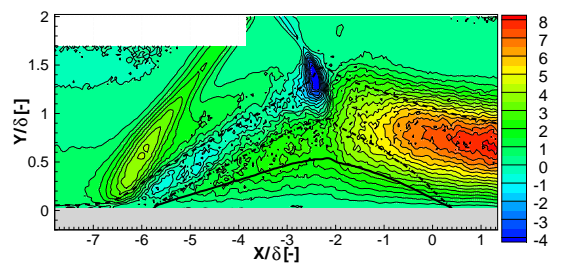
Figure 5.7: Reynolds shear stress, normalised by U_e^2 and multiplied by a factor 1000 for visualisation purposes: high Reynolds number (a) 6.0°; low Reynolds number (b) 5.5°; low Reynolds number separated cases (c) 8.0° and (d) 9.5°, from Piponniau (2009). The black solid line indicates the zero velocity contour, the dashed contour represents the sonic line and the dashed-dotted contour indicates the dividing streamline.

5.4 Instantaneous flow organisation

An overview of representative instantaneous realisations is given with a particular attention to the separation bubble state. This is done for each of the interactions presented in the previous chapter: the high Reynolds number and low Reynolds number incipient cases, see figures 5.8 and 5.9 respectively, and the low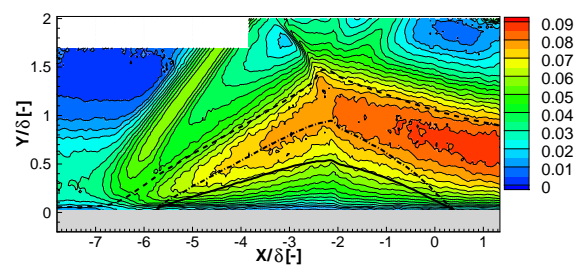 Reynolds number separated cases, see figures 5.10 and 5.11. The data for the separated cases have been taken from Piponniau (2009) and have been published in amongst others Piponniau *et al.* (2009).

For each interaction, three typical realisations are shown, representative for the thinnest, medium and thickest separation bubbles. The regions of reversed flow are shown in black. The non-validated vectors have been replaced with interpolated values for visualisation purposes. The horizontal axis is normalised by the interaction length L. For the incipient separation interactions, significant flow reversal occurs only for the thick bubble state. For the medium bubble state, small pockets of reverse flow are observed. For the shallow bubbles, the flow is completely attached, though a zone of retarded fluid can still be observed. For the separated interactions, flow reversal occurs practically all of the time, specifically for the $\varphi = 9.5°$ case. The shallow bubbles for the $\varphi = 8.0°$ case corresponds approximately to the thick bubbles for the incipient interactions. The height of the thickest bubbles is of the order of the boundary layer thickness.
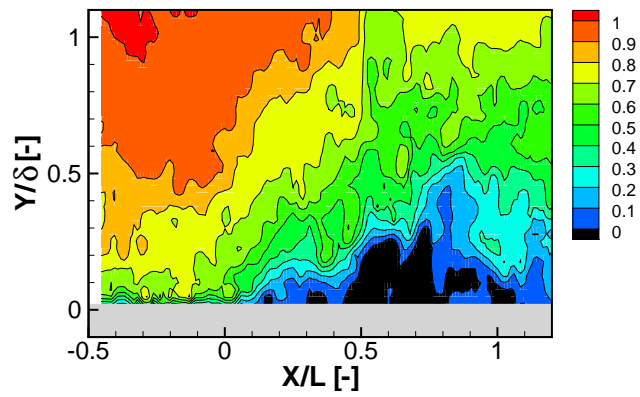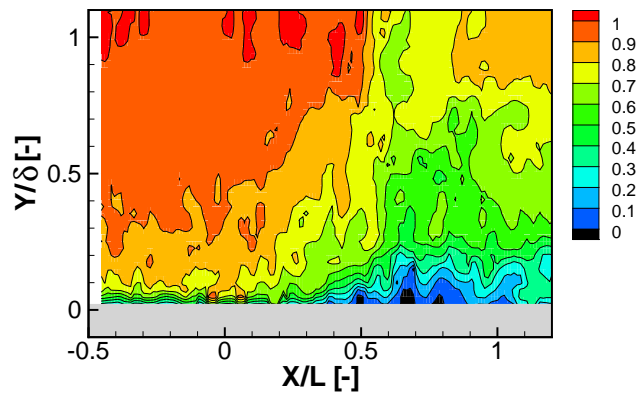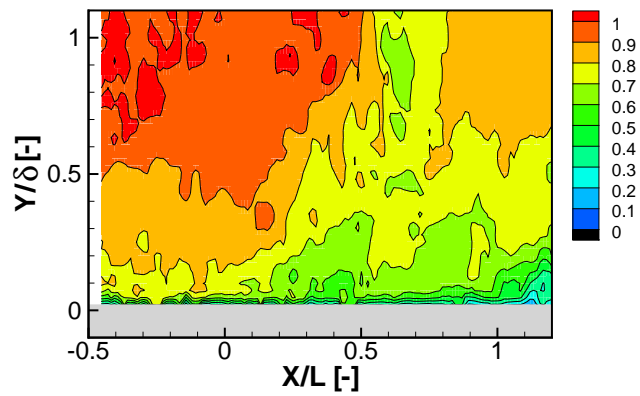
Figure 5.8: Instantaneous streamwise velocity realisations, normalised by U_e, high Reynolds number 6.0°: (a) shallow, (b) medium and (c) thick separation bubble.
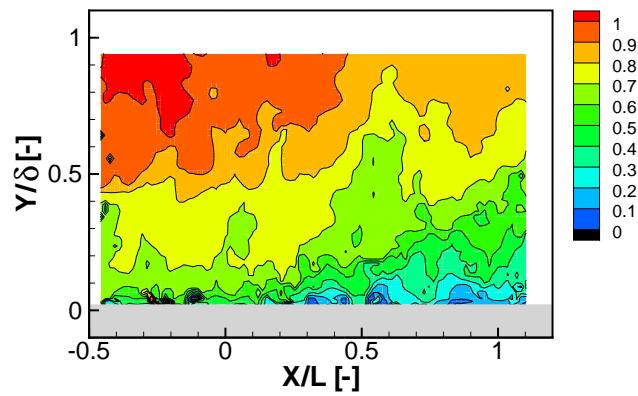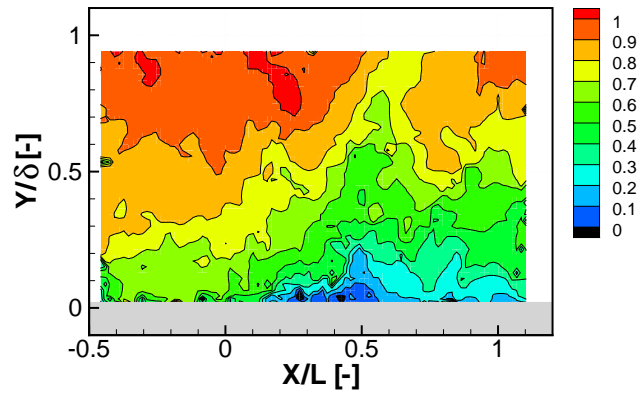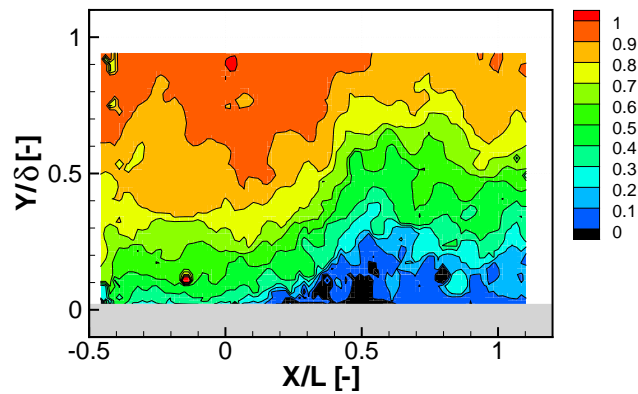
Figure 5.9: Instantaneous streamwise velocity realisations, normalised by U_e, low Reynolds number 5.5°: (a) shallow, (b) medium and (c) thick separation bubble.
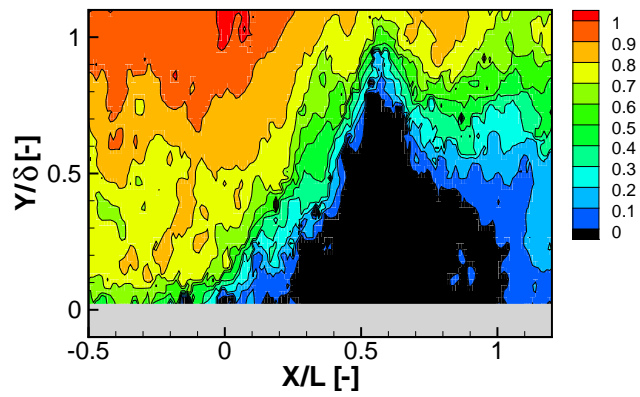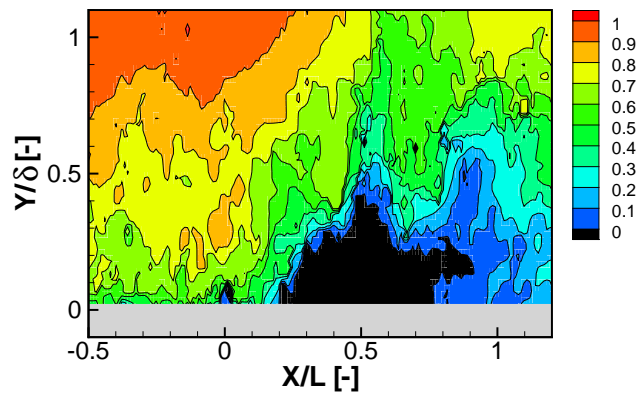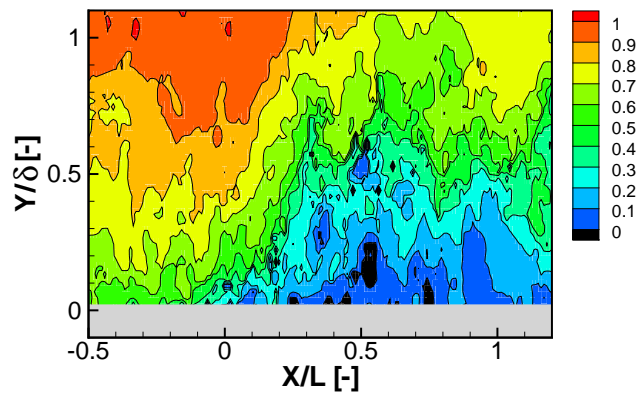
Figure 5.10: Instantaneous streamwise velocity realisations, normalised by U_e, low Reynolds number 8.0°: (a) shallow, (b) medium and (c) thick separation bubble; data from Piponniau (2009).
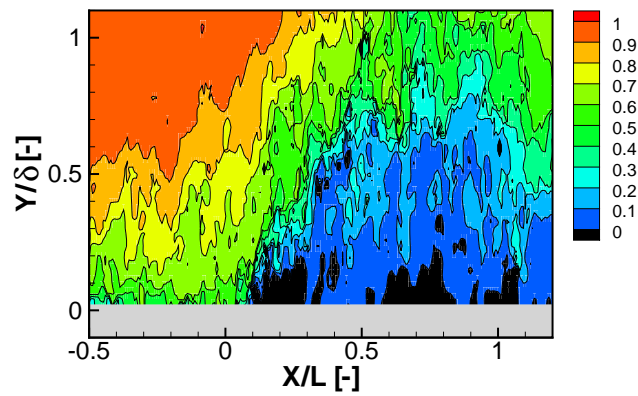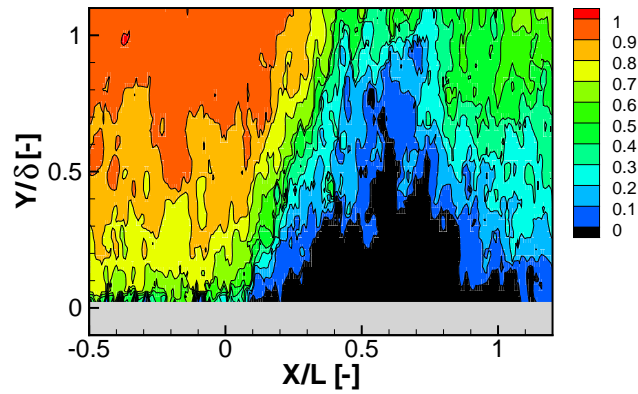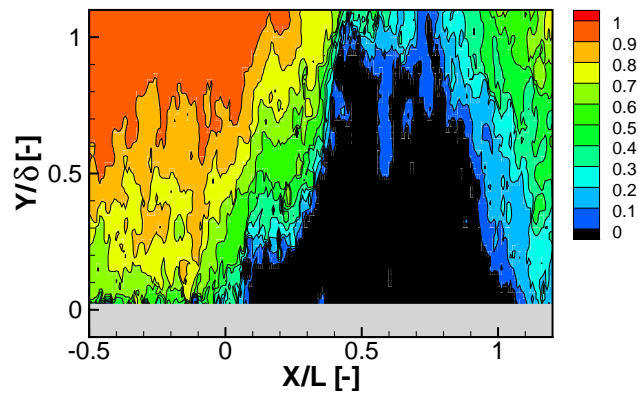
Figure 5.11: Instantaneous streamwise velocity realisations, normalised by U_e, low Reynolds number 9.5°: (a) shallow, (b) medium and (c) thick separation bubble; data from Piponniau (2009).

5.5   Discussion

From this direct comparison of the four interactions of different shock intensity and Mach number, and spanning an order of magnitude difference in Reynolds number, it can be concluded that the same types of flow features are present in all cases. The interactions show a very similar flow organisation, with the exemption of mean separation and a well developed shear layer that is detached from the wall, which appear only for the large shock intensities. In all cases, the flow is strongly retarded by the interaction, and there is a trace of the generation of large scale energetic structures in the separation zone. The reflected shock is clearly unsteady in all cases. It is displaced upstream over a significant distance with respect to the inviscid reflection case. The displacement thickness is significantly increased through the interaction and the sonic line is lifted away from the wall. A significant part of the boundary layer remains subsonic for a large distance downstream.

The characteristic time scales present within the high Reynolds number interaction will first be quantified in chapter 6. Chapter 7 will then investigate what the effect is of upstream disturbances on the interaction topology and the reflected shock dynamics. This to verify what the action the upstream boundary exerts on the separation bubble, and hence whether such upstream disturbances are an effective way to control an interaction with significant flow separation. Part II will consecutively take into account the current results and observations to propose a scaling that takes into account the Mach number and Reynolds effects. It will furthermore analyse the interaction unsteadiness, identifying different mechanisms behind it and their mutual relevance depending on the flow separation state.

Chapter 6

Experimental determination of time scales

The unsteady organisation and temporal dynamics of the interaction have been investigated experimentally for the high Reynolds number case by means of dual-plane particle image velocimetry (Dual-PIV). Two independent PIV systems were combined in a two-component mode to obtain instantaneous velocity fields separated by a prescribed small time delay, as described in section 3.3.3. This enables, in addition to mean and statistical flow properties (see chapter 5), also the determination of instantaneously time-resolved data to characterise the temporal dynamics of the flow phenomenon in terms of time scales, temporal correlations and convective velocities. Firstly, the ability of the system to track vortical structures, advecting within the interaction at several hundreds of meters per second, is evaluated. Secondly, the temporal auto-correlation coefficients are obtained in the complete flow domain for a range of time delays from $5\mu s$ to $2000\mu s$. Finally, characteristic time scales are determined, with special interest for the incoming boundary layer, the vortex formation and the low frequency reflected shock dynamics. These results have been reported in Souverein & Van Oudheusden (2008); Van Oudheusden & Souverein (2009). In addition, they have been published in Souverein *et al.* (2007a, 2008b, 2009b).

6.1 Time resolved tracking of flow structures

As a first illustration of the capabilities of the Dual-PIV approach, some individual flow realisations are considered in further detail. This with the aim to investigate the ability of the system to track vortical structures, advecting within the interaction at several hundreds of meters per second.

An example of the instantaneous occurrence of separation and the advection of vortical structures in the separated shear layer is shown in figure 6.1(a), together with its time-resolved counterpart in figure 6.1(b), captured
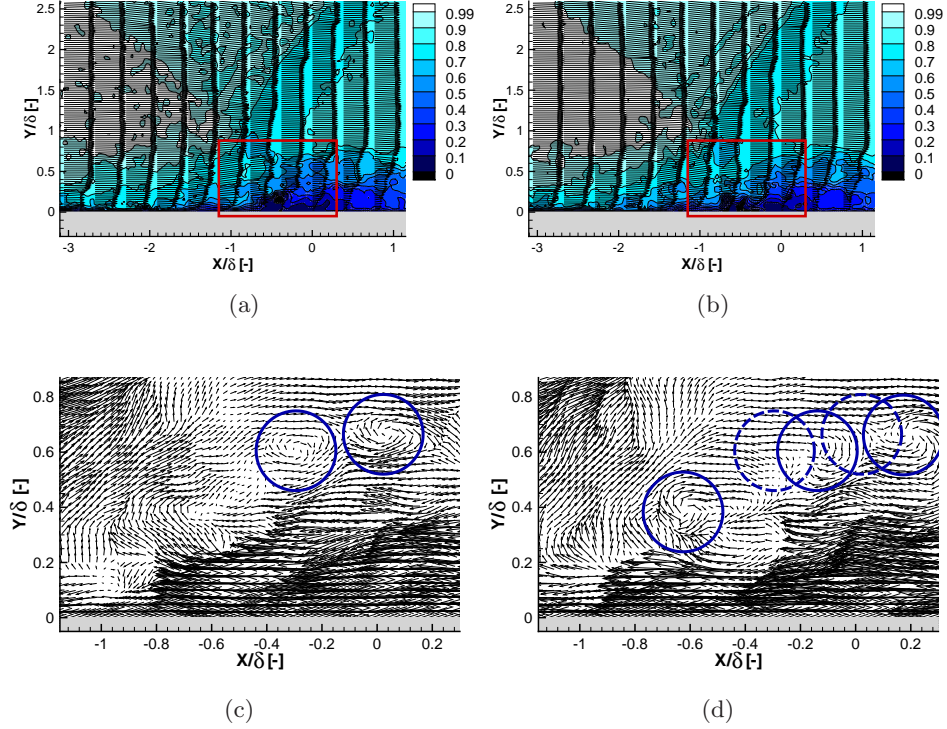
Figure 6.1: Instantaneous velocity fields: horizontal velocity component contours with velocity vectors, first realisation (a) and second realisation (b) separated by $\partial t_2 = 10\mu s$; zoom of the interaction region of the same acquisitions showing velocity vectors with a convective velocity of $290ms^{-1}$ subtracted, first realisation (c) and second realisation (d); the circles indicate vortical structures and their advection between the two realisations.

with a time delay of $10\mu s$. The flow can be seen to display reversal, as indicated by the occurrence of negative velocity values (visualised by the saturation of the zero velocity contour level in black). The maximum absolute value of the reversed flow velocity is $27.0ms^{-1}$ (6.0% of U_e) for the first realisation and $34.3ms^{-1}$ (7.7% of U_e) for the second realisation. The flow fields of figures 6.1(a) and (b) are selected for a closer investigation to identify the existence of advected vortical structures. To this purpose a zoom is made of the velocity fields, as indicated by the rectangular frame. The two consecutive velocity fields are temporally separated by a time $\partial t_2 = 10\mu s$ and a convective velocity of $290ms^{-1}$ is subtracted to optimally visualise the vortices (see figures 6.1(c), (d)). Two neighbouring vortex cores were identified in the first velocity field (indicated by the two solid circles, figure 6.1(c)). They can be seen to advect in the streamwise direction by slightly under $3mm$ within the time delay (original location indicated by the dashed

circles, new location by the solid circle, figure 6.1(d)), which is consistent with the estimated value of the convective velocity. Within the line of zero streamwise velocity another vortex core was identified in the second field that could not be matched to a vortex in the first field (solid circle, figure 6.1(d)). As a further observation, it can be remarked that the low speed region is expanding in upstream direction between the two realisations, as indicated by the displacement from $x/\delta_0 \approx -0.8$ to -0.9 of the pocket of negative velocities in the convective reference frame.

This confirms that vortical structures exist within the interaction region and that the development of flow structures moving with a convective velocity of several hundreds of meters per second can be resolved with Dual-PIV.

6.2 Determination of time scales

Since measurements were performed for a range of time separations from $\partial t_2 = 0\mu s$ to $2000\mu s$, making it possible to obtain time correlation data for the complete flow field as a function of the time delay. Those can then be exploited to determine the characteristic time scale at each position in the flow. Specific regions of interest are the incoming boundary layer, the recirculation region where vortex production and shedding occurs, the reflected shock and the recovering boundary layer. Figures 6.2 and 6.3 show the time correlation coefficient for the U-component of velocity, for small and large time delays respectively. The time correlation coefficient is defined by equation 6.1, where u_i' is the fluctuation component and σ represents the standard deviation. Furthermore, the indices 1 and 2 stand for the first and second measurement at a single point in the flow field, separated by ∂t_2:

$$R_{u_1 u_2} = \frac{\overline{u_1' u_2'}}{\sigma_{u_1} \sigma_{u_2}} \tag{6.1}$$

This correlation coefficient may be interpreted as a measure for assessing the duration of coherence of a flow phenomenon at a fixed spatial coordinate (it is identical to the autocorrelation at vanishing time delay). One can think of observing the passage of a vortical structure in the incoming boundary layer from a stationary point in space. For very small ∂t_2 (i.e. much smaller than the passing time of the vortex) the flow structure will hardly have moved and a very high correlation coefficient is obtained. For increasingly larger ∂t_2 the vortex will displace over a larger distance and the correlation coefficient will decrease accordingly, until the vortex has moved out of sight and hence the correlation vanishes. Alternatively, the structure may deform due to non-linear effects and loose correlation. Similar reasonings can be applied to other flow features as well. Low frequency phenomena or long wavelength flow structures will lead to higher values of the correlation coefficient at large ∂t_2.

An effect that has to be taken into account in the computation of the correlation coefficient is the slow temporal drift in the free-stream velocity inherent to blow-down facilities as a consequence of the total temperature drift condition in the supply vessel (see appendix A.1.2). The effect on the mean velocity is inferior to the free-stream turbulence and the measurement uncertainty. Nonetheless, a velocity trend does constitute a coherent very low frequency flow motion. In addition, combining multiple runs to compute the correlation statistics also introduces a low frequency artefact which is an indirect consequence of the velocity trend. Both effects could result in a residual non-zero value of the correlation coefficient at large ∂t_2. To remedy this, the velocity data have been corrected for any linear trends. The time correlation statistics have consecutively been computed for the correctly zero mean centred velocity fluctuations.

In the first place, it is observed that for $\partial t_2 = 0 \mu s$ (see figure 6.2(a)), in which case both measurements should be identical and thus have a correlation coefficient of unity, not all of the flow is fully correlated. Especially in the external flow, where the fluctuations are small, the correlation is medium to low. This may be attributed to measurement noise and may indeed be interpreted as a measure of the accuracy of the PIV technique. As a second remark, it may be noticed that the incident shock wave appears in the correlation results for small ∂t_2. Since the incident shock was verified to be steady and since it appears for the zero-time-delay case as well, this feature may also be attributed to limitations inherent to the PIV measurements technique close to the shock, as was observed in the case of the Reynolds stresses, see section 5.3.

A qualitative evaluation of the correlation coefficient in figures 6.2 and 6.3 shows that for small ∂t_2 below $10 \mu s$ all regions of interest (the incoming boundary layer, the interaction zone and the reflected shock in combination with the expansion fan) remain highly correlated with values close to unity. Evidently, on the scale of the measurement resolution, no flow regions display time scales that are substantially below $5 \mu s$, justifying the choice of this time delay as the smallest value in the investigation. The incoming boundary layer is the first region to decorrelate, starting from $\partial t_2 = 10 \mu s$. The boundary layer is largely decorrelated at $\partial t_2 = 50 \mu s$. At this time delay the interaction zone with the mixing layer and the subsequent vortex shedding and recovering boundary layer are still correlated. Somewhere between $\partial t_2 = 100 \mu s$ and $500 \mu s$, the mixing layer and vortex shedding regions also become decorrelated. The reflected shock shows high values of the correlation coefficient throughout most of the range of time delays considered so far. It starts to decorrelate only for the very large time delays. The correlation coefficient of the reflected shock has practically vanished at $\partial t_2 = 2000 \mu s$. This confirms the existence of different time scales within the flow domain, and in particular it evidences the low-frequency behaviour of the reflected shock.
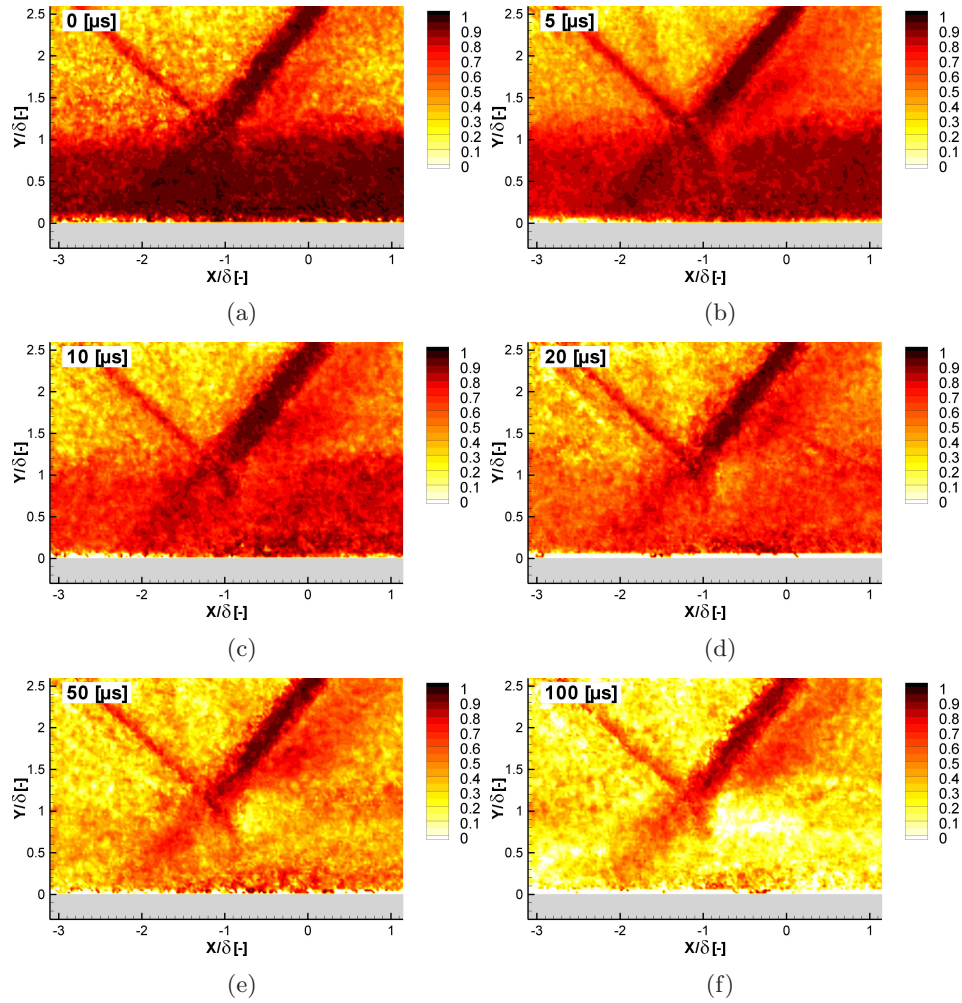
Figure 6.2: The temporal auto-correlation coefficient for small time delays ($\partial t_2 = 0$ to $100\mu s$).

This qualitative evaluation of the time scales can be quantified further by plotting the local time correlation coefficient against the time delay for different locations in the flow (see figure 6.4). The selected regions of interest are shown on the top of this figure (superimposed on the autocorrelation coefficient at $\partial t_2 = 200\mu s$ and contours of the Reynolds shear stress for reference; the dashed horizontal line indicates the approximate edge of the undisturbed boundary layer). Statistics have been computed over multiple points within confined regions representative of the flow phenomenon to aid the statistical convergence (note that only 200 realisations are available per time delay).
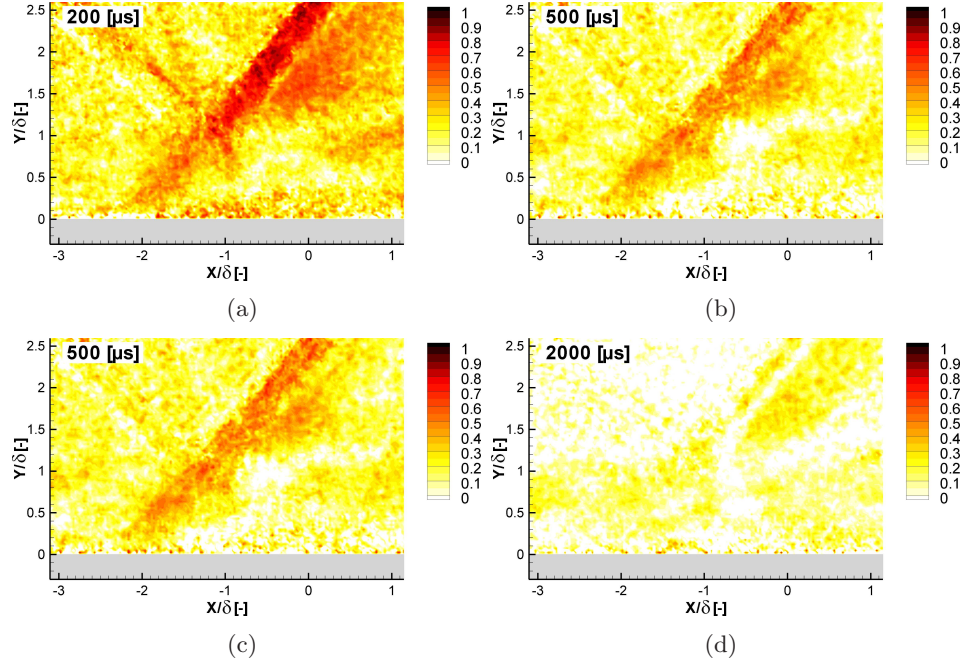
Figure 6.3: The temporal auto-correlation coefficient for large time delays
($\partial t_2 = 200$ to $2000\mu s$).

The fluctuations in each point are centred locally around a zero mean
value by means of the aforementioned detrend routine. The correlation
statistics are computed consecutively, treating the combination of points as
a single data ensemble while taking into account the proper weighting for
rejected vectors. It has been verified that no significant dependence of the
results exists on the selection of each region within the local flow domain
under consideration. For reference, the auto-correlation coefficient in the
free-stream is also shown. The results have been plotted in both linear and
semi-log representations, the latter to better visualise the different orders of
magnitude of the time scales.

The different orders of magnitude are clearly apparent from figure 6.4.
The auto-correlation coefficients of the reflected shock have not yet vanished
for the large time delays, while the values of the other regions have already
converged asymptotically to zero at approximately $\partial t_2 = 1000\mu s$. Taking
the crossing of the $\frac{1}{e}$-level of the auto-correlation coefficient as representa-
tive for the time scales, it is evident that the smallest time scales are found
in the incoming boundary layer, followed by the recovering boundary layer,
the vortex shedding, the reflected shock foot and the reflected shock. It is
noted that the free-stream value starts from the approximate $\frac{1}{e}$ level and is
hence only weakly correlated for the smallest time delays (including $0\mu s$).

(a)

(b)

(c)
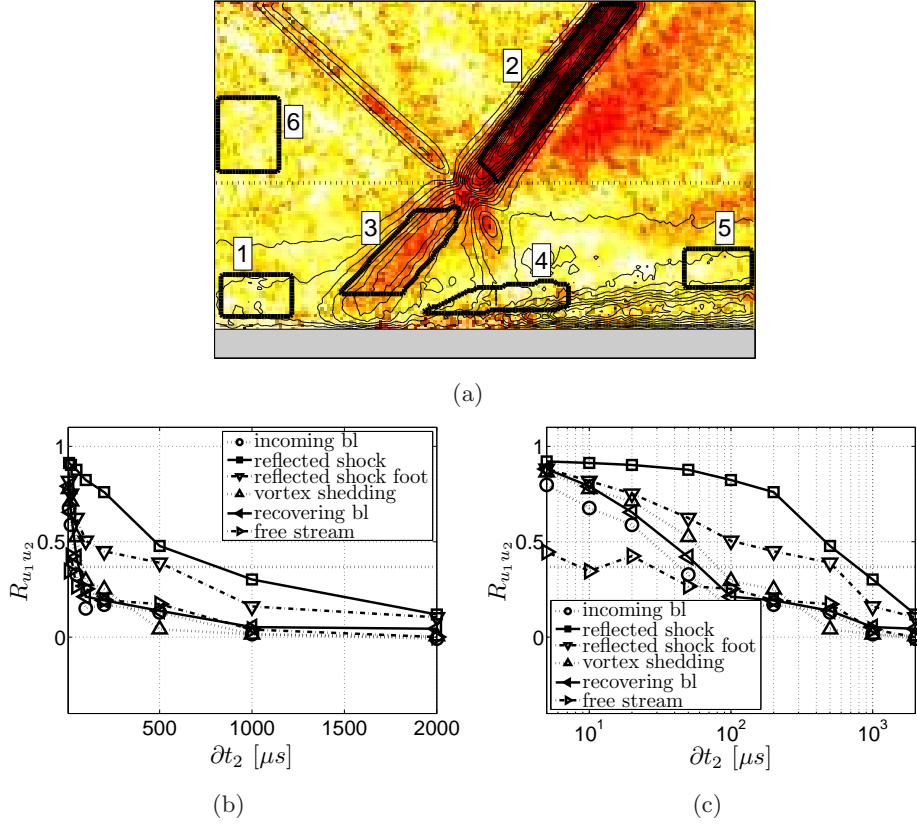
Figure 6.4: Local temporal auto-correlation coefficient for selected regions of the flow field: (a) regions under consideration (1: incoming boundary layer, 2: reflected shock, 3: reflected shock foot, 4: vortex shedding, 5: recovering boundary layer, 6: free-stream), Reynolds shear stress contour lines superimposed for reference; (b) auto-correlation coefficient for each respective region; (c) auto-correlation coefficient in semi-log representation.

In addition, the auto-correlation value itself in the free-stream is very small (one to two orders of magnitude smaller in comparison to the other regions) and it is likely dominated by measurement noise. Looking at the incoming boundary layer, a characteristic time is obtained of $40\mu s$ and hence an equivalent frequency of $25kHz$. Considering an integral length scale of $\frac{\Lambda}{\delta} = 0.5$ (see Dussauge & Smits (1995)) and a convective velocity of $0.8U_e$ yields an integral time scale of $24\mu s$ and hence a frequency of $42kHz$. The boundary layer time scales hence appear to be overestimated. It is unknown if this overestimated value is physical or whether it is a measurement artefact. As for the region of vortex formation, a characteristic time scale of $80\mu s$ is obtained, corresponding to $12.5kHz$. For the reflected shock, a time scale of $800\mu s$, or $1250Hz$, is obtained. These values can be non-dimensionalised

through the definition of the Strouhal number from Dupont *et al.* (2006), using the interaction length of $L = 37mm$ and the velocity downstream the first shock of $U_1 = 407ms^{-1}$:

$$S_L = \frac{fL}{U_1} \tag{6.2}$$

The value for the vortex formation region, $S_L = 1.1$, falls within the range reported in Dupont *et al.* (2006) for the initial part of the interaction. The Strouhal number for the shock unsteadiness, $S_L = 0.11$, is higher than the value of $S_L = 0.03$ for the low Reynolds number interactions reported in Dupont *et al.* (2006)). This can however be attributed to the Mach effect on the entrainment rate of the mixing layer, and a good agreement is obtained with the values reported for low supersonic (Mach=1.5) and subsonic separated flows ($S_L = 0.1 - 0.12$), see Piponniau *et al.* (2009).

Considering figure 6.4 in more detail, two further observations can be made. In the first place, the reflected shock foot, the vortex shedding and the recovering boundary layer regions all show the same behaviour for small time delays, and further follow more loosely the trend of the incoming boundary layer. For larger time delays, the downstream boundary layer seems to tend towards the incoming boundary layer, diverging from the vortex shedding trend. This is indeed indicative of the recovery process of the boundary layer. For larger time delays, the incoming boundary layer, the vortex shedding and the recovering boundary layer curves are more difficult to interpret since they become of the same order of magnitude as the free-stream value, i.e. essentially losing correlation.

A second observation is that the reflected shock foot auto-correlation coefficient displays behaviour intermediate to the incoming boundary layer and the reflected shock in the outer flow. At small time delays, the reflected shock foot responds rather similar to the incoming boundary layer while at larger time delays the reflected shock foot seems to behave like the reflected shock in the external flow. Hence, even though the signal is influenced by the passage of turbulent structures present in the incoming boundary layer, there is also a strong low-frequency component. This indicates that the low frequency reflected shock foot unsteadiness and the motion of the shock in the outer flow occur in harmony. Similar behaviour has indeed been observed in experiments and LES simulations of this kind of interaction (see Dupont *et al.* (2006) and Touber & Sandham (2008)).

6.3 Conclusions

A Dual-PIV approach was used to classify time-correlation phenomena in a shock-wave boundary layer interaction over a large range of time scales, including small values of the time delay that are not achievable by a single PIV system (maximum equivalent repetition rate $200kHz$). This classification has shown that the time scales span almost three orders of magnitude.

The smallest time scales are present in the incoming boundary layer. The obtained equivalent frequency of $25kHz$ seems to be underestimated with respect to the expected integral time scales. It is not known whether this is physical or a measurement artefact. The frequencies associated with the $\frac{1}{e}$ criterion of the autocorrelation function for the vortex shedding and the reflected shock, $12.5kHz$ and $1250Hz$ respectively, seem to be in accordance with the literature. The auto-correlation coefficient of the downstream boundary layer region follows the vortex-shedding trend for small time delays and converges towards the incoming boundary layer values for medium time delays. This could be indicative of the recovery of the boundary layer after the interaction.

This analysis confirms that the low-frequency motion of the reflected shock that has been observed in the well separated low Reynolds case (see Piponniau *et al.* (2009)), with a time scale that is one to two orders of magnitude larger than the integral time scale of the incoming boundary layer, is also present in the incipient interaction type for the high Reynolds number case. In addition, the results indicate that the shock foot moves in harmony with the low-frequency motion of shock in the outer flow.

The potential of Dual-PIV to provide time-resolved measurements in high-speed flows has clearly been demonstrated. The achievability of small time delays combined with the high spatial resolution enabled the tracking of structures with convection speeds of several hundreds of meters per second. In addition, the large temporal dynamic range enables the simultaneously identification of time scales of three orders of magnitude difference ($1kHz$ up to $100kHz$) within a complete flow field containing over 20.000 velocity vectors.

Chapter 7

Effect of control through upstream disturbances

In the following, the effect of continuous Air Jet Vortex Generators (AJVGs) on a shock wave turbulent boundary layer interaction is experimentally investigated in the case of a supersonic flow with a Mach number of $M_e = 2.3$. The interaction corresponds to the low Reynolds ($Re_\theta = 5,000$) case with a flow deflection of $\varphi = 9.5°$, showing a significant mean separation bubble in the uncontrolled case. In the first place, the general properties of the air jets are described. Secondly, the influence of the AJVGs on the incoming boundary layer and the subsequent modification of the separation bubble topology are examined. Finally, the unsteady aspects and the resulting modification of the shock dynamics are investigated. It is noted that the longitudinal coordinates in this chapter, X, refer to the start of the original tunnel measurement section, see section 2.2. The experiment set-up has been detailed in section 2.3. The results presented in this chapter have been reported in Souverein *et al.* (2008a), Dussauge *et al.* (2009), Souverein & Debiève (2009) and Souverein & Debiève (2010).

7.1 General description of the flow

In the first place, the properties of the jets are characterised. In addition, the effect of the AJVGs on the global flow topology in the streamwise-wall normal plane and in the wall parallel plane is visualised.

7.1.1 Jet flow conditions

The choice of the operating pressure for the AJVGs has been made such as to have a significant effect on the interaction topology in the streamwise-spanwise plane at a height of $h = 1mm$. The maximum effect was observed at the largest achievable stagnation pressure for the jets $p_{0_{jets}} = 0.4bar$,
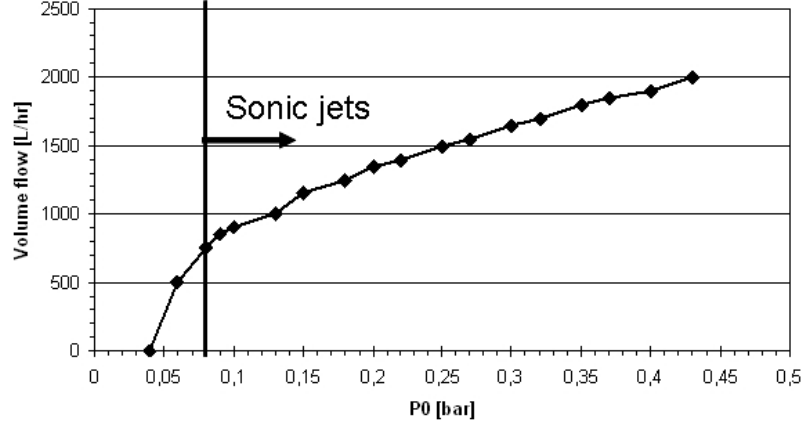
Figure 7.1: Measured AJVG total volume flow as a function of the stagnation pressure in the jet plenum chamber.

which is close to the stagnation pressure of the main flow at $0.5atm$. In such conditions, the orifices generating the jets act as sonic throats and control the injected mass flux. The stagnation pressure of the jets is adjusted by a tap of a volume-flux-meter. The dependency between the injected flux and the stagnation pressure of the jets measured in the plenum chamber is shown in figure 7.1, where the unit of the injected volume flux is $[liter/hour]$ for atmospheric conditions. As can be seen from the figure, the jets become sonic for a stagnation pressure of $p_{0_{jets}} = 0.08bar$, which is consistent with theory. The measurement of the volume-flux is only an estimation to control the good functioning of the sonic throat when pressure is varying. A direct estimation of the jet mass flux can be made, without use of the volume flux measurement, assuming sonic conditions at the jet exit. This gives a flux of $0.47g/sec$ or $1415liter/hour$ (compared to the measured value of $1900liter/hour$) under normal conditions for the complete array of 10 jets with a diameter of $\phi = 0.8mm$ each and at a total pressure and temperature of $p_{0_{jets}} = 0.4bar$ and $T_{0_{jets}} \approx 290K$. It was verified that the pressure spectrum in the chamber, which has been filled with a porous medium, does not show any resonance peaks.

7.1.2   Mass flow contribution to the boundary layer

The injected airflow was found to be negligible as compared to the mass flow deficit of the boundary layer: for an injection pressure of $p_{0_{jets}} = 0.4bar$, considering the contribution of the row of ten injectors over their span of $\Delta Z = 100mm$, and given the boundary layer displacement thickness of $\delta^* = 3mm$, the ratio of the jets mass flow ($0.47g/s$) to the boundary mass flow deficit is:
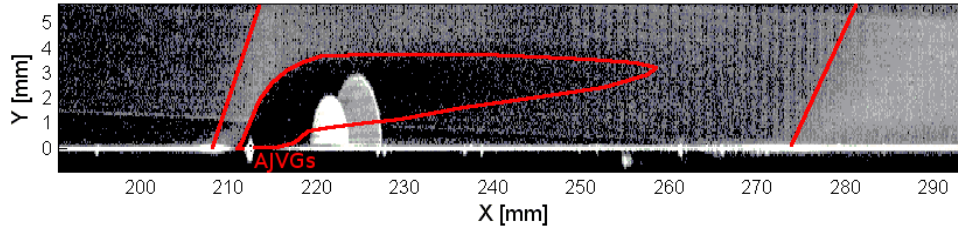
Figure 7.2: Mean image intensity of the vertical plane PIV measurements on the tunnel axis ($z = 0mm$) with AJVG control, ensemble average over 3000 acquisitions. The contrast has been enhanced for visualisation purposes.

$$\frac{Jet\ mass\ flow}{\rho_e U_e \delta^* \Delta Z} \approx 3\% \tag{7.1}$$

It is noted that with the measured volume flux of 1950 liter/hour a respective value of 4% is obtained for the mass flow ratio. This confirms that the injected mass flux should on the average not significantly contribute to the fullness of the boundary layer profile by means of the added mass flow alone.

7.1.3 Penetration height in the boundary layer

The penetration height of the AJVGs was evaluated from the PIV particle images. Since the jets themselves are not seeded, they should show up as a statistically less bright region in the ensemble average of the PIV images. This as a consequence of the lower particle density in these regions. To investigate this, the mean image intensity taken over 3000 vertical plane PIV-realisations was considered. The result for the measurements on the tunnel axis ($z = 0mm$) with AJVG control on is shown in figure 7.2 (the contrast has been augmented for visualisation purposes). Visible are the reflection of the AJVG orifices ($X = 212.5mm$) and the lack of seeding inside the injected fluid (indicated by the red contour). An increase in seeding density (image intensity) can be observed over the jet shock foot and the reflected shock foot (highlighted by the red lines), indicative of an increase in fluid density. It is remarked that the halos downstream of the jets are probably caused by an increase in seeding deposit on the wall in the wake of the jets, locally increasing the wall reflection intensity. From the lack of seeding it is deduced that the penetration height of the jets amounts to approximately $h = 4mm$.

7.1.4   Modification of the flow topology

The flow topology is depicted in figure 7.3, showing a Schlieren visualisation of the interaction with and without control. The baseline interaction at $\varphi = 9.5°$ has been extensively documented in literature (Dupont *et al.* (2006, 2008); Dussauge & Piponniau (2008)). As can be observed, the boundary layer is first perturbed by the AJVG array, which is located at the source of the weak shock-expansion system, upstream of the interaction. The free-stream velocity downstream of the jets has been verified to be identical to the undisturbed upstream value, and the boundary layer profile upstream of the jets has been shown to be in accordance with the undisturbed profile upstream of the interaction, see section 4.2. Approximately $5\delta_0$ downstream of the AJVG array, the incident shock wave impacts on the boundary layer, causing the boundary layer to thicken and to separate. The jets cause a thickening of the reflected shock, indicative of either an increased unsteadiness (shock excursion amplitude) or an increase in three-dimensionality (due to spanwise rippling). As can be observed, the interaction length (distance at the wall between the extrapolated incident and reflected shock) is not significantly affected. For the basic flow without jets, the interaction length obtained from the Schlieren images is at $L = 68.2mm$, a little smaller than the respective length obtained previously from the experiments with wall pressure measurements (where $L = 71.5mm$). This is in accordance with observations from Piponniau (2009).

The associated mean streamwise velocity is presented in figure 7.4. The figure shows the flow field for the plane corresponding to the minimum interaction length L_{min} (at $z = 2.5mm$) and the plane that transects the 'wake' of the jets (at $z = -2.5mm$). The flow is from left to right, showing the undisturbed incoming boundary layer on the left hand side of the domain of interest. As can be seen, the boundary layer is perturbed by the jet array at $X = 212.5mm$. The boundary layer thickens, but without a change in free-stream velocity. The reflected shock foot is located at approximately $X = 270mm$, where the flow is lifted away from the wall and a separation bubble appears. The solid black contour line indicates the zero velocity level. The dashed contour represents the extent of the zero velocity contour for the undisturbed case. The dashed line indicates the extrapolated incident shock, impacting at $X = 337mm$. As can be observed, the jets significantly decrease the separation bubble size. There is more high speed fluid close to the wall in the plane for L_{min}, whereas the fluid velocity is decreased in the wake of the jets for $z = -2.5mm$.

Figure 7.5 shows the U-velocity fluctuations in the same planes as for figure 7.4. It can be observed in figure 7.5(b) that the jets cause an increase in U-fluctuations that rises to about half the boundary layer height before entering the reflected shock foot. This is in accordance with the penetration height deduced from figure 7.2. These elevated fluctuation levels are indica-

(a)

(b)
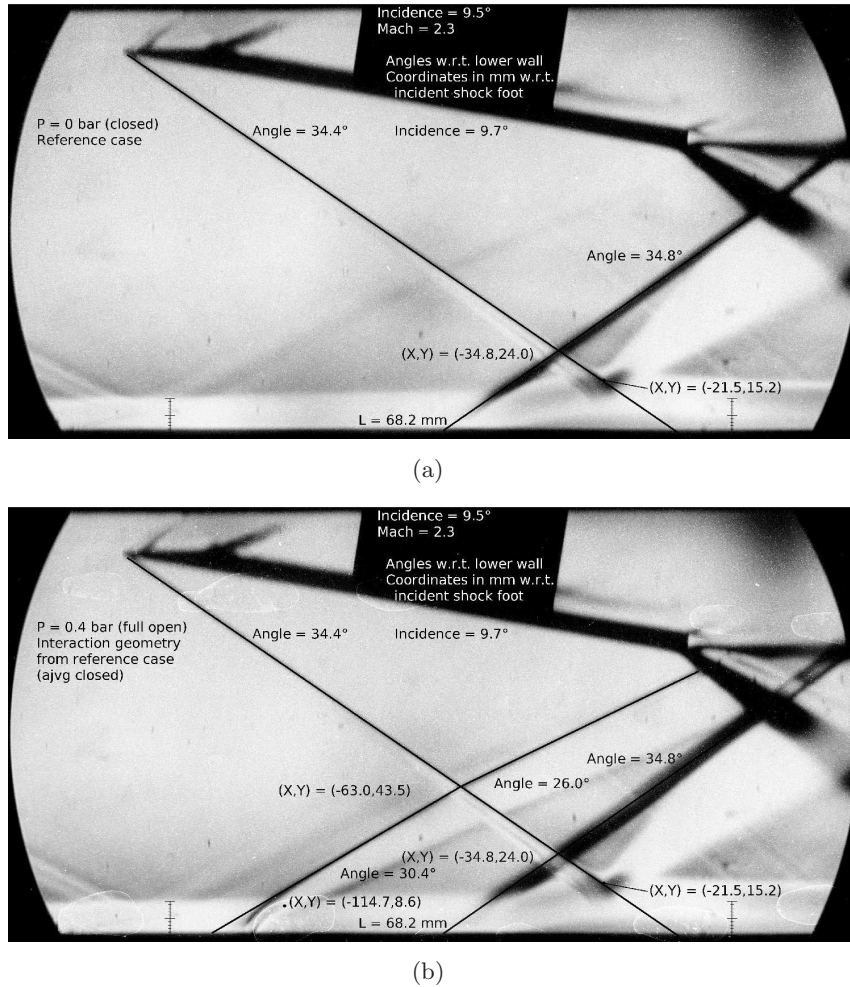
Figure 7.3: Schlieren visualisations: (a) baseline interaction topology without AJVG control; (b) interaction topology with AJVG control, jet stagnation pressure $p_{0_{jets}} = 0.4bar$.

tive of longitudinal vortices generated by the AJVGs, as will be confirmed in the following sections. The figures suggest that these vortices do not enter the separation bubble but rather pass over it. This is in accordance with observations in literature (see section 1.3). It appears therefore that the effect of AJVGs is to induce a change in the mean boundary layer profile which in turn affects the separation bubble size.

Figure 7.6 shows the mean streamwise velocity, spanwise velocity and out-of-plane velocity (respectively the components U, V and W) in the wall parallel plane at $y = 1mm$. The figures are composed of the measurements from two domains of interest: the incoming boundary layer and the
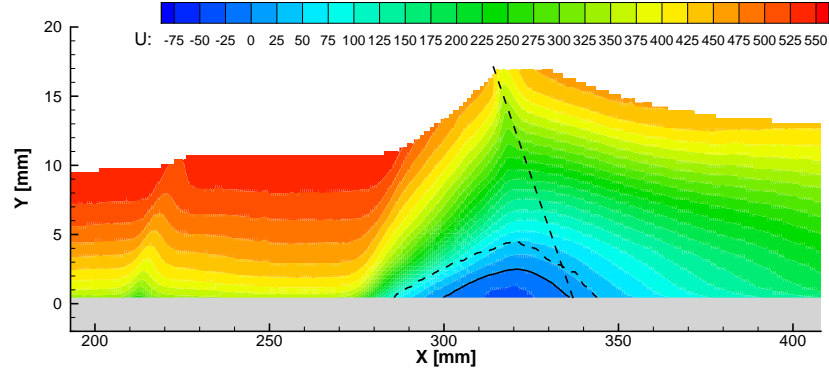
(a)
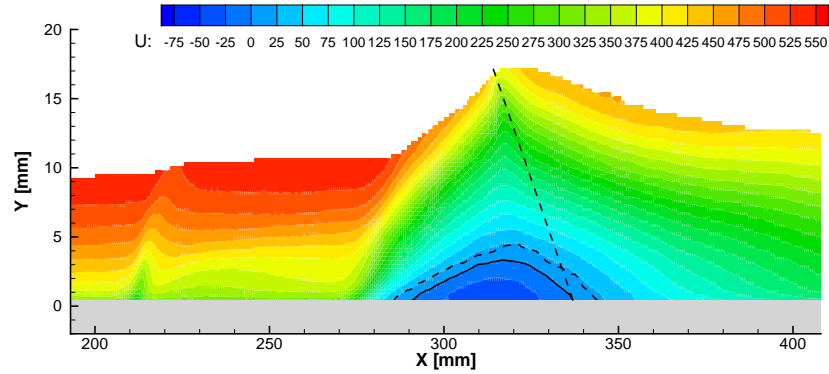
(b)

Figure 7.4: Mean U-component (ms^{-1}) in the streamwise-wall normal plane with AJVG control; the solid black contour indicates the zero-velocity level with control, the dashed black contour indicate the respective level without control, the dashed line indicates the path of the incident shock; (a) $z = 2.5mm$; (b) $z = -2.5mm$.

interaction region. The solid black contour lines in this figure indicate the streamwise velocity for $200ms^{-1}$ (taken as indicative for the extrapolated reflected shock foot location) and for $0ms^{-1}$ (representing the separation line and the reattachment line and hence the extent of the separation bubble). The horizontal solid lines and vertical line in figure 7.6(a) indicate the location of the four streamwise-wall normal measurement planes and the location of the reference boundary layer profiles respectively. Upstream of the jets, the boundary layer is homogeneous. Downstream of the AJVGs, a spanwise non-uniformity is introduced. A small streak of low speed fluid emanates from the jets, corresponding to the jet 'wake'. Between the wakes of

(a)

(b)
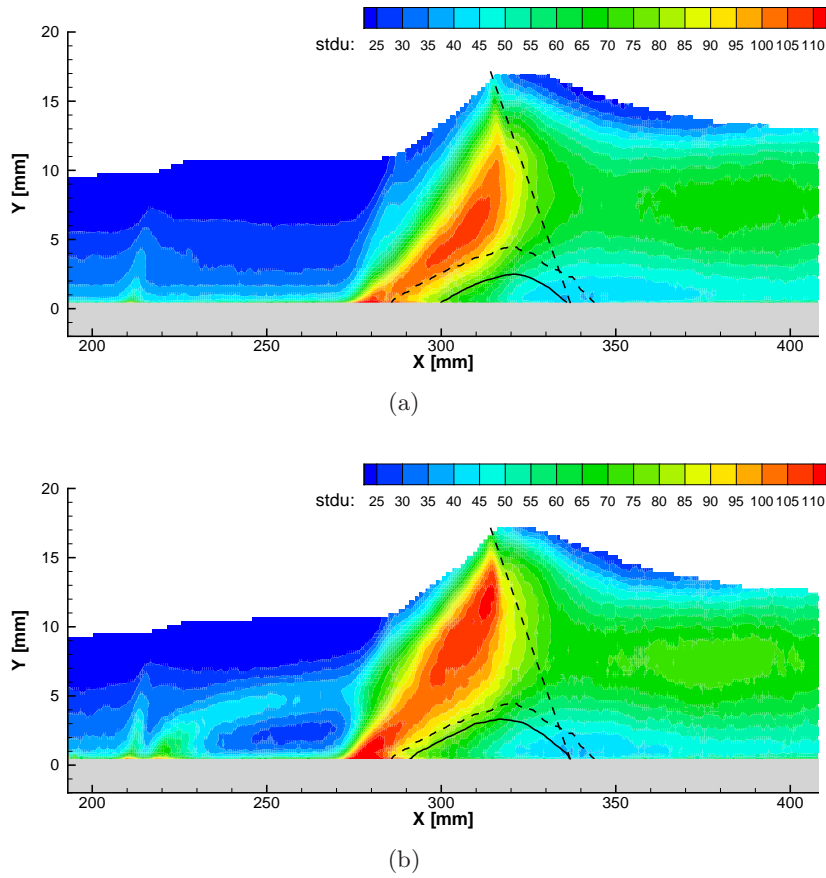
Figure 7.5: U-component fluctuations (ms^{-1}) in the streamwise-wall normal plane with AJVG control; the solid black contour indicates the zero-velocity level with control, the dashed black contour indicate the respective level without control, the dashed line indicates the path of the incident shock; (a) $z = 2.5mm$; (b) $z = -2.5mm$.

the jets, wide streaks of high speed fluid exist. Due to their inclined nature (see section 2.3), the jets induce a spanwise asymmetry, skewing the flow in the negative spanwise direction. The jet wakes (indicated for the central jet by the dashed black line in figure 7.6) have a small angle of approximately 2.8° with respect to the tunnel axis. It is remarked that both the shock and the separation line become corrugated due to the action of the jets. The most upstream location of the reflected shock foot and the separation line are linked to the wake of the jets, while the most downstream location is related to the high speed flow between the jets. In the following sections, the effect of the jets will be quantified in more detail.
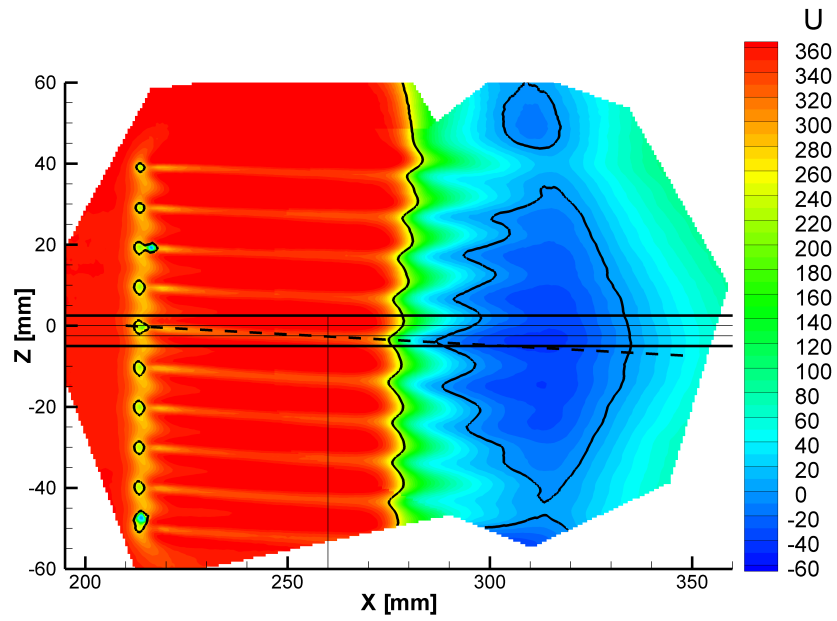
(a)
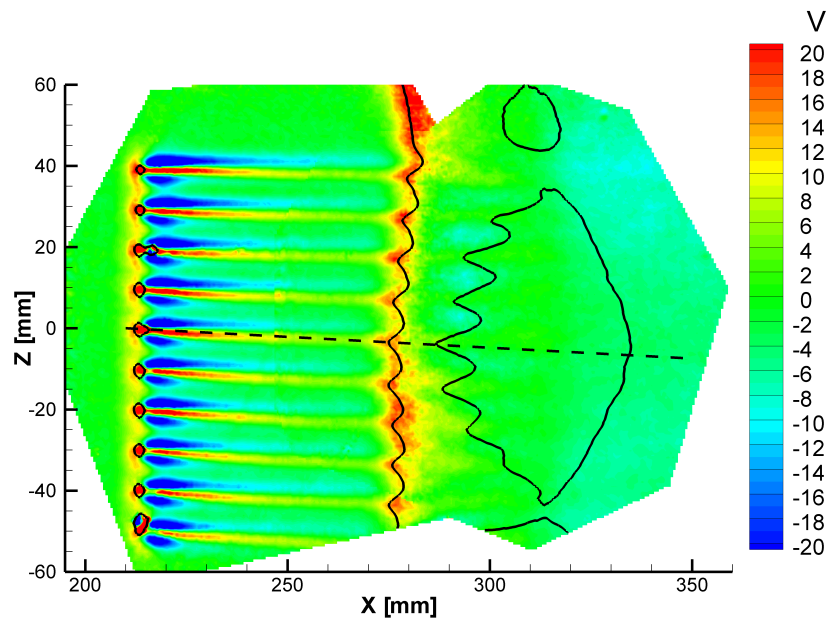
(b)

Figure 7.6: Mean velocities (ms^{-1}) in the horizontal plane with AJVG control, $y = 1mm$; caption on next page.
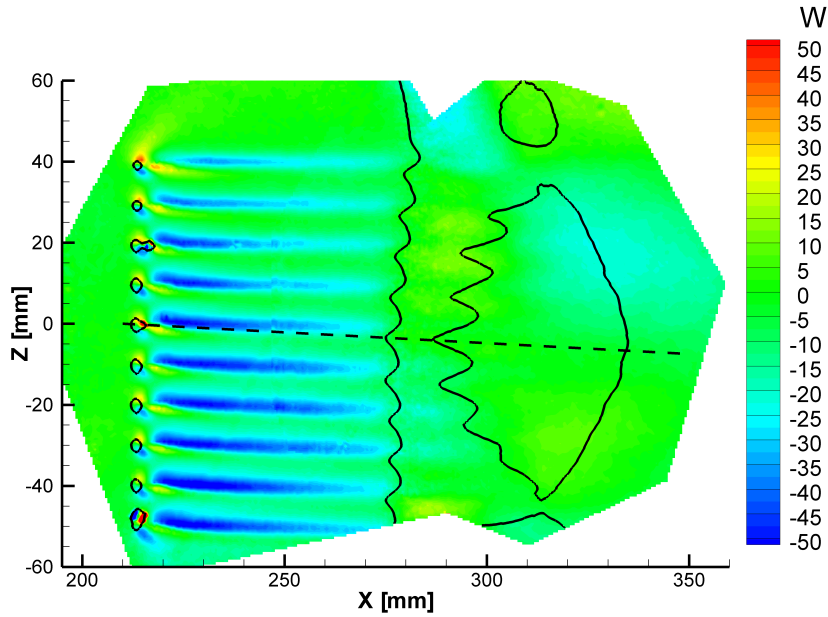
(c)

Figure 7.6: Mean velocities (ms^{-1}) in the horizontal plane with AJVG control, $y = 1mm$; the solid black contours indicate the approximate shock location and the separation contour, dashed line shows the skewing direction introduced by the jets; (a) longitudinal component U; (b) wall normal component V; (c) lateral component W.

7.2 Characterisation of the AJVG effect on the interaction

The effect of the Air Jet Vortex Generators is treated in detail in the following. Considered are consecutively the modification of the upstream boundary layer, the change in the separation bubble topology and the effect on the shock dynamics.

7.2.1 Modification of the upstream boundary layer

To quantify the effect of the jets on the incoming boundary layer topology, three-component PIV measurements have been made in the horizontal plane at four heights. The modification of the three velocity components (U, V and W) in the upstream boundary layer is shown in figure 7.7. Compared are the spanwise profiles with and without AJVGs for the four measurement plane heights. In the first place, it is remarked that a good alignment of the

lasersheet has been obtained, given the fact that the undisturbed (AJVG off) U-component is approximately constant in spanwise direction at each height. As can be observed, the jets induce a strong spanwise periodic modulation of the velocity. The modulation in the U-component at $h = 2 - 4mm$ has an amplitude of 5% (min-max variation of 10%) of the free-stream velocity. The effect of the jets is to locally increase the velocity close to the wall, while at the same time causing an overall decrease in the velocity higher up in the boundary layer. Considering the wall normal and spanwise components (V and W respectively), a modulation with the same wavelength is observed, but of a smaller amplitude (2% of the free-stream velocity). In addition, a consistent bias is introduced in the W-component due to the blowing direction of the jets, inducing a spanwise skewing of the flow.

The spanwise wall parallel measurements from the four measurement planes enable the visualisation of the flow field through a reconstruction of the mean three dimensional velocity data, encompassing the complete domain of interest from the incoming boundary layer up to reattachment. For this data volume, the angular velocity around the local velocity vector has been computed. Figure 7.8 shows the resulting iso-surfaces for values of $\alpha = -5 \times 10^3 rad/s$ and $\alpha = 5 \times 10^3 rad/s$, superimposed on the contour map of the streamwise mean velocity component at a height of $y = 1mm$ from figure 7.6(a).

As a first observation, it is confirmed that the jets induce a spanwise asymmetry, as already indicated by figures 7.6 and 7.7(c), skewing the flow with a small angle of approximately 2.8° with respect to the tunnel axis. Secondly, the flow is modulated in the spanwise direction. Pairs of counter-rotating longitudinal vortices, which are induced by each jets, are at the origin of this spanwise modulation. The blue angular velocity iso-surfaces show the main vortices produced by the AJVGs, having negative angular velocity values (turning counter-clock-wise (CCW) when looking downstream along the coordinate axis). Also visible are (in cyan) small vortex tubes with a positive angular velocity, which turn clock-wise (CW) when looking downstream. These correspond to small secondary vortices generated between the jets and the wall (the main vortices are generated between the jets and the outer flow, above the jets).

The formation of a symmetrical pair of counter rotating vortices is a well documented phenomenon for a jet in crossflow that has been evidenced both experimentally and numerically, and the formation of which has been explained theoretically (see section 1.3). In the case of inclined jet injection, pairs of asymmetric vortices have also been observed in low subsonic flows, both numerically (see Yang & Wang (2005)) and experimentally (see Yamagata *et al.* (2009)). It is noted that longitudinal vortices have also been put into evidence in experiments and computations for mechanical sub-boundary layer vortex generators (see for example Holden & Babinksy (2007); Blinde *et al.* (2009b); Lee *et al.* (2009); Lee & Loth (2009); Bur *et al.* (2009)). The
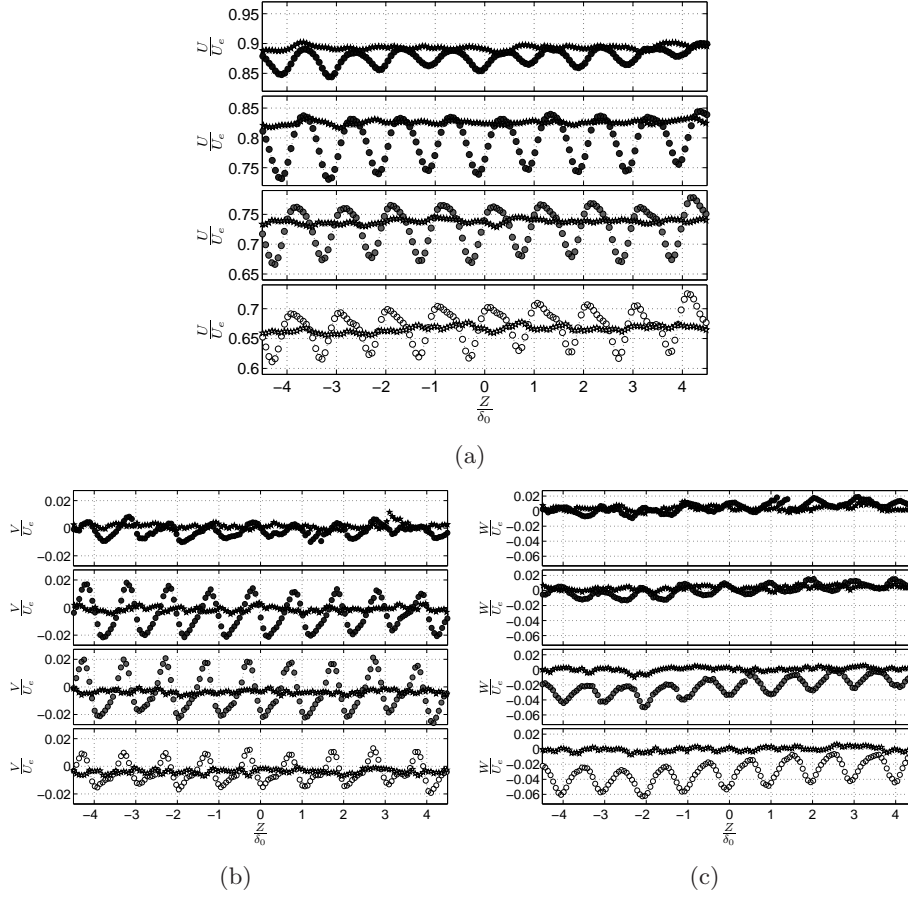
Figure 7.7: Spanwise distributions of the U, V and W-velocity components normalised by U_e, compared with and without AJVGs ((a), (b) and (c) respectively). Profiles taken at $X = 260mm$ for the four measurement planes ($h = 1$, 2, 4 and $6mm$). Grey-levels indicate the measurement plane height (ranging from white=$1mm$ to black=$6mm$).

numerical results of Lee *et al.* (2009) show furthermore that the roll-up of such longitudinal vortex structures is also observed instantaneously. The asymmetry in the current experiment appears to be the direct consequence of the inclination of the jet, 'squeezing' as it were one of the vortices between the wall and the jet, while reinforcing the vortex on top of the jet.

A zoom of the topology of these vortices is presented in figure 7.9. As can be observed from this figure, the mean velocity in between the jets is increased from $U = 350ms^{-1}$ to $U = 380ms^{-1}$, in accordance with figure 7.7(a). Since the velocity increase is directly associated to the two vortices, it seems to be an induced effect of the rotation of the longitudinal vortex
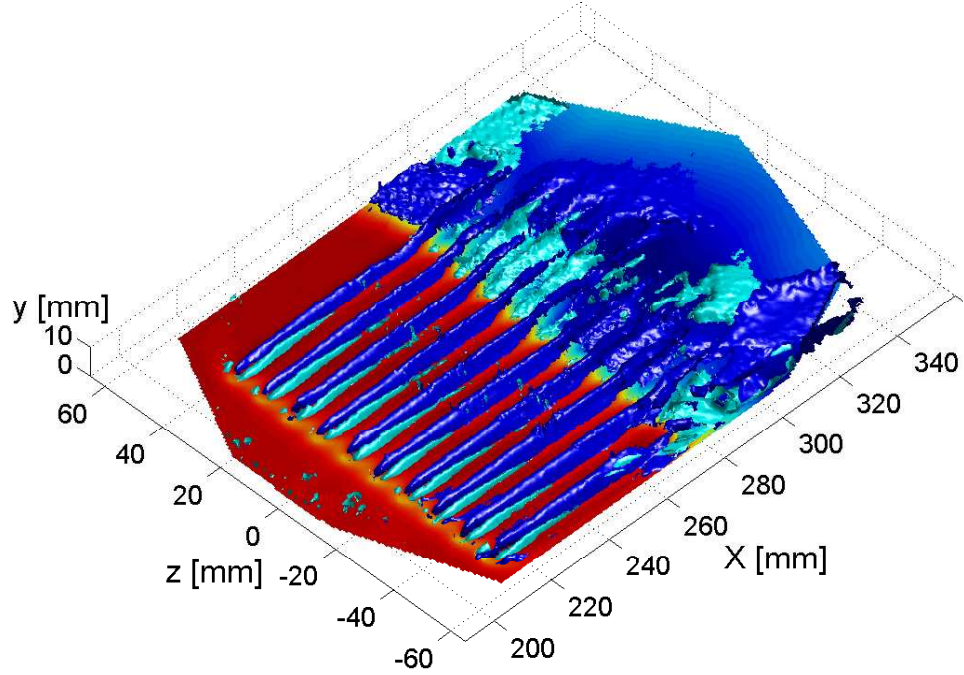
Figure 7.8: Iso-surfaces of the angular velocity (blue: $\alpha = -5 \times 10^3 rad/s$ and cyan: $\alpha = 5 \times 10^3 rad/s$), superimposed on contours of the mean longitudinal velocity at $y = 1mm$.

Table 7.1: Quantities used for the rotation rate estimate.

diameter:	$D = 6mm$	
distance from jet to interaction:	$L = 50mm$	
wall normal velocity:	$V = 10ms^{-1}$	
lateral velocity:	$W_1 = -30ms^{-1}$	(for $y = 1mm$)
	$W_4 = 10ms^{-1}$	(for $y = 4mm$)
longitudinal velocity:	$U_1 = 350ms^{-1}$	(for $y = 1mm$)
	$U_4 = 430ms^{-1}$	(for $y = 4mm$)

pairs, which transport fluid from higher up in the boundary layer towards the wall. At the same time, the mean velocity behind each jet is reduced, most likely as a result of the transport of low speed fluid away from the wall by the vortices, in combination with the generation of a wake by the jets themselves. The formation of such a wake has been studied in detail for a jet in crossflow by Fric & Roshko (1994), see section 1.3.

From the preceding plots, the following vortex structure can be deduced, as illustrated schematically in figure 7.10 (looking in upstream direction with
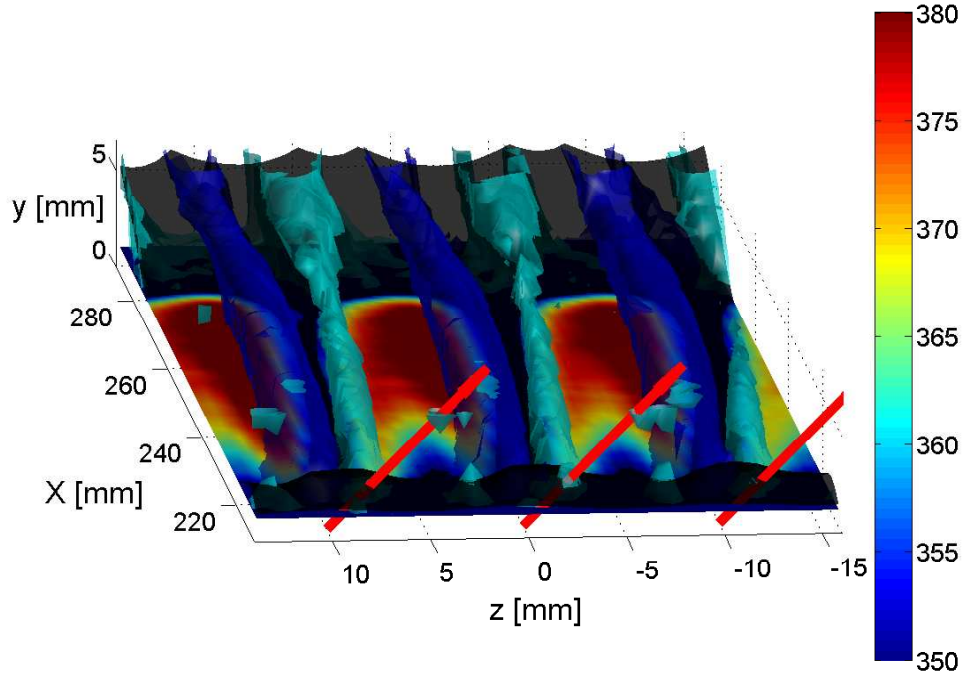
Figure 7.9: Iso-surfaces of the angular velocity, zoom on the longitudinal vortices (blue: $\alpha = -5 \times 10^3 rad/s$ and cyan: $\alpha = 1 \times 10^3 rad/s$). The black iso-surface represents a longitudinal velocity of $U = 350ms^{-1}$ (low speed fluid). Contours indicate longitudinal velocities at $y = 1mm$ in ms^{-1}, as indicated by the colour bar on the right. The red arrows represent the jet location and injection direction.

the negative spanwise coordinate pointing left). Using the velocities and the estimated diameter specified in table 7.1, an estimate can be obtained for the angular velocity of the large CCW vortex at mid-distance between jets and shock-foot. This leads to the following value of the rotation rate:

$$\alpha = \frac{W_4 - W_1}{2\pi D} = \frac{40}{2\pi \times 6 \times 10^{-3}} = 1000rot/s = 6.7 \times 10^3 rad/s \qquad (7.2)$$

This value is in good agreement with the values for the iso-surface for the principal longitudinal vortex in figure 7.9. The travel time from jets to interaction can be obtained as follows:

$$\tau = \frac{2L}{U_4 + U_1} = \frac{2 \times 50 \times 10^{-3}}{350 + 430} = 128\mu s \qquad (7.3)$$

The number of rotations executed by the large CCW vortex from its generation until the interaction is hence approximately: $\alpha\tau = 0.13$. Performing
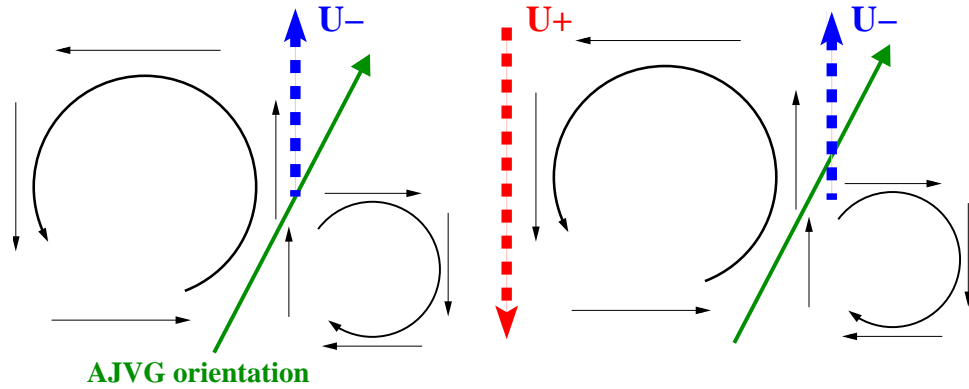
Figure 7.10: Schematic representation of the longitudinal vortices generated by the AJVGs, viewed in downstream direction (in accordance with figure 7.9). The green arrows represents the jets.

the same estimation just behind the jet, where the out of plane velocities are stronger, leads to a value of $\alpha\tau = 0.31$. The total number of rotations may hence be expected to be around $\frac{1}{4}$, certainly less than 1. This means that the mixing induced by the rotation of the longitudinal vortices is limited.

The mean longitudinal velocity profiles obtained at $X = 260mm$, just upstream of the reflected shock foot, are given by figure 7.11. Shown are the profiles for the reference case without jets (L_{ref}, in black) and all four profiles with jets (shown in blue). In accordance with the spanwise modulation of the flow, the two profiles for L_{min} and L_{max}, indicated by the blue filled symbols, represent the two extremes of the AJVG effectiveness. L_{min} corresponds to the fullest profile, leading to the smallest local separation length, and L_{max} represents the profile with the largest velocity deficit, inducing the largest local separation length. It should be noted that the profile for $z = -2.5mm$ is the most representative as inflow condition for the maximum separation length L_{max} at $z = -5mm$. This is due to the skewing of the flow: the plane for $z = -2.5mm$ transects the wake of the jets at $X = 260$, see figure 7.6(a). The properties of the boundary layer profiles are summarised in table 7.2. The values corresponding to L_{min} and L_{max} are highlighted in bold-face, taking into account the aforementioned skewing effect. Figure 7.11 shows that all profiles are self-similar in the outer part of the boundary layer ($\frac{y}{\delta_0} > 0.8$), confirming once more that the free-stream velocity is not affected by the weak shock-expansion system emanating from the jet array. It is reasonable to expect that the slight increase in boundary layer height caused by the jets (indicated by the solid vertical lines in figure 7.11(a)) falls within the measurement uncertainty. The increase in velocity observed in figure 7.9 corresponds well with the increase in fullness of the boundary profile for L_{min} ($z = 2.5mm$).
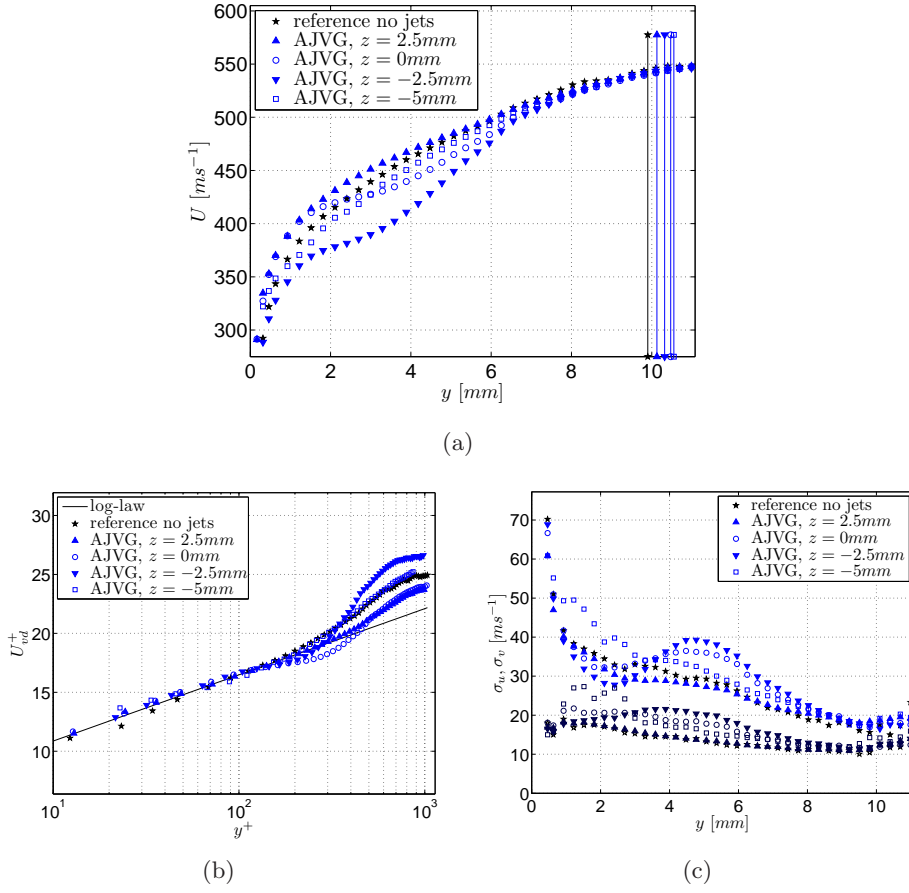
Figure 7.11: Incoming boundary layer profiles at $X = 260mm$; black: reference profile without jets; blue: profiles with AJVGs control; (a) U-component $[ms^{-1}]$; (b) log-law of the wall; (c) U and V-component fluctuations $[ms^{-1}]$.

Figure 7.11(b) shows the log-law for the Van Driest transformed velocity profile. It was obtained using $k = 0.41$ for the Von Kármán constant, keeping the second constant of the log-law fixed at $C = 5.25$. It appears that there are important variations in the constant of the wake law between the different profiles. The velocity fluctuations in figure 7.11(c) (light symbols: U-fluctuations; dark symbols: V-fluctuations) clearly show the imprint of the longitudinal vortex pairs: both fluctuation components attain approximately the values of the undisturbed reference case for L_{min} (in between the longitudinal vortices), whereas they show a significant peak within the path of the vortex pair for $z = -2.5mm$, corresponding to L_{max}. The latter is in agreement with the 'tube' of elevated U-fluctuation values from figure 7.5(b).

Table 7.2: Overview of flow properties with and without AJVGs.

Parameter		Reference	$z = 2.5mm$ L_{min}	$z = 0mm$	$z = -2.5mm$ Jet wake	$z = -5mm$ L_{max}
δ_0	$[mm]$	9.90	**10.1**	10.5	**10.3**	10.6
δ^*	$[mm]$	2.94	**2.86**	3.19	**3.67**	3.24
θ	$[mm]$	0.84	**0.84**	0.92	**0.98**	0.89
H	$[-]$	3.52	**3.42**	3.46	**3.75**	3.64
H_{ic}	$[-]$	1.40	**1.34**	1.35	**1.54**	1.49
C_f	$[10^{-3}]$	2.09	**2.30**	2.24	**1.81**	2.02
u_τ	$[ms^{-1}]$	24.7	**25.9**	25.5	**22.9**	24.3
L_{sep}	$[mm]$	53.3	**30.2**	33.7	41.4	**44.4**
h	$[mm]$	7.44	**4.18**	4.77	5.66	**5.66**
h_0	$[mm]$	4.48	**2.41**	2.71	3.29	**3.29**
U_{sep}	$[ms^{-1}]$	-57.0	**-32.9**	-38.3	-41.4	**-45.5**

The link between the peak fluctuations and L_{max} suggests that the primary cause of the local decrease in separation bubble length is not an increase in turbulence intensity, but rather the increase in mean fluid velocity. This seems to confirm the mechanism proposed in figure 7.10. The effect of this mechanism on the boundary layer fullness can be further quantified as follows: using the rotation rate above and an approximative radius of $3mm$ for the CCW vortex, and assuming a solid body rotation, it is estimated that the induced vertical displacement caused by the vortex rotation is at most $2mm$ ($\frac{y}{\delta_0} = 0.2$). Considering the reference boundary layer profile, such a displacement can indeed be held responsible for the change in fullness of the profiles with AJVGs, see figure 7.11(a), and hence the modulation of the mean longitudinal velocity observed in figures 7.7(a) and 7.9. This modulation is directly linked to the corrugations in the separation line.

7.2.2 Modification of the separation bubble

The effect of injection on the mean flow organisation has been investigated. The mean streamwise velocity component in the wall parallel plane at $y = 1mm$ is shown in figure 7.12. The solid black contour lines in this figure indicate the streamwise velocity for $200ms^{-1}$ (taken as indicative for the extrapolated reflected shock foot location) and for $0ms^{-1}$ (representing the separation line and the reattachment line and hence the extent of the separation bubble). The dashed lines indicate for reference the respective contours for the case without jets.

It was found that the $200ms^{-1}$ velocity contour at the reflected shock foot location becomes rippled by the jets, but that its mean spanwise position is only mildly affected, being pushed only slightly downstream as compared to the baseline interaction. This is in accordance with the thickening of the reflected shock observed in figure 7.3. The effect on the shock is small in comparison to the significant modifications in the upstream boundary layer that have been put into evidence above. Considering the separation bubble,
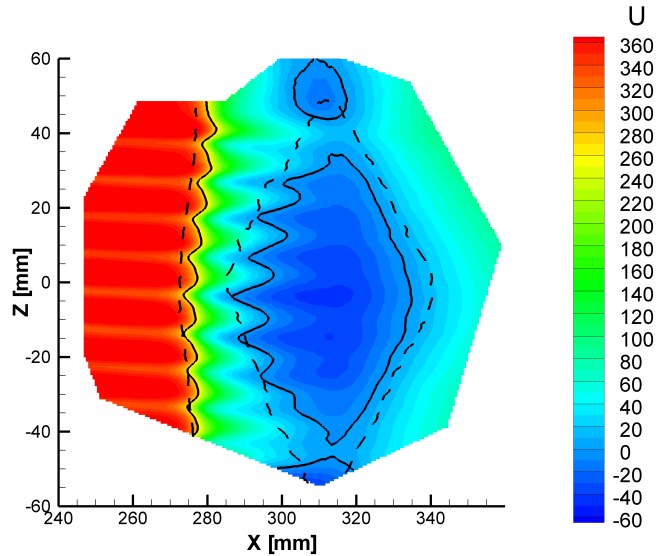
Figure 7.12: Mean longitudinal velocity component (ms^{-1}) in the horizontal plane with AJVG control, $y = 1mm$; The solid black lines indicate the approximate shock location and separation contour with control, the dashed black lines indicate the respective contours for the case without control.

it is clear that the separation line becomes highly corrugated in the injection case. This effect is more pronounced than the corrugation of the reflected shock. The reattachment line is displaced upstream with respect to the undisturbed case, but it shows no signs of corrugation. Hence the effect of the jets is to decrease the separation length at each spanwise location.

As a general remark, it is observed that although clear traces of AJVG induced longitudinal vortices exist upstream of the separation bubble, no trace of such vortices is found downstream of the interaction: the reattachment line is uncorrugated, and no sign of the vortex-patterns is visible downstream of the reattachment, see also figure 7.6. So either the longitudinal vortices are lifted over the interaction by the separation bubble and do not reappear at a height of $1mm$, or they are destroyed by the unsteady processes occurring in the interaction region or broken down under the effect of the shock. The experiments of Yamagata *et al.* (2009), who consider the control of the reattachment of a separated shear layer behind a backwards facing step at low subsonic conditions, would support the first hypothesis. They observe that the longitudinal vortices affect only the upper portion of the shear layer, while the lower portion remains unaffected. As a result, the reattachment line remains quasi-two dimensional in spanwise direction. Such a behaviour appears to be confirmed by the numerical results from
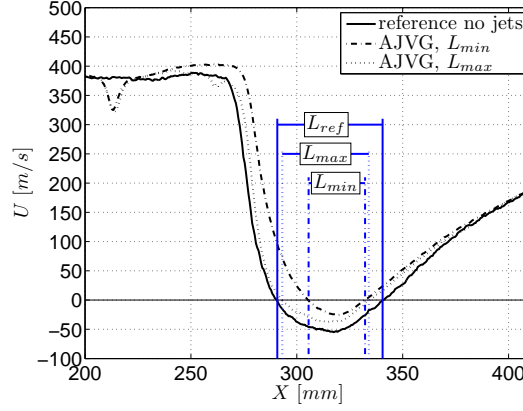
Figure 7.13: Longitudinal distribution of mean longitudinal velocity component (ms^{-1}) with and without AJVG control for L_{ref}, L_{min} and L_{max} at $y = 1mm$.

Lee & Loth (2009), which indicate that the longitudinal vortex pairs are also lifted over the separation region.

As was shown in the previous section, the AJVGs induce longitudinal vortices that entrain high speed fluid from higher up in the boundary layer. This fluid slightly displaces the reflected shock foot downstream and reduces the separation length. The effect on the separation line is more pronounced than the effect on the reflected shock. To quantify this effect, figure 7.13 shows the velocity distribution at $y = 1mm$ for L_{ref}, L_{min} ($z = 2.5mm$) and L_{max} ($z = -5mm$). It is noted that the velocity increase upstream of the interaction for L_{min} is due to due to the slight skewing of the flow by the action of the jets. The figure confirms that the reattachment point with AJVGs is moved upstream as compared to the reference case and that the effect of the jets disappears downstream of the interaction. The separation length for L_{min} is significantly smaller than for L_{ref}. In addition to reducing the separation length, the AJVGs equally reduce the separation bubble height, as observed in figure 7.4. The jets also cause an overall decrease in maximum reverse flow velocity.

The relevant separation bubble properties are summarised in table 7.2: the separation length L_{sep}, the maximum height of the dividing streamline h, the maximum height of the zero velocity contour h_0 and the maximum reverse flow velocity U_{sep}. Concerning the modulation of the boundary layer profile, it is observed that a decrease in friction coefficient for the jet 'wake' (L_{max}) is linked to a larger separation length. On the contrary, an increase of both quantities for the fullest profile in between the longitudinal vortices leads to a smaller separation length (L_{min}). The inverse effect has been

(a)   (b)
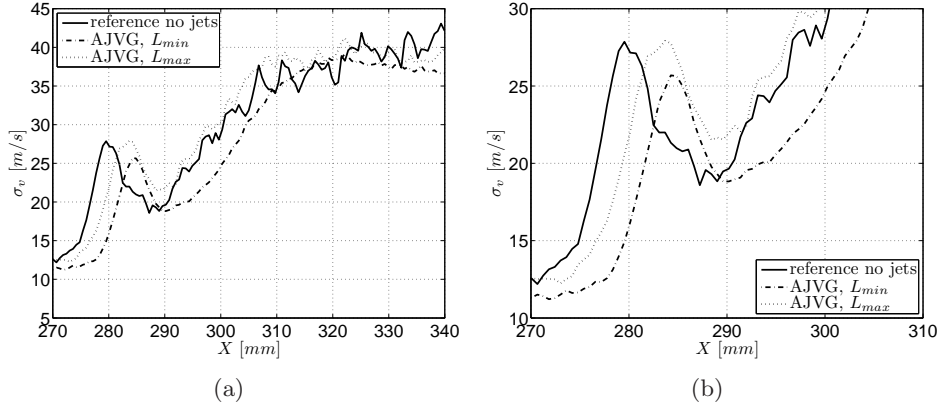
Figure 7.14: Shock position based on the V-fluctuation peak at $y = 8mm$: (a) complete interaction; (b) zoom of the shock.

observed for the shape factor, which is largest for the slim profile and smallest for the full profile. It seems therefore that the most important effect of the AJVGs is to modify the boundary layer length scales. Examining the four streamwise profiles, it turns out that there is a direct link between a reduction in separation length, the shape factor and the friction coefficient.

7.2.3 Modification of the shock dynamics

The shift in the shock position with and without jets has been determined in the first place by means of the peak in the V-component fluctuations at $y = 8mm$. Figure 7.14 shows that with AJVGs, the reflected shock is displaced downstream by approximately $4mm$. The downstream shift is slightly larger for L_{min} than for L_{max}, although the difference is small.

The intermittency in the shock position had been detected in the freestream using a hot wire. The RMS values of the HWA-signal induced by the passage of the shock are presented in figure 7.15(a) for different longitudinal positions with and without AJVG control. The maximum value of the RMS can be associated with the median shock location. A downstream shift in this location of approximately $4mm$ is observed for the AJVG control case. This is in agreement with the result from figure 7.14. It confirms the fact that the interaction length is slightly reduced with AJVG control. However, the shock excursion amplitude L_{ex} (indicated by the width of the peak) is not significantly altered. The observed thickening of the shock in figure 7.3 can therefore not be attributed to an increased shock excursion length.

The shock frequency range has been detected in the free-stream using a hot wire positioned on the median position of the separation shock. The resulting spectra of the HWA signal for the cases with and without injection

(a)   (b)
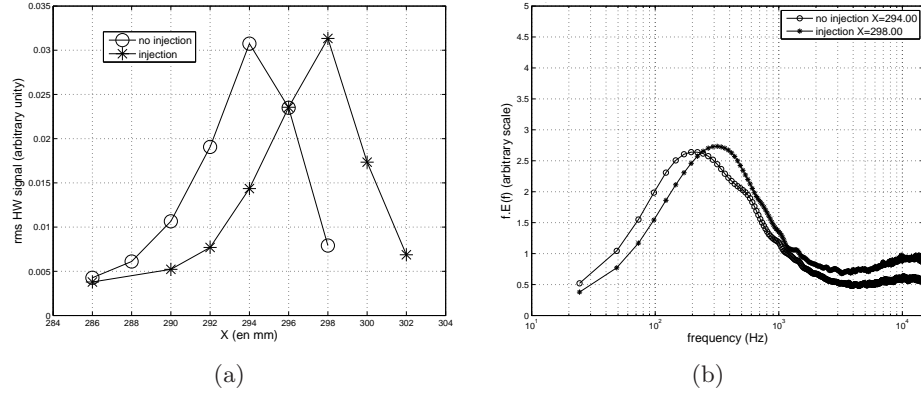
Figure 7.15: Shock position and frequency measurements at $y = 18mm$ (circles: AJVGs off, asterisks: AJVGs on): (a) RMS of the HWA-signal for different positions with and without AJVG control; (b) Pre-multiplied HWA spectrum for the reflected shock with and without jets.

is shown in figure 7.15(b). The spectrum is shown in pre-multiplied form ($f \cdot E(f)$ versus $\log(f)$, where f is the frequency) to correctly represent the energy concentration. A significant shift in the peak energy of the spectrum to higher frequencies can be noticed when the jets are activated. This is in agreement with a quasi constant Strouhal number for the shock frequency (see Piponniau *et al.* (2009)):

$$S_h = \frac{fh}{U} \tag{7.4}$$

Where h is defined as the maximum height of the dividing streamline. This can be demonstrated as follows. To determine the effect of the observed change in bubble height and shock frequency at constant reference velocity on the Strouhal number, one can write (using central differencing):

$$\frac{2\Delta S_h}{S_{href} + S_h} = \frac{2\Delta h}{h_{ref} + h} + \frac{2\Delta f}{f_{ref} + f} \tag{7.5}$$

The maximum height of the dividing streamline was found to be respectively $h_{ref} = 7.4mm$ for the reference case, and an average height of $h = 5.0mm$ for the case with jets ($h_{max} = 5.7mm$ for L_{max} and $h_{min} = 4.2mm$ for L_{min}). Referring to figure 7.15(b), the frequency is respectively $f_{ref} = 200Hz$ for the case without AJVGs and approximately $f = 300Hz$ with AJVGs. This leads to a negligible variation of the Strouhal number (approximately 1%) compared to a significant change in height and frequency (both about 40%). Such a modification of the frequency should be taken into account for practical control applications.

In a larger context, it can be remarked that the AJVGs have introduced important modifications into the upstream boundary layer. It is likely that the original structure is to a large extent destroyed and replaced by the longitudinal vortices, introducing a spanwise modulation of streamwise elongated low speed and high speed streaks. On the contrary, the shock unsteadiness has not disappeared. Instead, the shock frequency has increased inversely proportionally to the separation bubble size change, maintaining a constant Strouhal number. One could indeed state that this is the inverse experiment as the one performed numerically by Touber & Sandham (2008). Whereas structures of quasi infinite length were *introduced* in the current experiment, they simulated the same shock wave boundary layer interaction *in absence* of streamwise elongated structures in the upstream boundary layer. Indeed, the low frequency shock dynamics were still present, indicating that the unsteadiness is mainly caused by a downstream mechanism for this interaction with significant flow separation. On the other hand, the current results do show that an upstream mechanism can modify the frequency of the separation bubble pulsation. Furthermore, the upstream influence could be more pronounced in absence of a well developed separation bubble.

7.3 Discussion

7.3.1 Effect on the boundary layer

The horizontal and vertical plane PIV measurements indicate that the Air Jet Vortex Generators induce the formation of large longitudinal vortices. These vortices entrain high velocity fluid from higher up in the boundary layer and hence induce a local increase in the velocities closer to the wall. The effect of the jets is only noticeable up to $\frac{y}{\delta_0} = 0.8$. Above this height, the boundary layer seems not or only slightly affected. In the 'wake' of the jets, the boundary layer profile fullness is significantly lower compared to the reference boundary layer. At the same time, the boundary layer profile in between the jets is fuller than the reference boundary layer. This coincides with a decrease in friction coefficient for the jet 'wake' and a respective increase of both quantities for the fullest profile in between the jets. The inverse effect is induced on the shape factor, which increases for the slim profile and decreases for the full profile. Moreover the jets also induce a slight skewing of the flow in the upstream boundary layer, deflecting the flow sideways by approximately 2.8° at $1mm$ height from the wall. This is caused by the fact that the injection takes place perpendicular to the flow direction, see section 2.3.

7.3.2   Effect on the separation bubble

There is a noticeable effect of the jets on the separation bubble. The modifications of the incoming boundary layer lead to a more three-dimensional flow organisation. The overall separation length is reduced since the mean separation line is moved downstream while the reattachment line is moved upstream. The corrugation of the separation line is more significant than the corrugation of the reflected shock. The reattachment line is not corrugated and no trace of the jets is observed after reattachment.

Beyond these global properties, the following observations can be made on the effect of the spanwise modulation induced by the jets. The fullest boundary layer profile corresponds to the smallest separation length and the most downstream reflected shock position; the slimmest profile (the jet wake) corresponds to the largest separation length and the most upstream reflected shock position. The height of the separation bubble is also reduced, with the largest reduction corresponding to the smallest separation length. The most important effect of the AJVGs seems to be due to the boundary layer length scales and the mean velocity profile. A reduction in separation length is directly linked to the shape factor and the friction coefficient.

7.3.3   Effect on the reflected shock

The jets cause an overall corrugation of the reflected shock over its full height. This effect is observed as a thickening of the shock in the Schlieren images, and an undulation of the shock foot in the horizontal plane PIV measurements. The interaction length is only mildly affected, and no increase in shock excursion amplitude has been observed. The HWA results show an increase in reflected shock frequency caused by the AJVGs, in combination with a downstream displacement of the shock. This is in agreement with a constant Strouhal number for the shock frequency: a higher frequency corresponds to a smaller separation bubble size, at least in the case of well developed mean separation. This indicates that in such cases, the shock unsteadiness is caused mainly by a downstream mechanism.

7.4   Conclusions

The results demonstrate that Air Jet Vortex Generators (AJVGs), which are inclined under 45° with respect to the wall and blow in transverse direction, generate one pair of longitudinal counter rotative vortices per air jet. The vortices are of unequal strength, with the stronger vortex located above jet and the weaker vortex between the jet and the wall. The rotation rate of these vortices is small, notwithstanding the significant injection pressure and an important modification of the upstream boundary layer structure. Consequently, only a limited amount of mixing should be expected. How-

ever, it has been shown that the angular displacement induced by the flow is sufficiently large to entrain high speed flow towards to wall, hence locally increasing the fullness of the boundary layer profile. At the same time, the opposite effect is observed in the wake of the jets, where the fullness is decreased. The primary influence on the separation length hence appears to be due to the mean fluid velocity and not due to the local turbulence intensity in the boundary layer just upstream of the interaction. No significant effect has been observed of the AJVGs on the shock excursion amplitude, and only a minor effect on the shock position. However, the AJVGs do reduce the separation bubble size without suppressing it. As a direct consequence of the reduction in bubble size, the shock frequency is increased by about 50 percent, indicating that unsteadiness is caused mainly by a downstream mechanism. The current results show that an upstream mechanism can modify the frequency of the separation bubble pulsation. Furthermore, the upstream influence could be more pronounced in absence of a well developed separation bubble.

Part II

Analysis

Chapter 8

Scaling

The current work deals with the same basic interaction type, the incident shock reflection, but for a wide range of experimental parameters. Considered are variations in Mach number, Reynolds number, and flow deflection angle (in other words, shock strength). In addition, the effect of upstream control has been investigated. Given the observed resemblance between the different flow cases, it is verified whether their behaviour can be explained in part due to the global adherence to the conservation laws. Based on this reasoning, scaling parameters are deduced to take into account the effect of the changes in flow conditions and interaction geometry. The proposed scaling is applied to the interactions considered in the current work. In addition, it is verified whether it agrees with a large scope of different interactions documented in literature, both of the incident reflecting shock type and the compression ramp type. Finally, it is evaluated whether the new scaling can aid the interpretation of the mean and unsteady behaviour of the different interactions.

8.1 Background

As discussed in section 1.2.3, several scalings have been used based on the interaction length L and the shock intensity Δp. An example is given in figure 1.14 on page 18. It proposes that $\frac{L}{\delta^*} \sim \frac{\Delta p}{\tau_w}$, a reasoning that finds its origins in the Free-Interaction concept, see Délery & Marvin (1986). In the case of Dupont *et al.* (2006) and Laurent (1996), the shock intensity is taken over the incident shock only and it is scaled by the wall shear stress in the incoming boundary layer with the aim of defining a tendency to separate for the incoming flow. The boundary layer thickness is used to scale the interaction length. The scaling collapses data from the IUSTI S8-facility and data from a similar facility at ONERA taken under close measurement conditions. Both also incorporate the effect of a heated wall (see Laurent (1996), Benkemoun & Salaun (1988)). The resulting curve shows a monotonically

increasing dependence between L and ΔP. An alternate scaling has been described by Ginoux (1973), see section 1.2.3, figure 1.15. It considers the ratio $\frac{\Delta p}{\frac{1}{2}\rho_e U_e}$. An obvious difference between these two approaches is of course the Reynolds number dependence. The second scaling could therefore be a good choice if properties do not depend (or depend only weakly) on the Reynolds number.

Considering figure 1.14, section 1.2.3, the effectiveness of the first scaling option to capture the observed behaviour for the low Reynolds number case ($Re_\theta = 5 \times 10^3, M_e = 2.3$) is encouraging at first sight. Therefore, the high Reynolds number interaction ($Re_\theta = 5 \times 10^4, M_e = 1.7$) is added, see figure 8.1. In addition, different flow cases documented in literature are included, encompassing both incident reflecting shock interactions and compression ramp interactions for a wide range of flow conditions (Mach number, Reynolds number, flow deflection angle) and flow facilities. Moreover, the effect of control with AJVGs is shown (control off, and control on with profiles at two spanwise stations, corresponding to the maximal and minimal interaction length, see chapter 7). Finally, one DNS simulation is also included. To be able to compare the ramp flow and reflected shock cases, the pressure rise is defined over the complete interaction. The literature sources and the short names used in the figures are summarised in table 8.1. The symbol legend for the figures is shown below the table. It is remarked that while the Settles *et al.* (1976) data is represented by a cross, the publication states that incipient separation angle is in the range of $\varphi = 15 - 18°$. Depending on the author, the flow over a Mach=3 ramp at $\varphi = 12°$ is classified as attached (see Dolling & Or (1985)) or as displaying a very small separation bubble (see Kuntz *et al.* (1987)). For the current purposes, the incipient separation range for the Mach=3 ramp cases will therefore be taken in the range $\varphi = 12 - 18°$. The result is shown in figure 8.1(a). It is noted that the interaction geometry is included as a parameter, since it is believed that the relation between the pressure jump and the interaction length should be properly captured, independent of the particular geometry imposing the pressure jump. This seems to be a reasonable point of view, given the observations in literature that notwithstanding the difference in flow geometry, the wall pressure distributions are nearly coincident, at least in the case of compression ramps and incident shock reflections (see Délery & Marvin (1986)).

The interaction length for the compression ramp cases is based on the distance between the ramp corner and the peak in the wall pressure fluctuations, p'_w. This quantity is not always specified in literature, and hence in absence of this data, the separation point is taken as an estimate. It is noted that this introduces a slight ambiguity into the compilation, since the separation length is not identical to the interaction length. In addition, the interaction length for attached flows is non-zero, even though the sep-

aration length vanishes. However, the error introduced by this approach is judged acceptable in absence of more complete information. For the shock reflection cases, the interaction length is based on the distance between the reflected shock foot and the extrapolated wall impact point of the incident shock. The scatter for the University of Princeton high Reynolds ramp flow (excluding the Settles *et al.* (1976) data) is due to the variation in the specified incoming boundary layer properties from one reference to the other. As stated by Selig *et al.* (1989), these variations do not correspond to physically different boundary layer states, but are due to differences in definitions and determination methods. The dispersion in the reported values of δ^* amounts to $\pm 15\%$. In addition, the uncertainty in the determination of the interaction length is reasonably no less than 5%. Given these uncertainties and the wide range of measurement techniques, it should hence be expected that any attempt to collapse data onto a single curve will be faced with with an experimental dispersion that could amount up to $\pm 20\%$.

Figure 8.1(a) shows that the new data do not collapse onto the original curve of figure 1.14, neither for the shock reflection cases, nor for the compression ramp cases. Scaling the interaction length with the displacement thickness δ^*, which would be the proper parameter according to the Free-Interaction concept (see Délery & Marvin (1986)), does not improve the situation, see figure 8.1(b). Considering interactions with the same separation state (attached / separated), the values of $\frac{L}{\delta^*}$ and $\frac{\Delta p}{2\tau_w}$ show a dispersion amounting up to 400%. It is remarked that there is a general Reynolds number trend in the figures from top left (low Reynolds cases) towards bottom right (high Reynolds cases). The scaling clearly does not correctly take into account the Reynolds number effects, the Mach number effects and the different interaction geometries (incident reflecting shock and compression ramp).

It is noted that flow separation is necessarily initiated close to the wall where $\frac{\partial p}{\partial x} \simeq \frac{\partial \tau}{\partial y}$ (in the viscous sub-layer). This being said, outside the viscous sub-layer one has $\frac{\partial p}{\partial x} \gg \frac{\partial \tau}{\partial y}$. An order of magnitude analysis yields $\frac{\Delta p}{L} \gg \frac{\tau_w}{\delta_0}$, or equivalently $\frac{\Delta p}{\tau_w} \gg \frac{L}{\delta_0}$, a condition that is indeed satisfied by the current experiments, see figure 8.1(a). It is therefore justified to consider only the effects of pressure and inertia forces, even though viscous effects exist, remaining however confined to a region very close to the wall. From another point of view, $\tau_w = \rho_w u_\tau^2$, where u_τ is a measure of the velocity defect in the outer part of the turbulent boundary layer. It is known that u_τ decreases for increasing Reynolds numbers, *reducing* the velocity defect while *increasing* $\frac{\Delta p}{\tau_w}$. It should be expected that a smaller velocity defect reduces the tendency of the flow to separate. This is in contradiction with the trend indicated by figure 8.1, which implies that the flow should be *more separated* for larger $\frac{\Delta p}{\tau_w}$. Considering these elements, it seems that the wall shear stress is not the correct scaling parameter to describe the tendency

Table 8.1: Interactions considered in subsequent figures.

Short	Institute	Literature
Incident shock reflections		
ITAM	ITAM, Novosibirsk	Polivanov *et al.* (2009)
IUSTI	IUSTI, Marseille	Laurent (1996), Dupont *et al.* (2006), Piponniau *et al.* (2009), Souverein *et al.* (2009a), Piponniau (2009)
TUD	Delft University of Technology	Souverein *et al.* (2009b), Souverein *et al.* (2009a), Humble (2009), Humble *et al.* (2009b), Humble (2009)
Compression ramps		
UP	University of Princeton	Ringuette *et al.* (2009), Wu & Martin (2008), Settles *et al.* (1979), Dolling & Or (1985), Selig *et al.* (1989), Settles *et al.* (1976)
IUSTI	IUSTI, Marseille	Debiève (1983)
UND	University of Notre Dame	Thomas *et al.* (1994)
UI	University of Illinois	Kuntz *et al.* (1987)
UA	University of Texas at Austin	Erengil & Dolling (1991a), Erengil & Dolling (1991b), Hou (2003), Ganapathisubramani *et al.* (2007a)

Incident shock reflections
$\circ$ ITAM: $Re_\theta = 2.8 \times 10^3$, $M_e = 2.0$
$\triangledown$ IUSTI: $Re_\theta = 5.0 \times 10^3$, $M_e = 2.3$
$\blacktriangledown$ IUSTI: $Re_\theta = 5.0 \times 10^3$, $M_e = 2.3$, AJVGs
$*$ IUSTI: $Re_\theta = 5.0 \times 10^3$, $M_e = 2.3$, $\frac{T_w}{T_{aw}} = 2$
$\star$ TUD: $Re_\theta = 50 \times 10^3$, $M_e = 1.7$
$\star$ TUD: $Re_\theta = 50 \times 10^3$, $M_e = 2.1$
Compression ramps
$\lozenge$ UP: $Re_\theta = 2.3 \times 10^3$, $M_e = 2.9$, DNS
$\blacklozenge$ UP: $Re_\theta = 2.4 \times 10^3$, $M_e = 2.9$
$\star$ IUSTI: $Re_\theta = 5.0 \times 10^3$, $M_e = 2.3$
$\square$ UND: $Re_\theta = 17.5 \times 10^3$, $M_e = 1.5$
$\triangle$ UI: $Re_\theta = 21 \times 10^3$, $M_e = 2.9$
$\triangleright$ UA: $Re_\theta = 26 \times 10^3$, $M_e = 5.0$
$\triangleleft$ UA: $Re_\theta = 35 \times 10^3$, $M_e = 2.0$
$\diamond$ UP: $Re_\theta = 70 \times 10^3$, $M_e = 2.9$
$\times$ UP: Re_θ-range, $M_e = 2.3$, Settles (1976)

of the flow to separate, at least not for the Reynolds number range under consideration.

Give the above results it is concluded that there exists a dependence between the interaction length L and the shock intensity Δp, but that the scaling with δ_0 (as done by Dupont *et al.* (2006)) or δ^* and τ_w is not satisfactory. Data taken under the same reference conditions do indeed collapse onto a single curve, but the scaling breaks down when changing the flow parameters or the interaction geometry. This might indicate that the physical cause for the upstream displacement of the reflected shock is not properly captured, and that the origin of this displacement is not limited to an up-
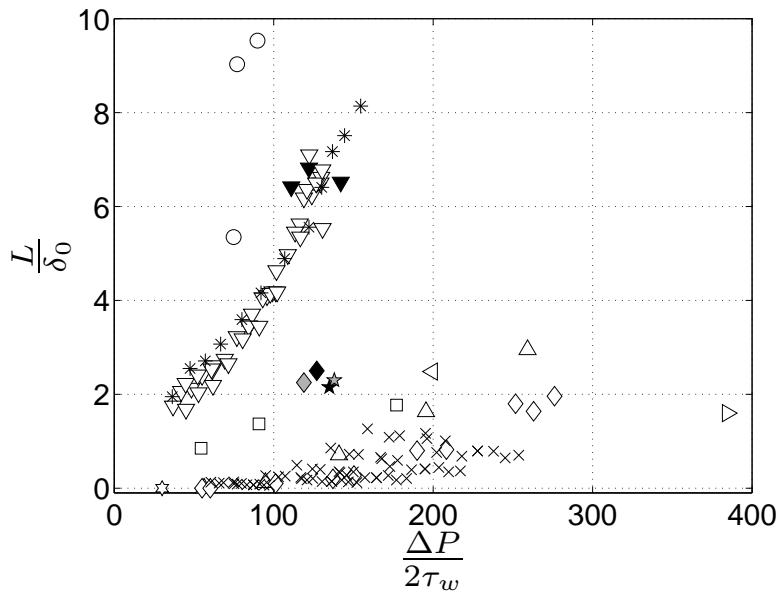
(a)
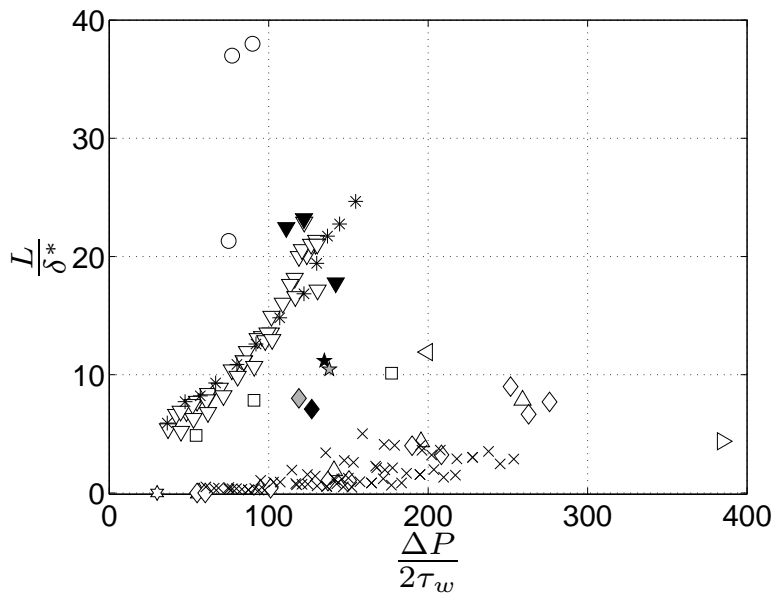
(b)

Figure 8.1: Scaling: (a) $\frac{L}{\delta_0}$ vs. $\frac{\Delta p}{2\tau_w}$; (b) $\frac{L}{\delta^*}$ vs. $\frac{\Delta p}{2\tau_w}$. Symbols according to table 8.1 on page 126.

stream reference scale. Redefining only one of the axis in figure 8.1 cannot make the curves collapse in a way that makes physical sense: redefining the scaling for either Δp and L only may make all data collapse, but in the best case, the most separated compression ramp interactions will collapse with the attached incident reflecting shock cases. A new scaling must therefore be defined for both Δp and L. It is assumed that L is some function F_1 of the reference flow conditions, see equation 8.1.

$$L = F_1(M_e, Re_x, \varphi, \frac{T_w}{T_{aw}}, \text{geometry}, ...) \qquad (8.1)$$

It is now attempted to define a relation between a non-dimensional interaction length (L^*) and an interaction strength parameter that represents the tendency of the flow to separate (S^*), in other words:

$$L^* = F_2(S^*) \qquad (8.2)$$

Where F_2 is a yet to be identified function. Given the above observations, the occurrence of flow separation is expected to be mostly governed by the inertial forces in the incoming flow, at least at sufficiently high Reynolds numbers. To elaborate this, it is attempted to define a separation criterion (S^*) based on the Euler equations, leading to a scaling for Δp. In addition, a scaling (L^*) for the interaction length will be derived representing the relation between L and the change in boundary layer state induced by Δp by considering the integral form of the mass and momentum balance for both interaction cases (incident reflecting shock and compression ramp). In the sections below, both scalings (for Δp and L) will first be considered separately. For each scaling it will be evaluated whether it leads to a better classification of the separation states (attached, incipient, separated) and a better collapse of the interaction data, notably of the two interaction cases. The new scaling will then be formalised by verifying whether it makes all data fall onto a single curve representing relation 8.2.

8.2   Separation criterion

As stated in the previous section, scaling the pressure jump on the wall shear stress does not lead to a flow case independent description of the tendency of the flows to separate. In this section, the one-dimensional, steady, inviscid momentum balance will be invoked in its differential form to analyse whether the occurrence of separation can be linked to a ratio between the pressure force and the inertia forces in the incoming flow. This with the aim of defining a scaling for Δp for use as separation criterion in equation 8.2.

Under the assumptions stated above, the momentum equation takes on the following form, see equation 8.3:

$$-\frac{\partial p}{\partial x} = \rho U \frac{\partial U}{\partial x} = \frac{1}{2}\rho\frac{\partial U^2}{\partial x} \tag{8.3}$$

It is observed that the adverse pressure gradient Δp imposed by the shock system acts approximately over the length of the interaction, decelerating the incoming fluid over the same length. Hence, performing an order of magnitude analysis and using equation 8.3, one may write:

$$\frac{\Delta p}{L} \sim \rho\frac{\Delta U^2}{L} \tag{8.4}$$

The aim is to obtain a flow separation criterion. It is therefore assumed that the flow separates when the incoming streamwise velocity U vanishes, in other words, when $\Delta U^2 = U^2$. Consequently, at separation, the following relation can be written:

$$\Delta p_{sep} \sim \rho_c U_c^2 \tag{8.5}$$

Where U_c and ρ_c are a reference velocity and density respectively for the incoming momentum flux. Given the arguments in section 8.1, indicating that the flow is governed by pressure and inertia forces in most of the boundary layer, it is expected that ρ_c and U_c are of the order of ρ_e and U_e respectively. This leads to the following separation criterion:

$$S = K\frac{\Delta p}{\rho_c U_c^2} \tag{8.6}$$

Where K is a constant of order 1 that will be chosen such as to obtain a value of approximately 1 at the onset of separation. Based on the definition of the separation criterion, the separation state can be quantified according to the criteria in table 8.2.

Table 8.2: Quantification of the separation states.

Value	Separation state
$S < 1$	Attached flow
$S \approx 1$	Incipient separation
$S > 1$	Separated flow

Substituting $U_c \sim U_e$ and $\rho_c \sim \rho_e$ into relation 8.6 yields the following equation for the separation criterion:

$$S_e = K_1\frac{\Delta p}{\rho_e U_e^2} \tag{8.7}$$

The subscript e is used to refer to the free-stream based values. The current results (notably figure 8.2) indicate that choosing $K_1 = 8$ yields a
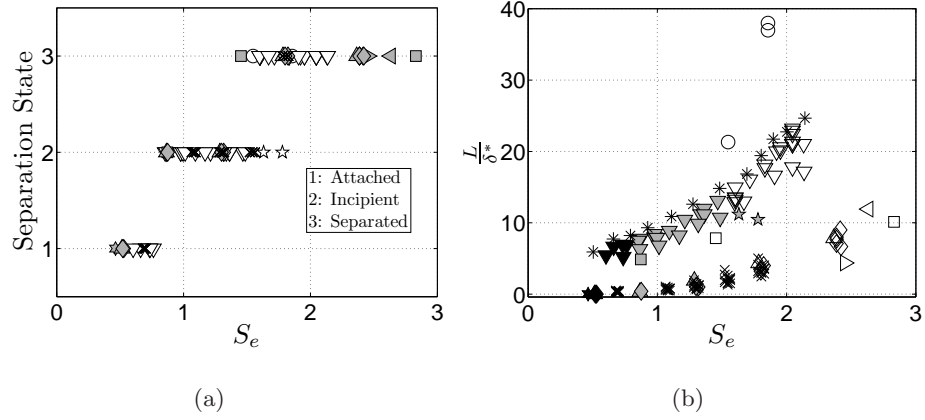
Figure 8.2: (a) Separation criterion S_e and documented separation states of reference interactions, colours represent the two flow geometries (white: shock reflection; grey: compression ramp); (b) intermediate new scaling results, horizontal axis only, colours represent the separation state (black: attached; grey: incipient; white: separated). Symbols according to table 8.1 on page 126.

value of unity that closely approximates the onset of separation. Hence this convention is adopted in the analysis below. Using the ideal gas law and the definition of the speed of sound, the above equation can be rewritten as:

$$S_e = \frac{8}{\gamma} \frac{\frac{p_{post}}{p_{pre}} - 1}{M_e^2} \qquad (8.8)$$

Where $\frac{p_{post}}{p_{pre}}$ is the ratio of the pressure before (p_{pre}) and after (p_{post}) the shock system. For a particular flow organisation (for example compression ramp, incident reflecting shock) and using oblique shock wave theory (see for example Anderson Jr. (1991)), it can be written analytically as a function of the free-stream Mach number M_e, the imposed flow deflection angle φ and the specific heat ratio γ:

$$\frac{p_{post}}{p_{pre}} - 1 = f(M_e, \varphi, \gamma) \qquad (8.9)$$

The following expression final is obtained for the separation criterion (assuming a constant specific heat ratio γ):

$$S_e = \frac{8}{\gamma} \frac{f(M_e, \varphi, \gamma)}{M_e^2} = g_1(M_e, \varphi) \qquad (8.10)$$

It is reiterated that g_1 is a function that depends on the particular shock system (for example compression ramp, incident reflecting shock).

The separation criterion S_e is put to the test in figure 8.2(a), evaluating it with respect to the flow states as documented in literature (represented on the vertical axis as the three states: 1. Attached; 2. Incipient; 3. Separated). The same symbols are used as in figure 8.1, and the colours correspond to the two interaction cases (white: incident reflecting shock; grey: compression ramp). A good agreement is obtained between the documented separation states and the values of the separation criterion specified in table 8.2, whatever the geometry, Reynolds number and Mach number of the flow. For all considered data, the attached, incipient and separated flow states are correctly regrouped, showing a coherent and progressive trend from attached to separated flows with increasing S_e. There is a slight overlap between the states, as should be expected given the experimental ambiguity in the determination of the separation state. It is noted that the heated flow cases of figure 8.1 are omitted here, since the considered references have not documented precisely the separation state. It can therefore not be ascertained whether the state of flow separation is affected by wall heating. Although it is clear that the interaction length increases when heating the wall, it could not be verified with the data considered here whether the separation state is actually altered by wall heating.

The separation criterion seems to correctly represent the state of the occurrence of flow separation. This makes it a good candidate for S^* in equation 8.2. The scaling with δ^* will be retained for the moment for the non-dimensionalisation of L. Referring to figure 8.1, this approach enables the evaluation of the effect of a heated wall on the horizontal axis with respect to the classical scaling on the vertical axis. The result is shown in figure 8.2(b), defined by the equation 8.10. The same symbols are used as in figure 8.1. It is clear that S_e leads to a better collapse on the horizontal axis than the former scaling with τ_w. Given the observations made so far, it seems reasonable that the effect of the change in the state of the boundary layer due to wall heating should be taken into account through the scaling of the interaction length rather than by the scaling of Δp.

In conclusion, it is proposed to consider that the separation criterion can be represented by a (flow case dependent, for example compression ramp or incident reflecting shock) analytic relation with as only parameters the free-stream Mach number and the flow deflection angle. Alternatively, it can be written as a (flow case independent) function of the pressure jump and the free-stream Mach number. According to the current formulation, the scaling of the shock intensity and the occurrence of separation are Reynolds number independent. These result are in accordance with the observations from Ginoux (1973), see section 1.2.3, figures 1.15 and 1.16. It should therefore be expected that the Reynolds number effects appear mainly through the scaling of the interaction length (the vertical axis in figure 8.1).

8.3   Interaction length scaling

It can be observed that, even though the collapse of the data on the horizontal axis (Δp) is significantly improved, see figure 8.2(a), there is still no collapse on the vertical axis (L), see figure 8.2(b). Notably, there is a large discrepancy between the two interaction cases. It appears that a simple scaling of the interaction length through a division by an upstream boundary layer length scale is unsatisfactory. As the Reynolds number effect is no longer represented in the scaling of Δp, it would be natural to think that it will occur in the scaling of the interaction length. It will therefore be attempted to define a more suitable scaling that represents the relation between L and the state of the boundary layer for use as L^* in equation 8.2.

8.3.1   Model definition and assumptions

An inviscid model is defined based on the integral form of the conservation laws. The presence of the boundary layer is taken into account through the integral of the upstream and downstream velocity profiles (in other words: δ^* and θ). Furthermore, it is assumed that at the exit plane, the pressure jump imposed by the shock system (Δp) equals the inviscid value, and that the fluid is parallel to the wall. One may visualise this in terms of the inviscid model mentioned in Délery & Marvin (1986), see figure 1.9 in section 1.2.1, with the difference that a displacement thickness is added at the wall. The physical cause of the interaction length may now be interpreted as a change in displacement thickness between the upstream and downstream states, creating a kind of 'equivalent' step at the wall. In the current model, it is attempted to define a scaling that links the interaction length to the change in boundary layer state induced by the processes within the interaction resulting from the imposed pressure jump. The downstream evolution of the length scales (due to a recovery of the boundary layer and boundary layer growth) are therefore by definition not relevant to the formulation of the scaling.

   To concretise these ideas, a control volume approach is defined, enclosing the interaction region. It is assumed that the flow is two dimensional and steady on the mean. In the formulation of the inviscid flow model, the viscous terms are inherently neglected with respect to the pressure force and the inertial terms in the deduction of the momentum conservation based formulation (see section 8.3.3). This seems justifiable, both in view of the the vanishing wall friction within the separation region, and given the fact that $\frac{\Delta p}{\tau_w} \gg \frac{L}{\delta_0}$ (see section 8.1).

   For the definition of the control volume, a thought experiment is made. It is imagined that we are looking at the interaction from far away, such that $\frac{\delta_0}{L_{cv}}, \frac{\delta_0}{H_{cv}} \rightarrow 0$, where L_{cv} and H_{cv} are the length and the height of the control volume respectively. In that case, the interaction is reduced

to almost a single point and the flow is essentially the same as for the inviscid case. Now let us image that we zoom in again, putting ourselves close enough to see the complexities of the interaction, but far away enough such that the reflected shock, the reflected expansion fan and the successive recompression waves have all coalesced to form the single shock prescribed by the inviscid flow solution. Putting ourselves in this position, we can model the interaction as a black box that modifies the state of the boundary layer. The flow conditions on all sides of the control volume are prescribed by the free-stream conditions and the inviscid oblique shock relations and the presence of the boundary layer can be taken into account through the definition of the displacement thickness.

In the proposed model, the free-stream conditions must adhere to the inviscid shock reflection conditions. Imposing an increase in the displacement thickness across the interaction (in other words: a 'step'), the only way for the flow to assure a mass and momentum conservation in the presence of the boundary layer is to translate the reflected shock. The translation can be cast into an algebraic equation by considering the difference between the inviscid case (the perfect fluid solution without boundary layer and interaction) and the viscous case (with interaction, the viscous effects being modeled as discussed above).

Both the mass balance and the momentum balance will be considered. Each approach can be used to formulate a physical relation between the upstream and downstream boundary layer length scales and the interaction length. Since both quantities must be conserved across the interaction, they should in principle yield compatible relations. These formulations will be used to define a scaling for the interaction length. It is also investigated whether a commonality may be expected in the scaling for the incident reflecting shock interactions and the compression ramp flows.

It is reiterated that the basic assumptions are that the shock intensity is the same as in the perfect fluid flow case, and that at the outflow plane, the flow conditions outside the boundary layer become uniform and approach the perfect fluid solution. Indeed, in reality one is confronted with deviations from the model assumptions. One may think of the presence of the expansion fan and velocity gradients that curve the path of the shock within the control volume, inducing a discrepancy in for instance the measured shock position (by means of wall pressure distributions) and the position as defined by the model. In addition, this curving causes entropy gradients, leading to a non-homogeneous velocity and density distribution downstream of the interaction. Another observed effect is an over-expansion, leading to slightly higher measured velocities at the exit plane (see appendix B). Although the conservation laws must inherently be satisfied, difficulties are hence to be expected, particularly when modeling the outflow conditions by an integral boundary layer length scale in combination with a uniform velocity and density. All these effects will play a role when one would want to employ

Figure 8.3: Control volume: incident shock reflection case.

the model for predictive purposes. However, the current aim is to determine the most dominant mechanisms that govern the interaction length rather than to make precise length estimations. In this context, the deviations are thought to be only of secondary importance. The basic assumptions are therefore believed to be reasonable approximations for the cases under consideration.

8.3.2   Mass conservation

In the first place, the mass balance is considered in its integral form, following the control volume approach described above. This is done for both the incident shock reflection and the compression ramp case.

Incident shock reflection

The resulting control volume for the incident reflecting shock interaction is shown in figure 8.3. Writing the mass flow balance for the inviscid flow case (without interaction, as indicated by the dashed reflected shock) the following equality is obtained:

$$\rho_1 U_1 H_{cv} + \rho_2 V_2 L_{cv} - \rho_3 U_3 H_{cv} = 0 \tag{8.11}$$

where H_{cv} and L_{cv} are the height and length of the control volume respectively. At the same time, the following equality is obtained for the viscous case (with interaction, as indicated by the solid reflected shock):

$$\rho_1 U_1 \left(H_{cv} - \delta_1^* \right) + \rho_2 V_2 \left(L_{cv} - L \right) - \rho_3 U_3 \left(H_{cv} - \delta_3^* \right) = 0 \tag{8.12}$$

Figure 8.4: Control volume: compression ramp case.

Subtracting equation 8.11 from 8.12, the following algebraic relation is obtained for the interaction length for the shock reflection case:

$$L = \frac{\rho_3 U_3 \delta_3^* - \rho_1 U_1 \delta_1^*}{\rho_2 V_2} \tag{8.13}$$

The interaction length is hence completely determined through the upstream and downstream boundary layer displacement thickness, since the densities and velocities are specified by oblique shock wave theory (depending only on M_e and φ). The expression is independent of the height and length of the control volume as long as the interaction is included.

Compression ramp

The compression ramp case is now considered. The resulting control volume is shown in figure 8.4. Writing again the mass flow balance for the inviscid flow case, the following equality is obtained:

$$\rho_1 U_1 H_{cv_1} - \rho_2 U_2 H_{cv_2} = 0 \tag{8.14}$$

At the same time, the following equality is obtained for the case with interaction:

$$\rho_1 U_1 \left(H_{cv_1} - \delta_1^* \right) - \sin(\varphi)\rho_2 U_2 L - \rho_2 U_2 \left(H_{cv_2} - \delta_2^* \right) = 0 \tag{8.15}$$

Subtracting equation 8.14 from 8.15, the following algebraic relation is obtained for the interaction length for the compression ramp case:

$$L = \frac{\rho_2 U_2 \delta_2^* - \rho_1 U_1 \delta_1^*}{\sin(\varphi)\rho_2 U_2} \tag{8.16}$$

The interaction length is again completely determined through the up-stream and downstream boundary layer displacement thickness, since the densities and velocities are specified by oblique shock wave theory (depending only on M_e and φ). The expression is independent of the height and length of the control volume as long as the interaction is included.

Common formulation

Given the great resemblance between relations 8.13 and 8.16, it is tempting to see whether both equations can be cast into a common form. To this aim, the denominator of each equation is reformulated in terms of the upstream conditions by means of the oblique shock wave relations. The shock angle β and the flow deflection angle φ are defined positive for both interaction cases. Invoking mass conservation across the incident shock for the shock reflection case, the following equality is obtained:

$$\rho_1 U_1 \sin(\beta) = \rho_2 V_2 \frac{\sin(\beta - \varphi)}{\sin(\varphi)} \tag{8.17}$$

Similarly, considering mass conservation across the shock for the compression ramp case gives:

$$\rho_1 U_1 \sin(\beta) = \rho_2 U_2 \sin(\beta - \varphi) \tag{8.18}$$

Rewriting each of the equations above and substituting in their respective relations (equation 8.13 for the incident shock interaction and 8.16 for the compression corner) gives the same final equation, which can be cast into the following common form, when using the subscripts *in* and *out* for the inflow and outflow conditions respectively:

$$\frac{L}{\delta_{in}^*} = \frac{\sin(\beta - \varphi)}{\sin(\beta)\sin(\varphi)} \left(\frac{\rho_{out} U_{out} \delta_{out}^*}{\rho_{in} U_{in} \delta_{in}^*} - 1 \right) \tag{8.19}$$

The shock angle β is an algebraic relation in terms of the flow deflection angle φ and the upstream Mach number M_e. The interaction length is therefore a direct algebraic function of the M_e, φ and the mass flow deficit ratio between the incoming boundary layer and the outgoing boundary layer. Defining the mass flow deficit as $\dot{m}^* = \rho U \delta^*$ we can hence write:

$$\frac{L}{\delta_{in}^*} = g_3(M_e, \varphi) \left(\frac{\dot{m}_{out}^*}{\dot{m}_{in}^*} - 1 \right) \tag{8.20}$$

With $g_3(M_e, \varphi)$ the ratio of sinus functions:

$$g_3(M_e, \varphi) = \frac{\sin(\beta - \varphi)}{\sin(\beta)\sin(\varphi)} \tag{8.21}$$

Based on this relation, it can be concluded that the interaction length is a direct result of the mass flow deficit ratio between the incoming and

outgoing boundary layer, and that it can be estimated algebraically when all quantities in the equation are known. Alternatively, the equation can be interpreted in terms of a ratio between the upstream and downstream Reynolds numbers, assuming a constant wall temperature:

$$\frac{L}{\delta_{in}^*} = g_3(M_e, \varphi) \left(\frac{Re_{\delta_{w,out}^*}}{Re_{\delta_{w,in}^*}} - 1 \right) \tag{8.22}$$

Where the Reynolds number is defined as follows:

$$Re_{\delta_w^*} = \frac{\rho_e U_e \delta^*}{\mu_w} \tag{8.23}$$

The analysis above based on the mass conservation consideration leads to a physical insight concerning the scaling parameters for the interaction length (the vertical axis of figure 8.1). Relations 8.19, 8.20 and 8.22 seem to indicate that the proper scaling of L is indeed with δ^*, but that a trigonometrical correction factor is required in the form of function g_3. In fact, the non-dimensional interaction length represents the change of state between the incoming boundary layer and the outgoing boundary layer. It should be interpreted in terms of the mass flow deficit ratio, or equivalently as a ratio of displacement thickness based Reynolds numbers in the case of a constant wall temperature. This explains why a simple scaling by a single boundary layer length scale did not manage to collapse the data. The proper scaling, with $\tilde{L}$ the non-dimensional interaction length, would hence be:

$$\begin{aligned}
\tilde{L} &= \frac{L}{\delta_{in}^*} G_3(M_e, \varphi) + 1 \tag{8.24} \\
&= \frac{\dot{m}_{out}^*}{\dot{m}_{in}^*} \\
&= \frac{Re_{\delta_{w,out}^*}}{Re_{\delta_{w,in}^*}}
\end{aligned}$$

With:

$$G_3(M_e, \varphi) = \frac{\sin(\beta)\sin(\varphi)}{\sin(\beta - \varphi)} \tag{8.25}$$

As a verification, both scaling options, the original $\frac{L}{\delta^*}$ and the new scaling $\tilde{L}$ defined by equation 8.24 are compared by plotting them against the documented separation state, as was done for the separation criterion in the previous section. The result is shown in figure 8.5, with symbols corresponding to table 8.1 and colours representing the two interaction cases (white: incident reflecting shock; grey: compression ramp).

The new scaling leads to a better classification of the known separation states, and there is a larger consistency between the ramp flow cases and

(a)   (b)
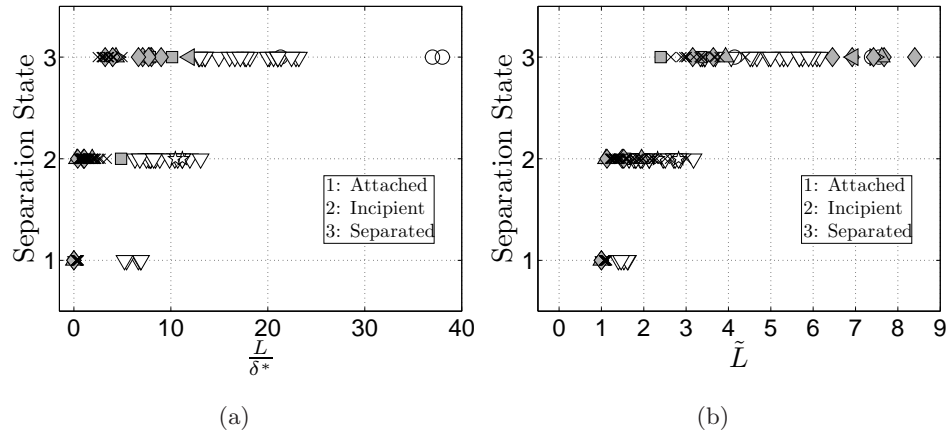
Figure 8.5: Interaction length scaling and documented separation states of the reference interactions: (a) original scaling with δ^*; (b) new scaling based on mass conservation. Symbols according to table 8.1 on page 126, colours represent the two flow geometries (white: shock reflection; grey: compression ramp).

the shock reflection cases, since data corresponding to both geometries are no longer clearly distinct. The attached flow cases take on the value close to one, as is to be expected from the definition of the scaling: the interaction length becomes small and consequently, the mass flow deficit is only slightly altered. It is noted that due to the previously mentioned limitations of the compilation (L is not always available from literature, and hence the separation length was taken as approximation for some references, see section 8.1), a value of $L \equiv 0$ is obtained for some of the attached interactions. This is not true strictly speaking, however, L will be very small and hence the attached flow cases will indeed approach $\tilde{L} \downarrow 1$, with a value identical to one for vanishing shock intensity. The incipient interactions have a non-dimensional interaction length with a value centered around two. The separated interactions take on a value larger than three. We can summarise these properties as follows:

Table 8.3: $\tilde{L}$ versus the separation states.

Value	Separation state
$\tilde{L} \downarrow 1$	Attached flow
$1 < \tilde{L} < 3$	Incipient separation
$\tilde{L} > 3$	Separated flow

8.3.3 Momentum conservation

In analogy to the mass conservation approach, the same analysis has been applied for the momentum conservation. Since both conservation laws must hold across the interaction, the momentum balance should in principle also yield a formulation that is equivalent to the one obtained from the mass balance. If the conservation approach holds, this should also lead to a valid scaling for the interaction length that is compatible to the one obtained above. This is verified in the current section. The same assumptions are applied as in section 8.3.2, and body forces are neglected. The X-momentum balance is considered for both the incident shock reflection and the compression ramp.

The analysis based on the momentum conservation confirms the physical insight gained from the mass balance. Only the final result is stated here, the complete derivation is given in appendix C. For the analysis below, it is noted that the proper boundary layer length scale for the momentum deficit is $\theta(1+H)$, where H is the shape factor, see equation C.1. Relations C.10 and C.12 show that the non-dimensional interaction length does indeed represent the change of the characteristic length scale between the incoming boundary layer and the outgoing boundary layer. In addition to the representations obtained from the mass balance, the interaction length can equally well be interpreted in terms of the momentum deficit ratio, or equivalently as a ratio of momentum thickness based Reynolds numbers. It turns out that the interaction length takes on a value that satisfies both the momentum balance and the mass balance. It is equally well a consequence of the modification of the displacement thickness through the interaction as it is a result of the modified momentum thickness. Both interpretations are complementary since both conservation laws must be respected.

The proper scaling for the vertical axis in terms of the momentum deficit ratio, with $\hat{L}$ the non-dimensional interaction length, would hence be:

$$\hat{L}_1 = \left(\frac{L}{\theta_{in}(1+H_{in})}G_3(M_e,\varphi)G_4(M_e,\varphi) + 1\right)\frac{1}{C(\varphi)} = \frac{I^*_{out}}{I^*_{in}} \qquad (8.26)$$

Or in terms of the Reynolds number ratio:

$$\begin{aligned}\hat{L}_2 &= \left(\frac{L}{\theta_{in}(1+H_{in})}G_3(M_e,\varphi)G_4(M_e,\varphi) + 1\right)\frac{G_5(M_e,\varphi)}{C(\varphi)} \quad (8.27)\\ &= \frac{Re_{\theta_{w,out}}}{Re_{\theta_{w,in}}}\frac{(1+H_{out})}{(1+H_{in})}\end{aligned}$$

With:

$$
\begin{aligned}
G_3(M_e, \varphi) &= \frac{\sin(\beta)\sin(\varphi)}{\sin(\beta - \varphi)} \\
G_4(M_e, \varphi) &= \frac{\cos(\beta)\cos(\varphi)}{\cos(\beta - \varphi)} \\
G_5(M_e, \varphi) &= \frac{U_{in}}{U_{out}}
\end{aligned}
\tag{8.28}
$$

Where $C(\varphi)$ is defined by equation C.10. Note that these two equations are equivalent but not identical, the difference being the factor $G_5(M_e, \varphi)$ that is either included in the left hand side (equation 8.26) or in the right hand side (equation 8.27). It is not *a priori* clear which formulation represents the most appropriate scaling, although both follow from the momentum balance and are hence equally valid.

As a verification, the original scaling $\frac{L}{\theta}$ and $\frac{L}{\theta(1+H)}$, and the new scaling options $\hat{L}_1$ and $\hat{L}_2$ defined by equations 8.26 and 8.27 are compared by plotting them against the documented separation state. The result is shown in figure 8.6, with symbols corresponding to table 8.1 and colours representing the two interaction cases (white: incident reflecting shock; grey: compression ramp).

It is evident that neither of the two original scaling options manages to properly distinguish the separation states. In particular, the compression ramp cases and the reflected shock cases are still clearly dissociated. Both new scaling options show a significant improvement: The separation states are correctly regrouped, and the ramp flows and incident shock reflection are more consistently distributed. From figures 8.6(c) and 8.6(d) it is difficult to determine which of the normalisations, $\hat{L}_1$ or $\hat{L}_2$, performs better. Due to its simpler form, preference is given to $\hat{L}_1$ for the moment.

Similar to the mass conservation based scaling, the properties of $\hat{L}_1$ are summarised in table 8.4. The same comments concerning the interaction length for the attached flow cases are applicable as for table 8.3.

Table 8.4: $\hat{L}_1$ versus the separation states.

Value	Separation state
$\hat{L}_1 \downarrow 1$	Attached flow
$1 < \hat{L}_1 < 3$	Incipient separation
$\hat{L}_1 > 3$	Separated flow
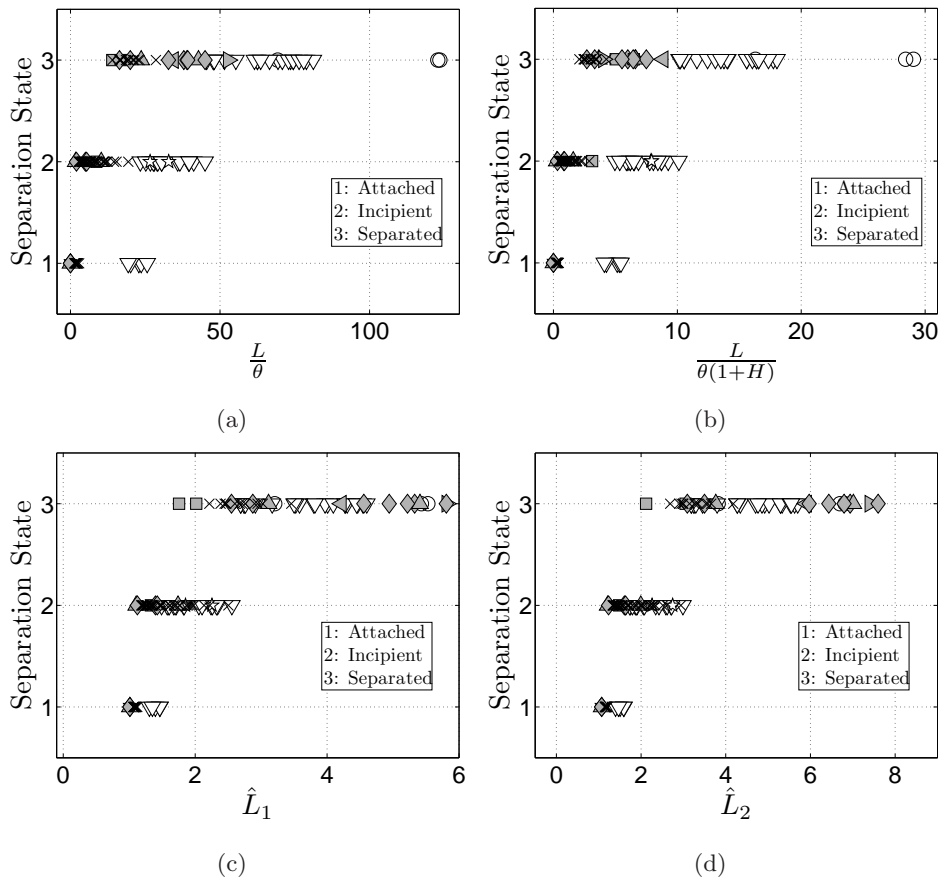
Figure 8.6: Interaction length scaling and documented separation states of the reference interactions: (a) and (b) original scaling with θ and $\theta(1 + H)$; (c) and (d) new scaling based on momentum conservation. Symbols according to table 8.1 on page 126, colours represent the two flow geometries (white: shock reflection; grey: compression ramp).

8.4 New scaling results

The results from the previous sections give enough confidence for redefining the scaling for Δp and L on figure 8.1(a). The separation criterion proposed in section 8.2 seems to correctly represent the physics of the occurrence of separated flow, yielding a scaling in terms of the free-stream Mach number and the imposed flow deflection. It has therefore been retained as a candidate for the scaling of Δp (the horizontal axis) on the merits of figure 8.2. The mass conservation model and momentum conservation model have been formulated, leading to a scaling for the interaction length which was found to produce a proper classification of the separation states. This makes the

two non-dimensional interaction lengths ($\tilde{L}$ and $\hat{L}_1$) equally good candidates for the vertical axis. The next logical step is to plot both scaled variables in the same figure and to verify whether the new scaling actually is a viable alternative for the original scaling in figure 8.1(a), producing a trend line in accordance with relation 8.2.

The new scaling for L is put to the test in figure 8.7. Both the mass balance based scaling and the momentum balance based scaling are considered (figures 8.7(a) and 8.7(b) respectively), as defined by equations 8.24 and 8.26. The same symbols are used as in figure 8.1 with the exception that the symbols are filled according to the three documented separation states: black for attached, grey for incipient and white for separated. The data fall onto a single trend line for both scaling options on the vertical axis, making them complementary but non-identical. In addition, there is a classification of separation states along the curve (attached, incipient, separated), with a progressive increase in the extent of flow separation when moving from left to right along the trend line. The new scaling hence appears to satisfy the desired properties concerning the separation state, while producing a curve that represents the function F_2, as defined by equation 8.2.

The only points not collapsing onto the curve are the $\varphi = 12°$ ramp of Thomas *et al.* (1994), and the $\varphi = 8°$ incident reflection of Polivanov *et al.* (2009). The $\varphi = 12°$ ramp configuration of Thomas *et al.* (1994) is however on the very limit between two distinct flow solutions (oblique shock and normal shock), and the post shock flow has in either case surpassed the sonic limit (the flow behind the shock is hence completely subsonic), raising questions as to the stability of this particular measurement point. It may be expected that the actual flow organisation for this interaction is particularly sensitive to small variations in the experimental conditions (upstream and downstream of the interaction), resulting possibly in large deviations from the modeled flow organisation. Concerning the Polivanov *et al.* (2009) data, it appears from their Schlieren visualisations that the reflected shock is relatively thick, indicating important shock dynamics. It is not known whether the mean shock trace or the most upstream shock position has been used to determine the interaction length. The latter case would be in accordance with the approximate magnitude of the overestimation. In addition, according to the trends in figure 1.16 (section 1.2.3), this interaction appears to be of the transitional type ($Re_x \approx 2 - 3 \times 10^6$). This regime likely requires a Reynolds number dependent scaling for Δp given the fact that the onset of separation is Reynolds number dependent (the current model predicts that this should not affect the scaling of L, contrary to what is suggested by figure 1.15).

The effectiveness of the new scaling becomes clear when comparing figure 8.7 to the scaling from figure 8.1. Initially, the data points for similar separation states showed a dispersion of up to 400%. The new scaling makes all points fall onto a single curve to within a dispersion of approximately $\pm 15\%$,
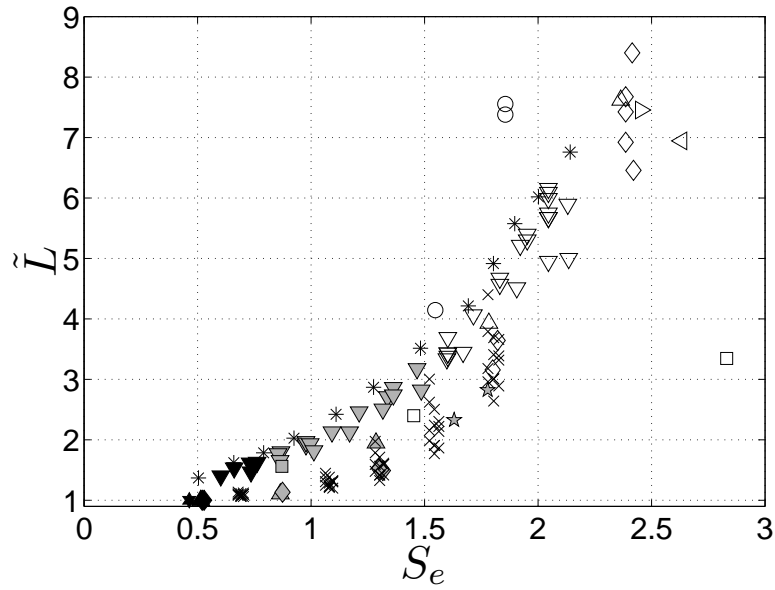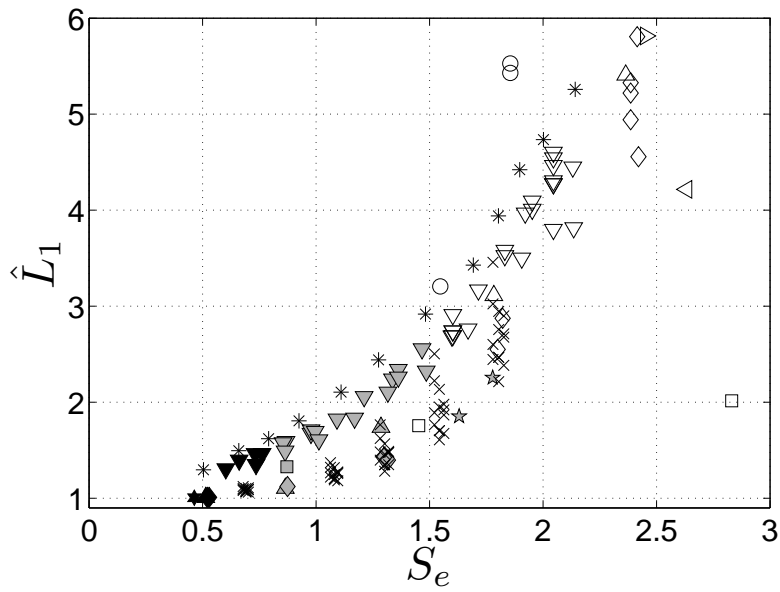
Figure 8.7: New scaling results: (a) mass balance based (see equation 8.24) and (b) momentum balance based (see equation 8.26). Symbols according to table 8.1 on page 126, colours represent the separation state (black: attached; grey: incipient; white: separated).

(a)   (b)

Figure 8.8: Dependence of S_e on the Reynolds number: (a) Re_θ; (b) $Re_{\delta_w^*}$.
Symbols according to table 8.1 on page 126, colours represent the separation
state (black: attached; grey: incipient; white: separated).

which is of about the same order as the expected measurement uncertainty,
see section 8.1.

Finally, it is remarked that the results show that there is indeed a relation
between the change in boundary layer state (represented here by the bound-
ary layer length scales δ^* and θ) and the interaction length. It should be
expected that this change in boundary layer state is related to the pressure
jump and hence S_e, in accordance with equation 8.2. It is however unclear
from simple theoretical considerations what this relationship is, which would
be necessary for independent interaction length predictions. The trend line
represented by figure 8.7 can be used as an experimental correlation for
equation 8.2. This makes it possible to estimate the interaction length for a
given upstream boundary layer state (δ_{in}^*), free-stream condition (M_e) and
flow deflection across the shock (φ, determining the pressure jump $\frac{p_{post}}{p_{pre}}$).
Provided the experimental dispersion in $\tilde{L}$, the error in the estimated L is
in the range of $20 - 65\%$ for the interactions under consideration (listed in
table 2.1 on page 33).

8.5   Parametric dependence: Mach, Reynolds, φ

It has been verified whether the new scaling of each axis shows a direct
dependence upon either of the following parameters: the momentum thick-
ness based Reynolds number (Re_θ), the Reynolds number appearing in the
scaling equations ($Re_{\delta_w^*}$ and Re_{θ_w}), the Mach number (M_e) and the flow
deflection angle (φ). A monotonous dependence on the Reynolds number
and the Mach number should not be expected since the collapsed curve com-

(a)

(b)
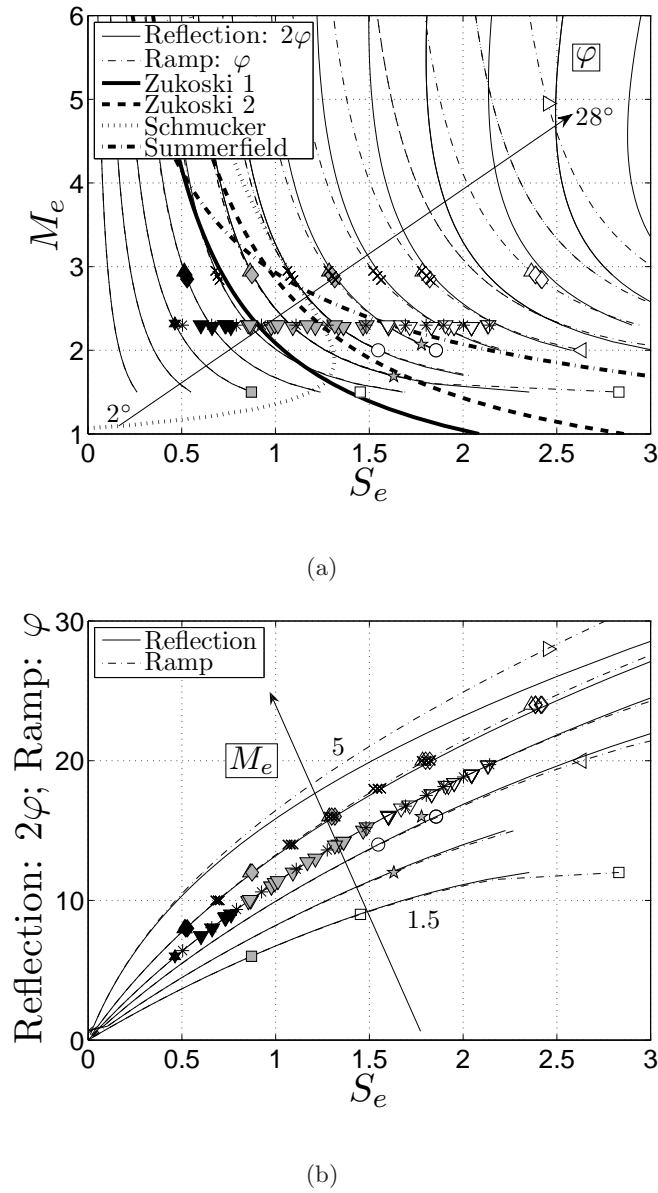
Figure 8.9: Dependence of S_e on the Mach number and the flow deflection: (a) Mach dependence M_e, including three common separation criteria (Zukoski, Schmucker and Summerfield); (b) Flow deflection dependence φ [deg]. Symbols according to table 8.1 on page 126, colours represent the separation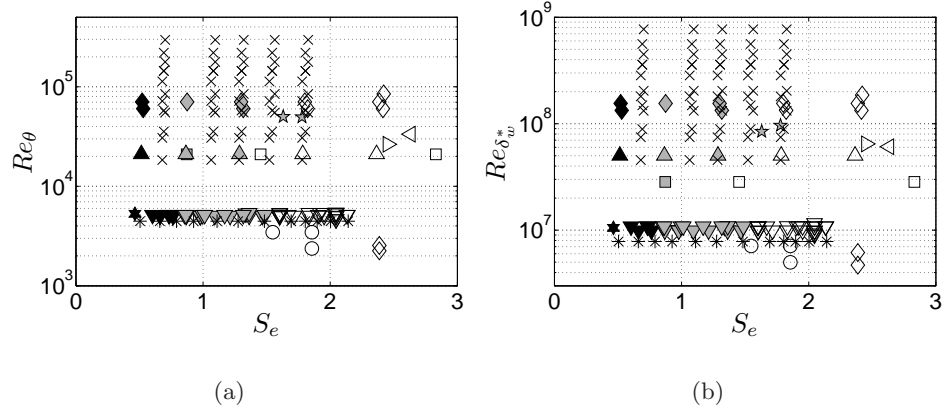 state (black: attached; grey: incipient; white: separated). Figures include the theoretical dependence of S_e on M_e and φ for both the incident reflection and the compression ramp.

prises data over a wide range of both parameters. In addition, the Mach number and Reynolds numbers are defined upstream, and they are hence independent of the shock intensity generating the separation state represented by the curve. The occurrence of flow separation is indeed Reynolds independent for turbulent interactions, in accordance with Ginoux (1973). Therefore, only the flow deflection angle is expected to show some sort of dependence on the scaling parameters, as becomes evident from figures 8.8 to 8.11: neither the scaling parameters nor the occurrence of separation show a direct Reynolds or Mach number dependence. On the contrary, there is a dependence on φ. For the separation criterion S_e, this dependence can be written as a function of M_e, see figure 8.9.

Figure 8.9 enables the graphical determination of the Mach-deflection angle combination leading to a particular flow separation tendency. Referring to figure 8.9(b), for small Mach numbers, the incident shock deflection angle can be multiplied by two to obtain the equivalent ramp angle that yields the same value of S_e. The figure shows that, for example, the same flow separation state should be expected for the Mach=5, $\varphi = 28°$ compression ramp as for the Mach=3, $\varphi = 24°$ ramp. Similarly, due to the Mach number effect, the flow over a $\varphi = 20°$ ramp at Mach=2 should be more separated than a ramp at Mach=3 for the same deflection angle. For completion, this same dependence has also been illustrated in figure 8.9(a), confirming the well known property that an increase in Mach number tends to postpone the onset of flow separation at constant deflection angle (see also Ginoux (1973) and figure 1.16 on page 20). It is noted that the current results equally indicate that an increase in M_e leads to a reduction of the interaction length at constant φ (S_e decreases and $G_3(M_e, \varphi)$ increases; figure 8.7(a) and equation 8.24 now show that $\tilde{L}$ must decrease and consequently also L for constant δ_{in}^*). In addition, it is remarked that for a Mach=3 interaction, the flow will always be separated for ramp angles larger than $\varphi = 12 - 14°$ (incident shock deflections of $\varphi = 6 - 7°$). Alternatively, a ramp of approximately $\varphi = 6°$ (an incident shock deflection of $\varphi = 3°$) will be attached for any Mach number that does not involve a normal shock solution. Also shown in figure 8.9(a) are the pressure ratios for flow separation expressed in terms of S_e, as predicted by three common separation criteria: Zukoski, Schmucker and Summerfield (see respectively Zukoski (1967); Schmucker (1973); Summerfield *et al.* (1954)). The Zukoski criterion consists of two formulations, the first (labeled '1') predicts the pressure ratio at separation, the second (labeled '2') predicts the plateau value in the wall pressure distribution. The criteria are given by equation 8.29.

As can be observed from the figure, the Zukoski criteria delimit particularly well the interaction data classified in literature as 'incipient'. It corresponds approximately to a value of $S_e \approx 1$ for the current data range.
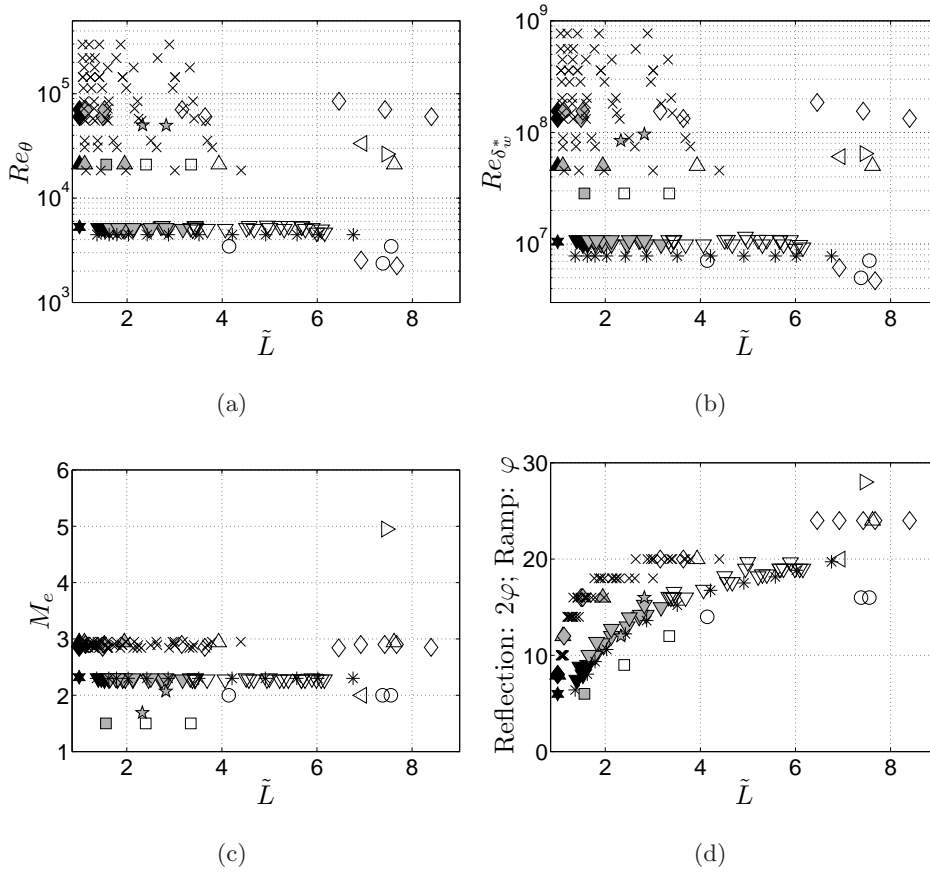
Figure 8.10: Dependence of $\tilde{L}$ on respectively: (a) Re_θ; (b) $Re_{\delta_w^*}$; (c) M_e; (d) φ [deg]. Symbols according to table 8.1 on page 126, colours represent the separation state (black: attached; grey: incipient; white: separated).

$$
\begin{aligned}
&\text{Zukoski 1:} &\frac{p_{post}}{p_{pre}} &= 1 + 0.73\frac{M_e}{2}\\[2mm]
&\text{Zukoski 2:} &\frac{p_{post}}{p_{pre}} &= 1 + \frac{M_e}{2}\\[2mm]
&\text{Schmucker:} &\frac{p_{post}}{p_{pre}} &= (1.88M_e - 1)^{0.64}\\[2mm]
&\text{Summerfield:} &\frac{p_{post}}{p_{pre}} &= \frac{1}{0.4}
\end{aligned}
\tag{8.29}
$$
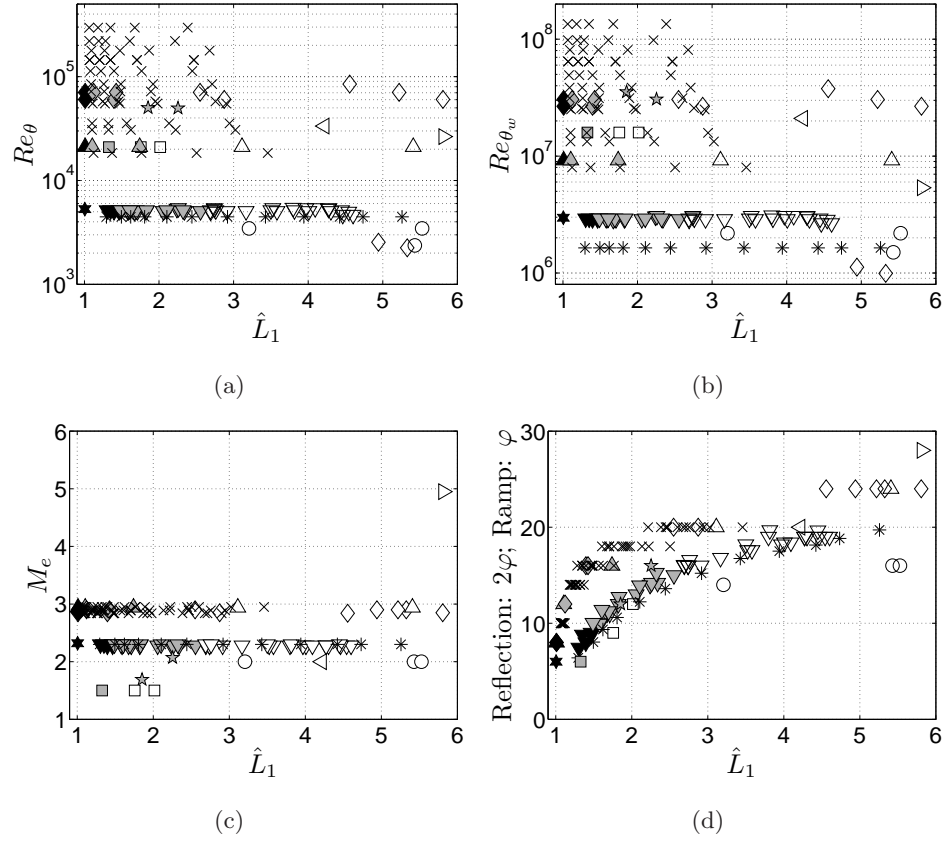
Figure 8.11: Dependence of $\hat{L}$ on respectively: (a) Re_θ; (b) Re_{θ_w}; (c) M_e; (d) φ [deg]. Symbols according to table 8.1 on page 126, colours represent the separation state (black: attached; grey: incipient; white: separated).

8.6   Expected effects of control

Given the scaling proposed in figure 8.7, at least two options for controlling the interaction can be identified. To suppress flow separation, the trend line indicates that one should either act on S_e, imposing $\Delta p \to 0$, or on $\frac{L}{\delta_{in}^*}$, imposing $\delta_{in}^* \to 0$. The first option ($\Delta p \to 0$) actually modifies the physical separation state of the flow. In the case of the second option, keeping the value of S_e fixed (in other words, $\varphi = cst$ and $M_e = cst$) means that the separation state is inherently prescribed, while $\frac{L}{\delta_{in}^*}$ is a constant determined by the trend line. The second option implies that to reattach the flow, one should make L vanish, which is achieved when $\delta_{in}^* \to 0$, in other words when $Re_{\delta^*} \to 0$. For upstream control, this appear to be the only option when the interaction geometry and free-stream conditions are fixed. It is reiterated

that this approach does not alter the flow separation state, but that it diminishes the separation bubble size by a reduction in the interaction size. It is noted that such a reduction of the the extent of an existing separation bubble also increases the unsteadiness frequency of the shock for a constant Strouhal number, as observed in the case of the AJVGs, see section 7.2.3.

It has been investigated what the effect of control is, taking into account the results from the conservation model and the new scaling parameters. This has been done for the air jet vortex generator (AJVG) control, see chapter 7. To this aim, two spanwise stations were considered: the station for the maximum interaction length at $Z = 2.5mm$ (corresponding to the least full boundary layer profile) and the station for the minimum interaction length at $Z = -5mm$ (corresponding to the fullest profile). In addition, the reference interaction was considered on the tunnel axis. The points with AJVG control have been represented in figure 8.7. There is a minor variation on the vertical axis between the points with AJVG control. The effect is small however, and the points practically collapse with the uncontrolled case. Notwithstanding possible 3D-effects due to the disturbances introduced in the upstream boundary layer, the scaling analysis based on the 2D-conservation model indicates that the interaction is not very sensitive to the perturbations introduced by the AJVGs. The upstream and downstream displacement thickness and momentum thickness seem to balance each other in such a way as to minimise the effect on the interaction length. In addition, given the fact that the free-stream conditions are not strongly altered, the position on the horizontal axis is approximately fixed. The value of the separation criterion S_e is likely not significantly influenced by the AJVGs, and the tendency of the flow to separate remains approximately the same. This would explain the observed difficulties in reattaching the flow. Such difficulties in reattaching the flow have also been observed in other control investigations, for example in the numerical results with micro-vortex generators on the same interaction geometry from Lee & Loth (2009). As in the current experiment, they observe a change in shape and distribution of the separation regions, but they do not manage to make the complete separation bubble vanish over the full span of the flow domain.

The same reasoning might hold for the effect of heat transfer at the wall. Like for AJVG control, wall heating might mostly affect the size of the interaction with only a small influence on the tendency of the flow to separate, at least at high Reynolds numbers. The validity of this statement could not be verified with the available data represented in figure 8.1 since the flow separation state was not documented, however Délery (1992) provides evidence for such a behaviour. In addition, the results with a cooled wall from Spaid & Frishett (1972) seem to indicate that the separation state is only mildly affected, whereas the main effect is a decrease in interaction length and separation bubble size. Modifications of the separation state are reported for a limited range of ramp angles in the incident separation regime

($6° < \varphi < 8°$), where the separation bubble is small ($L_{sep} < 1mm$). The dependence of the separation state on the value of S_e in the case of a wall with heat transfer would therefore merit further investigation, particularly in the incipient domain.

8.7   Geometrical implications of the new scaling

It will be investigated what the geometrical implications are of the new scaling for the flow fields under consideration in the current research. The interaction length L will be selected as relevant longitudinal length scale. Correspondingly, the dimensionless longitudinal coordinate is defined as $X^* = (x - X_0)/L$, where X_0 is the mean position of the reflected shock foot. It will be evaluated whether it is possible to define a proper scaling for the wall normal coordinate y by the non-dimensional interaction length $\tilde{L}$, based on the results from the previous section. Part of this work has been published in Souverein *et al.* (2009a, 2010).

For the scaling of the vertical coordinate, one might intuitively choose the boundary layer thickness. However, this quantity does not take into account the variations in interaction properties for the different deflection angles. The same holds for a scaling based on other upstream length scales. Three options for the vertical dimensionless coordinate that do take into account such effects are therefore retained: $Y^* = y/H$, $Y^* = y/L$ and a scaling based on $\tilde{L}$ defined by equation 8.24. In this case, $H = \frac{1}{2}L\tan(\beta)$ (with β the incident shock angle), representing the theoretical elevation of the shock crossing point ('interaction height'). Table 8.5 gives an overview of the relevant interaction characteristics, partly taken from table 5.3, see section 5.1.

Table 8.5: Interaction length comparison.

Experiment	**High Re**	**Low Re**		
Flow deflection	6.0°	5.5°	8.0°	9.5°
$L(mm)$	37	25	46	71
L/δ_0	2.2	2.3	4.2	6.5
H/L	0.45	0.30	0.32	0.34
$\tilde{L}$	2.33	1.92	3.43	5.67
$\hat{L}_1$	1.85	1.67	2.74	4.27
$\hat{L}_2$	2.26	1.87	3.25	5.29

Scaling with the interaction height

Given the geometry of the shock system, the interaction height H might be a logical choice for scaling the wall normal coordinates: in combination with X^*, it makes the shock crossing point for all interactions collapse at $y/H \approx 1$. The result for the U-fluctuation field is shown in figure 8.12. This scaling hence takes into account the changes in flow topology in the outer part of the flow, imposed by the shock geometry. However, the 'inner flow' below the shock crossing point is clearly not correctly taken into account, particularly considering the two Reynolds number cases: the path of the maximum U-velocity fluctuation is much closer to the wall for the high Reynolds number case than for the low Reynolds number. It seems therefore that the particular geometry of the shock system, which is a pure Mach effect, is of no importance for the flow within the interaction. The governing parameter must be the pressure jump that is the result of the shock system, which is in accordance with the result obtained in section 8.4. On the contrary, the height of the interaction seems a relevant parameter when considering the shock motion, since in that case the shocks are concerned directly, as mentioned in section 5.1.

Scaling with the interaction length

Since the interaction height does not correctly scale the inner flow, it is attempted to non-dimensionalise the wall normal coordinate with the interaction length L. Using this scaling, the mean and fluctuating flow organisation show great similarity for the different flow cases (incipient and well separated), see figures 8.13 and 8.14 respectively. Particularly, the resemblance of the path of the maxima of the U-component fluctuations for the two incipient interactions has improved with respect to figure 8.12. The crossing between the incident and reflected shock occurs in the vicinity of $y/L \approx 0.3$ in the $M = 2.3$ low Reynolds cases and of $y/L \approx 0.49$ in the $M = 1.7$ high Reynolds one. This is because the scaling does no longer take into account the change in shock geometry.

The figures show a very encouraging resemblance between both incipient flow cases and between both separated flows, both concerning the organisation of the retarded flow region within the interaction, and the region of increased fluctuation intensities. However, the incipient and separated interactions are still distinct.

Scaling using the mass balance

The geometric scaling with L does not take into account the results from section 8.3. It is verified whether evoking the new scaling can lead to insights concerning the flow organisation. Considering equation 8.24, two options
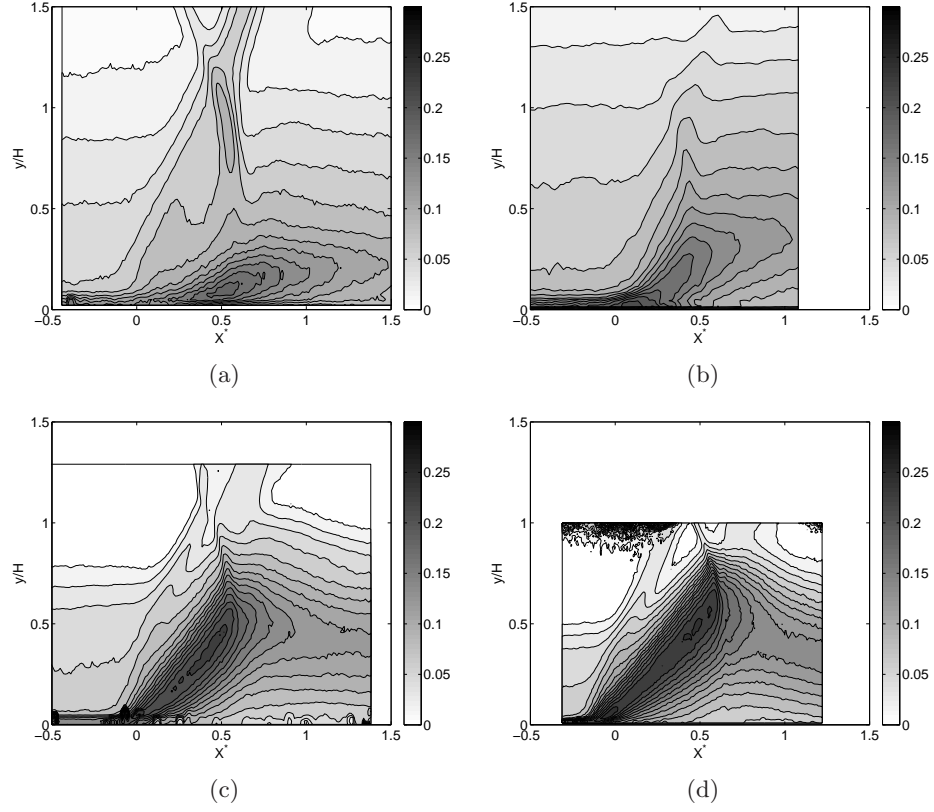
Figure 8.12: U-component fluctuations, wall normal coordinate normalised by the interaction height H: high Reynolds number incipient, (a) 6.0°; low Reynolds number incipient, (b) 5.5°; low Reynolds number separated cases, (c) 8.0° and (d) 9.5°. Fluctuation values are normalised by the free-stream velocity.

are identified. In the first place, one can scale the wall normal coordinate directly by L as follows:

$$\frac{y}{LG_3(M_e, \varphi)} = \frac{y}{\delta_{in}^*(\tilde{L} - 1)} \tag{8.30}$$

Where $G_3(M_e, \varphi)$ is an analytical function, see equation 8.25. For the second option, the following normalisation is proposed:

$$\frac{y}{LG_3(M_e, \varphi) + \delta_{in}^*} = \frac{y}{\delta_{in}^* \tilde{L}} \tag{8.31}$$

The first option can be interpreted as a conceptual (due to the mechanisms taken into account by the conservation model, see section 8.3.1) change in displacement thickness across the interaction $\Delta \delta^*$. It is defined in terms

(a)

(b)

(c)

(d)
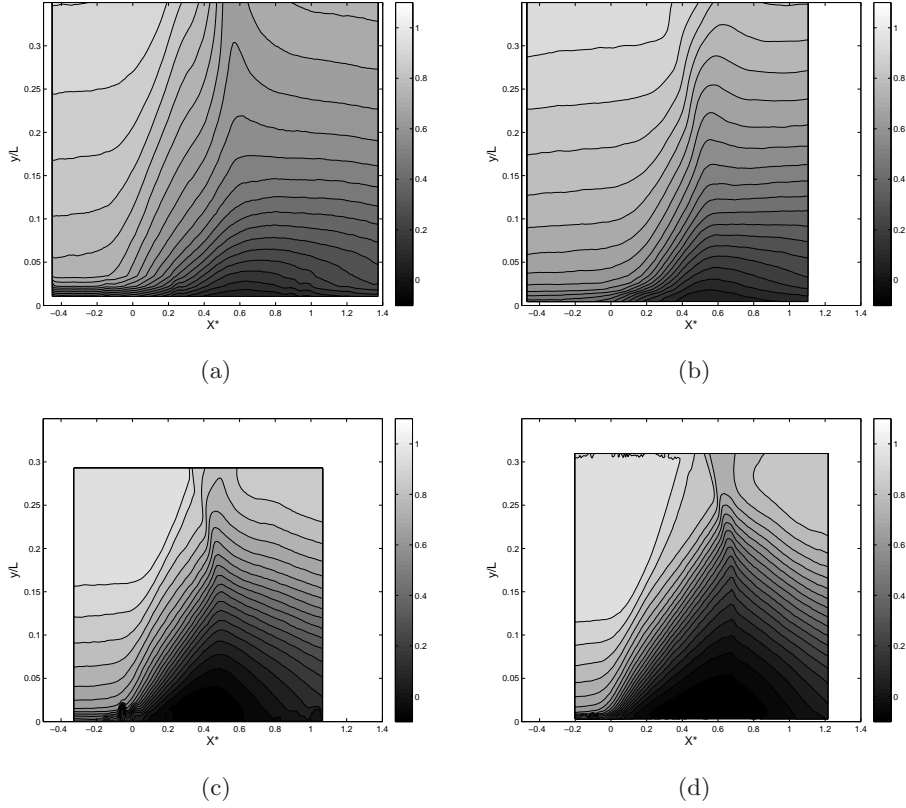
Figure 8.13: Mean U-component: high Reynolds number incipient, (a) 6.0°; low Reynolds number incipient, (b) 5.5°; low Reynolds number separated cases, (c) 8.0° and (d) 9.5°.

of the upstream conditions by means of the definition of $\tilde{L}$ (see equation 8.24), with Δm^* the change in mass flow deficit across the interaction, m^* being defined by equation 8.20, section 8.3.2:

$$\frac{y}{LG_3(M_e, \varphi)} = \frac{\rho_{in}U_{in}y}{\rho_{out}U_{out}\delta^*_{out} - \rho_{in}U_{in}\delta^*_{in}} = \frac{\rho_{in}U_{in}y}{\Delta m^*} = \frac{y}{\Delta \delta^*} \qquad (8.32)$$

Figure 8.15 shows the result obtained when scaling the wall normal coordinate using equation 8.30. The extent of the vertical axis of figure 8.15(a) has been blocked with respect to figure 8.14(a). The path of the maximal U-fluctuation intensity now shows a large resemblance in the first part of the interaction, independent of the Mach number, the Reynolds number and the flow defection angle. The unity value for the y-axis corresponds to the approximate maximum height that the peak U-fluctuations achieve, as indicated by the black dashed line.
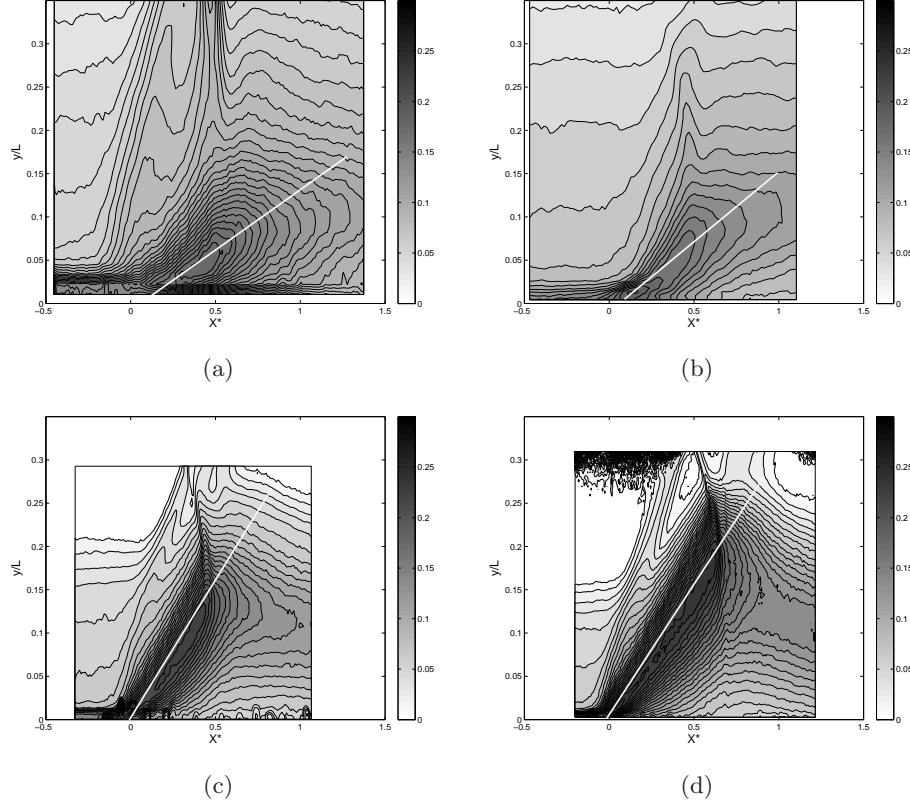
Figure 8.14: U-component fluctuations: high Reynolds number incipient, (a) 6.0°; low Reynolds number incipient, (b) 5.5°; low Reynolds number separated cases, (c) 8.0° and (d) 9.5°. Fluctuation values are normalised by the free-stream velocity. The white lines indicate the approximate path of the peak turbulence intensity within the first part of the interaction.

Considering now the second option, it is observed that applying the definition of the displacement thickness using to this scaling for the wall normal coordinate for the incoming boundary layer directly yields the conceptual mass deficit ratio, which can be linked to the vertical axis of figure 8.7(a) through equation 8.24. It corresponds hence to the ratio of the upstream and downstream deficits:

$$\frac{y}{LG_3(M_3, \varphi) + \delta_{in}^*} = \frac{\rho_{in} U_{in} y}{\rho_{out} U_{out} \delta_{out}^*} \tag{8.33}$$

Using this representation, the scaled inflow conditions are now directly linked to the interaction length and the separation state. The U-component fluctuations employing for the y-normalisation of equation 8.31 are shown in figure 8.16. The extent of the vertical axis of figure 8.15(a) has again
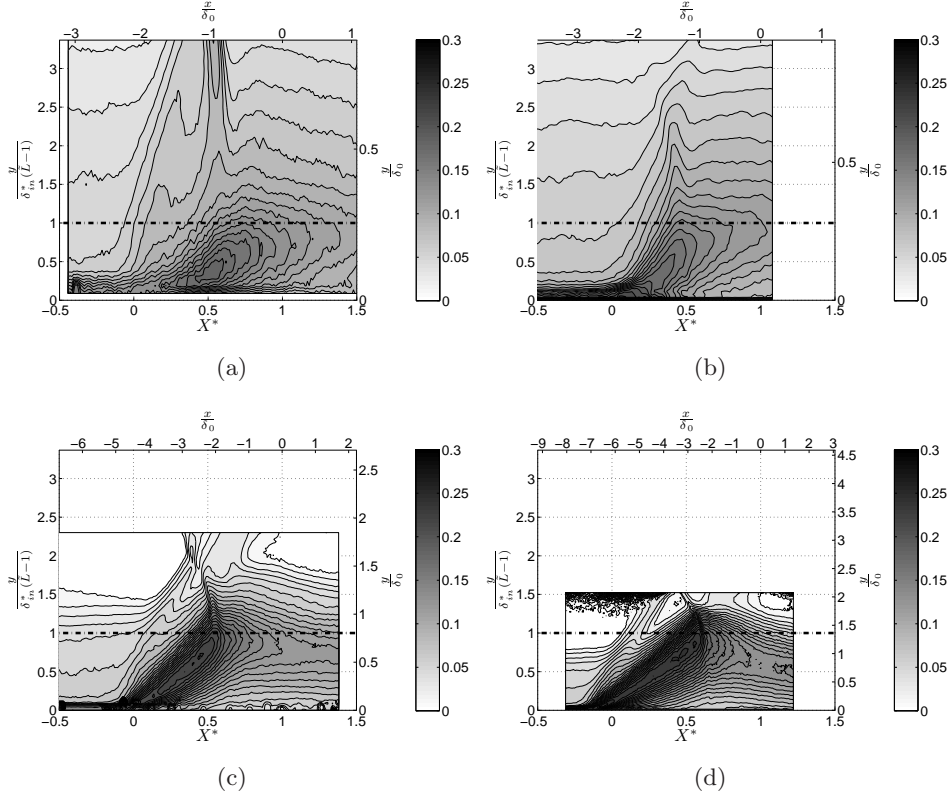
Figure 8.15: U-component fluctuations using the first $\tilde{L}$ scaling option (see equation 8.30): high Reynolds number incipient, (a) 6.0°; low Reynolds number incipient, (b) 5.5°; low Reynolds number separated cases, (c) 8.0° and (d) 9.5°. Fluctuation values are normalised by the free-stream velocity. The black horizontal dashed line indicates the unit-value for the y-axis. The horizontal and vertical scale on the top and right axis represent the coordinates normalised by δ_0 for reference.

been blocked with respect to figure 8.14(a). The horizontal black line indicates the value of unity for the y-scaling. This line represents the conceptual downstream displacement thickness, expressed in the upstream flow conditions ($y = \frac{\rho_{out} U_{out} \delta^*_{out}}{\rho_{in} U_{in}}$). It appears to impose a 'ceiling' for the inner flow. The black dashed line represents the line from figure 8.15, obtained by substituting $y = \Delta \delta^*$ into equation 8.31. Its value is given by $1 - \frac{\rho_{in} U_{in} \delta^*_{in}}{\rho_{out} U_{out} \delta^*_{out}}$. The dashed line will therefore fall onto the horizontal axis if the ratio between the upstream and downstream mass flow deficit is one, in other words for attached flows, see figure 8.7(a). The more important the downstream mass flow deficit, the more elevated the dashed line will be. In the limit, when $\delta^*_{out} \to \infty$, the dashed line will collapse with the black line. Using this
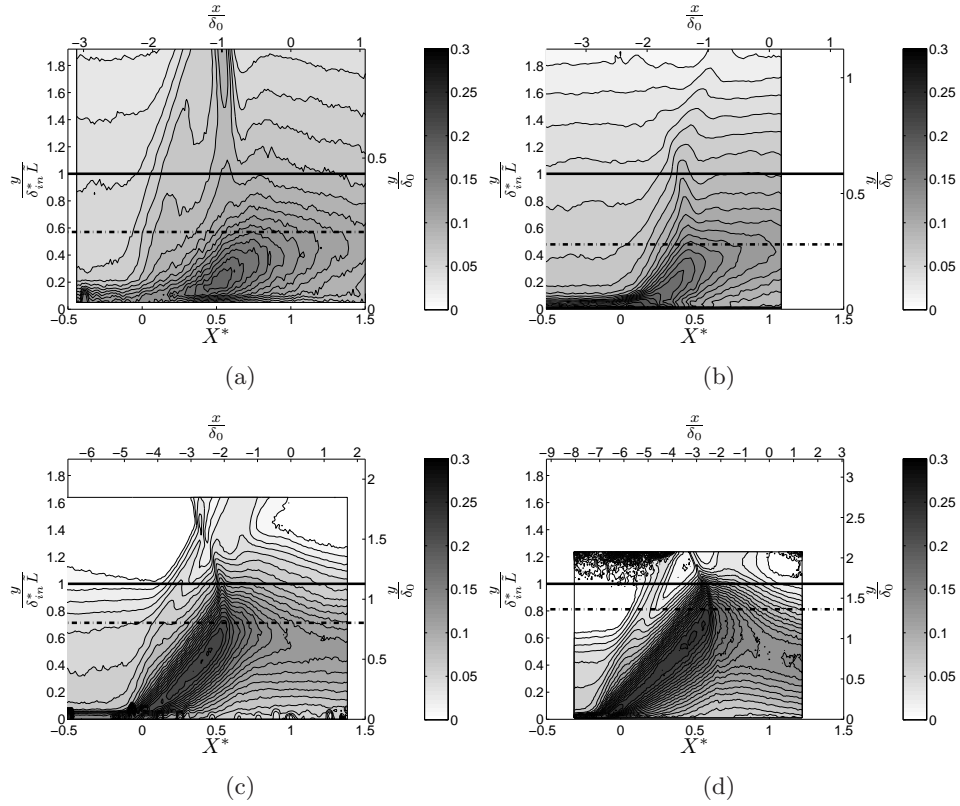
Figure 8.16: U-component fluctuations using the second $\widetilde{L}$ scaling option (see equation 8.31): high Reynolds number incipient, (a) 6.0°; low Reynolds number incipient, (b) 5.5°; low Reynolds number separated cases, (c) 8.0° and (d) 9.5°. Fluctuation values are normalised by the free-stream velocity. The black horizontal line indicates the unit-value for the y-axis, the black dashed line indicates the unit value from figure 8.15. The horizontal and vertical scale on the top and right axis represent the coordinates normalised by δ_0 for reference.

scaling, the geometric organisation of the flow is directly linked to the position on the trend line of figure 8.7(a): interactions with the same position on the curve (same value of S_e) will show a large resemblance, independent of the Mach number, the Reynolds number and the flow deflection angle.

The generation of the peak U-component fluctuations has been linked to the presence of a mixing layer developing within the initial part of the interaction, at least for separated interactions, see Dupont *et al.* (2008). In this context, one could tentatively interpret the generation of these peak turbulence intensities in view of the schematic of a reattaching flow shown in Bradshaw & Wong (1972), see figure 1.11(a) in section 1.2.1. It proposes

that the mixing layer develops underneath the original shear layer, displacing it upwards. The new shear layer hence causes an increase in displacement thickness. This seems to reflect what is observed in figure 8.16: for mass deficit ratios close to unity, the generation of peak turbulence intensities within the interaction will be small or absent and the elevation of the black dashed line will be small. For increasingly small mass deficit ratios, the change in displacement thickness due to the mechanism generating the peak U-fluctuations will be dominant with respect to the incoming boundary layer length scales and the difference between the solid and dashed black lines in figure 8.16 will consequently vanish. Figure 8.15 on the contrary normalises the wall normal coordinate with respect to the increase in displacement thickness caused by this mechanism.

It is clear that using the scaling based on the mass balance, notably figure 8.15, leads to a better collapse than the scaling by L alone, see figure 8.14. Indeed, looking back at the original flow fields of figure 5.5 on page 78, the resemblance has significantly increased through the use of this scaling: a large likeness is attained in the geometrical organisation of the flow fields within the interaction, independent of Mach number, Reynolds number and deflection angle. It is remarked that similar results are obtained for the momentum balance based scaling.

8.8 Conclusions

A new scaling for the data of figure 8.1 was proposed based on the conservation equations, in an attempt to describe the relation between the interaction length (L^*) and the shock strength (S^*), both non-dimensional: $L^* = F_2(S^*)$, see equation 8.2. The shock strength (on the horizontal axis) is defined in terms of the pressure jump normalised by the momentum of the incoming flow, and it can be interpreted as a separation criterion. It is an inviscid criterion representing the effect of the Mach number and the imposed flow deflection: $S_e = f(M_e, \varphi)$. Figure 8.8 can be used to determine a Mach-φ combination yielding a particular flow separation state. Two complementary scalings exist for the interaction length (on the vertical axis), derived from either the mass balance or the momentum balance considerations. A common formulation has been found for incident shock reflections and for compression ramps. The non-dimensionalised form of the interaction length consists of a division by the upstream boundary length scales and a correction that takes into account the shock deflection angle and the Mach number effects: $\tilde{L} = \frac{L}{\delta_{in}^*} G_3(M_e, \varphi) + 1$ and $\hat{L}_1 = \left(\frac{L}{\theta_{in}(1+H_{in})} G_3(M_e, \varphi) G_4(M_e, \varphi) + 1 \right) \frac{1}{C(\varphi)}$, where the function G_3 and G_4 are defined by equation 8.28. This scaling of the interaction length can be interpreted as a ratio of the upstream and downstream mass and momentum deficit: $\tilde{L} = m_{out}^*/m_{in}^*$ and $\hat{L}_1 = I_{out}^*/I_{in}^*$. Plotting either $\tilde{L}$ or $\hat{L}_1$ on the vertical axis leads to a proper classification

of attached, incipient and separated flows. The proposed scaling makes a multitude of interactions of varying shock intensity over a large range of Mach numbers and Reynolds numbers fall onto a single trend line representing the function F_2 in equation 8.2. The dispersion is in the order of the measurement uncertainty ($\pm 15\%$), see figure 8.7.

Given the scaling proposed in figure 8.7, two options for controlling the interaction have been identified. One should either act on S_e, imposing $\Delta p \to 0$, or on $\frac{L}{\delta_{in}^*}$, imposing $\delta_{in}^* \to 0$. The first option actually modifies the physical separation state, whereas the second option implies that one should make L vanish, in other words when $Re_{\delta^*} \to 0$. The latter approach does not alter the flow separation state, instead it diminishes the separation bubble size by a reducing in interaction size. For upstream control, this appear to be the only option when the interaction geometry and free-stream conditions are fixed. For a constant Strouhal number, this will also increase the shock unsteadiness frequency. The results with AJVG control seem to point in this direction: considering figure 8.7, neither the position on the vertical axis, nor the position on the horizontal axis are significantly affected. Hence, the tendency of the flow to separate would be largely un-altered. It was indeed found to be impossible to reattach the flow using the current jet array configuration, notwithstanding the strong modification of the upstream boundary layer. A reduction of the bubble size was achieved, leading to an inversely proportional increase in the unsteadiness frequency.

Two options for the scaling of the wall normal coordinate were considered: $\frac{y}{LG_3(M_e,\varphi)}$ and $\frac{y}{LG_3(M_e,\varphi)+\delta_{in}^*}$, both derived from $\tilde{L}$. The second option represents the ratio of the upstream and downstream deficits. It seems to link the geometric organisation of the flow to the position on the trend line of figure 8.7(a): interactions with the same position on the curve will show a large resemblance, independent of the Mach number, the Reynolds number and the flow deflection angle, see figure 8.16. The first option represents the increase in displacement thickness, which is linked to the development of the peak turbulence intensities. It leads to a large geometrical resemblance of the flow organisation within the interaction, see figure 8.15. Scaling with L only already gives a reasonable collapse of the flow fields, but appears to be only a first approximation of the second scaling option. Looking back at the original flow fields of figure 5.5 on page 78, the resemblance has significantly increased through the use of the conservation approach based scaling.

Chapter 9

Sources of unsteadiness

One of the key issues in shock wave boundary layer interaction research is the origin of the low frequency of the large scale motion of the shock, as discussed in section 1.2.2. The two principal sources for the unsteadiness that have been proposed in literature are large scale elongated structures in the upstream boundary layer, and a pulsation of the downstream separation bubble that is induced by the entrainment of mass by the mixing layer and subsequent vortex shedding. It is however unclear in this 'upstream-downstream' debate what the effect is of the imposed shock intensity, nor whether the Reynolds number has an influence on the interaction unsteadiness. It appears from section 1.2.2 that particularly for interactions with a significant mean separation bubble the low frequency large scale shock excursions must be governed by a downstream mechanism. However, this does not exclude that upstream effects contribute to the shock unsteadiness, and it is seems likely that their role could be more important for interactions at moderate shock intensity (attached flows and flows without significant mean separation).

With this in mind, the current chapter will investigate which mechanisms are present within shock wave boundary layer interactions through a systematic variation of the shock strength. Furthermore, the universality of these mechanisms with respect to an order of magnitude variation in the Reynolds number (based on the momentum thickness) is evaluated for weak shock strengths (incipient separation). Considered are again the flow cases presented in chapter 5, which have been analysed with respect to the new scaling in section 8.7.

In the first place, the unsteadiness in the separation zone is quantified. Next, the role of the separation bubble with respect to the low frequency shock dynamics is considered. This is done by means of conditional statistics based on the instantaneous separation bubble height defined by the dividing streamline. To investigate whether the shock dynamics depend on a downstream mechanism, it is verified whether there is a dependence of the

large scale shock excursion on the occurrence of flow separation. In addition, the dependence on the shock strength of the development of large vortical structures in the interaction is addressed for both cases: incipient and well separated interactions. To verify the existence of an upstream mechanism, it is also investigated whether the bubble height variations can be linked to the state of the incoming boundary layer. The same conditional analysis is made, considering the pulsation of a retarded fluid region instead of the dividing streamline. At the end of the chapter, a synthesis is made of the observed mechanisms for the interaction unsteadiness. This work has been published in Souverein *et al.* (2009a) and Souverein *et al.* (2010).

9.1 Characterisation of instantaneous flow separation

In previous studies of the low Reynolds number case which display significant flow separation on the mean, see Dupont *et al.* (2008) and Piponniau *et al.* (2009), the low frequency shock motions were related to the low frequency pulsation of the separation bubble. The latter was associated, like in subsonic separations, to the flapping of the mixing layer which develops downstream of the reflected shock and which corresponds to the shear region between the relatively slow moving flow in the separation bubble and the fast moving fluid outside it, see Kiya & Sasaki (1983) and Cherry *et al.* (1984). The associated time scale was derived by means of a simple model based on the entrainment process in the mixing layer (Piponniau *et al.* (2009)), see figure 1.13(b) on page 15. In chapter 6 it was demonstrated that also an interaction of the incipient type still displays unsteady shock movements that occur at frequencies that are 1-2 orders of magnitude below those present in the incoming boundary layer. This while flow separation occurs only intermittently without a well developed separation bubble on the mean, but with evidence for shedding of large scale vortices. Given the existence of common flow features, it will therefore be investigated whether the unsteadiness in incipiently separated interactions is governed by similar mechanisms as interactions with significant mean separation. In addition, the effect of the Reynolds number will be considered for two equivalent incipient interactions.

Two quantitative criteria were used for the definition of the equivalence of the shock strength between the two Reynolds number cases. They are both based on the probability and intensity of the occurrence of flow reversal. In the first place the iso-contours of the flow reversal probability were considered, giving an indication of the intermittency of the flow separation. In the second place, the maximum height of the instantaneous dividing streamline was determined for each realisation, giving an indication of the separation bubble height. The considered interactions are a low Reynolds number $\varphi = 5.5°$ incipient interaction and a high Reynolds number $\varphi = 6.0°$

incipient case. These interactions are compared to the separated flow cases ($\varphi = 8.0°$ and $\varphi = 9.5°$) from the 'PIV champs larges 2006' dataset, see section 3.1.2 in Piponniau (2009). The unsteadiness properties of the flow separation for the different interactions are described in detail in the next sections.

9.1.1 Flow reversal rate

Figures 9.1 shows the rate of the instantaneous occurrence of flow separation for each point in the flow domain, computed as the ratio of the number of realisations with reverse flow over the total number of realisations. The iso-contours of the mean vertical velocity are superimposed on the figure. To visualise the subsonic region of the interaction, the sonic line is also reported, in accordance with figure 5.4 on page 76. It has been obtained using the modified Crocco-Busemann relation assuming adiabatic wall conditions (see White (1991)). It can be seen that the rate of flow separation increases with the shock strength. For the smallest shock strength ($\varphi = 5.5°$ low Reynolds and $\varphi = 6.0°$ high Reynolds), the flow reversal occurs in less than half of the realisations, which is consistent with the fact that no mean separation bubble is observed. The low Reynolds number case is statistically very similar to the high Reynolds number case. Both display a separation rate of approximately 40% and a reversed flow region with similar horizontal and vertical extent when normalized by the interaction length and the boundary layer thickness respectively. At $\varphi = 8.0°$ flow reversal occurs locally in 90% of the realisations, and for $\varphi = 9.5°$ in 95% of the realisations.

Appendix D proposes a definition of incipient separation that is convenient for use with full field velocity data. This criterion links the flow reversal rate to the statistical significance of the back-flow with respect to the mean velocity (defined as $R = \frac{U}{\sigma_u}$). This criterion embodies the gradual nature of the occurrence of flow separation, classifying a flow as attached or separated only when the flow reversal has attained a statistically significant threshold (respectively $R > 1$ and $R < 1$, corresponding to 1σ). According to the proposed convention, the $\varphi = 5.5°$ low Reynolds and $\varphi = 6.0°$ high Reynolds interactions are indeed of the incipient type.

9.1.2 Bubble height statistics

In the previous paragraph, it was confirmed that both incipient cases present similar velocity reversal rates. Here, it will be verified that the separation bubble also corresponds to a similar organisation of the flow. The instantaneous dividing streamline will be determined for each realisation in accordance with previous work, see Piponniau *et al.* (2009). It is defined as the set of points $\{y_j(x)\}$ where $\overline{Q}_H = \int_0^{y_j(x)} u\,dy = 0$, where $\overline{Q}_H$ denotes the imposed iso-flux value. The main limitation of this procedure is to neglect the
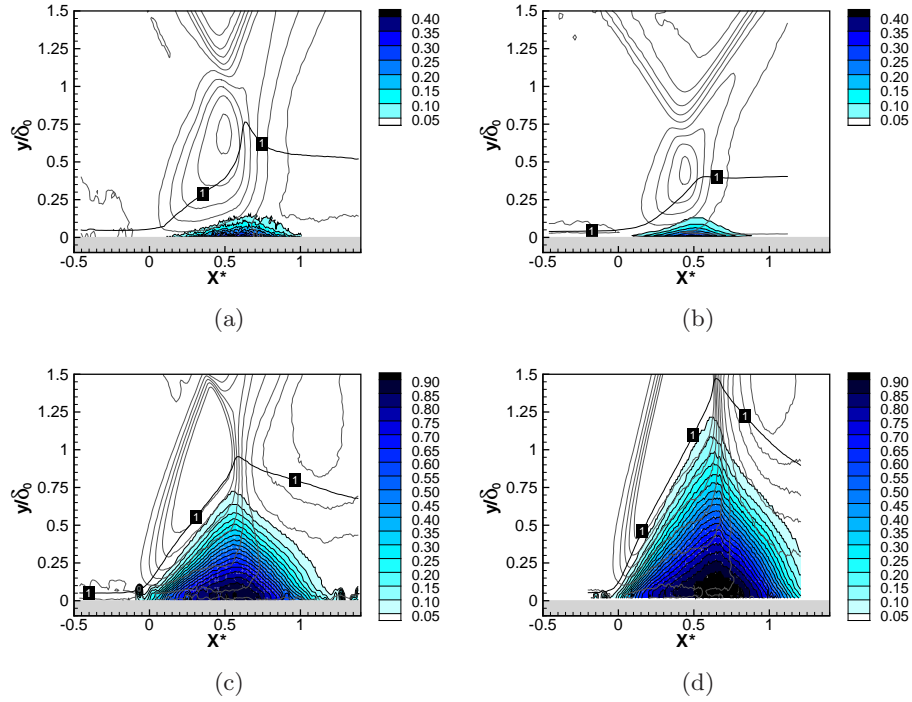
Figure 9.1: Flow reversal iso-probability contours: high Reynolds number incipient, (a) 6.0°; low Reynolds number incipient, (b) 5.5°; low Reynolds number separated cases, (c) 8.0° and (d) 9.5°. Iso-contours of the vertical velocity component are shown in grey for reference, see also figure 5.4. The solid black line, labeled with '1', indicates the approximate mean sonic line.

density variations in the low velocity part of the interaction. The maximum instantaneous elevation of the dividing line (determined for $0 < X^* < 1$) will be denoted h. Of course, when no reversed flow is observed, h is zero by definition.

The histogram of this maximum bubble height h (with the vertical axis normalized by the total number of realisations) is shown in figure 9.2. It can be observed that the height of the separation bubble increases with increasing shock strength. For the weakest interactions, the separation bubble only exists part of the time, the flow being fully attached in a significant part of the realisations, see figures 9.2(a) and 9.2(b). For the larger shock strength, a separation bubble is practically always present: a substantial separation bubble of over a quarter of the boundary layer thickness in height can be observed to be present at all time, and the bubble extends to well beyond the incoming boundary layer edge in part of the realisations, see figures 9.2(c) and 9.2(d). It can be seen that the histogram of the high Reynolds number case shows a large resemblance to the one for the $\varphi = 5.5°$ shock angle.

(a)

(b)

(c)

(d)
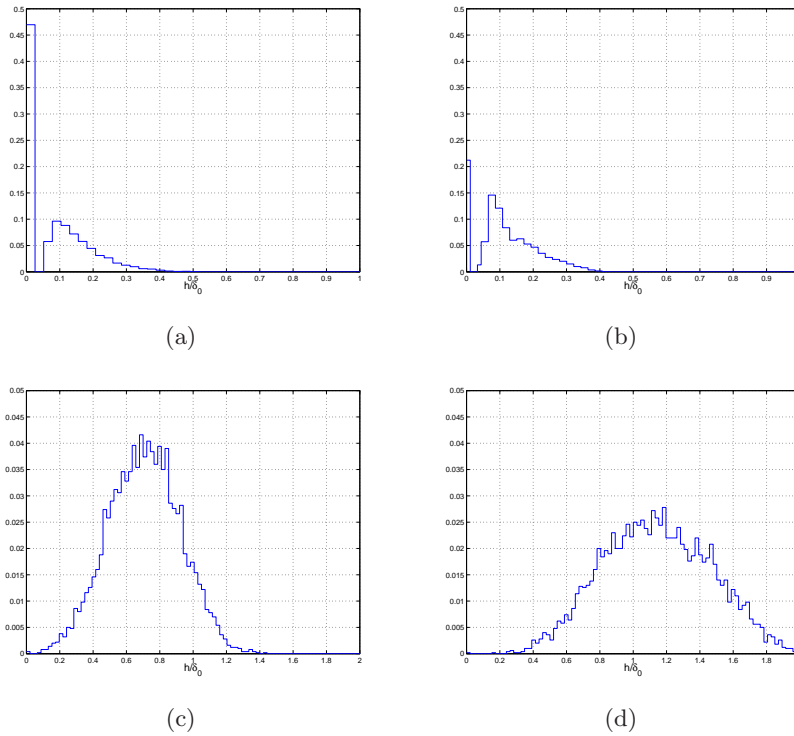
Figure 9.2: Separation height $(\frac{h}{\delta_0})$ histograms: high Reynolds number incipient, (a) 6.0°; low Reynolds number incipient, (b) 5.5°; low Reynolds number separated cases, (c) 8.0° and (d) 9.5°.

Given the similarity in the flow reversal probability, the bubble height histograms, and the criterion for incipient separation, the two incipient cases are considered as equivalent flows. This gives rise to the evaluation of the Reynolds number influence on the unsteadiness in the incipient interactions. The two incipient cases will be compared with the low Reynolds number separated cases ($\varphi = 8.0°$ and $\varphi = 9.5°$) which have already been analysed, as previously published in Dupont *et al.* (2006) and Piponniau *et al.* (2009).

9.2 Interaction characteristics comparison

The equivalence between both incipient interactions, at low Reynolds number ($\varphi = 5.5°$) and at high Reynolds number ($\varphi = 6.0°$), will now be considered in more detail, and will be compared to the low Reynolds separated cases ($\varphi = 8.0°$ and $\varphi = 9.5°$), referring to section 8.7. As can be seen from figure 8.13, the mean velocity approaches zero close to the wall for the incipient cases, without producing a mean back flow. Figure 8.14, and
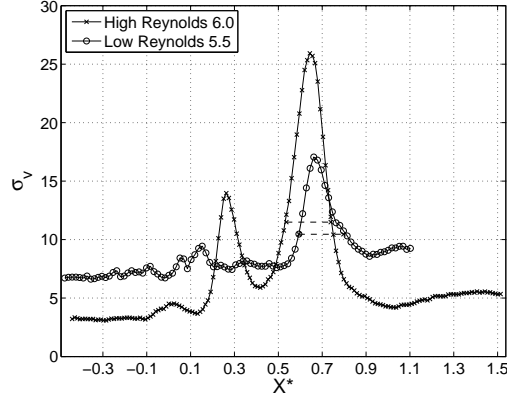
Figure 9.3: Longitudinal evolution of the RMS of the normal velocity fluctuations across the shocks for the two incipient cases ($\frac{y}{H} = 1.56$).

the equivalent figures 8.16 and 8.15, show that in all cases, increased U-component fluctuations occur starting from the reflected shock foot. This region of high turbulence intensity develops between $0 < X^* < 0.5$ along an inclined path, see the white lines in figure 8.14. The generated high turbulence intensities are advected in the downstream re-attached boundary layer.

If the global organisation of the flow fields looks very similar between the two incipient cases, a major difference can be observed concerning the reflected shock in the boundary layer (i.e. $y/\delta_0 < 1$ or $y/L < 0.5$). Figure 8.14(a) shows a clear imprint of a well focused shock for the high Reynolds number case down to $y/L \approx 0.1$, whereas the shock is hardly distinguishable in the low Reynolds incipient case. Indeed, for the latter case, the reflected shock appears as a continuous velocity decrease rather than a well defined step in the turbulent part of the flow, this notwithstanding the smoothing effect introduced by the particle lag in the PIV measurements. Hence, the reflected shock foot constitutes a fan of compression waves rather than a well focalised shock wave (Délery & Marvin (1986)), see figure 8.14(b). Such a dependence of the separation shock on the Reynolds number was already observed in the case of compression ramps, both from experiments and DNS (see Ringuette & Smits (2007); Wu & Martin (2008); Ringuette *et al.* (2008)). With increasing shock strength, the reflected shock becomes more focused, as can be observed for the low Reynolds $\varphi = 8.0°$ case, see figure 8.14(c). This is confirmed for the largely separated low Reynolds case ($\varphi = 9.5°$), which exhibits a well defined focused reflected shock, as in the high Reynolds incipient case, see figure 8.14(d).

In all cases, the reflected shock is clearly unsteady. This is best illustrated from the longitudinal evolution of the RMS of the V-component

Table 9.1: Interaction excursion length comparison.

Experiment	High Re	Low Re		
Flow deflection	6.0°	5.5°	8.0°	9.5°
$L(mm)$	37	25	46	71
L_{ex}/L	0.2	0.2	–	0.1

fluctuations, see figure 9.3. The amplitude of the oscillation of the reflected shock can be estimated from the width of the peak of the RMS fluctuations. For the incipient cases, the region under the point of shock crossing is in the turbulent part of the flow and it becomes difficult to identify a well defined peak, in particular in the low Reynolds number case, where the shock is not well focused. If measurements above the crossing point are considered, the length L_{ex} can be estimated for all cases. Hence, all values for the excursion length have been obtained at the same non-dimensional height ($\frac{y}{H} = 1.56$), corresponding to the height $\frac{y}{\delta_0} = 3.45$ for the $\varphi = 9.5°$ interaction (Dupont et al. (2006)). When a width criterion based on $1/e$ of the maximum peak height is used, an estimated shock oscillation amplitude of $L_{ex} \approx 0.2\ L$ is inferred for the incipient cases, compared to the value of $L_{ex} \approx 0.1L$ for the separated cases obtained through hot wire (see Dupont et al. (2006)). It has been verified that the same result is obtained from hot wire and PIV based data given the same flow case. The values are reported in table 9.1. In the high Reynolds case, the measurements are significantly more affected by optical effects related to the large density jump across the shock. This is known to lead to measurement artifacts in the vicinity of the shock waves (Elsinga et al. (2005b,a)). For example, the incident shock measurements generate significant RMS levels despite the fact that it is stationary (see figure 9.3). Therefore, L_{ex} could be overestimated for the high Reynolds number case with respect to the low Reynolds measurements. Nevertheless, the RMS peak for the reflected shock is significantly wider and higher than the peak for the incident shock, which is a direct consequence of the unsteadiness of the reflected shock. The RMS caused by the unsteadiness is larger than the measurement uncertainties. The determination of the oscillation amplitude is therefore thought to be sufficiently reliable for the present purposes.

The results presented here support the notion that the selected incipient interactions, which would be classified as being of similar nature based on figure 8.7, are also equivalent from the perspective of the observed shock unsteadiness. In the following part, it will therefore be to attempt to identify whether the mechanisms behind the shock dynamics are also of a similar nature.

9.3   Separation bubble height based conditioning

In the previous section, it has been shown that significant differences exist for the turbulence fields between incipient and separated cases: in both cases there is evidence of new energetic structures developing downstream of the reflected shock foot, but an important variation is observed in the energy peak level and in the vertical extent. In the separated cases, these new turbulent scales have been related to the development of a mixing layer in the interaction (Dupont *et al.* (2006, 2008)) leading to the shedding of large vortices downstream of $X^* = 0.5$. In the incipient cases, a similar organisation is not intuitively evident, as no mean separation occurs. Nevertheless, the probability to observe separated flow remains large, see figure 9.1. Therefore, conditional analysis based on the instantaneous existence of reversed flow has been carried out, similar to that already performed for the separated cases, see Piponniau *et al.* (2009). It is remarked that within a more general framework that, under certain simplifying assumptions, it is possible to relate the variations in the height of a stream tube for a fixed iso-flux $\overline{Q}_H$ (in this case $\overline{Q}_H{=}0$) to the velocity fluctuations at a fixed height, see appendix E. This is especially applicable to the fluctuations in the incoming boundary layer, where spatial averaging can be applied, but it might be useful to put the current iso-flux approach in context.

Three classes will be considered for the conditional analysis: shallow, medium and thick. The classes are selected based on the histograms of figure 9.2, taking 10% of the realisations at the lower end of the histogram, 10% in the middle and 10% at the higher end. For the incipient interactions, all of the attached flow cases are taken to represent the shallow class. For the selection of the medium and thick classes, only the part of the histogram corresponding to the separated flow cases is considered. This was done to eliminate a biasing of the results due to the large weight of the attached flow. To this aim, the peak at zero was eliminated from the histogram. Consecutively, the medium bubble height was based on 10% of the remaining realisations in the middle of the histogram and similarly the thick bubble height was defined based on 10% of the realisations at the higher end.

9.3.1   Development of mean separation

Based on the bubble height selection described above, the following mean flow results have been obtained (see figure 9.4). Only the negative mean U-component is shown, with the shallow class on the top and the thick class on the bottom. As can be observed, mean flow reversal only occurs for the 10% highest separation bubbles for both incipient cases. Evidently, no mean flow reversal occurs for the lowest class, as all these realisations correspond to an attached flow. For the medium case, separation does occur instantaneously, but no mean flow reversal occurs. It is likely that these cases correspond
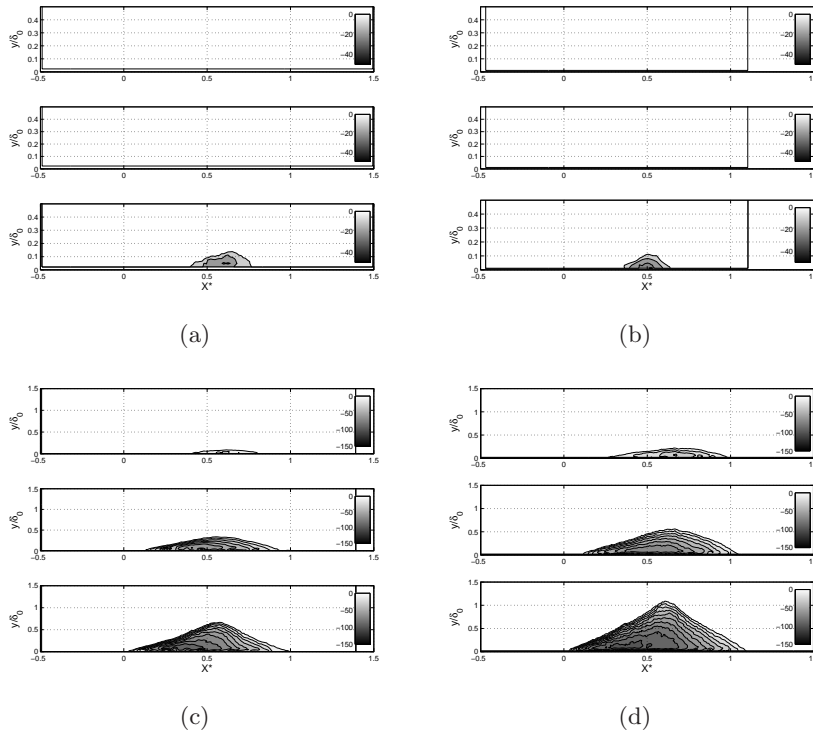
Figure 9.4: Mean reversed flow (*U*-component, only negative velocities are shown; subplots from top to bottom: shallow, medium, thick): high Reynolds number incipient, (a) 6.0°; low Reynolds number incipient, (b) 5.5°; low Reynolds number separated cases, (c) 8.0° and (d) 9.5°. The separated cases have been reported in (Piponniau *et al.* (2009)).

to small pockets of separated flow that occur randomly in space. These pockets would not produce a mean flow reversal as a consequence of their random distribution in space. This is in agreement with the instantaneous realisations in section 5.4. The fact that the same results are obtained for both incipient separation cases is another confirmation of their equivalence in separation state, see section 9.1.

Another observation is that the thick separation bubbles for the incipient cases (high Reynolds $\varphi = 6.0°$, low Reynolds $\varphi = 5.5°$) correspond approximately to the shallow separation bubbles for the $\varphi = 8.0°$ case. Similarly, the thick bubble for $\varphi = 8.0°$ corresponds to the medium bubbles for $\varphi = 9.5°$. (Note that the incipient separation plots in figure 9.4 use a different scale for the vertical axis.) It may therefore be speculated that there is a 'spectrum of flow separation' that develops as a function of the shock strength. This could be indicative of the fact that the similar mechanisms are at work

(a)

(b)

(c)

(d)
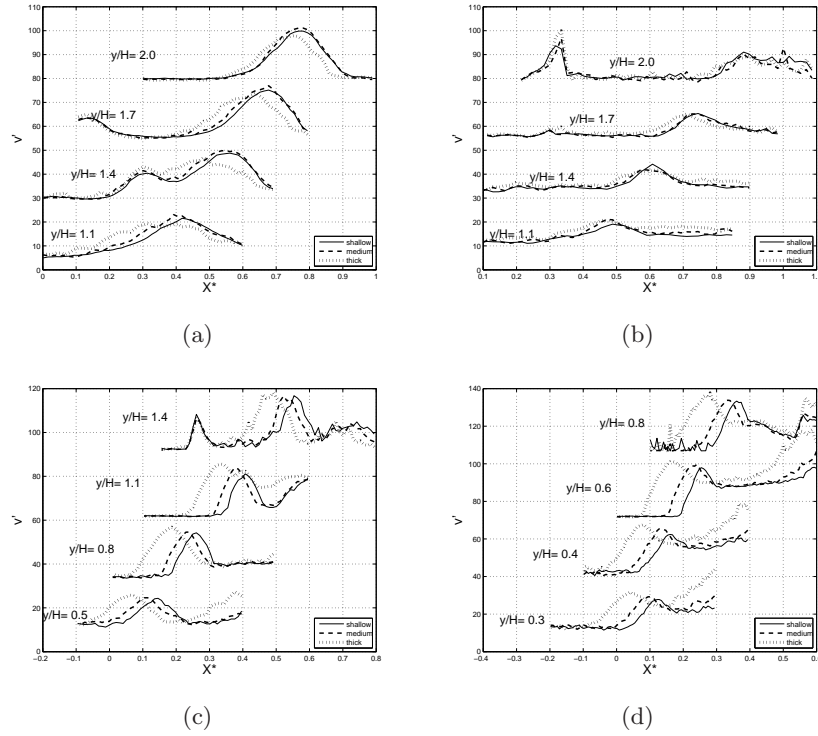
Figure 9.5: Conditional shock position, defined as the maximum of the conditional normal velocity standard deviation: high Reynolds number incipient, (a) 6.0°; low Reynolds number incipient, (b) 5.5°; low Reynolds number separated cases, (c) 8.0° and (d) 9.5°. The separated cases have been reported in (Piponniau *et al.* (2009)).

in the incipient flows as in the separated flows, with a gradual shift in the dominance of each mechanism depending on the separation state.

9.3.2   Correlation with the shock position

It has been shown in section 9.2 that the reflected shock is found to be unsteady in all cases. In the incipient cases, the shocks crossings occurs near the edge of the boundary layer, and the estimation of L_{ex} was hence necessarily constraint to heights with $y/H > 1$. In this region, the excursion length was determined to be about $0.2L$, or $\approx 0.40\delta_0$. For the $\varphi = 9.5$ separated case (Dupont *et al.* (2006)), L_{ex} was found to decrease from about $0.3L$ at the wall to $0.1L$ for $y/H = 1.6$. It is therefore quite difficult to conclude, based on the magnitude of L_{ex} alone, whether similar mechanisms can be associated to the shock movements between the incipient and separated cases. However, in the separated cases, the shock motions were found to be

strongly linked with the bubble height, see Piponniau *et al.* (2009). In section 9.3.1 it was shown that in the incipient cases, the separation bubble is non-existent most of the time, even if spots of reverse flow occur. Nevertheless, a bubble of rather limited extent can develop in rare cases. Therefore, it is of interest to check if all, or at least a part, of the shock unsteadiness can be related to the unsteady flow reversal as in the separated interactions.

To determine the correlation between the state of the separation region and the reflected shock position, the conditional turbulence fields are considered. The shock position is deduced from the longitudinal evolution of the V-component fluctuations: its mean conditional position is associated with the conditional RMS-peak. The results are shown in figure 9.5. To take into account the different aspect ratios of the interaction between the high and low Reynolds number (H/L, see table 8.5), the comparisons between the different interactions are made at the same non-dimensional height (y/H): positions for $y/H > 1$ correspond to the flow above the shock crossing point. The observed peak upstream of the reflected shock corresponds to the incident shock. It is clear that for both incipient cases, no particular motion of the reflected shock can be related to the shallow or medium states, see figures 9.5(a)-(b). This is a direct consequence of the hypothesized randomly occurring pockets of separation (see section 9.3.1), which cannot be expected to cause a consistent upstream displacement the reflected shock. However, when a separation bubble is formed (thick bubbles case), a slight correlation between the bubble height and the shock displacement appears. Nevertheless, the amplitude of the motion is smaller than for the separated cases, see figures 9.5(c)-(d), (about $0.05L$, while $0.1L$ is observed in separated cases). The opposite tendency is observed for the total extent of the shock oscillations ($0.2L$ in the incipient cases compared to $0.1L$ for separated cases). Hence, the contribution of the shock displacement linked to the separation bubble exits for the incipient cases, but it is less significant than in the case of the separated interactions.

9.3.3   Correlation with the incoming boundary layer

To complete the comparisons between incipient and separated cases, conditional statistics based on the separation bubble height have been performed for the upstream boundary layer. Results are reported in figure 9.6.

In separated cases, no significant correlation between the different states of the bubble was found, see figures 9.6(c) and 9.6(d). In the incipient cases on the contrary, a correlation, although rather limited, can be observed: the shallow and medium bubbles correspond to slightly fuller profiles than the thick bubbles. Again, no dependence on the Reynolds number is observed. Consequently, it seems that in the incipient cases, the upstream boundary layer is more involved in the unsteadiness of the interaction zone, with an intermittent development of a separation bubble.

(a)   (b)

(c)   (d)
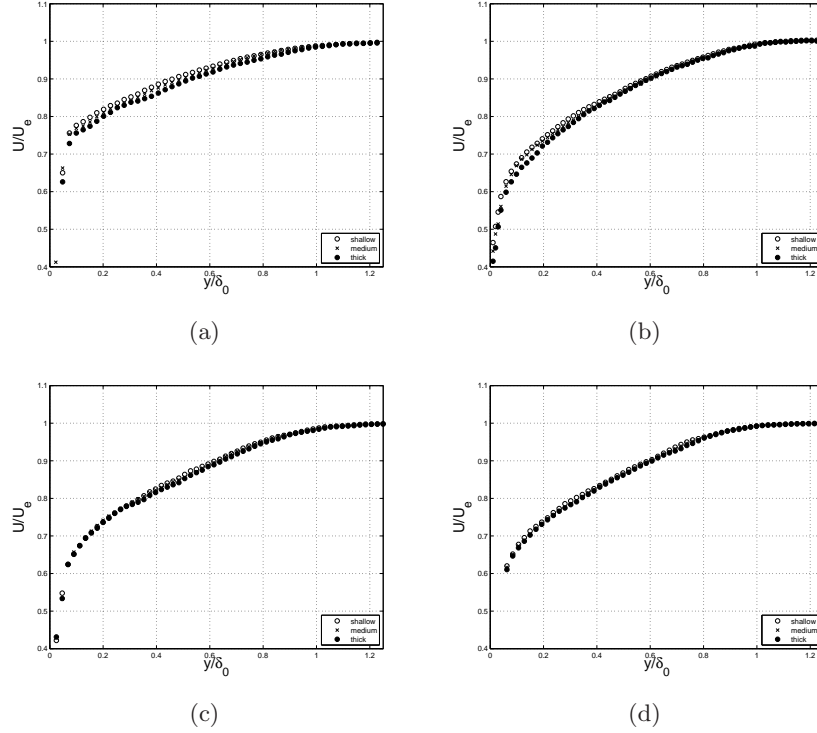
Figure 9.6: Conditional mean velocity in the upstream boundary layer (U-component): high Reynolds number incipient, (a) 6.0°; low Reynolds number incipient, (b) 5.5°; low Reynolds number separated cases, (c) 8.0° and (d) 9.5°. The separated cases have been reported in (Piponniau *et al.* (2009)).

Therefore, the incipient case appears as an intermediate case between a fully attached interaction, where shock unsteadiness is expected to be governed by the turbulent structures of the upstream boundary layer, and a separated interaction where the dynamics are mostly related to the downstream unsteadiness developing in the interaction region. Accordingly, it should be expected that the associated time scales differ significantly between incipient and separated cases. Indeed, it has been shown that, in shock induced separation, the characteristic shock frequency f_s is such that the Strouhal number equals $S_L = \frac{f_s L}{U_1} \approx 0.03$ for a Mach number $M > 2$ and for a wide range of geometries, see Dussauge *et al.* (2006). On the contrary, such well defined low frequency content has not been observed in the low Reynolds incipient case, which exhibits broadband spectra in the vicinity of the reflected shock, as shown in Piponniau *et al.* (2009); there exists a low frequency content in the range of $S_L \approx 0.03$, but it does not contribute to the main part of the energy of the signals related to the shock unsteadiness.

This confirms again that, if similar mechanisms are present in both types of interactions, they do not occur with similar importance.

9.3.4   Correlation with the occurrence of vortex shedding

It has been shown in previous sections that the different interactions exhibit very similar properties. Mainly, the development of peak turbulence intensities downstream of the reflected shock foot, which has been observed in all cases. When a mean separation occurs, it is classical to relate this to the development of a mixing layer and the creation of large vortical structures (Mabey (1972); Eaton & Johnston (1981); Driver *et al.* (1987); Simpson (1989)), see figure 1.11 on page 13. This has indeed been demonstrated for the separated cases, where the region of high turbulence intensities was associated with the development of a mixing layer in the first part of the interaction, followed by the shedding of large vortices, see Dupont *et al.* (2006, 2008); Piponniau *et al.* (2009). It is not intuitively straightforward to expect that such properties can be observed when no separation occurs. Nonetheless, a large resemblance of the regions of peak turbulence intensity was achieved under the geometrical scaling proposed in figure 8.15, independent of the separation state. The existence and origin of large vortical structures in the incipient interactions will therefore be investigated here in more detail.

In order to highlight the existence of such vortical structures, a vortex detector has been applied on the instantaneous PIV velocity fields. It is based on a non-local criterion (Graftieaux *et al.* (2001)), and has been found efficient for extracting the large coherent structures in the separated cases, see Dupont *et al.* (2008). It is normalised between -1 and 1 and can be interpreted as the vorticity. It is however defined as an integral, making it less sensitive to measurement noise and therefore more convenient for use with PIV data. Typical instantaneous fields of the vortex detector are shown in figure 9.7. The iso-contours of the U-component fluctuations have been superimposed onto the figure. It is clear that the regions of high turbulence levels are directly related to the development downstream of the reflected shock foot of large scale energetic structures, interpreted as a mixing layer with consecutive vortex shedding in Dupont *et al.* (2008). Its presence does not depend on the existence of an instantaneous bubble of recirculation in the incipient cases: the examples reported in figures 9.7(a) and 9.7(b) correspond to realisations without flow separation, belonging to the case $h = 0$ in figures 9.2(a) and 9.2(b). The average of the vortex detector has also been estimated over the complete data ensemble, defining the region where the vortices are statistically present, see figure 9.8. Whatever the flow, there is always an important probability to observe large vortical structures. It is noted that these fields would show an even larger geometric resemblance when scaling the wall normal coordinate by $LG_3(M_e, \varphi)$, as in figure 8.15.

(a)

(b)

(c)

(d)
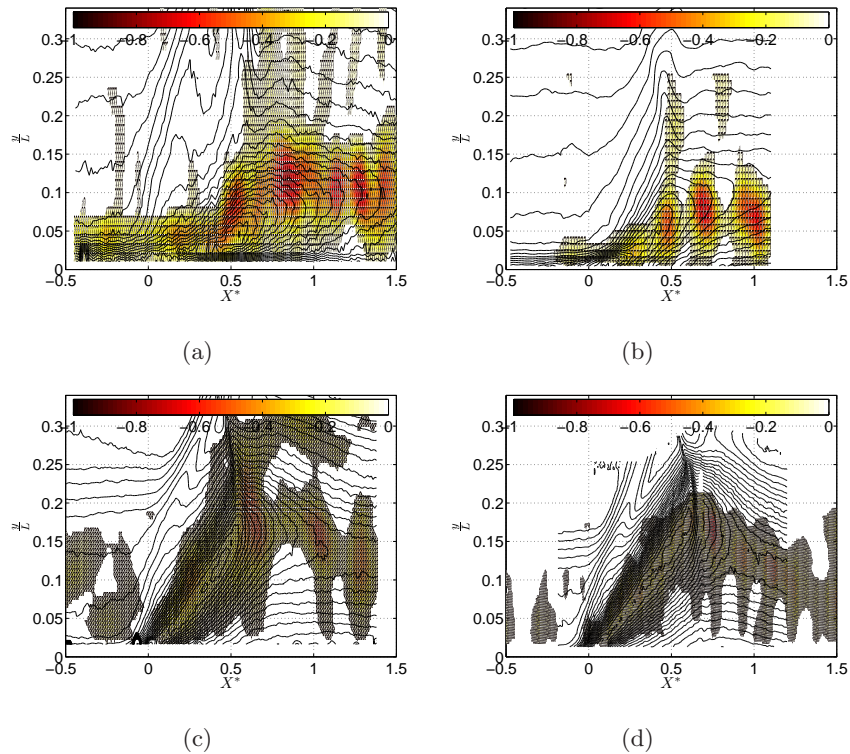
Figure 9.7: Instantaneous visualisations of the mixing layer with consecutive vortex shedding: high Reynolds number incipient, (a) 6.0°; low Reynolds number incipient, (b) 5.5°; low Reynolds number separated cases, (c) 8.0° and (d) 9.5°. Iso-contours of the U-component fluctuations (see figure 8.14) are shown for reference.

9.4   Non-zero iso-flux height based conditioning

Given the strong correlation obtained between the pulsation of the separation bubble and the large scale shock excursions for the separated cases, one might wonder if an equally strong correlation could exist between the pulsation of a low speed fluid region and the shock motion for the incipient separation cases. However, the dividing streamline (in other words, zero iso-flux height) may not be the proper conditioning variable. This due to the fact that no mean separation bubble exists for these cases, notwithstanding the fact that there is a large retarded flow region, see figure 8.13 in section 8.7. It has nonetheless been shown above that vortex formation exists, even in absence of a separation bubble, see figures 9.7 and 9.8. This might be the driving mechanism behind a pulsation of the retarded fluid region, similar to the flapping mechanism proposed in Piponniau *et al.* (2009). This line of thought is encouraged by figure 8.16 in section 8.7, which shows a large re-

(a)

(b)

(c)

(d)
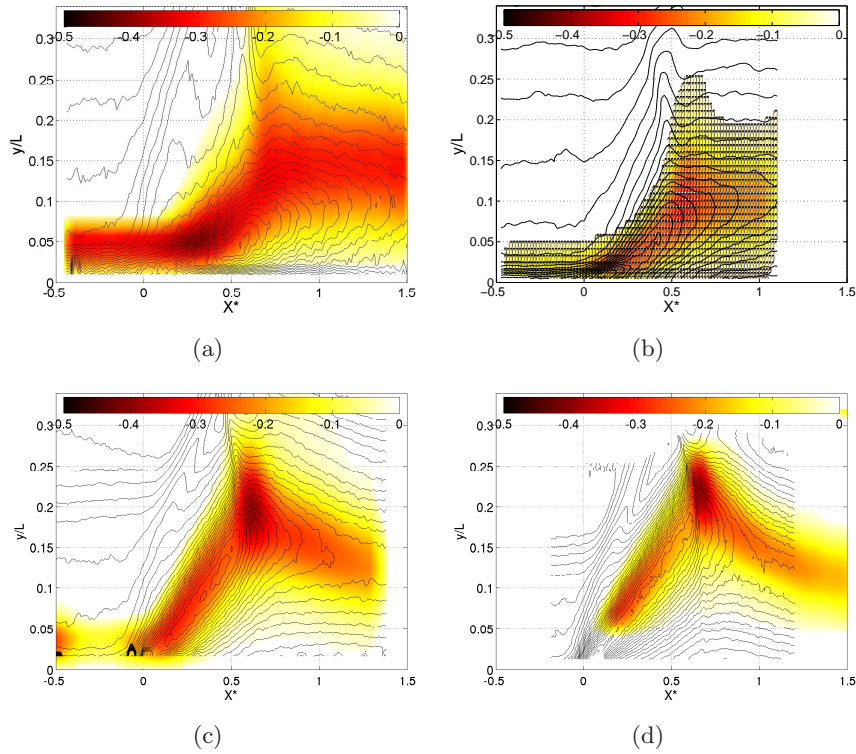
Figure 9.8: Ensemble mean of the vortex detector: high Reynolds number incipient, (a) 6.0°; low Reynolds number incipient, (b) 5.5°; low Reynolds number separated cases, (c) 8.0° and (d) 9.5°. Iso-contours of the U-component fluctuations (see figure 8.14) are shown for reference.

semblance for the turbulence intensity fields in all cases. This might indicate that a similar 'flapping' mechanism exists in all cases, causing excursions of the reflected shock. Alternatively, the upstream boundary layer might drive a pulsation of the low speed fluid region within the interaction, induced by the low speed elongated structures described by Ganapathisubramani *et al.* (2007b). It may therefore be useful to verify whether the retarded fluid region (with a *non-zero* iso-flux) also shows pulsation dynamics, and whether this can be linked to either the separation bubble or the upstream boundary layer.

The aim of this section is therefore in the first place to define a iso-flux for which the pulsation of the retarded fluid region is maximal. Next, conditional statistics will be performed in analogy to section 9.3. Finally, it will be attempted to put the results into a conceptual framework.

9.4.1   Iso-flux optimisation

It is thought that there may exist some iso-flux $\overline{Q}_H$ that yields the largest pulsation dynamics of the low speed fluid region. To visualise this, one may imagine an accordion fixed between the wall and the external flow. Neither at the wall, nor at the outer flow will there be any pulsations: at the wall, the velocity is zero, and in the outer flow the velocity is constant. These may hence be considered as fixed points. Returning to the image of the accordion, one might consider that between these 'clamping points', there is a point were the fluctuation dynamics are maximal. To determine the iso-flux belonging to this maximum, the histogram of the streamline heights $h(\overline{Q}_H)$ is calculated within the interaction $(0 < X^* < 1)$ using equation 9.1, in analogy to figure 9.2, assuming again that density variations are negligible. This is done for a range of iso-fluxs, $\overline{Q}_H$. The optimum iso-flux corresponds to the value yielding the largest dynamics in $h(\overline{Q}_H)$, in other words, the largest standard deviation: $\max(\sigma_h)$.

$$\int_0^{h(\overline{Q}_H)} u\, dy = \overline{Q}_H \tag{9.1}$$

Figure 9.9 shows the resulting variation of σ_h with the choice of iso-flux, where $\overline{Q}_H$ has been normalised by the total flux of the incoming boundary layer. As expected, the separated cases yield an optimum for $\overline{Q}_H = 0$. It may hence be concluded that for these cases, the dominant pulsation dynamics are due to the separation bubble. For the incipient cases, an optimum is obtained for a non-zero iso-flux. The maximum pulsation dynamics hence seem to correspond to a streamline corresponding to a positive iso-flux. This would be in agreement with the pulsation of the retarded fluid region. The optimum is 45% of the flux in the incoming boundary layer for the Delft 6.0° case and about 20% for the Marseille 5.5° case.

Figure 9.10 shows the histograms of the instantaneous height $h(\overline{Q}_H)$ corresponding to the optimal iso-flux. It is noted that $h > 0$ all of the time. The mean height is approximately $0.8\delta_0$ for the high Reynolds case and $0.5\delta_0$ for the low Reynolds 5.5° case. The histograms for the other low Reynolds cases are unaltered with respect to figure 9.2, since they concern the dividing streamline $(\overline{Q}_H = 0)$.

Following the same approach as in section 9.3, conditional statistics have been performed, defining three classes: shallow (or thin), medium and thick retarded flow regions. The selection of the cases is made based on the histograms of figure 9.10, taking 10% of the realisations at the lower end of the histogram, 10% in the middle and 10% at the higher end. The analysis will be carried out for the incipient cases only, since the results for the separated cases have already been reported in section 9.3.
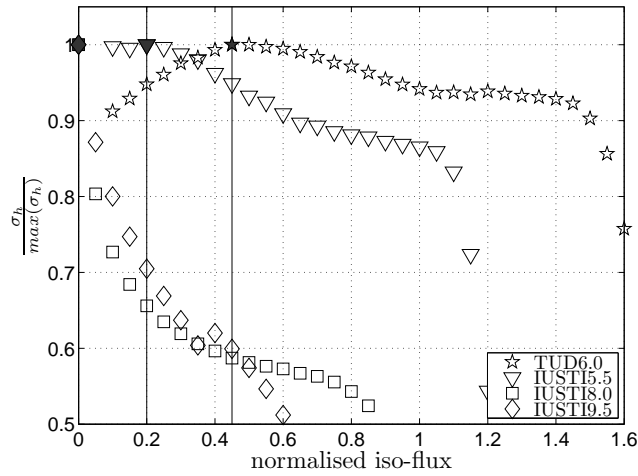
Figure 9.9: Optimisation of the pulsation dynamics with respect to the iso-flux; solid vertical lines and filled symbols indicate the maximum fluctuation dynamics. The iso-flux has been normalised by the total flux of the incoming boundary layer.

(a)   (b)
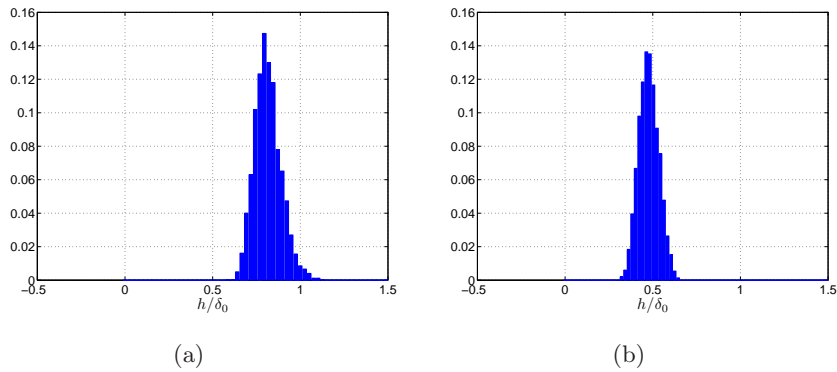
Figure 9.10: Height histograms ($\frac{h}{\delta_0}$) for the streamline corresponding to the optimal iso-flux: high Reynolds number (a) 6.0°; low Reynolds number (b) 5.5°.

9.4.2   Pulsation of the retarded zone

Figure 9.11 shows the results for the conditioning based on the optimal iso-flux as determined in section 9.4.1. A clear pulsation of the retarded fluid region within the interaction is observed in figures 9.11(a)-(b), with an increase in the elevation of the contour lines of up to $\frac{y}{\delta_0} \approx 0.2$ between the thin and the thick states. The fluid pulses over a long distance downstream,

(a)   (b)

(c)   (d)
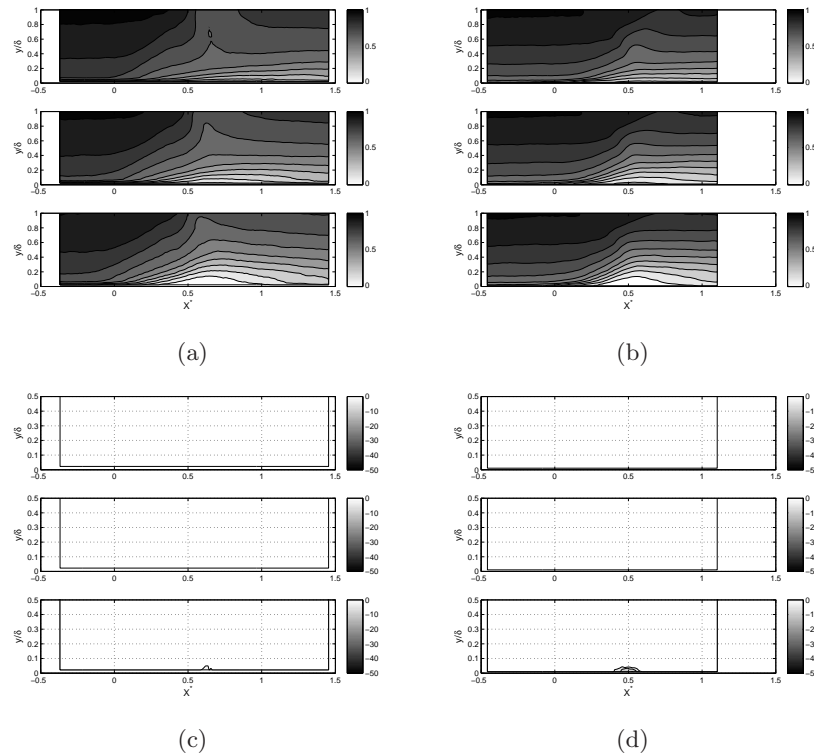
Figure 9.11: Mean conditional U-velocity and conditional separation bubble, respectively: (a),(c), high Reynolds number 6.0°; (b),(d), low Reynolds number 5.5°.

and the complete recovering boundary layer height is affected, see figures 9.11(a)-(b). However, the link with the separation bubble size has become even less pronounced, as can be observed when comparing figures 9.11(c)-(d) to figures 9.4(a)-(b). This is probably due to the fact that for the conditioning on the separation bubble height, the attached realisations were not considered for the definition of the medium and thick classes. This contrary to the current approach, where all realisations are taken into account since the iso-flux height is always non-zero.

9.4.3 Time scale of the iso-flux height variations

A correlation between the pulsation of the separation bubble and the reflected shock was put in evidence. For the incipient interactions, this link could be extended to the pulsation of the retarded fluid zone within the interaction. It is therefore verified for the high Reynolds incipient case (where temporally resolved Dual-PIV data is available) what the time scale of the pulsation of this retarded fluid region is. This has been done by computing

(a)   (b)
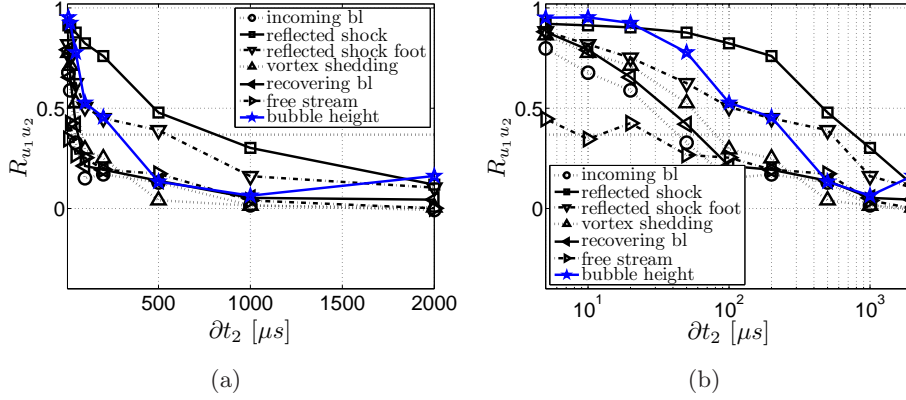
Figure 9.12: Auto-correlation coefficient for the optimal iso-flux 'bubble height' (see section 9.4.1) super-imposed onto the results from figure 6.4.

the auto-correlation coefficient of the optimal iso-flux height (defined in section 9.4.1). The result is shown in figure 9.12, superimposed onto the results from figure 6.4. As can be observed, the pulsation occurs at a characteristic frequency that is significantly below those of the incoming boundary layer, the vortex shedding and the recovering boundary layer. Taking again the crossing of the $\frac{1}{e}$-level as representative, a characteristic time scale of $250\mu s$ is obtained, corresponding to $4000Hz$. This holds the middle between the characteristic frequencies for the vortex shedding and the reflected shock. It is likely that the optimum iso-flux height does indeed contain contributions from both the mixing layer and a general pulsation motion, which would probably be at a lower frequency. This could explain why the curve in figure 9.12(b) shows a behaviour intermediate to the reflected shock and the vortex shedding.

9.4.4   Correlation with the shock position

A significant pulsation of the low speed fluid region has been observed, and it is therefore verified whether there exists a link between the height of the retarded fluid zone and the shock position. The results are shown in figure 9.13. In analogy to section 9.3, the peak in the RMS values of the V-component fluctuations is again considered to determine the conditional shock position. Comparisons are made at the same non-dimensional height (y/H). The shock position is more discriminative with respect to the retarded fluid regions: a shallow region corresponds to a downstream shock position, whereas a thick region is linked to an upstream shock position. However, the extent of the shock excursions is unaltered in comparison to figure 9.5.

(a)   (b)
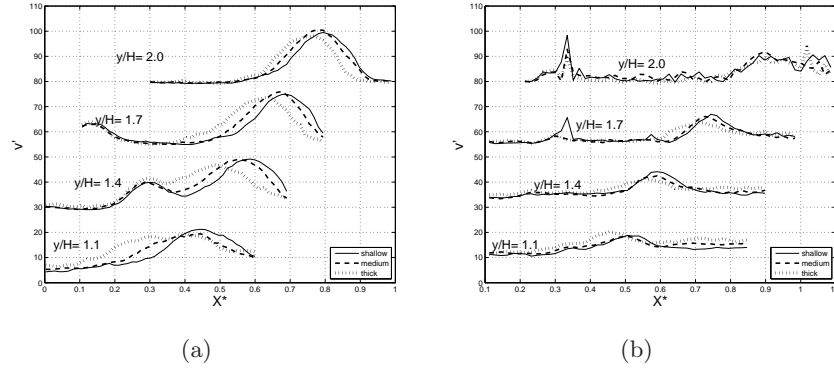
Figure 9.13: Correlation between the retarded fluid region height and shock position: high Reynolds number (a) 6.0°; low Reynolds number (b) 5.5°.

9.4.5   Correlation with the incoming boundary layer

Conditional statistics have been performed for the upstream boundary layer based on the retarded fluid region height. The results are shown in figure 9.14. The conditioning has been performed for the optimal iso-flux, as defined above. The iso-flux corresponding to the total flux of incoming boundary layer (in other words: $\overline{Q}_H = \int_0^{\delta_0} \overline{U} dy$, with $\overline{U}$ the mean velocity profile of the incoming boundary layer) has also been considered in figure 9.15, in view of equation E.7. In both cases, the profiles for the three states have become more dissociated than in figure 9.6, putting in evidence a larger correlation with the low speed fluid zone within the interaction. The differences between the velocity profiles for a given y amount to $5\%U_e$ over a large part of the boundary layer, where the profile for the high Reynolds case is affected over a larger height than the profile for the low Reynolds incipient case. Such a strong correlation has not been observed for the separated interactions, neither when considering the dividing streamline, nor when conditioning on the full boundary layer flux. The conditional boundary layer properties for the optimal iso-flux are summarised in table F.1 in appendix F. The range of variations in boundary layer properties decreases with increasing shock intensity. The variations are largest for the incipient interactions. The high Reynolds case does indeed show the largest amplitude of boundary layer thickness changes, as intuited from the figure. The changes in velocity for the low Reynolds number incipient case appear to take place lower in the boundary layer. The variations in friction coefficient, given by the log-law, amount to about 10% of the mean value and the shape factor changes are about 3% for both incipient cases.

Conditioning on the full boundary layer (figure 9.15) flux rather than on the optimal iso-flux (figure 9.14) shows a slightly stronger correlation with

the incoming boundary layer profile for the incipient interactions. It is likely that the results for the zero iso-flux (the dividing streamline) capture mostly the downstream effects, the optimal iso-flux contains a mix of upstream and downstream effects, and the full boundary layer flux results are biased towards the upstream effects only. Increasing the reference flux value from zero to non-zero values increases the correlation with the incoming boundary layer and deteriorates the correlation with the separation bubble (as confirmed by figures 9.11(c) and 9.11(d)). This indicates that the dynamics for the incipient cases are governed by both upstream and downstream effects. The fact that a clear link with the upstream boundary layer is absent for the separated cases, also when conditioning on the full boundary layer flux, indicates that the downstream effects are dominant.

It appears hence that for the incipient interactions, a major part of the dynamics is determined by the upstream boundary layer. Under certain simplifying assumptions, the changes in iso-flux height can be linked to the changes in height of a stream tube, see equation E.6, more particularly to changes in displacement thickness by means of equation E.7, see appendix E. It is likely that upstream changes in height of this stream tube, caused by streamwise elongated streaks of low momentum fluid (such as reported in Ganapathisubramani *et al.* (2007a) and Humble *et al.* (2009a)), will lead to changes in the height of the same stream tube within the interaction. This produces the perceived pulsation of the retarded fluid region. Or, equivalently, coherent upstream changes in the local velocity will lead to perceived fluctuations in velocity in the retarded fluid region. In the incipient case, this might also be a trigger for the occurrence of a separation bubble, the collapse of which may however have its own time-scale. Hence, a mix of both effects might be present. It is noted that the pulsation of the stream tube must have a characteristic streamwise length scale of at least the order of the length of the field of view of the data domain to be observed by means of the current conditioning method. Taking $U \approx 500m/s$ and $\Delta X \approx 100mm$, this means a characteristics frequency of these streamwise coherent fluctuations of about $5kHz$ or less.

9.4.6   Conditional flow deflection

In the following, the conditional flow deflection within the interaction is investigated in more detail, considering again the three states as described in section 9.4.1. Figure 9.16 shows iso-contours of the *local* flow deflection angle ($\tan(\varphi) = \frac{V}{U}$) within the interaction ($\frac{y}{H} < 1$). Only positive values outside the separation bubble (indicated by the large white region within the interaction) are shown. The increase in flow deflection angle close to the separation bubble edge is due to the fact that the horizontal velocity component vanishes. The incipient interactions (figures 9.16(a) and (b)) display a change in flow angle, corresponding to 2-3 contour levels, each

(a)   (b)
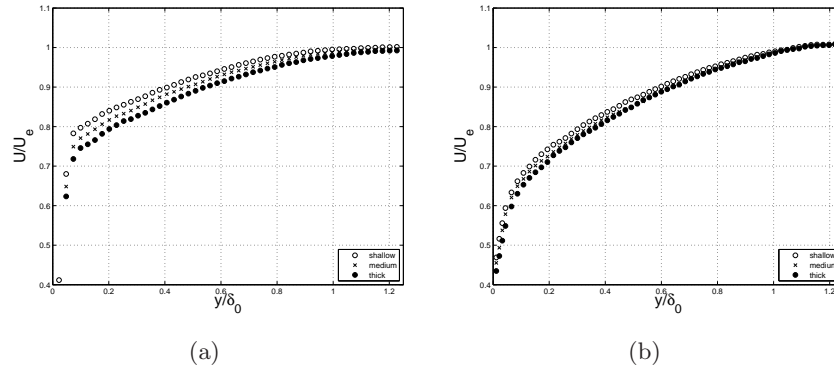
Figure 9.14: Correlation between the retarded fluid region height and the incoming boundary layer, based on the optimal iso-flux: (a) high Reynolds number 6.0°; (b) low Reynolds number 5.5°.

(a)   (b)
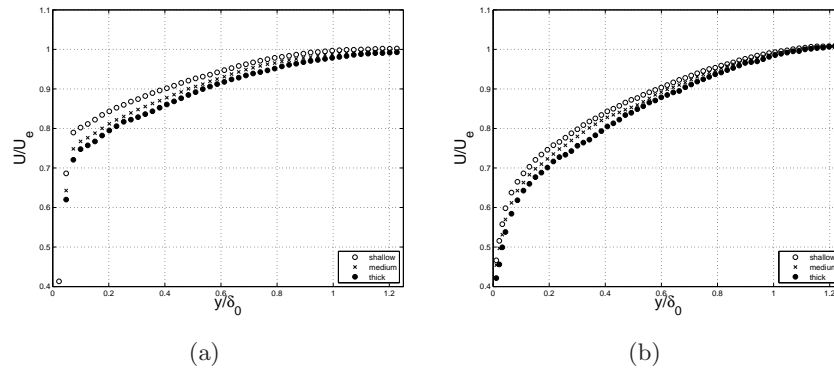
Figure 9.15: Correlation between the retarded fluid region height and the incoming boundary layer, based on the full mean incoming boundary layer flux: (a) high Reynolds number 6.0°; (b) low Reynolds number 5.5°.

level representing 2°. The separated interactions (figures 9.16(c) and (d)) appear to have a more constant flow deflection, the value changing at most 1 contour level. The shift in the upstream location of the contour lines confirm that large scale shock excursions occur for all four interactions.

To confirm the variation in the flow deflection angle, Figure 9.17 shows conditional profiles of the flow deflection at $X^* = 0.3$. The wall normal coordinate is scaled with the conditional interaction height H_i, defined as:

$$H_i = \frac{1}{2} L_i \tan(\beta) \; ; \quad \text{with:} \; L_i = \begin{cases} \text{thin:} & L - L_{ex} \\ \text{medium:} & L \\ \text{thick:} & L + L_{ex} \end{cases} \qquad (9.2)$$
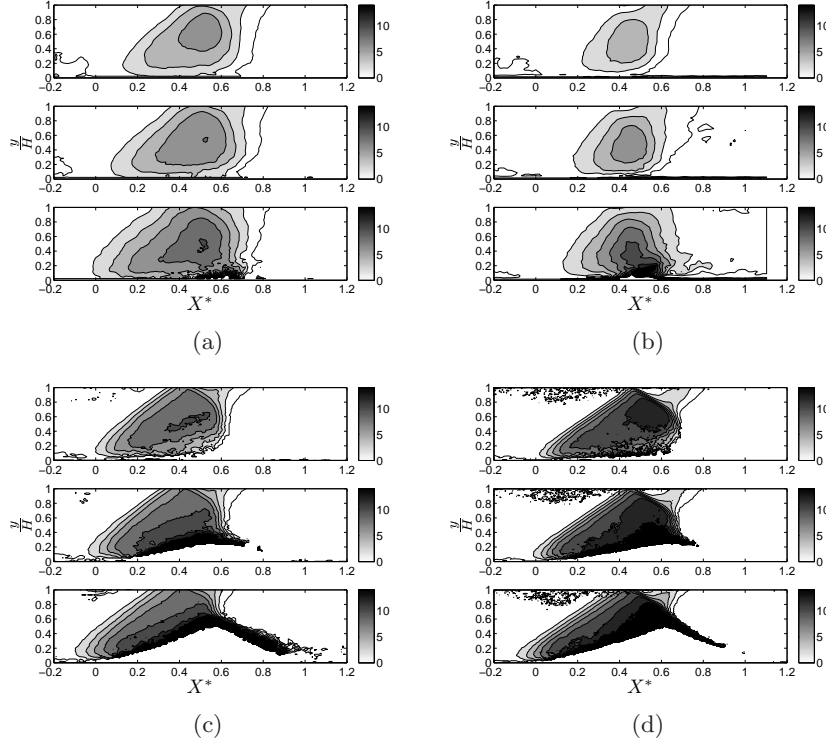
Figure 9.16: Iso-contours of the conditional flow deflection angle ($\tan(\varphi) = \frac{V}{U}$), only positive values are shown. High Reynolds case: (a) 6.0°; Low Reynolds case: (b) 5.5°, (c) 8.0°, (d) 9.5°. The wall normal coordinate is scaled by the mean interaction height H.

Where L_i is the conditional interaction length, and L_{ex} is the shock excursion amplitude outside the boundary layer, estimated from figure 9.5 ($L_{ex} = 0.05L$ for the incipient interactions and $L_{ex} = 0.1L$ for the separated cases). The profile traverses the reflected shock foot for $\frac{y}{H_i} = 0.6 - 0.8$. The incipient cases do indeed show a significant variation in the local flow deflection angle within the interaction of $\pm 2°$, whereas the angle for the separated cases is approximately constant. The deflection angle is slightly larger than the imposed flow deflection for the separated interactions (approximately 12° for the $\varphi = 9.5°$ interaction).

Figure 9.18 shows the iso-contours of the horizontal velocity fluctuations to verify whether this variation in angle can be to the dynamics of the mixing layer. The wall normal coordinate has been normalised according to the scaling proposed in figure 8.15 (see section 5.1) to highlight the region of peak turbulence intensities within the interaction. The dashed white line shows the flow deflection angles for each conditional state, deduced from figure 9.17
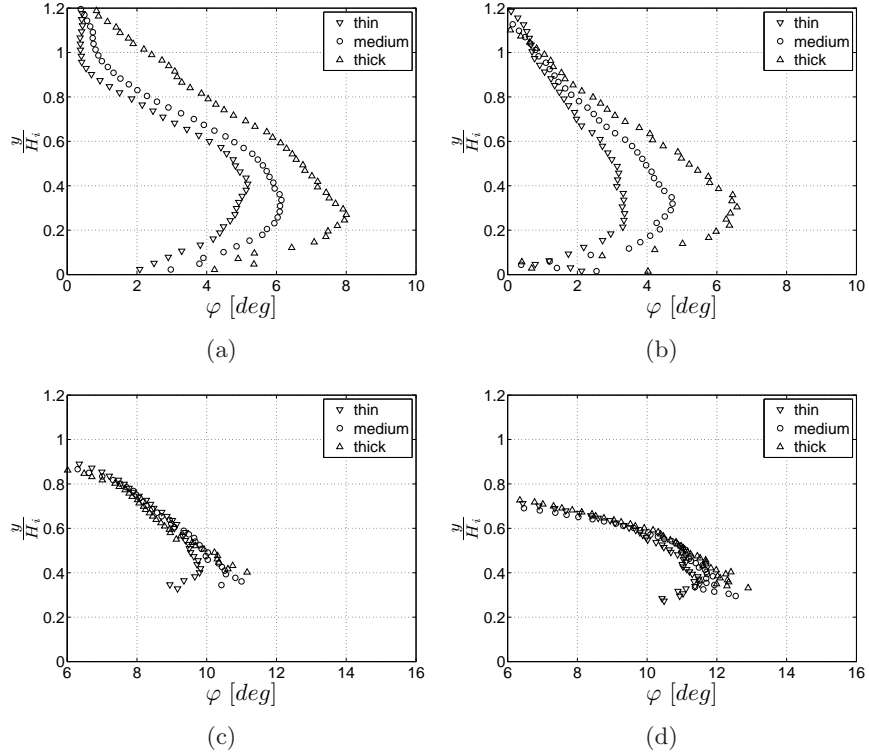
Figure 9.17: Profiles of the conditional flow deflection angle ($\tan(\varphi) = \frac{V}{U}$) at $X^* = 0.3$. High Reynolds case: (a) 6.0°; Low Reynolds case: (b) 5.5°, (c) 8.0°, (d) 9.5°. The wall normal coordinate is scaled by the conditional interaction height H_i, see equation 9.2.

and the solid white line indicates the deflection angle corresponding to the medium state. The streamwise location of all lines has been corrected for the conditional shock position determined using L_i, as defined by equation 9.2. The changes in the flow deflection for the incipient interactions can be attributed to a lifting of the mixing layer, which is practically attached to the wall for the thin state, whereas it is clearly detached from the wall for the thick state. This rotational motion of the mixing layer seems to be less severe for the separated interaction. Instead, the mixing layer appears to translate along the horizontal axis, following the shock excursions and imposing an approximately constant flow deflection. The elevation angle of the region of high turbulence intensities remains constant during this translation, at least for the initial part of the developing mixing layer. This does not prohibit that a flapping motion occurs after the initial development phase (as observed by Dupont *et al.* (2007)).

It is conjectured that the difference between a lifting motion of the shear

layer and a translating shear layer might be at the origin of the different flow separation probabilities observed in figure 9.1. It may be imagined that a mixing layer that shows mostly a lifting dynamics coincides with a flow that displays a large intermittency between an attached and separated state. On the other hand, it seems likely that a mixing layer that shows a translating motion requires a significant separation bubble to be present most of the time. This distinction could be in accordance with the definition of effective incipient separation, see Délery & Marvin (1986), which proposes that a flow is separated when the separation bubble is large enough to cause significant changes to the flow field. It could be that such a state is achieved when the shear layer starts to translate and hence causes large scale shock excursions, which likely requires a flow that is separated most of the time. This would coincide with a free interaction behaviour of the separation. Before the occurrence of a 'pure' translation, the lifting motion induces shock dynamics that contain a mix of translation and rotation, hence limiting the extent of the shock excursion amplitude, and leading to a flow that is attached for a large proportion of the time.

9.5 Shock dynamics mechanisms

A quasi-steady interpretation of the mass and momentum balance based scaling for the interaction length, see chapter 8, notably section 8.4, would lead to the conclusion that a change in the upstream boundary layer state (specifically δ_{in}^*) should be accompanied by a proportional change in the interaction length L, everything else being equal. This by merits of equation 8.24 on page 137, maintaining $\tilde{L} = \frac{L}{\delta_{in}^*}G_3(M_e, \varphi)+1 = cst$. Such a behaviour is illustrated by the blue dot (labeled '1') in figure 9.19 (representing the curve of figure 8.7(a) on page 143). This is of course only true if one assumes that the reflected shock motion response to δ_{in}^* variations constitutes a pure translation. Otherwise, there might be mechanisms at work that violate these model assumption. Such interaction length variations, at constant shock strength outside the boundary layer ($S_e = cst$), would lead to the behaviour that is schematised by the red arrows in figure 9.19 (labeled '2').

The results from section 9.4.6, in particular figure 9.17(d), show that for the separated cases the assumption of a pure translation for the shock motion is satisfied, since the flow deflection behind the shock is approximately constant. It however is evident that the dynamics are not determined by variations in the upstream boundary layer, most notably for the $\varphi = 9.5°$ interaction, by virtue of figure 9.6(d). Indeed, it was shown that the shock motion is caused by a pulsation of the separation bubble. Therefore, it must be concluded that for this interaction $\tilde{L} \neq cst$). The shock dynamics for this separated interaction can be represented as in figure 9.19, label '2'.

Concerning the incipient interactions, it has been shown that a mix of
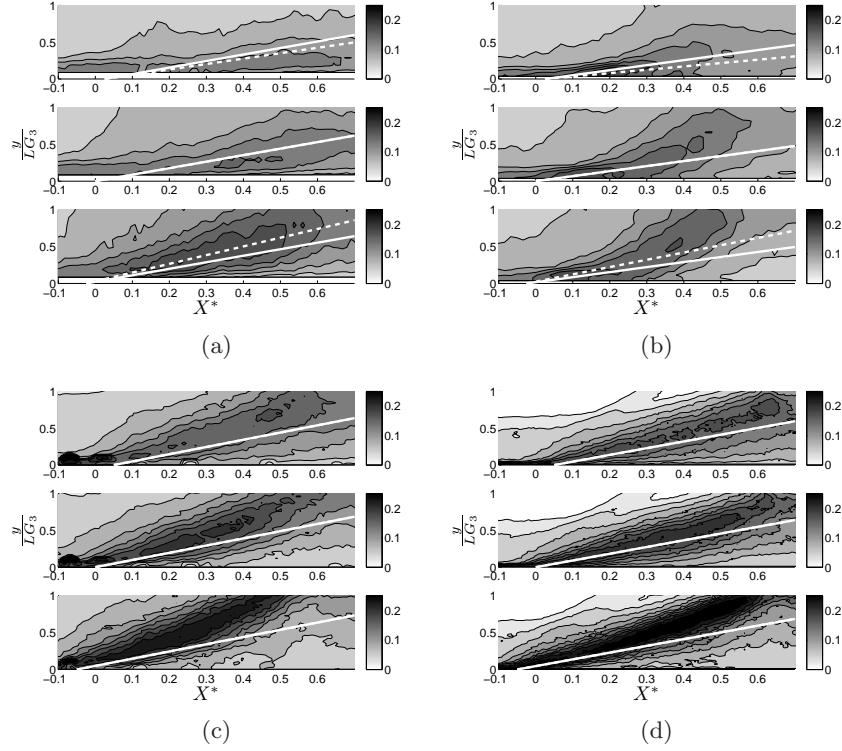
Figure 9.18: Iso-contours of the U-component fluctuations. High Reynolds case: (a) 6.0°; Low Reynolds case: (b) 5.5°, (c) 8.0°, (d) 9.5°. The wall normal coordinate is scaled as in figure 8.15 on page 155.

upstream and downstream effects is present. Based on equation 8.24, it can be estimated what the shock excursion amplitude should be for a pure translation if $\tilde{L} = cst$, for constant shock strength and in absence of downstream effects:

$$L_{ex} = \frac{\tilde{L} - 1}{G_3(M_e, \varphi)} \left(\delta^*_{in_3} - \delta^*_{in_1} \right) \tag{9.3}$$

Where the $\delta^*_{in_1}$ and $\delta^*_{in_3}$ represent respectively the 'thin' and 'thick' states from section 9.4.1. It is noted that $\frac{\tilde{L}-1}{G_3(M_e,\varphi)} = \frac{L}{\delta^*}$. Using the conditional displacement thicknesses reported in table F.1 in appendix F, one obtains: $L_{ex} = 0.3L$ for the high Reynolds case $\varphi = 6°$, and $L_{ex} = 0.1L$ for the low Reynolds $\varphi = 5.5°$ case. These values are over-estimated with respect to the results from figure 9.5 ($L_{ex} = 0.05L$ for the incipient interactions). This leads to think that the dynamical representation of a translating shock breaks down in the incipient cases, and that the reflected shock foot also changes in strength. This is in accordance with the varying flow deflection
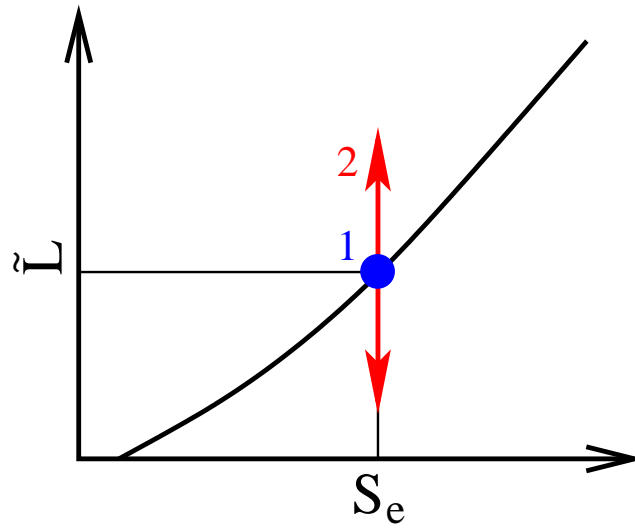
Figure 9.19: Proposed shock unsteadiness mechanisms based on the scaling results of figure 8.7(a).

angle in figures 9.17(a)-(b). This rotation of the shock limits the observed excursion amplitude with respect to a pure translation. The lifting motion of the mixing layer, inducing (local) change in the shock angle, constitutes another downstream mechanism that influences the interaction length such that $\tilde{L} \neq cst$ (see label '2' in figure 9.19). It is noted that this mechanism probably works locally on the shock foot. Such a reflected shock foot of changing strength is not necessarily in contradiction with a constant downstream external velocity (as has been observed experimentally). It is likely that the change in reflected shock strength also entrains a change in incident shock strength below the intersection point of both shocks and equally a change in expansion fan strength. The reflected shock 'far away' (after interaction with the expansion fan) is possibly of constant strength and exhibiting a translation dominated motion such that $\tilde{L} = cst$ (see label '1' in figure 9.19). Hence, even though the strength of the reflected shock foot changes, the strength of the total shock system likely remains approximately constant ($S_e \approx cst$).

Based on the above observations, the following proposition is made for the shock dynamics mechanisms at approximately constant shock intensity ($S_e \approx cst$): in absence of any downstream mechanisms influencing the interaction length, it may be expected that L varies proportionally with δ_{in}^* in response to large scale low frequency upstream effects, maintaining $\tilde{L} = cst$ (label '1' in figure 9.19). Two mechanisms have been identified that cause a (local) deviation from this purely upstream behaviour (label '2' in figure 9.19):
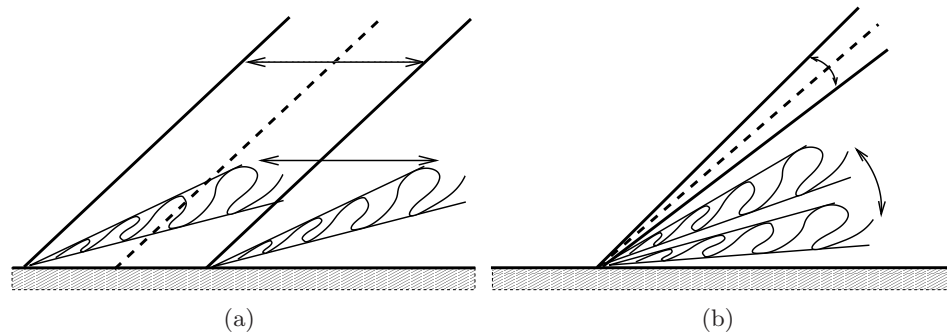
Figure 9.20: Shock dynamics mechanisms: (a) translational motion of the reflected shock at constant flow deflection angle; (b) a change in shock foot strength due to a non-constant flow deflection angle induced by a rotational motion of the mixing layer.

1. a translation of the reflected shock at constant flow deflection angle, induced by a separation bubble pulsation, see figure 9.20(a).

2. a rotation of the reflected shock, induced by a lifting motion of the mixing layer, leading to varying deflection angles downstream of the shock foot, see figure 9.20(b).

At large flow deflection angle interactions, the first mechanism seems to dominate. The shock foot is of constant strength, and the shock dynamics are dominated by a translatory motion such that $\tilde{L} \neq cst$. Such a motion would be in accordance with a free interaction behaviour as described in Délery & Marvin (1986). For the incipient interactions, the dynamics are dominated by the second mechanism. The pulsation of the retarded fluid zone is induced by a mix of upstream effects and the rotational motion of a mixing layer (both of which may be, but are not necessarily, linked). The flow deflection angle behind the shock foot is not constant. The shock motion consists of a combination of translation and rotation, again with $\tilde{L} \neq cst$. The shock rotation mechanism leads to smaller than expected shock excursions at the wall in comparison to a pure translation motion. For very weak interactions the mixing layer might be absent and hence no downstream mechanisms exists. In such cases, the shock motion could be governed uniquely by upstream effects, leading to a motion that maintains $\tilde{L} = cst$.

In the context of the debate on upstream and downstream effects, the passage of a streamwise elongated structure such as observed by Ganapathisubramani *et al.* (2007a) and Humble *et al.* (2009a), will induce a proportional change in L such as to keep $\tilde{L} = cst$, in absence of other mechanisms. One might imagine this as a low frequency pulsation of a stream

tube, in view of the results from appendix E. A shock motion imposed by downstream mechanisms such as proposed by Piponniau *et al.* (2009) implies that $\tilde{L} \neq cst$ (zero $\tilde{L}$ fluctuations). The conditional analysis results indicate that both mechanisms are at work and can occur simultaneously, depending on the shock intensity (the value of S_e).

9.6 Conclusions

From the different experimental results presented, some general features of the unsteadiness mechanisms developing in the shock boundary layer interactions can be deduced. First of all, it appears that when similar interactions are considered based on the flow reversal statistics (reverse flow iso-probability and bubble height), the unsteadiness observed in the interactions shows a large resemblance, whatever the Reynolds number.

Concerning the unsteadiness mechanisms, it has been shown previously that in the case of separated interactions, the low frequency shock dynamics are strongly correlated with the separation bubble pulsation. In the current work, two incipient cases were considered, without mean separation but with a large probability of instantaneous flow reversal. This has been done for Reynolds numbers based on the momentum thickness of respectively 5,000 and 50,000. In both incipient interactions, the development of large coherent structures downstream of the reflected shock foot has been put into evidence, with a very similar behaviour as compared to the separated cases. At the same time it has been shown that, despite the absence of mean separation, intermittent recirculation bubbles do occur, albeit with a very low probability (less than 4% of the realisations). In the case of such an event, a mild correlations with the reflected shock movements have been observed, which seems to be a reminiscence of the much stronger correlation observed for the fully separated interactions. At the same time, a slight correlation with the upstream boundary layer profile fullness has been observed. This dependence of the separation bubble on the upstream boundary layer, notwithstanding the fact that it is rather limited, is larger than for the separated cases. A stronger correlation is observed when considering the pulsation of the retarded fluid zone within the interaction, indicating that upstream mechanisms in their own right can also play a role in the unsteadiness for the incipient cases. Such a stronger correlation has not been observed for the separated interactions.

Considering the shock dynamics, the flow angle downstream of the shock foot has been observed to vary for small flow deflections (incipient interactions) and to remain approximately constant for large imposed flow deflection (interactions with significant separation). It appears therefore that the shock must display both a translatory motion as well as a rotational motion for weak shock intensities, whereas for large shock intensities, a preference

seems to exist for the translatory motion. The latter would be in accordance with free interaction behaviour. The rotational motion leads to smaller than expected shock excursions at the wall in comparison to a pure translation motion.

With respect to a purely upstream effect, the scaling of figure 8.7 appears to impose that the shock follows the low frequency (and hence quasi-steady) boundary layer state changes in order to maintain $\tilde{L} = cst$. In contrast, a downstream mechanism would inherently cause a change in the position of the vertical axis in figure 8.7, and hence $\tilde{L} \neq cst$. This behaviour has been schematised in figure 9.19. Depending on the shock intensity, the downstream mechanism appears to impose either a rotation (for incipiently separated flows) or a translation (for significantly separated flow) of the reflected shock.

It seems that similar mechanisms are present in both cases (separated or incipient), independently of the Reynolds number. On the contrary, the predominance of a particular mechanism for the shock unsteadiness (upstream boundary layer state or downstream separation bubble dynamics) appears to depend on the mean state of the interaction. It is therefore conjectured that the resulting frequency spectrum of the overall unsteadiness can be considered as the consequence of different characteristic time scales with a weighting function depending on the state of the flow:

- when no separation occurs at all, upstream events are expected to govern the flow unsteadiness entirely, with rather high frequencies; $\tilde{L} = cst$;

- when separation occurs most of the time, downstream unsteadiness, related to the separation bubble pulsation, will become predominant and involve very low frequencies; $\tilde{L} \neq cst$ and the initial part of the mixing layer translates at a constant elevation angle, imposing a constant flow deflection angle and shock dynamics that are governed by a translating motion;

- finally, for the incipient cases, there is a superposition of different mechanisms, involving time scales which can differ by at least one decade; this will produces spectra that are more or less similar to separated ones, depending on the extent of flow separation; $\tilde{L} \neq cst$ and the mixing layer shows a lifting motion, imposing variations in the flow deflection angle, and shock dynamics that constitute a mix of translation and rotation.

Chapter 10

Conclusions

An experimental investigation has been made into the mean flow topology and the unsteadiness mechanisms governing incident reflected shock wave turbulent boundary layer interactions. To this aim, an extensive comparison has been made between different interactions at a variety of flow conditions: a Mach 1.7 incipient interaction at a high Reynolds number ($Re_\theta = 50,000$) and a number of Mach 2.3 interactions of varying shock intensity at low Reynolds number ($Re_\theta = 5,000$) with possibility of control by means of an array of air jet vortex generators. A large amount of data has been collected using several measurement systems: particle image velocimetry (notably 2C-PIV, 3C-PIV and Dual-PIV), Schlieren visualisations and hot wire anemometry (HWA). Highly consistent results were obtained for multiple interactions by means of a range of flow diagnostics techniques, increasing the confidence in the validity of the results and enabling a comprehensive physical analysis. The application of the Dual-PIV technique in a supersonic flow has been demonstrated. A full field temporal classification shows that characteristic time scales spanning almost three orders of magnitude are present within the high Reynolds shock wave boundary layer incipient interaction. The existence of low frequency shock dynamics has been put into evidence.

An analysis of the acquired data has put in evidence that multiple mechanisms are at work in both incipient and separated interactions, irrespective of the Mach number and the Reynolds number. The generation and successive shedding of large coherent structures has been demonstrated for the incipient interactions, also in absence of instantaneous flow separation. For the incipient cases, a link has been put into evidence between the pulsation of the retarded fluid region within the interaction, the shock unsteadiness, and the state of the upstream boundary layer. It is proposed that the relative importance of the different mechanisms shifts with the imposed shock intensity. For interactions without instantaneous flow separation, upstream events are likely to govern the flow unsteadiness completely, with rather high frequencies. When separation occurs most of the time, downstream

unsteadiness, related to the separated bubble pulsation, will become predominant and involve very low frequencies. For the incipient cases, there is a superposition of different mechanisms, involving time scales which can differ by at least one decade; this will produces spectra that are more or less distinct from the separated ones, depending on the rate of flow separation.

The experiments with flow control confirm this view. The air jet vortex generators reduce the separation bubble size by approximately $24 - 44\%$. The interaction length is only mildly affected. However, notwithstanding the important modifications to the upstream boundary layer, the separation bubble could not be suppressed. The increase in frequency of the shock unsteadiness by 50% can be linked directly to the decrease in separation bubble size. This is in accordance with shock dynamics that are governed by downstream conditions.

A scaling analysis was made, aimed at reconciling the observed discrepancies between interactions documented in literature (geometry, Reynolds number effects, Mach number effects, shock intensity, ...). As part of this analysis, a separation criterion has been formulated that depends on the free-stream Mach number and the flow deflection angle only. It successfully classifies the separation states for a large scope of documented interactions (compression ramp and incident reflecting shock) over a large Reynolds number and Mach number range:

$$
\begin{aligned}
S_e &= \frac{\Delta p}{\frac{1}{8}\rho_e U_e^2} \qquad\qquad\qquad (10.1)\\
S_e &< 1 \quad \text{Attached flow}\\
S_e &\approx 1 \quad \text{Incipient separation}\\
S_e &> 1 \quad \text{Separated flow}
\end{aligned}
$$

In addition, a scaling approach has been derived for the interaction length based on the mass balance:

$$
\tilde{L} = \frac{L}{\delta_{in}^*}G_3(M_e,\varphi) + 1 \qquad\qquad (10.2)
$$
$$
\text{with: } G_3(M_e,\varphi) = \frac{\sin(\beta)\sin(\varphi)}{\sin(\beta-\varphi)}
$$

The separation criterion S_e in combination with either of the normalisations $\tilde{L}$ represents a single trend line onto which all data for a large scope of documented interactions over a large Reynolds and Mach range fall together with a moderate scatter of approximately $\pm15\%$, which is of the same order as the measurement uncertainty. This curve is valid both for compression ramp interactions and for incident reflecting shock interactions. A similar formulation has be obtained from the momentum balance ($\hat{L}_1$). Both results are equivalent.

A scaling for the wall normal coordinate has been defined based on this scaling approach for the interaction length: $\frac{y}{LG_3(M_e,\varphi)}$. It produces a large resemblance in the geometric organisation of the mean and turbulent flow fields within the interactions for the considered flow cases, independent of the Mach number and Reynolds number and of the separation state.

The trend line obtained from the scaling analysis predicts that the only way to effectively eliminate a separation bubble (without massive separation) by means of upstream control is by decreasing the displacement thickness of the incoming boundary layer, since the tendency of the flow to separate is not very much affected if the free-stream flow conditions remain unchanged ($S_e \approx cst$). This view seems to be confirmed by the results with the air jet vortex generators.

A quasi-steady interpretation of the proposed scaling indicates that an upstream and a downstream mechanism do not act in the same way. It seems that a purely upstream mechanism should act such as to maintain $\tilde{L} = cst$ in the case of a translating shock of constant strength. A purely downstream mechanism leads to a shock motion with $\tilde{L} \neq cst$, since δ_{in}^* cannot be affected by downstream effects. Two downstream unsteadiness mechanisms have been observed:

1. a translation of the reflected shock at constant flow deflection angle, induced by a separation bubble pulsation, see figure 9.20(a).

2. a rotation of the reflected shock, induced by a lifting motion of the mixing layer, leading to varying deflection angles downstream of the shock foot, see figure 9.20(b). The strength of the total shock system remains however approximately constant.

It seems likely that weak interactions without instantaneous flow separation should be governed by upstream effects only. For incipient interactions, downstream effects start to occur, with the region of high turbulence intensities displaying mainly a lifting motion, producing a shock foot of varying strength. Interactions with significant flow separation show mainly a translating motion, producing a shock foot of constant strength, which is in accordance with a free interaction behaviour.

Concerning the Reynolds number and Mach number effects, it can be concluded that for turbulent boundary layers, the onset of flow separation is Reynolds number independent. It seems to be governed principally by the Mach number and the imposed flow deflection angle; an increase in Mach number tends to reduce the deflection angle for the onset of flow separation. The Reynolds number effects appear implicitly through the scaling of the interaction length by the displacement thickness of the incoming boundary layer. However, the interaction length is also governed by the Mach number through a correction factor that also involves the imposed flow deflection angle.

Chapter 11

Perspectives

As a results of this work, several perspectives are proposed. Of course, these are not exhaustive and they can only be suggestions in the hope of inspiring further research.

From a flow diagnostics point of view, the potential of the Dual-PIV technique can be further exploited by making space-time correlations, either based on a direct point-wise cross-correlation of the velocity data (or a single point with the full field) as investigated by Jöbsis *et al.* (2010) and Jöbsis (2009), or based on a correlation between a conditioning variable (bubble size, upstream boundary layer state) and the full velocity field. The possibilities of deducing a low–order dynamical system for the shock wave boundary layer interaction could also be explored in more depth, the limited dataset size at the optimal time delay being the limiting factor at the moment, see Lang (2008).

For turbulent interactions, the state of separation seems to be determined by the imposed flow deflection angle and the free-stream Mach number. A systematic documentation with a single separation criterion would therefore be of interest, sweeping the Mach number - Reynolds number - deflection angle state space. The criterion of appendix D is suggested, enabling a cross-comparison between PIV and CFD results. Concerning the spatial resolution, it is proposed to make the comparison at equivalent $\Delta X^* = \frac{\Delta X}{L}$ and $\Delta Y^* = \frac{\Delta Y}{LG_3(M_e,\varphi)}$. In parallel, the interaction lengths should be documented using a single criterion, derived from flow visualisations. The same verifications should be made for heated and cooled walls. This will add more data to the trend line of figure 8.7(a) on page 143 and give indications as to the range of its applicability, in addition to confirming the validity of the suspected equivalence of the separation state for different Mach numbers and flow deflection angles, as indicated by figure 8.9(a). At the same time, the prosed geometrical scaling for the wall normal coordinate merits a comparison including more cases, encompassing both compression ramps and incident reflecting shocks, and for more measurement conditions.

Concerning the control of interactions by upstream perturbations, it needs to be confirmed that the separation bubble can only be suppressed by diminishing the displacement thickness, since the separation state appears to be determined by external conditions. In addition, a further parametric optimisation of the jet array used in the current experiments is in place. One could think of for example the injection pressure, the injection speed (sonic versus supersonic jets), the injection angle and direction, the jet spacing, etcetera. Finally, one might investigate whether dynamic control with pulsed injection might increase its effectiveness.

It is necessary to formalise the relation between the non–dimensional interaction length (based on the mass balance) and the imposed pressure jump (represented by the separation criterion), as proposed by equation 8.2 on page 128. In other words, it should be determined how exactly the pressure jump acts to increase the displacement thickness of the boundary layer. This would enable predicting the interaction length as a function of the shock strength. The relation should be derived for all upstream boundary layer states (laminar, transitional, turbulent), hence for all Reynold number regimes in figure 1.16 on page 20. One should expect that at lower Reynolds numbers, viscous forces should gain in importance. It might hence be imagined that depending on the Reynolds number, the pressure jump should be scaled by a different combination of viscous forces and inertial forces, where inertial terms dominate in the turbulent regime, viscous terms dominate in the laminar regime, and that the transitional regime is governed by a mix of both terms. By definition, being derived from the mass balance, the proposed scaling of the interaction length cannot depend on the boundary layer state (laminar, transitional, turbulent). Contrary to what is shown in figure 1.15, it seems hence that the boundary layer state should be taken into account by the scaling of the pressure jump (the horizontal axis), while maintaining the same scaling for the interaction length (the vertical axis). In addition, it might be attempted to add other flow geometries as well by defining for each geometry an (equivalent) interaction length and pressure jump.

It was shown that for separated interactions, the shock foot dynamics are governed by a translatory motion, in accordance with free interaction behaviour, whereas in the case of incipient separation, the shock foot is of variable strength. A further clarification of these mechanisms and their implications is justified. This is particularly true for the incipiently separated interactions, where a mix of multiple effects seems to occur. The role of vortex shedding in absence of mean separation merits further investigation. The precise occurrence of the different mechanisms as a function of the shock strength (position along trend line of figure 8.7(a)) and their effect on the timescales for the shock unsteadiness needs to be made more explicitly. A tentative option is to link a prediction of the interaction length based on the trend line (as proposed above) to the model for the shock unsteadi-

ness frequency derived by Piponniau *et al.* (2009), since this model uses the interaction length as input. This would enable a direct prediction of the unsteadiness frequency based on the shock strength, at least for separated interactions.

As a general remark, there is a large potential in a more profound exploitation of combined experimental and numerical work, as promoted by the UFAST project. Numerical simulations now appear to give a good representation of reality. DNS (see for example Pirozzoli & Grasso (2006); Wu & Martin (2008)) and particularly LES (see for example Garnier (2009); Touber & Sandham (2009); Pirozzoli *et al.* (2009); Agostini *et al.* (2009); Larchevêque *et al.* (2009)) have become a useful research tool in combination with a cross–verification with measurements, making it possible to obtain results that are not attainable with experimental work alone, although wind tunnel measurements will remain indispensable.

Appendices

Appendix A

Data validation

Several verifications have been performed to validate the quality of the acquired datasets, both concerning the flow conditions and the measurement data. This appendix quantifies in the first place whether reproducible and stable operating conditions were attained during the measurements. It treats furthermore the optimisation of the statistical validation settings, as well as the consistency of the datasets. Finally, it details the achieved alignment accuracy of the Dual-PIV systems.

A.1 Flow conditions validation

To characterise the free-stream conditions of each flow facility, a number of verifications have been performed. For the high Reynolds number case, in the first place the stability of the tunnel operating point has been evaluated for the chosen flow conditions. Secondly, the stagnation temperature drift inherent to the blow down operation of the wind tunnel has been quantified. Thirdly, the consistency of the free-stream velocity measurements has been verified for the different datasets and the different runs. For the low Reynolds number case, the Mach number in the test section has been verified.

A.1.1 Operating point stability

To evaluate the stability of the operating point, the tunnel start/unstart has been evaluated for a range of operating conditions (stagnation pressure and Mach number) in the high Reynolds number TST-27 facility , see figure A.1. Note that the figure indicates the measured Mach number, which is approximately 0.05 lower than the Mach number setting of the tunnel. Unless specified otherwise, reference is made to the actual measured Mach number. The tunnel is well started when a stable flow is achieved with an attached shock system on the leading edge and a fully supersonic flow over
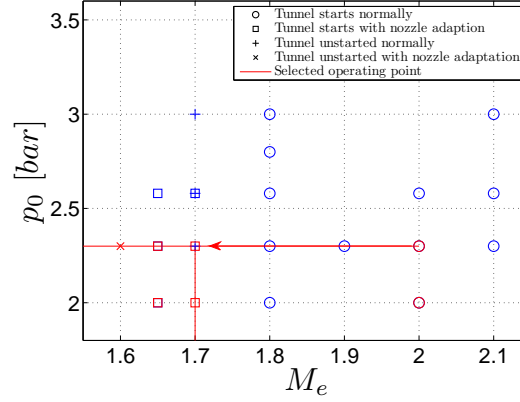
Figure A.1: Tunnel operating point selection; symbol colours indicate shock generator position (blue: initial position, red: final position)

both sides of the shock generator. The tunnel is unstarted when the shock system on the leading edge is detached with locally subsonic flow regions, hence not achieving a stable supersonic flow on either side of the model. This verification has been made for two shock generator positions. The tunnel start/unstart has been verified by means of the static pressure read-outs in the test section to see whether the desired Mach number is achieved. It was verified by means of PIV measurements that the final operating conditions corresponded to the topology for a well started flow.

The initial position of the shock generator in figure A.1 corresponds to the location used in previous Mach=2.1 experiments (see Humble (2009)). The final position corresponds to the location that has been selected for current experiments, see section 2.1. The tunnel start and unstart conditions did not vary noticeably between the two generator positions.

No dependence of the tunnel start on the stagnation pressure could be observed, leading to a preference for lower pressures to increase the total run time and to under standard operations. The facility is hence started at a higher Mach number, allowing an attached shock system to form on the model leading edge. The Mach number is then gradually reduced by means of the flexible tunnel nozzle, avoiding the transient effects of the low Mach number shock system formation at startup. Using this procedure, the unstart Mach number has been reduced to $M_e = 1.6$. It has been verified that the tunnel still starts using this procedure for a Mach number of $M_e = 1.65$ and for pressures as low as $p_0 = 2.0bar$. The tunnel start/unstart conditions with and without nozzle adaptation are shown in figure A.1.

The final operating point has been selected at $M_e = 1.7$ and $p_0 = 2.3bar$, taking a margin with respect to the tunnel unstart. It is indicated in figure
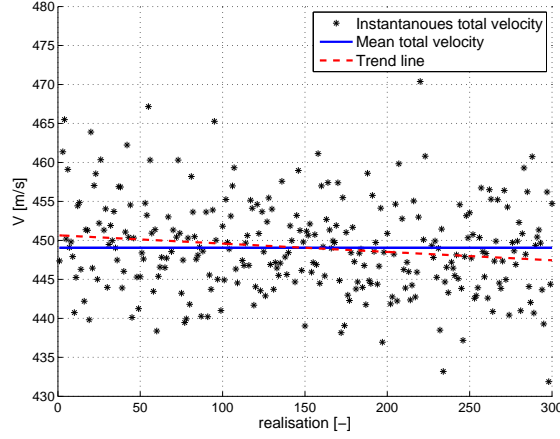
Figure A.2: Free-stream total velocity gradient

A.1 by the intersection point of the red lines. The red arrow indicates the startup procedure with the nozzle adaptation, starting from $M_e = 2.0$.

A.1.2 Stagnation temperature drift

The stagnation temperature for the high Reynolds number case. Due to the blow down operation of the TST-27, the temperature in the settling chamber will gradually decrease as a consequence of the expansion of the air in the supply vessel. This inherent drift has been quantified by considering a free-stream total velocity measurement by means of a linear trend based on a least squares fit. This has been done for a single run from the Panoramic dataset (ensemble size: 300 realisations). It has been verified that the Mach number and the total pressure (both controlled variables) remain constant throughout the run, based on the pressure read-out from the tunnel. The result is shown in figure A.2. Only the valid data has been taken into account.

The trend line indicates a decrease in total velocity of $3.2 ms^{-1}$, or 0.7% of the mean free-stream velocity, over the total run time (300 image pairs at $5Hz$, hence 60 second). This corresponds to a decrease in stagnation temperature of $3.9K$, or 1.4%, obtained through the isentropic relations and the definition of the speed of sound, see for example Anderson Jr. (1991), given the fact that the Mach number is constant. The velocity gradient is hence approximately $5 \times 10^{-2} ms^{-2}$, the stagnation temperature gradient is $6 \times 10^{-2} K s^{-1}$. Therefore, since the velocity gradient falls well within the range of measured free-stream fluctuations, and given its small magnitude, the effect of the stagnation temperature drift is concluded to be negligible.

A.1.3   Free-stream velocity and flow repeatability

In addition to the stagnation temperature drift, one might expect run-to-run variations in the flow conditions for a blow down wind tunnel. Therefore, the consistency and the repeatability of the free-stream velocity has been verified for all datasets and all runs of the high Reynolds number case. The mean free-stream velocity for each dataset has been determined per run (and per camera for the Dual-PIV case). Consecutively, the RMS variation of the mean velocity between the runs within each dataset has been computed to give an indication of the consistency of the obtained value.

A comparison of the free-stream velocity statistics is given in table A.1, for the different PIV datasets (see for reference table 3.2). In addition to the free-stream velocity, also the inferred total temperature is given (based on the Mach number $M_e = 1.69$, that is determined independently from wall-pressure measurements). It can be concluded that in all cases, the mean velocity within a dataset is very stable with run-to-run variations of the order of less than a percent of the free-stream velocity. This justifies combining data from different runs to obtain better converged statistics.

Table A.1: Free-stream velocity statistics.

	Dual			*Pano*	*IntZoom*	*BLZoom*
	Cam1	**Cam2**	**Combined**			
U_e mean $[ms^{-1}]$	445.8	449.3	448.2	433.5	421.1	397.2
RMS $[ms^{-1}]$	1.9	2.3	2.7	2.1	3.6	–
RMS [%]	0.4	0.5	0.6	0.5	0.8	–
$T_0[K]$			273.0	255.4	242.7	216.0
after correction for the pulse-delay error						
U_e *mean* $[ms^{-1}]$				*448.2*	*450.5*	*445.7*
$T_0[K]$				*272.9*	*277.8*	*269.9*

A significant discrepancy is detected, however, between the mean values of the free-stream velocity in the different experiments, with progressively lower values for the *Panoramic*, *Interaction Zoom* and *BL Zoom* datasets. Moreover, the inferred total temperature values are unrealistically low in view of the ambient storage conditions. Therefore, the agreement between the incoming boundary layer profile from each dataset has been verified, see figure A.3. Figure A.3(a) shows all available upstream boundary layer profiles, normalised by their proper free-stream velocity from table A.1 and by the boundary layer thickness ($\delta_0 = 17.2mm$). As can be seen, the profiles are self similar (discrepancies close to the wall are due to PIV measurement uncertainties). However, the velocity levels are different by a uniform multiplicative factor which is constant along the complete profile (approximately

(a)   (b)
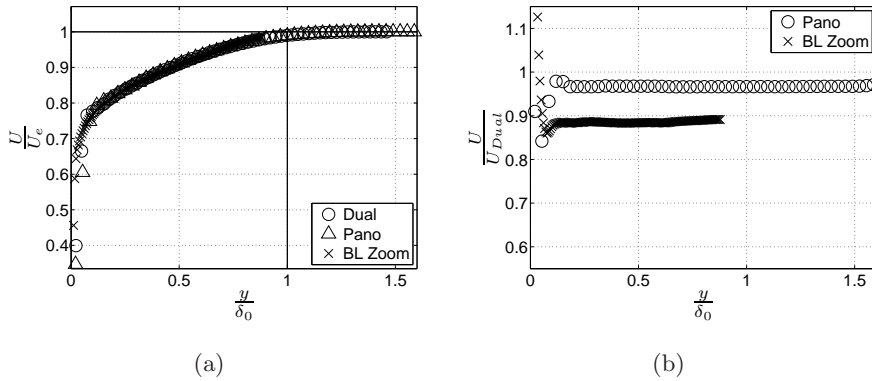
Figure A.3: Uncorrected boundary layer profiles; (a) similarity between the different profiles, (b) local velocity ratio of the *Pano* and *BL Zoom* profiles with respect to the Dual-PIV profile.

0.886 for the *BL Zoom* data and 0.967 for the *Pano* data), see figure A.3(b). It is remarked that the free-stream velocity for the *BL Zoom* data in table A.1, which is not directly measured, was obtained from a fit to the *Pano* velocity profile. The fact that profiles are self similar justifies this approach.

The fact that the profiles are identical up to a multiplicative factor in the velocity suggests that there is a bias in the pulse delay setting. Therefore, the set pulse delay has been plotted versus the free-stream particle displacement for each dataset, see figure A.4. The figure clearly shows that the particle displacement does not vanish for a zero time delay. There is a small bias in the otherwise perfectly linear trend (which is again a confirmation of the consistency between all datasets). Closer inspection of the three last datasets from table A.1, obtained at different values of the pulse delay, reveals that the trend of particle displacement with pulse delay time is consistent with a free-stream velocity of 448 m/s (which agrees well with the Dual-PIV data) but with a time-delay offset of approximately 65 ns. Correcting the free-stream measurements gives values for both velocity and total temperature that are very much in agreement with the Dual-PIV data (see table A.1 for the corrected values).

Although the existence of the time-delay offset has not been confirmed independently and its origin is unknown, this is the likely cause for the discrepancy observed above. The affected datasets were all acquired with the same version of the data acquisition software and pulse delay timer, whereas the Dual-PIV data were obtained with a newer version, which apparently is not (seriously) affected. The effect of the time-delay offset on the measurements is removed from the datasets by scaling them with the free-stream velocity. For consistency of the datasets, the nominal flow conditions in dimensional terms are based on the Dual-PIV results.
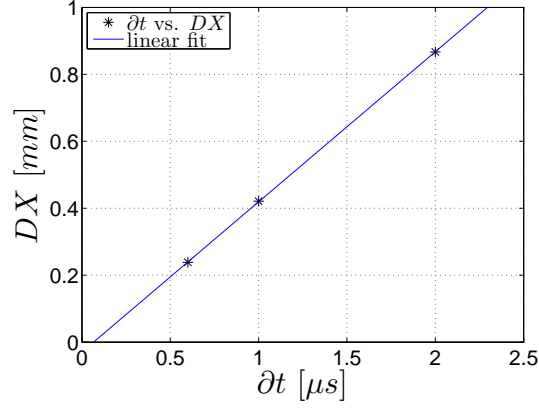
Figure A.4: Free-stream particle displacement versus set time delay.

A.1.4   Mach number verification

For the low Reynolds number case, the Mach number is determined by the fixed throat. The actual Mach number in the test section is also influenced by the correct installation of the wall piece. To verify the cleanness of the test conditions after the installation of the new set-up for the AJVGs (see section 2.3), a traverse has been made along the x-axis with a static pressure probe at $y \approx 60mm$ (the tunnel axis). Simulaneously, the stagnation pressure has been measured. The resulting Mach number has been deduced using the Rayleigh-Pitot tube formula, see for example Anderson Jr. (1991). The resulting mean and RMS results are given in table A.2, and the Mach number distribution along the tunnel centre line is shown in figure A.5.

Table A.2: Test section Mach number verification.

quantity	$p_o[kPa]$	$p_{pitot}[kPa]$	$M_e[-]$
mean	50.7	29.8	2.29
RMS	0.010	0.328	0.015
RMS [%]	0.02%	1.10%	0.63%

The stagnation pressure is a controlled quantity and it is therefore essentially constant. The pitot pressure and consequently the Mach number show some slight variations along the tunnel axis (note that the jump at $X = 260mm$ is due to the traversal of the incident shock). Most notably, there is a small irregularity in the distribution at $X = 100mm$. This peak is most likely due to a Mach wave originating from the start of the wall insert ($X = -38mm$), given the fact that the Mach angle is $sin^{-1}\left(\frac{1}{M_e}\right) = 25.9°$.
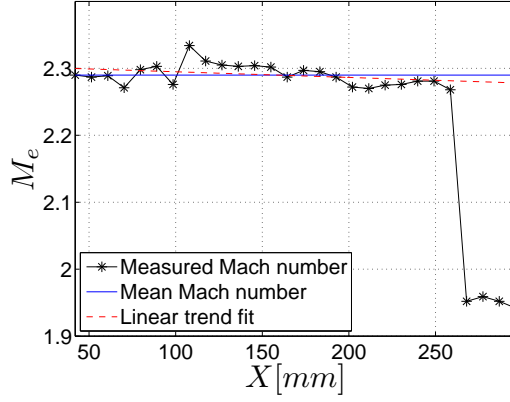
Figure A.5: Mach number distibution in the S8 test section.

There also seems to be a slight decreasing trend in the Mach number indicating a slightly adverse pressure gradient which might be caused by the growth of the boundary layer (not withstanding the fact that the section has a slight opening angle). The Mach gradient is $-8.4 \times 10^{-5} mm^{-1}$. Using the isentropic relations, see for example Anderson Jr. (1991), the corresponding pressure gradient can be obtained, see equation A.1, yielding a value of $5.5 \times 10^{-4} kPa/mm$. This is 0.5% of the pressure gradient imposed by the $\varphi = 9.5°$ interaction ($\frac{DP}{L} \approx 0.1 kPa/mm$). Given the small magnitude, the effect is concluded to be negligible.

$$\frac{\partial p}{\partial X} = \frac{\partial p}{\partial M}\frac{\partial M}{\partial X} = -\gamma p_0 M \left(1 + \frac{\gamma - 1}{2}M^2\right)^{\frac{1-2\gamma}{\gamma-1}} \frac{\partial M}{\partial X} \qquad \text{(A.1)}$$

A.2 Statistical validation

During all steps in the data-acquisition and data-processing, care has been taken to assure a sufficient data quality. This particularly in view of the generation of the databank input for the UFAST project (Doerffer (2007)). These data have been reported in Souverein & Van Oudheusden (2008); Souverein *et al.* (2008a). Apart from the consistency and reproducibility of the operating condition of the wind tunnel, the experimental set-up and the PIV-correlation and validation parameters (detailed in the chapter 3), the data quality also depends on the statistical validation settings. It was found that particularly the Reynolds shear stress is sensitive to a too strict setting of the validation parameters, yielding underestimated values. On the other hand, too loose validation settings yield noisy turbulence intensity measurements, depending on the quality of the source data. The Reynolds shear

stress, due to its nature, representing the correlation between the velocity
fluctuations, is less sensitive to measurement noise. It was therefore evaluated what the effect is on the Reynolds stress measurements of the choice
of the particular filtering method and the settings of the filter thresholds.
This is illustrated here for the vertical plane measurements, notably the low
Reynolds *VerZoom*-dataset.

Two filtering approaches were considered: the 'median' filter and the
'sigma' filter. Both approaches work along the same principle, that is, a
statistical threshold is imposed on the maximal allowed fluctuation value.
This is done as follows:

$$R(U_{i,j}) = \frac{U_{i,j} - E(U_{i,j})}{S(U_{i,j})} \leq \epsilon_{thr} \qquad (A.2)$$

Where (i,j) represent the spatial indices of the instantaneous velocity
measurement, and E and S the estimators for the mean value and the standard deviation of the quantity under consideration. In the case of the sigma
filter, these values are estimated using the ensemble mean and standard
deviation of the raw velocity data at each grid point. Hence:

$$R(U_{i,j}) = \frac{U_{i,j} - \overline{U_{i,j}}}{\sigma(U_{i,j})} \leq \epsilon_{thr} \qquad (A.3)$$

However, since the data incorporates measurement noise and outliers,
the values in equation A.3 can only be predictors of the actual ensemble
mean and standard deviation. In other words, the method requires prior
knowledge of the statistical quantities that are being computed ($\overline{U}$ and σ_u) in
order to estimate them. This poses a problem in case of relatively noisy data,
since the predicted standard deviation values will in general be overestimated
with respect to the actual value. To remedy this, several iterations can be
performed (in this case two) to obtain a better prediction.

As an alternative, one might use the median to estimate both the mean
value and the standard deviation as follows:

$$R(U_{i,j}) = \frac{U_{i,j} - median(U_{i,j})}{median\left(|U_{i,j} - median(U_{i,j})|\right)} \leq \epsilon_{thr} \qquad (A.4)$$

This filter needs no prior knowledge of the actual values of the mean
and the standard deviation. Large outliers do not bias the result since they
do not influence the median. This filter may hence be expected to be more
robust with respect to such erroneous vectors. As a general remark it is
noted that both filtering methods (sigma and median) are susceptible to
eliminating any sort of (extremely) rare physical events.

In the current implementation, the threshold for the sigma filter was
actually applied for each velocity component separately:

(a)

(b)   (c)
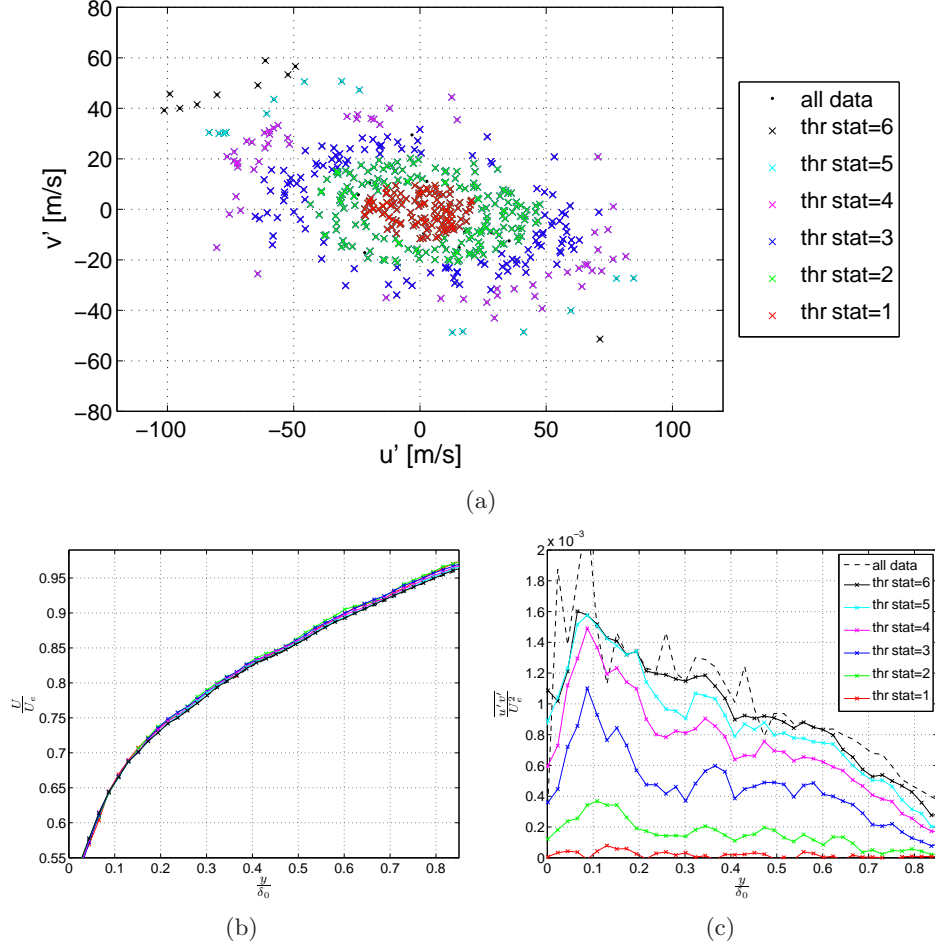
Figure A.6: Dependence of the statistical results on the threshold setting for the median filter: (a) u', v'-phase plot; (b) U/U_e; (c) $-\overline{u'v'}/U_e^2$. Colour coding corresponds to the threshold setting.

$$R(U_{i,j}) \leq \epsilon_{thr}; \quad R(V_{i,j}) \leq \epsilon_{thr}; \quad R(W_{i,j}) \leq \epsilon_{thr} \tag{A.5}$$

For the median filter, the threshold was applied to the norm of the fluctuation ratios:

$$\sqrt{R(U_{i,j})^2 + R(V_{i,j})^2 + R(W_{i,j})^2} \leq \epsilon_{thr} \tag{A.6}$$

This signifies that the sigma filter eliminates outliers by means of a rectangular contour in the velocity phase space, while the median filter eliminates erroneous data using a elliptical contour.

(a)

(b)

(c)
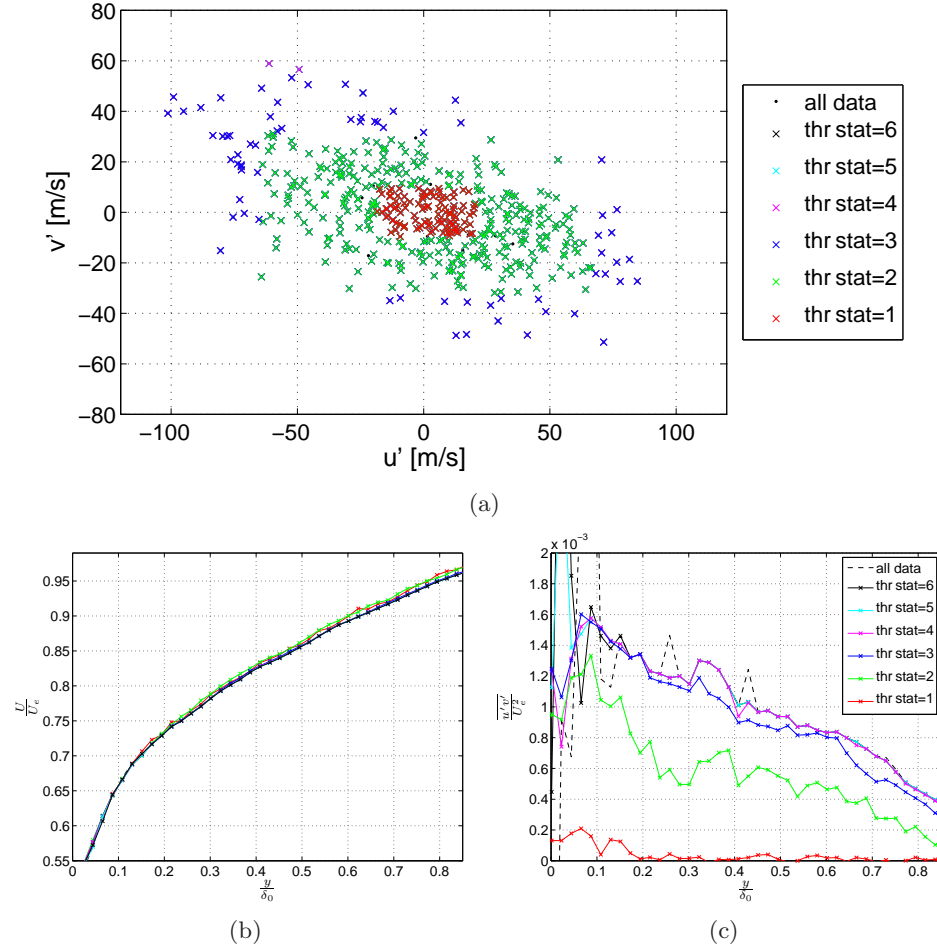
Figure A.7: Dependence of the statistical results on the threshold setting for the sigma filter: (a) u', v'-phase plot; (b) U/U_e; (c) $-\overline{u'v'}/U_e^2$. Colour coding corresponds to the threshold setting.

Figures A.6 and A.7 present the respective results for the median filter and the sigma filter. Comparing the phase plots of the U and V-fluctuations, see figures A.6(a) and A.7(a), the threshold value for the median filter should be set twice as large with respect to the sigma filter threshold to obtain a similar result. Furthermore, the elliptical and rectangular filter contours can clearly be observed. The colour coding indicates the part of the data that is retained for each threshold setting ('thr stat'). The entry 'all data' represents the results for a large threshold value (20 for the median filter and 10 for the sigma filter). The figures indicate that threshold values below $\epsilon_{thr} = 6$ for the median filter and below $\epsilon_{thr} = 3 - 4$ start to deteriorate

the central data cloud. Hence, it would be preferable to choose $\epsilon_{thr} \geq 6$ for the median threshold and $\epsilon_{thr} \geq 4$ for the sigma threshold. This has been confirmed for all datasets, and at multiple locations in the flow.

It has been verified what the effect is of the threshold values on the mean U-velocity and on the Reynolds shear stress in the upstream boundary layer. The result for the mean velocity is shown in figures A.6(b) and A.7(b) for the median and sigma filters respectively. It can be concluded that the mean velocity is insensitive to the threshold value. This is in agreement with experience. The Reynolds shear stress on the other hand, shown in figures A.6(c) and A.7(c), appears to be particularly sensitive to the filter settings. It is confirmed that the Reynolds shear stress is relatively insensitive to measurement noise when comparing the curves for 'all data' and the optimum filter settings. As can be observed, the values of the Reynolds shear stress quickly deteriorate for threshold values of $\epsilon_{thr} < 6$ for the medium filter and $\epsilon_{thr} < 3-4$ for the sigma filter. It is noted that this conclusion may equally well have its relevance to the optimisation of the neighbourhood filter in the iterative PIV-correlation process, which in general also makes use of a 'sigma' or 'median' like criterion (see for example Scarano & Riethmuller (1999)).

In general, it has been observed that the median filter is indeed more robust than the sigma filter when the data quality deteriorates. The former performs better, even for large threshold settings, whereas the latter gives more noisy results. This can be remedied by the application of a range filter before using the sigma filter. The median filter does not require range filtering, even for data with many erroneous vectors.

As a final remark, it is noted that the validation rate has been properly taken into account in the computation of all statistical quantities. This in order to prevent a bias in the results when one ensemble and/or variable has a larger validation rate than the other. This has been found particularly relevant for the time correlation results discussed in chapter 6, since they combine velocity measurements from two different sources (two PIV-systems were employed), with different validation rates.

A.3 Dataset self-consistency

It was furthermore verified that consistent results are obtained under the same measurement conditions, independent of the dataset and the particular PIV set-up. The results have been reported in amongst others Souverein & Van Oudheusden (2008) and Souverein *et al.* (2008a).

A.3.1 High Reynolds number dataset

The self consistency of the high Reynolds number dataset is verified by means of a comparison of the Dual-PIV data ensemble to those obtained
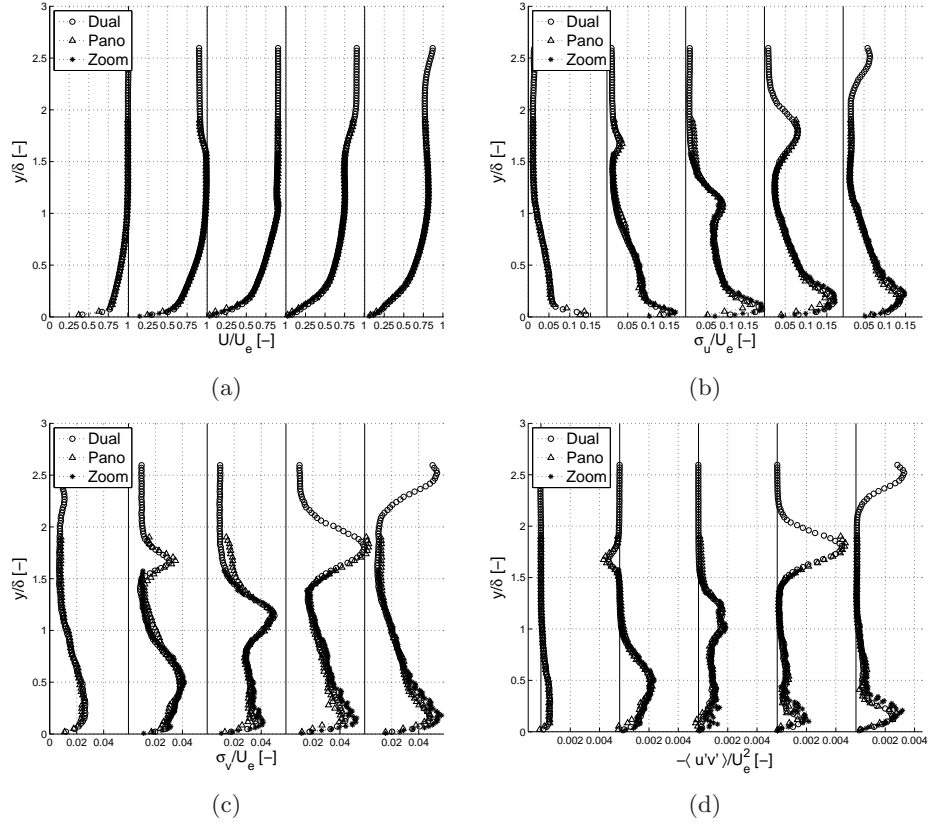
Figure A.8: Comparison of statistical profiles within the interaction region: (a) U/U_e; (b) σ_u/U_e; (c) σ_v/U_e; (d) $-\overline{u'v'}/U_e^2$. (From Souverein *et al.* (2008b).)

from the *Panoramic* and *Interaction Zoom* datasets, see table 3.2. Figure A.8 shows the statistical profiles at different stations within the interaction region. The profiles (from left to right) correspond to the incoming boundary layer ($x \approx -50mm$), the reflected shock foot ($x \approx -30mm$), the shock crossing point ($x \approx -20mm$), the vortex shedding region ($x \approx -10mm$) and the extrapolated incident shock foot ($x \approx 0mm$). A very good agreement is obtained for the mean velocity profiles. Some dispersion is observed for the V-component fluctuations and the Reynolds shear stress. This can however be attributed to statistical convergence uncertainties.

In summary, the datasets of the high Reynolds number case are found to be self-consistent. In addition, apart from the measurement points close to the wall, the results show no dependence of the flow quantities on the spatial resolution, see table 3.8. It may thus be concluded that the datasets are of consistent quality and that the same physical phenomena are observed in all datasets. In particular, the *IntZoom* data is in good agreement with the

other datasets. Therefore, the state of the incoming boundary layer (which cannot be evaluated directly for the *IntZoom* field of view) may be assumed identical to that of the other datasets.

A.3.2 Low Reynolds number dataset

The consistency of the obtained results for the horizontal and vertical plane measurements is verified, with and without air jet vortex generator control. The data under consideration concerns the *HorAJVG* and *VerAJVG* datasets, see tables 3.5 and 3.8. The Reynolds stresses for the *HorAJVG* were found to be biased due to a problem internal to the Dynamics Studio software. Since the source of the problem could not be corrected for by means of the analysis settings, the Reynolds stress values are not considered in the current work. The mean velocity data was not affected and will be compared to the *VerAJVG* dataset. The validation is based on the U and V-components of velocity (the W-component is not available for the *VerAJVG* dataset). The evaluations are made with and without AJVGs.

Firstly, the velocity measurement in the spanwise and the wall-normal directions are compared, see figure A.9. The comparison is made at $X = 260mm$, just before the reflected shock foot. The profiles for the different measurement planes are distinguished by the line types. For each sub-figure (A.9(a)-(d)), the left sub-plot shows the spanwise sections (along the Z-axis), and the right sub-plot shows the wall normal sections (along the Y-axis). The intersections of the wall-normal planes with the horizontal planes are represented by the symbols in the left sub-plot (distinguishing the height by mean of the different symbol types). The error-bars in the right sub-plot represent the standard deviation of the respective spanwise distributions for the horizontal planes, taken from the left sub-plot. A good agreement is obtained in all cases. The height of the *HorAJVG*-data-planes could be calibrated based on figure A.9(a). This has lead to a correction of $\Delta Z = -0.4mm$, and the actual height of the horizontal planes is hence $h = [0.6, 1.6, 3.6, 5.6]mm$.

A cross-comparison has also been performed in the lateral direction (along the X-axis), along the intersection lines between the planes. The result is shown in figure A.10 for the U-component and in figure A.11 for the V-component. The comparison has been made at the actual (calibrated) height given above. The extrapolated impact point of the incident shock is at $X = 337mm$. The figures also mention the 'set' height for reference. The solid curves (four in total, one for each measurement plane) represent the *VerAJVG*-data and the dashed lines (four in total) the corresponding *HorAJVG*-data. It is noted that the strong peaks in the U-component at $h = 1mm$ and $h = 2mm$ with jets on are induced by the jet array, which is located at $X = 212.5mm$. They are caused by wall reflection and a lack of seeding inside the jets. A particularly good agreement is obtained

for the case without control, where the curves collapse almost identically. Some dispersion is observed for the case with jets, which is caused by the strong spanwise velocity gradients induced by the streamwise modulation of the flow (see figures A.9(c)-(d)). An identical collapse of the curves can therefore not be expected as a consequence of the large sensitivity to small misalignments. Nonetheless, the agreement is reasonably good, since the data show the same trends.

In summary, the data from both AJVG datasets and all measurement planes are self-consistent. It may hence be concluded that the datasets are of consistent quality and that the same physical phenomena are observed. In particular for the 3D-PIV data (the *HorAJVG*-dataset) this means that the out-of-plane component (the V-velocity), the most difficult component to measure, is well resolved. By induction, it seems reasonable to assume that the remaining in-plane component (the W-velocity) is also correctly measured.

A.4   Dual-PIV camera alignment

Since the operating principle of the Dual-PIV system is based on the fact that the same field of view is observed with two individual cameras (see section 3.3.3), a verification is made of the mutual alignment of both cameras. In the ideal case, the alignment would be perfect and both cameras would have the exact same field of view, imaged at the same magnification factor. Hence, acquisitions at zero time delay between both systems would be identical to within the 2C-PIV measurement noise. The accuracy of the alignment is verified in the following sections. Firstly, the correspondance of the two camera images is quantified in terms of the image transformation parameters. Secondly, the statistical agreement between the data from each camera is verified. These results have been published in Souverein *et al.* (2009b).

A.4.1   Camera alignment accuracy

In setting up the Dual-PIV measurement system, particular attention was given to the alignment of the FOV of both cameras. The alignment of the cameras was assessed by means of the displacement field obtained for $\partial t_2 = 0\mu s$ and zero flow velocity (no airflow through the tunnel). The corresponding homogeneous deformation was obtained in terms of the dilatation, the rotation and the translation components according to Gurtin (1981), see equation A.7.

$$\mathbf{u} = (\mathbf{VQ} - \mathbf{I})\,\mathbf{x} + \mathbf{c} \qquad\qquad (A.7)$$

where $\mathbf{u}$ is the displacement field, $\mathbf{V}$ is the left stretch tensor, $\mathbf{Q}$ is the
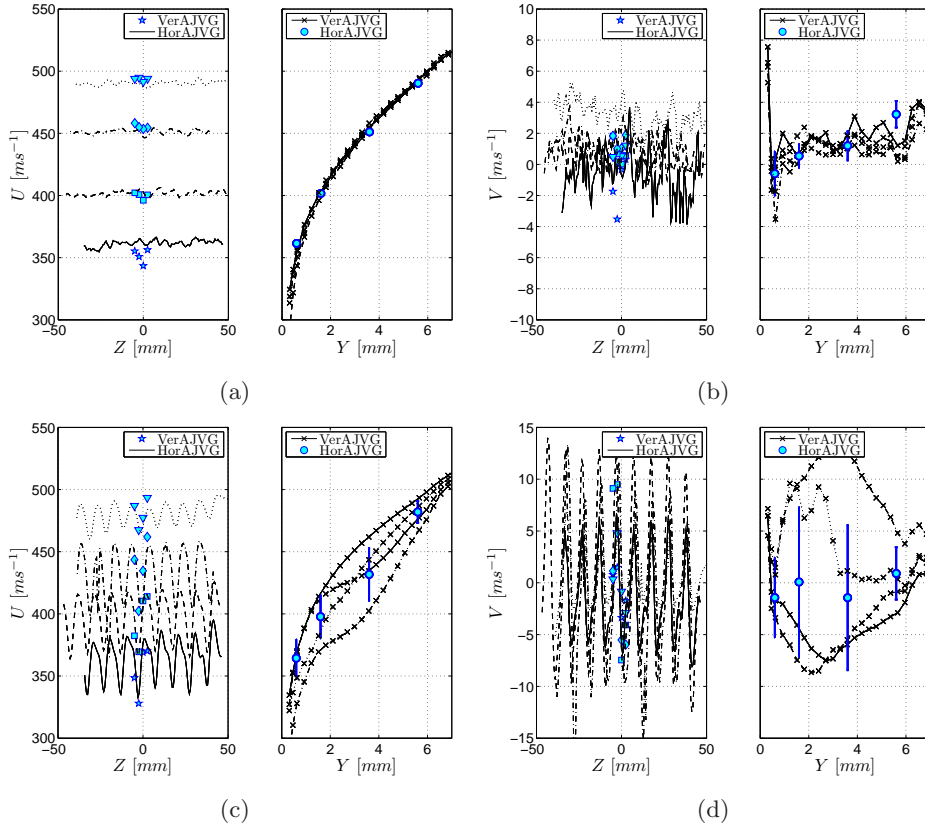
Figure A.9: Cross-comparison of the *HorAJVG* and *VerAJVG* datasets. Left sub-plot concerns the spanwise direction Z [mm], right sub-plot concerns the wall-normal direction Y [mm]. AJVGs off: (a) U-component, (b) V-component; AJVGs on: (c) U-component, (d) V-component.

rotation tensor, $\mathbf{I}$ is the unit tensor, $\mathbf{x}$ is the coordinate vector and $\mathbf{c}$ is the translation vector. With $\mathbf{u}$ and $\mathbf{x}$ provided from measurement, the aim is to determine $\mathbf{V}$, $\mathbf{Q}$ and $\mathbf{c}$. The following system of equations results when assuming an isotropic deformation field, see equation A.8.

$$\begin{bmatrix} u \\ v \end{bmatrix} = \begin{bmatrix} \lambda\cos\theta - 1 & -\lambda\sin\theta \\ \lambda\sin\theta & \lambda\cos\theta - 1 \end{bmatrix} \begin{bmatrix} x \\ y \end{bmatrix} + \begin{bmatrix} c_x \\ c_y \end{bmatrix} \tag{A.8}$$

This is an over-determined system with the measured displacement field components u and v and coordinates x and y in terms of the scalar parameters λ (dilatation) and θ (rotation), and the translation components c_x and c_y. Since the origin is not prescribed by the problem, it was chosen at the centre of the field of view, which is considered to be the approximate physical centre of dilatation. The corresponding nonlinear least-squares optimization problem was solved by means of the Levenberg–Marquardt algorithm (see
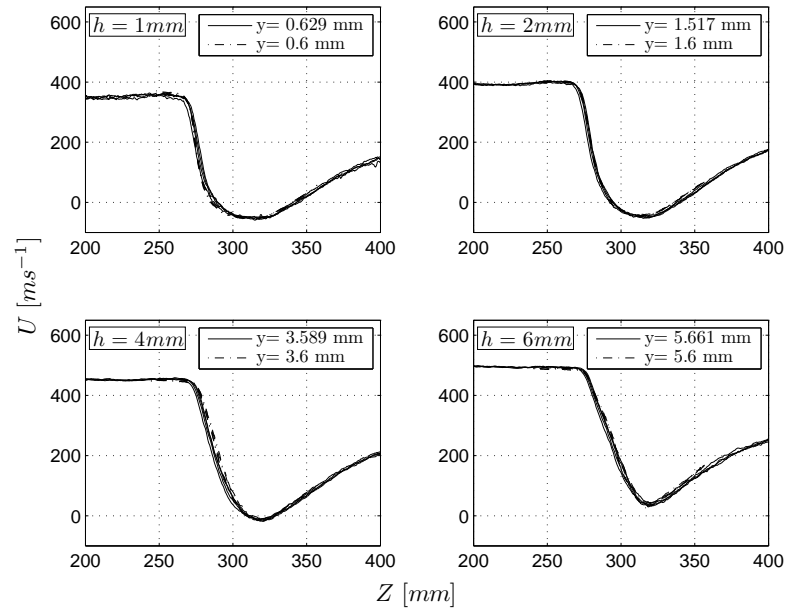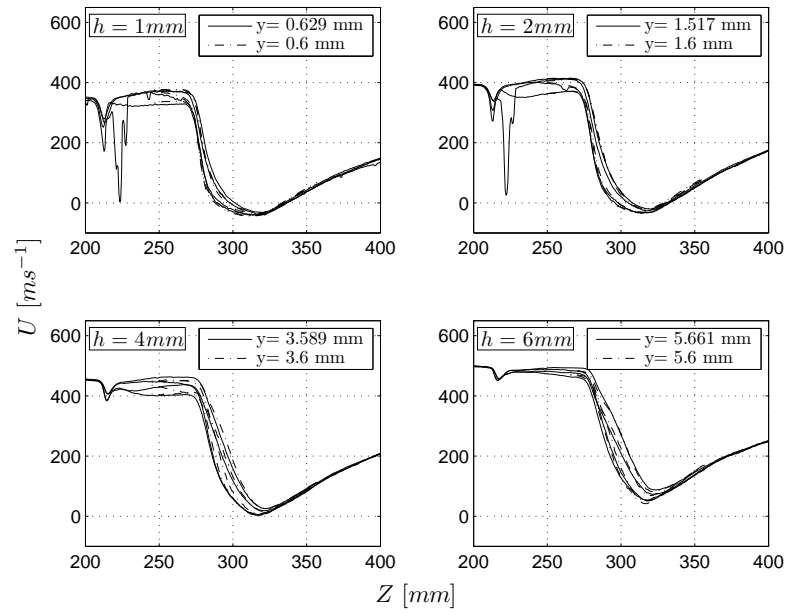
Figure A.10: Cross-comparison of the *HorAJVG* and *VerAJVG* datasets, *U*-component. Solid lines show vertical plane measurements, dashed-dotted lines indicate horizontal plane data. AJVGs off (a); AJVGs on (b).

(a)

(b)
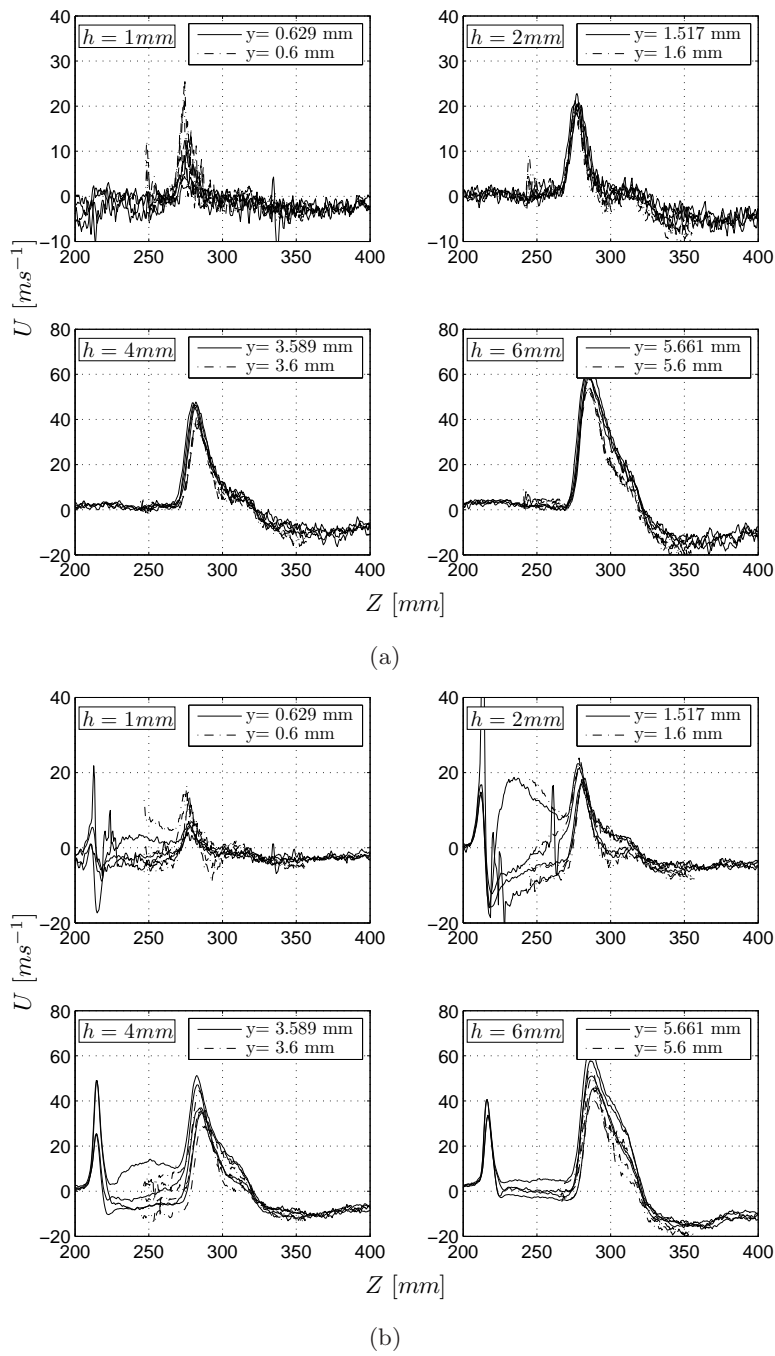
Figure A.11: Cross-comparison of the *HorAJVG* and *VerAJVG* datasets, *V*-component. Solid lines show vertical plane measurements, dashed-dotted lines indicate horizontal plane data. AJVGs off (a); AJVGs on (b).

Levenberg (1944) and Marquardt (1963)). Two approaches were followed: in the first place, the parameters of the deformation field were determined based on the mean displacement field (based on an ensemble of 75 realisations). Secondly, the same parameters and their mean and RMS values were also computed based on the instantaneous realisations. The deformation parameters thus obtained are listed in table A.3.

Table A.3: Dual-PIV homogeneous deformation results.

Parameter		Mean field based	Instantaneous fields based	
			Mean	RMS
λ	$[-]$	0.998	0.997	5×10^{-5}
θ	$[deg]$	0.052	0.049	0.005
c_x	$[pix]$	0.50	0.40	0.38
c_y	$[pix]$	-1.74	-2.34	0.66

Using the mean parameters based on the instantaneous velocity fields, the optimum interpolated deformation field was reconstituted. The computed displacement field based on the homogeneous deformation is found to be a good representation of the measured displacement field. A comparison of the reconstructed field to the measured field shows a discrepancy less than 1 pixel in absolute mean displacement.

Table A.3 shows that the difference in magnification and rotation between the two FOVs is negligible: the difference in magnification is in the order of 0.1% and the rotation is in the order of 10^{-2} degrees. Furthermore, both the magnification factor and the angular alignment between both cameras are very stable, as may be concluded from the RMS values in table A.3. The extremely small value of the RMS of the magnification factor may be considered a measure of the quality of the determination of the homogeneous displacement field parameters, since the magnification factor is *a priori* fixed by the camera objective lens, and the optical system is thought to be the least sensitive to vibrations in the out-of-plane direction. The horizontal and the vertical mismatch between the FOVs are in the order of 1 pixel with standard deviations that do not exceed 0.4 pixels and 0.7 pixels, respectively. In this respect it is reiterated that the location of the origin is not prescribed by the problem. Indeed, in Souverein *et al.* (2007a), the origin was taken in the top-right corner yielding an absolute displacement of 2.85 pixels, as opposed to 1.81 pixels for the values in table A.3 (mean field based). Depending on the choice of the origin within the FOV, the length of the vector **c** varies between the minimum value and the maximum value of the absolute misalignment (0.14 pixels to 4.3 pixels) with a mean value of 2.19 pixels. It may be concluded that the displacement mismatch is small as compared to the interrogation window size (31×31 pixels) and that the
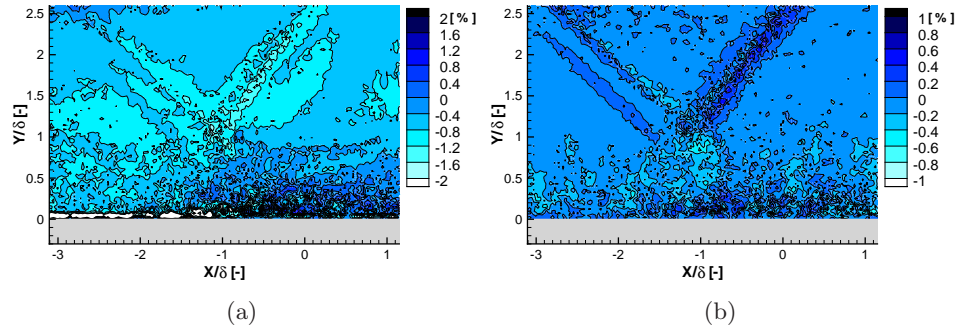
Figure A.12: Difference between mean flow statistics obtained from each individual camera (values are given in percentages): (a) $\Delta U/U_e[\%]$; (b) $\Delta V/U_e[\%]$. Statistics based on 2000 acquisitions per camera. Spatial coordinates normalized by the boundary layer thickness δ_{99}. Origin taken at the extrapolated incident shock foot. (From Souverein *et al.* (2009b).)

image of both cameras is dynamically stable to within a pixel accurate.

Based on this analysis it is concluded that the physical alignment of the cameras was made to such a degree of accuracy that an image dewarp is not required.

A.4.2   Inter-camera data consistency

Since the field of view for each indidivual camera for the Dual-PIV measurements is identical, the velocity statistics obtained from each PIV system should be identical to within the statistical convergence error. Therefore, a comparison has been made between the mean and fluctuation statistics obtained from each camera individually. The flow statistics obtained for the combined data from both cameras are discussed in full detail in chapter 5 (see figures 5.3(a)-5.7(a)).

Figure A.12 shows the difference in the mean velocity for both components ($\Delta U = U_1 - U_2$ and $\Delta V = U_1 - V_2$, where subscript numbers indicate the respective cameras), expressed as a percentage of the free-stream velocity (refer to figures 5.3(a) and 5.4(a) for the combined mean fields). The difference between the two U-component fields is practically constant in most of the flow. It shows a bias error of the order of 0.7% (or $3ms^{-1}$), which could be due to a small difference in camera alignment around the vertical axis (introducing a small viewing angle with respect to the flow plane) in combination with the slight difference in magnification mentioned in section A.4.1. It is noted that the magnification factor discrepancy alone, due to its small value, is insufficient to explain the bias. The largest velocity differences occur in the regions with large gradients and large fluctuations (the
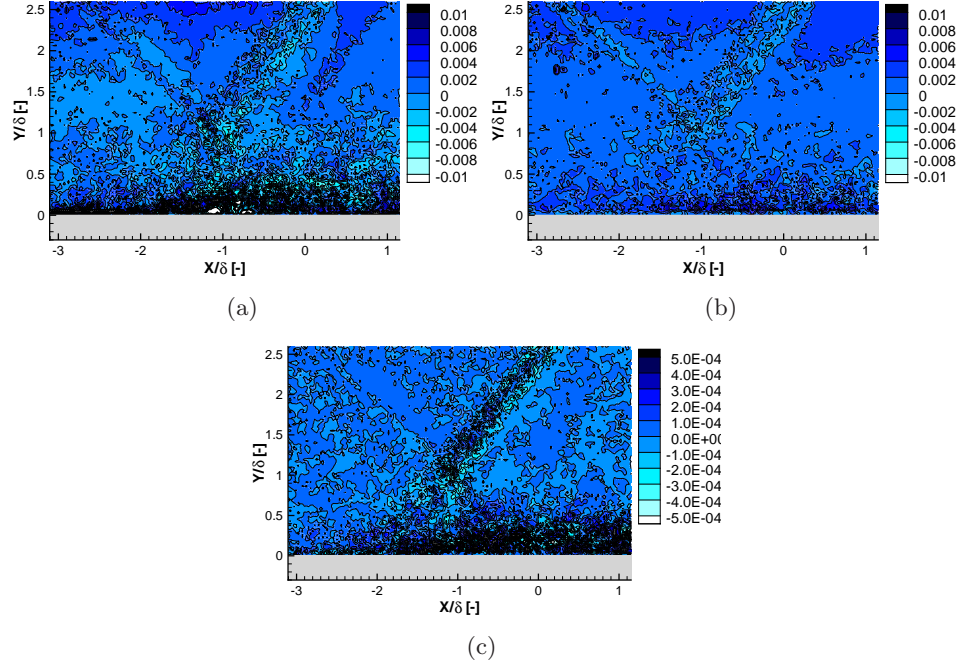
Figure A.13: Difference between fluctuation statistics and Reynolds stress obtained from each individual camera: (a) $\Delta\sigma_u/U_e$; (b) $\Delta\sigma_v/U_e$; (c) $\Delta\langle u'v'\rangle/U_e^2$. Statistics based on 2000 acquisitions per camera. Spatial coordinates normalized by the boundary layer thickness δ_{99}. Origin taken at the extrapolated incident shock foot. (From Souverein *et al.* (2009b).)

reflected shock, the boundary layer and the interaction region), notably in the incoming boundary layer close to the wall where the velocity profiles are the fullest. The near-wall deviations are typically below 4% ($18ms^{-1}$) and can be explained due to the combined action of the large velocity gradients close to the wall and the small misalignment mentioned in section A.4.1; these errors at the wall do not occur within the interaction where the velocity profiles are much less full. It is noted that this region does not extend more than $2mm$ away from the wall, which is approximately one iteration window size ($1.7mm$). It can be seen that the V-component is identical to within $0.1-0.2\%$ in most of the flow field. There is no observable bias error in the V-component in the free-stream.

Figure A.13 shows the difference between the measurements from both cameras of the fluctuation components (σ_u/U_e, σ_v/U_e and the Reynolds shear stress ($\Delta\langle u'v'\rangle/U_e^2$, where $\langle\rangle$ represents the mean). As for the mean flow above, the data from the second camera are subtracted from the data obtained with the first camera. Note that the legend values are not presented in terms of percentages to allow a direct order of magnitude comparison with

figures 5.5(a)-5.7(a). The velocity statistics from both cameras should again be identical, provided that statistical convergence is reached.

The differences in the fluctuation component statistics are very small, at least one to two orders ofmagnitude smaller than the local absolute values of the statistics (see figures 5.5(a)-5.7(a)), and may be largely attributed to measurement noise and the fact that convergence is not yet achieved due to the limited ensemble size. This is underlined by the fact that the autocorrelation of the velocity fluctuations in the external flow, particularly for the V-component, is systematically larger for the first camera as compared to the second while the measured fluctuation values are close to zero in this part of the flow (see figures 5.5(a)-5.7(a)). This is consistent with an increase in the measurement uncertainty introduced by remnant traces of laser pulses from the second system in the second exposure of camera 1 (see figure 3.4). The fact that these fluctuations are measurement noise is confirmed by the fact that the Reynolds shear stress in the potential flow regions is zero, as is the difference between both cameras of this quantity. The additional fluctuations are hence not correlated. Furthermore, the hypothesis that a limited statistical convergence is at the source of the differences is strengthened by the fact that the largest deviations occur within regions with large fluctuations (boundary layer, mixing layer and vortex shedding) and display a granular pattern with a structure larger than the order of magnitude of the misalignment between the images. It is remarked that the fluctuation statistics and the Reynolds shear stress require a larger ensemble size to converge than the mean flow quantities. This is especially the case for the latter, which shows the most granular nature of all quantities, particularly in the interaction region and the recovering boundary layer where the velocity fluctuations are the largest. The only systematic deviation that can be attributed to the shift is found for σ_u close to the wall in the incoming boundary layer at the same location where the maximum error in the mean U-component is found. This could be a result of a misalignment between the cameras since the autocorrelation of this component shows a very sharp rise close to the wall. It is hence particularly sensitive to small misalignments in this region, as is the mean U-velocity.

It is noted that the PIV measurement error on the velocity is approximately 0.1 pixel, or 0.8% of the free-stream velocity. Furthermore, the near-wall region (first iteration window) is a notoriously difficult region to obtain reliable PIV measurement, leading to increased measurement uncertainties and bias errors. Therefore it can be concluded that most of the deviations between the data from both cameras do not surpass the regular PIV measurement uncertainty level.

In conclusion, no significant tendency due to a misalignment affecting the topology and qualitative nature of the velocity statistics could be deduced from the above analysis. Small misalignments between the two cameras appear to affect mostly the flow within the first interrogation window next

to the wall; the results obtained from each individual system are identical to within the statistical convergence in all other relevant parts of the flow. It is therefore concluded that the data are of sufficiently high quality.

A.4.3   Conclusions

The physical alignment of the cameras has been verified by means of an evaluation of the homogeneous displacement field obtained from zero time-delay measurements. The alignment was found to be of high quality (translational mismatch of the order of 1 pixel with an RMS of less than 1 pixel, rotational mismatch of five hundredth of a degree and a constant discrepancy in the magnification factor of the order of a tenth of a percent). The inter-camera statistical data compatibility is high and differences seem to be governed by statistical convergence uncertainties and PIV measurement uncertainties rather than camera misalignments.

Appendix B

Downstream velocity distribution

The downstream flow conditions have been verified to examine the agreement with the values predicted by inviscid theory. This evaluation has been made for five datasets, see table B.1. Concerning the TUD6.0 and IUSTI5.5 datasets, large field of view data are used in stead of the *Dual-PIV* and *VerZoom* data respectively (see table 3.8 for details on these datasets) to evaluate the conditions as far downstream as possible. It was verified that the same results were obtained.

Table B.1: Datasets used for the estimation of L.

Short	Re_θ	M_e	φ	Dataset
TUD6.0	5×10^4	1.7	6.0°	Pano / Dual, see table 3.8
TUD8.0	5×10^4	2.1	8.0°	Humble (2009)
IUSTI5.5	5×10^3	2.3	5.5°	Large FOV / VerZoom, see table 3.8
IUSTI8.0	5×10^3	2.3	8.0°	Piponniau (2009)
IUSTI9.5	5×10^3	2.3	9.5°	Piponniau (2009)

The external velocity distribution, determined at the local edge of the boundary layer, is displayed in figure B.1. The local velocity attains a plateau value just behind the end of the interaction (at $X^* = 1$, indicated by the solid vertical line). The increase for $X^* > 2$ for the TUD data is due to the expansion fan emanating from the shoulder of the shock generator. The horizontal solid lines indicate the post-interaction velocity as predicted by oblique shock wave theory. As can observed, there is an overshoot of the measured velocity with respect to the theoretical value for most of the interactions, but it is limited to no more than 6% of U_e. This overshoot is probably due to an over-correction of the flow deflection by the expansion fan. A similar effect has also been observed experimentally and explained
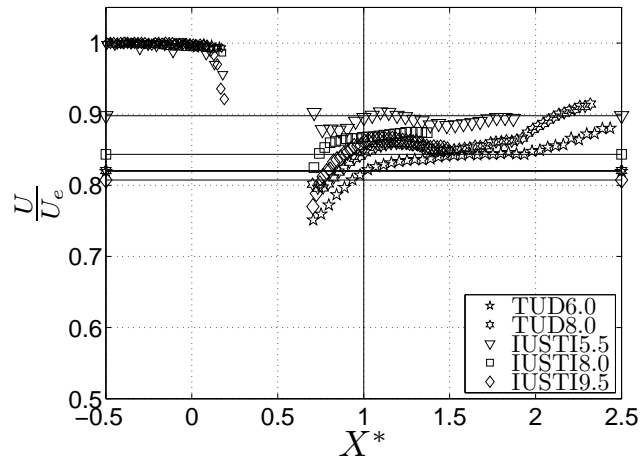
Figure B.1: Longitudinal upstream and downstream distribution of the local external velocity U.

theoretically for shocks on a curved wall, where a convex wall induces a post-expansion (see Ackeret *et al.* (1946); Lin & Rubinov (1948); Oswatitsch & Zierep (1960); Zierep (2003)). This makes the shock appear weaker than predicted by the Rankine-Hugoniot relations, hence leading to an overshoot in the post shock velocity. This phenomenon might be comparable to the over-correction observed here, since the separation bubble also induces a curved flow geometry. The discrepancy between the measured velocity and the predicted value is small however. It may therefore be assumed that the inviscid conservation model formulation is quite a reasonable approximation of reality for the considered flow cases.

Appendix C

Momentum conservation based scaling

In analogy to the mass conservation approach in section 8.3.2, the same analysis has been applied for the momentum conservation. This is done for both the incident shock reflection and the compression ramp case. In the end, a common formulation is derived. The implications of the momentum balanced based scaling are discussed in section 8.3.3. For completion, it is noted that the length scale for the momentum deficit is obtained by integrating the momentum flux within the boundary layer profile (with H the shape factor) as follows:

$$
\begin{aligned}
\frac{1}{\rho_e U_e^2} \int_0^\infty \left(\rho_e U_e^2 - \rho U^2 \right) dy \;\; &= \;\; \int_0^\infty \frac{\rho U}{\rho_e U_e} \left(1 - \frac{U}{U_e} \right) dy \qquad \text{(C.1)} \\
&\quad + \int_0^\infty \left(1 - \frac{\rho U}{\rho_e U_e} \right) dy \\
&= \;\; \theta + \delta^* = \theta(1 + H)
\end{aligned}
$$

Incident shock reflection

First, the incident shock reflection case is analysed. Evaluating the X-momentum equation over the control volume shown in figure 8.3 the following equality is obtained for the inviscid flow case:

$$
\rho_1 U_1^2 H_{cv} + \rho_2 U_2 V_2 L_{cv} - \rho_3 U_3^2 H_{cv} = (p_3 - p_1) H_{cv} \qquad \text{(C.2)}
$$

At the same time, the following equality is obtained for the case with interaction:

$$
\begin{aligned}
\rho_1 U_1^2 \left(H_{cv} - \theta_1(1 + H_1) \right) &\; + \\
\rho_2 U_2 V_2 \left(L_{cv} - L \right) &\; - \\
\rho_3 U_3^2 \left(H_{cv} - \theta_3(1 + H_3) \right) &\; = \; (p_3 - p_1)\, H_{cv}
\end{aligned}
\tag{C.3}
$$

Eliminating the pressure term, the following equation is obtained for the interaction length for the shock reflection case:

$$
L = \frac{\rho_3 U_3^2 \theta_3 (1 + H_3) - \rho_1 U_1^2 \theta_1 (1 + H_1)}{\rho_2 U_2 V_2}
\tag{C.4}
$$

In analogy to the result from the mass conservation approach, the interaction length obtained from the momentum conservation approach is completely determined by the upstream and downstream boundary layer momentum thickness and shape factor, the densities and velocities being specified by oblique shock wave theory. The equation is once again independent of the height and length of the control volume.

Compression ramp

Next, the compression ramp case is analysed. Evaluating the X-momentum equation over the control volume shown in figure 8.4 the following equality is obtained for the inviscid flow case:

$$
\rho_1 U_1^2 H_{cv_1} - \rho_2 U_2^2 H_{cv_2} \cos(\varphi) = (p_2 - p_1)\, H_{cv_1}
\tag{C.5}
$$

At the same time, the following equality is obtained for the case with interaction:

$$
\begin{aligned}
\rho_1 U_1^2 \left(H_{cv} - \theta_1(1 + H_1) \right) &\; - \\
\rho_2 U_2^2 L \sin(\varphi) \cos(\varphi) &\; - \\
\rho_2 U_2^2 \left(H_{cv_2} - \theta_2(1 + H_2) \right) \cos(\varphi) &\; = \; (p_2 - p_1)\, H_{cv_1}
\end{aligned}
\tag{C.6}
$$

Eliminating the pressure term, the following equation is obtained for the interaction length for the compression ramp case:

$$
L = \frac{\rho_2 U_2^2 \theta_2 (1 + H_2) \cos(\varphi) - \rho_1 U_1^2 \theta_1 (1 + H_1)}{\rho_2 U_2^2 \sin(\varphi) \cos(\varphi)}
\tag{C.7}
$$

Again, the interaction length obtained from the momentum conservation approach is completely determined by the upstream and downstream boundary layer momentum thickness and shape factor, the densities and velocities being specified by oblique shock wave theory. The equation is independent of the height and length of the control volume.

Common formulation

In analogy to the mass conservation approach, it is attempted to find a common formulation for equations C.4 and C.7. To this aim, the denominator of each equation is reformulated in terms of the upstream conditions by means of the oblique shock wave relations. Using the fact that the velocity tangent to the shock is conserved, the following equality is obtained:

$$U_1 \cos(\beta) = U_2 \frac{\cos(\beta - \varphi)}{\cos(\varphi)} \tag{C.8}$$

Similarly, considering mass conservation across the shock for the compression ramp case gives:

$$U_1 \cos(\beta) = U_2 \cos(\beta - \varphi) \tag{C.9}$$

Using equations 8.17 and 8.18, rewriting each of the equalities above and substituting all in their respective relations (equation C.4 for the incident shock interaction and C.7 for the compression corner) gives an equation of the same form, which can be written as follows when using the subscripts *in* and *out* for the inflow and outflow conditions respectively and when defining the momentum deficit as $I^* = \rho U^2 \theta(1 + H)$:

$$\frac{L}{\theta_{in}(1 + H_{in})} = g_3(M_e, \varphi) g_4(M_e, \varphi) \left(\frac{I^*_{out} C(\varphi)}{I^*_{in}} - 1 \right) \tag{C.10}$$

Where:

$$\text{Shock reflection:} \quad C(\varphi) = 1$$
$$\text{Compression ramp:} \quad C(\varphi) = \cos(\varphi)$$

And with $g_3(M_e, \varphi)$ a ratio of sinus functions, and $g_4(M_e, \varphi)$ a ratio of cosine functions:

$$g_3(M_e, \varphi) = \frac{\sin(\beta - \varphi)}{\sin(\beta) \sin(\varphi)}; \quad g_4(M_e, \varphi) = \frac{\cos(\beta - \varphi)}{\cos(\beta) \cos(\varphi)} \tag{C.11}$$

The factor $C(\varphi)$ appears in the compression ramp equation due to the definition of U_{out}: the X-momentum is considered, while the outgoing velocity is aligned with the ramp. The equation gives an alternative algebraic relation for the interaction length as a function of M_e, φ, the incoming boundary layer fullness, and the momentum deficit ratio between the incoming boundary layer and the outgoing boundary layer. In analogy to the mass conservation result, it can be concluded that the interaction length is also a direct consequence of the momentum deficit ratio between the incoming and outgoing boundary layer. The equation can again be interpreted in terms of a ratio between the upstream and downstream Reynolds numbers, assuming a constant wall temperature:

$$\frac{L}{\theta_{in}(1+H_{in})} = \tag{C.12}$$

$$g_3(M_e, \varphi)g_4(M_e, \varphi)\left(\frac{Re_{\theta_{w,out}}}{Re_{\theta_{w,in}}} \frac{(1+H_{out})U_{out}C(\varphi)}{(1+H_{in})U_{in}} - 1\right)$$

Where the Reynolds number is defined as follows:

$$Re_{\theta_w} = \frac{\rho_e U_e \theta}{\mu_w} \tag{C.13}$$

The ratio $\frac{U_{out}}{U_{in}}$ can be expressed in terms of M_e and φ through the oblique shock relations. Although less evident than for the mass conservation approach, the interaction length can still be non-dimensionalised in such a way that it expresses a ratio of Reynolds numbers by means of equation C.12.

Appendix D

Definition of incipient separation

Given the absence of mean separation but the occurrence of instantaneous separation for a significant portion of time, the high Reynolds $\varphi = 6.0°$ case and the low Reynolds $\varphi = 5.5°$ case have been classified as incipient interactions. Classically, incipient separation has been detected by means of a triple inflection point in the surface pressure distribution, or alternatively from the occurrence of stagnation points (separation and reattachment) in surface flow visualisations, see Délery & Marvin (1986). In this respect, a distinction is made between 'true' incipient separation, defined as the first appearance of a tiny separation bubble, and 'effective' incipient separation or significant separation, interpreted as the the occurrence of a separation bubble that is sufficiently large to produce significant changes in the flow field.

In the light of the use of PIV as the main experimental tool for investigating flow separation, and in absence of flow visualisations and wall pressure measurements, it might be useful to define a PIV-based criterion for incipient separation that fits the description above. As a first definition, one might consider the first occurrence of mean flow reversal. This is a rather discrete criterion however, that does not take into account the dynamics of the flow, nor the observed gradual (non-discrete) nature of the onset of separation, see Délery & Marvin (1986). The bubble height histogram and the flow reversal rate both seem to be good candidates, taking into account the flow dynamics. Both criteria however require additional statistical processing of the data and they are not well documented in literature.

It is therefore proposed to use the inverse of the turbulence intensity as a basis to define incipient separation for velocity field data. The use of the ratio $\frac{U}{\sigma_u}$ is not coincidental. It has a physical interpretation in terms of the normal distribution. Assuming a Gaussian distribution for the velocity fluctuations, the probability of occurrence of flow reversal is given by the

cumulative distribution function, which can be expressed in terms of the error function as follows:

$$
\begin{aligned}
F_{U,\sigma_u}(u) &= \frac{1}{\sigma_u\sqrt{2\pi}} \int_{-\infty}^{u} e^{-\frac{(u-U)^2}{2\sigma_u^2}} du \\
&= \frac{1}{2}\left[1 + \mathrm{erf}\left(\frac{u-U}{\sigma_u\sqrt{2}}\right)\right]
\end{aligned}
\tag{D.1}
$$

Substituting $u = 0$, the following relation is obtained:

$$
F_{U,\sigma_u}(0) = \frac{1}{2}\left[1 + \mathrm{erf}\left(\frac{1}{\sqrt{2}}\frac{U}{\sigma_u}\right)\right]
\tag{D.2}
$$

It is suggested to use the convention of equation D.3 to define the incipient separation limits. The advantage of this criterion is that it is based on standard PIV statistical data that is commonly available in literature. In addition, it represent the transitional nature of the occurrence flow separation, taking into account the dynamics of the flow.

$$
\frac{U}{\sigma_u} = R \;\; \text{with} \;\;
\begin{cases}
R > 1 & \text{Attached flow} \\
1 \geq R \geq -1 & \text{Incipient Separation} \\
R < -1 & \text{Separated flow}
\end{cases}
\tag{D.3}
$$

This criterion is applied to the flow field data, including the high Reynolds $\varphi = 8.0°$ case at $M_e = 2.1$ documented in Humble (2009), in figure D.1. The wall normal coordinate has been normalised by L, notice the difference in scale and colour map range for the incipient and separated interactions. The solid white line indicates the contour for $U = 0$, the solid black contour indicates the dividing streamline. Both are evidently absent in the incipient cases. The grey dashed lines with the black labels indicate the respective contours of the iso-probability of flow reversal from figure 9.1. By definition, $U = 0$ yields $\frac{U}{\sigma_u} = 0$, and the 50% flow reversal probability levels are found in the vicinity of this contour.

There is a direct link between the definition of incipient separation based on $\frac{U}{\sigma_u}$ and the reverse flow probability by the merits of equation D.2: $\frac{U}{\sigma_u} = 1$ yields a 16% probability of flow reversal, $\frac{U}{\sigma_u} = 0$ gives 50%, and $\frac{U}{\sigma_u} = -1$ gives 84% (or 16% attached flow). These values show a good agreement with the iso-contours of the separation rate in figure D.1. Only a slight discrepancy is observed for the 50% contour line. Therefore, assuming a Gaussian distribution seems a reasonable approximation. The resulting flow reversal probability contours are shown in figure D.2 for the low Reynolds $\varphi = 5.5°$ and $9.5°$ cases. The black and white solid line represent contours for $\frac{U}{\sigma_u} = 1$ and -1 respectively. The dashed lines for $\varphi = 5.5°$ show the
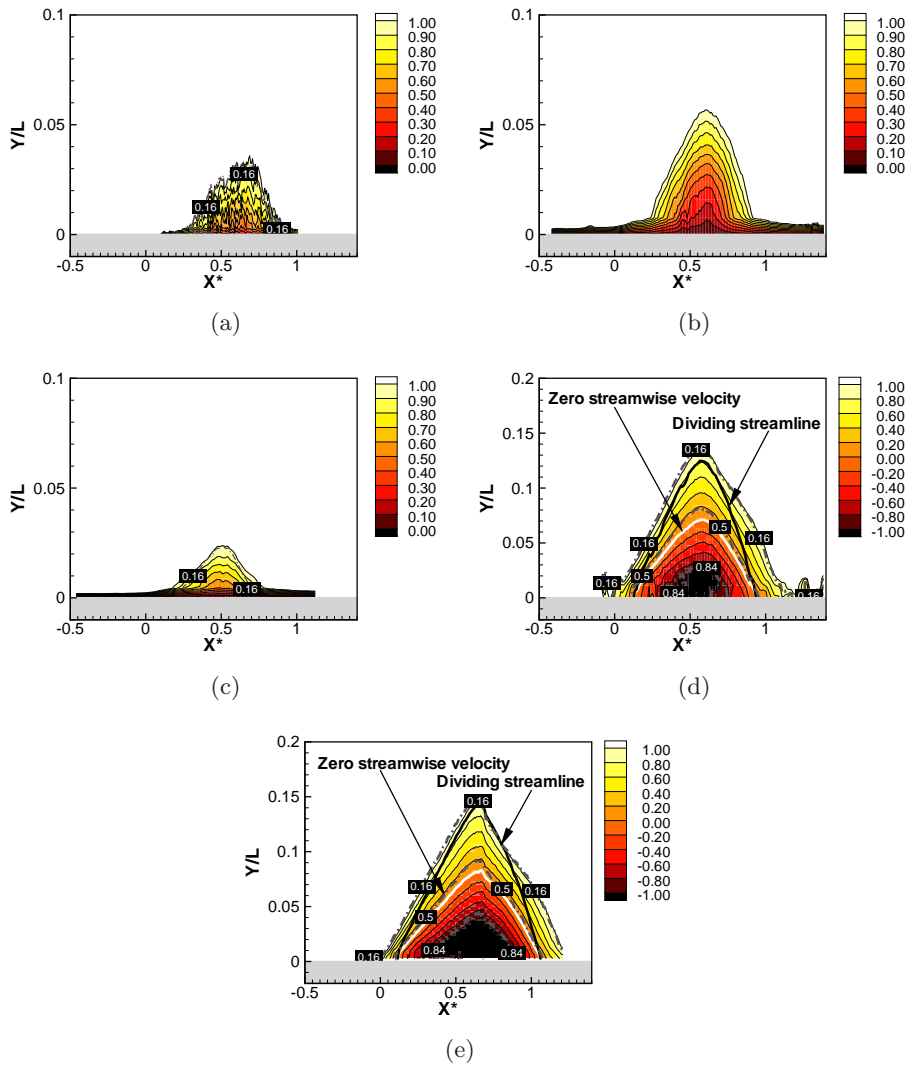
Figure D.1: Incipient separation criterion: high Reynolds number incipient cases, (a) 6.0° and (b) 8.0°; low Reynolds number incipient case, (c) 5.5°; low Reynolds number separated cases, (d) 8.0° and (e) 9.5°.

separation rate contours from figure 9.1 at 0.1, 0.2 and 0.3. Analogously, for $\varphi = 9.5°$, the contours for 0.1, 0.5 and 0.9 are shown.

Recalling the assumption of a Gaussian velocity distribution and referring to the definition in equation D.3, $R > 1$ represents flows that are attached 84% of the time, $R < -1$ signifies flows that are detached 84% of the time, and the intermediate values indicate flows that have a large intermittency of attachment/detachement. Even though for $-1 \leq R < 0$,

(a)   (b)
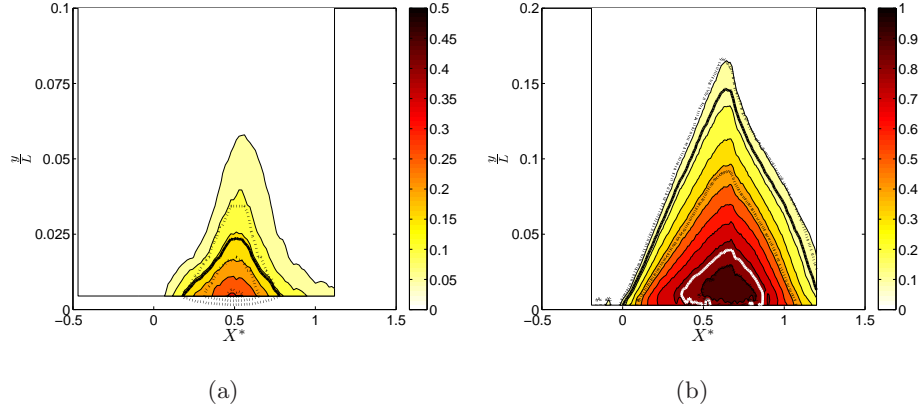
Figure D.2: Incipient separation criterion: flow reversal probability (filled contours, with in black the contour for $R = 1$ and in white the contour for $R = -1$) and comparison to the flow separation rate contours from figure 9.1 (selected dashed contours): low Reynolds (a) 5.5° and (b) 9.5°.

these flows do have a mean separation bubble, this bubble will be small, and the flow will be attached a significant portion of the time. It seems therefore fair to include them in the incipient separation 'range' in a symmetric manner to the flows with $0 < R \leq 1$. Given these considerations, flows with $R = 0$ could be considered 'true' incipient separation, and flows with $R = -1$ could be considered to start to display significant separation. The range $1 \geq R \geq -1$ represents the smooth and gradual transition between attached and separated flows mentioned in Délery & Marvin (1986). This interpretation of incipient separation is in accordance with the new scaling proposed for the interaction in figure 8.7, where the transition from attached to separated flow cases is also gradual. According to figure D.1 the high Reynolds $\varphi = 8.0°$ case would be slightly more detached than the high Reynolds $\varphi = 6.0°$ case, but without showing mean separation. This also corresponds with the behaviour predicted by figure 8.7. The two incipient cases under consideration here show again a large resemblance.

Appendix E

Correspondence between iso-flux and velocity fluctuations

It is possible to show that tracking changes in height of a streamtube of constant flux is directly liked to tracking velocity fluctuations at a height corresponding to a constant mean velocity (in other words: for a given mean streamtube). To demonstrate this, it is assumed that above a certain height, notwithstanding near wall deformations of the instantaneous profile, the profile shape remains approximately constant. Under this assumption, the changes in fullness of the profile can hence be interpreted as a translation in vertical direction of the same velocity profile shape. This model has been illustrated in figure E.1. This means that the flux inside the instantaneous streamtube of height h corresponds to the flux in the (non-translated) mean streamtube of height H. It is noted that this approximation only holds when the data has been filtered for small scale and/or high frequency fluctuations (either temporally or spatially). The following analysis is therefore particularly relevant when averaging over a certain streamwise distance, in other words, when considering variations due to large scale stream wise elongated structures.

It is recalled that the instantaneous iso-flux height is defined in terms of the constant mean iso-flux at height H, see equation 9.1: $\int_0^{h(\overline{Q}_H)} u\,dy = \overline{Q}_H$. This is equivalent to writing:

$$Q_h = \int_0^h U\,dy = \int_0^H \overline{U}\,dy = \overline{Q}_H \qquad (E.1)$$

Where Q is the instantaneous flux and $\overline{Q}$ is the mean flux, see also figure E.1, in particular $\overline{Q}_H$ is the imposed iso-flux value. Linearising the variation of the instantaneous flux in a streamtube contained between the varying height h and the fixed height H one can write:
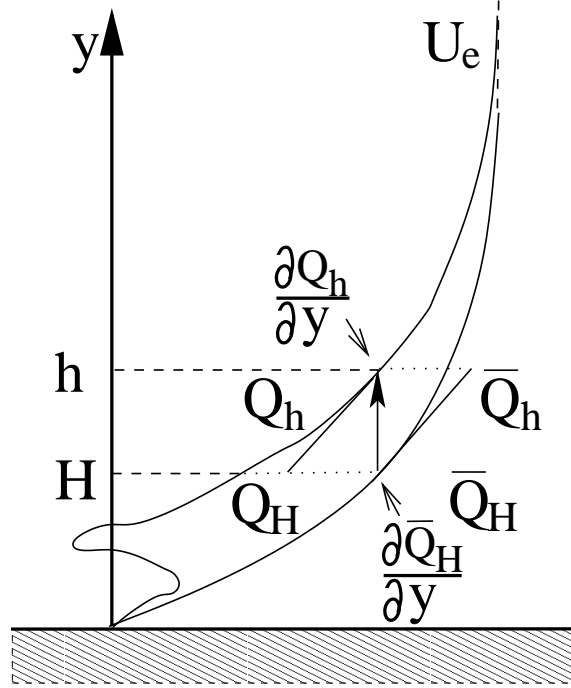
Figure E.1: Schematic model for iso-flux fluctuations.

$$Q_h - Q_H \approx \left.\frac{\partial Q}{\partial y}\right|_h (h - H) \approx \left.\frac{\partial \overline{Q}}{\partial y}\right|_H (h - H) \tag{E.2}$$

Note that the basic assumption concerning the velocity profile shape was used to approximate the gradient of the instantaneous flux in terms of the slope of the mean flux. The definition of the flux is now invoked:

$$Q_y = \int_0^y U\,dy \quad \Leftrightarrow \quad \left.\frac{\partial Q}{\partial y}\right|_y = U_y \tag{E.3}$$

$$\Rightarrow \quad \left.\frac{\partial \overline{Q}}{\partial y}\right|_H = \overline{U}_H$$

Equation E.2 can hence be rewritten as follows:

$$Q_H - Q_h = -\overline{U}_H(h - H) \tag{E.4}$$

Combining equations E.4 and E.1 gives:

$$Q'_H = Q_H - \overline{Q}_H = -\overline{U}_H(h - H) \tag{E.5}$$

Rearranging, the final result is obtained:

$$h' = h - H = -\frac{Q'_H}{\overline{U}_H} \tag{E.6}$$

In words, this equation means that an increase in height h' of a tube of constant flux ($\overline{Q}_H$, or iso-flux) is equivalent to a decrease in flux Q'_H for a tube of constant height H. The factor of proportionality is the mean velocity at height H (the mean tube height).

As a side-note, it is remarked that there is a link with the variations in displacement thickness. Taking H equal to the boundary layer thickness δ_0, and using equation E.3, one can write:

$$
\begin{aligned}
h' = h - \delta_0 \quad &= \quad -\int_0^{\delta_0} \frac{U'}{\overline{U}_e} dy \\
&= \quad \int_0^{\delta_0} \left(1 - \frac{\overline{U} + U'}{\overline{U}_e}\right) dy - \int_0^{\delta_0} \left(1 - \frac{\overline{U}}{\overline{U}_e}\right) \\
&= \quad \delta^* - \overline{\delta^*} = \delta^{*\prime}
\end{aligned}
\tag{E.7}
$$

The iso-flux height histogram for the mean boundary layer flux hence represents the variations in displacement thickness of the boundary layer.

The iso-flux can be linked to the conditional approach using variations in velocity in the incoming boundary layer as follows. In analogy to the iso-flux and referring to equation E.1, one can determine the instantaneous height h such that:

$$U_h = \overline{U}_H \tag{E.8}$$

Following the same approach as for the iso-flux, one can write:

$$U_h - U_H \approx \left.\frac{\partial U}{\partial y}\right|_h (h - H) \approx \left.\frac{\partial \overline{U}}{\partial y}\right|_H (h - H) \tag{E.9}$$

Combining equations E.8 and E.9 yields:

$$U'_H = U_H - \overline{U}_H = -\frac{\partial \overline{U}_H}{\partial y}(h - H) \tag{E.10}$$

Rearranging, the final result is obtained:

$$h' = h - H = -\frac{U'_H}{\frac{\partial \overline{U}_H}{\partial y}} \tag{E.11}$$

The increase in height h' of a line of constant velocity $\overline{U}_H$ is hence equivalent to a decrease in the observed velocity at a constant height H. The factor of proportionality is the wall normal gradient of the mean U-velocity at height H.

Since the iso-flux is defined as the integral of the velocity, it is not surprising to find a different factor of proportionality: for the former it is the mean velocity, for the latter it is the gradient of the mean velocity. Equations E.6 and E.11 demonstrate however that the iso-flux height and the velocity fluctuations are directly linked: under the current assumptions, an increase in height h' of the streamtube will lead to a decrease of the observed velocity at the fixed height H. It is therefore reasonable to assume that conditioning on either the velocity fluctuations or on the iso-flux height will give the same results.

Appendix F

Conditional boundary layer properties

Table F.1: Conditional incoming boundary layer properties for the optimal iso-flux, see section 9.4. States correspond to the three conditional cases: 1. shallow, 2. medium, 3. thick.

Short	case	δ_0 [mm]	δ_{ic}^* [mm]	θ_{ic} [mm]	H_{ic} [−]	δ^* [mm]	θ [mm]	H [−]	C_f [−]	u_τ [m/s]
TUD6.0	1	16.1	1.74	1.42	1.22	2.92	1.25	2.34	1.56×10^{-3}	15.4
	2	17.1	2.00	1.61	1.24	3.33	1.40	2.38	1.48×10^{-3}	15.0
	3	18.9	2.34	1.85	1.26	3.84	1.59	2.41	1.40×10^{-3}	14.6
IUSTI5.5	1	10.2	1.58	1.16	1.36	2.99	0.86	3.48	2.09×10^{-3}	24.7
	2	10.4	1.73	1.25	1.39	3.23	0.91	3.53	1.97×10^{-3}	23.9
	3	10.6	1.81	1.29	1.41	3.33	0.94	3.57	1.89×10^{-3}	23.5
IUSTI8.0	1	10.4	1.66	1.20	1.39	3.09	0.87	3.53	1.98×10^{-3}	23.7
	2	10.3	1.68	1.22	1.39	3.14	0.89	3.53	1.98×10^{-3}	23.7
	3	10.5	1.77	1.28	1.39	3.30	0.93	3.53	1.97×10^{-3}	23.6
IUSTI9.5	1	10.6	1.69	1.25	1.35	3.24	0.94	3.46	2.00×10^{-3}	23.8
	2	10.6	1.78	1.29	1.38	3.34	0.95	3.50	1.92×10^{-3}	23.3
	3	10.5	1.78	1.29	1.38	3.34	0.96	3.50	1.93×10^{-3}	23.4

Bibliography

ACKERET, J., FELDMANN, F. & ROTT, N. (1946). Untersuchungen an Verdichtungsstossen und Grenzschichten in schnell bewegten Gasen. *Mittelungen aus dem Institut für Aerodynamik*, **10**.

ADRIAN, R.J., MEINHART, C.D. & TOMKINS, C.D. (2000). Vortex organization in the outer region of the turbulent boundary layer. *Journal of Fluid Mechanics*, **422**, 1–53.

AGOSTINI, L., LARCHEVÊQUE, L., GARNIER, E. & DE MARTEL, E. (2009). Numerical study of three–dimensional modulations in a shock-induced separation. In *3rd EUCASS conference, Versailles, France, EUCASS2009-395*.

ALIZARD, F. & ROBINET, J. (2008). Influence of 3d perturbations in separated flows. In *Proc. IUTAM Symposium on Unsteady Separated Flows and Their Control*.

ANDERSON JR., J.D. (1991). *Fundamentals of Aerodynamics*. McGraw-Hill, New-York, 2nd edn.

ANDREOPOULOS, J. & RODI, W. (1984). Experimental investigation of jets in a crossflow. *Journal of Fluid Mechanics*, **138**, 93–127.

ARDONCEAU, P.L. (1984). The structure of turbulence in a supersonic shock-wave/boundary-layer interaction. *AIAA Journal*, **22**, 1254–1262.

ASHILL, P.R., FULKER, J.L. & HACKETT, K.C. (2001). Research at DERA on sub boundary layer vortex generators (SBVGs). In *39th Aerospace Sciences Meeting and Exhibit, Reno, Nevada, USA, AIAA-2001-0887*.

ATKIN, C.J. & SQUIRE, L.C. (1992). A study of the interaction of a normal shock wave with a turbulent boundary layer at mach numbers between 1.30 and 1.55. *European J. Mechanics*, **11**, 93–118.

BENKEMOUN, L. & SALAUN, M. (1988). Développement d'une couche limite turbulente supersonique sur une paroi chauffée: Propriétés du champ tubulent et exploitation théorique. Tech. rep.

BERESH, S.J., CLEMENS, N.T. & S.DOLLING, D. (2002). Relationship between upstream turbulent boundary layer velocity fluctuations and separation shock unsteadiness. *AIAA Journal*, **40**, 2412–2422.

BLINDE, P.L., HUMBLE, R.A., SCARANO, F. & VAN OUDHEUSDEN, B.W. (2009a). Effects of micro–ramps on a shock wave / turbulent boundary layer interaction. *Shock Waves*, **19**, 507–520.

BLINDE, P.L., HUMBLE, R.A., SCARANO, F. & VAN OUDHEUSDEN, B.W. (2009b). Effects of micro–ramps on a shock wave / turbulent boundary layer interaction. In *39th Fluid Dynamics Conference and Exhibit, San Antonio, Texas, USA, AIAA-2009-3714*.

BOURGOING, A. & REIJASSE, P.H. (2005). Experimental analysis of unsteady separated flows in a supersonic planar nozzle. *Shock Waves*, **14**, 251–258.

BRADSHAW, P. & WONG, F.Y.F. (1972). The reattachment and relaxation of a turbulent shear layer. *Journal of Fluid Mechanics*, **52**, 113–135.

BROADWELL, J.E. & BREIDENTHAL, R.E. (1984). Structure and mixing of a transverse jet in incompressible flow. *Journal of Fluid Mechanics*, **148**, 405–412.

BRUCE, P.J.K. & BABINSKY, H. (2008a). Unsteady normal shock wave boundary layer interactions with control. In *46th AIAA Aerospace Sciences Meeting and Exhibit, Reno, Nevada, USA, AIAA-2008-0721*.

BRUCE, P.J.K. & BABINSKY, H. (2008b). Unsteady shock wave dynamics. *Journal of Fluid Mechanics*, **603**, 463–473.

BRUSNIAK, L. & DOLLING, D.S. (1994). Physics of unsteady blunt-fin-induced shock wave/turbulent boundary layer interactions. *Journal of Fluid Mechanics*, **273**, 375–409.

BUENO, P.C. (2006). *The Effects of Upstream Mass Injection by Vortex Generator Jets on Shock-Induced Turbulent Boundary Layer Separation*. Doctoral thesis, The University of Texas at Austin.

BUENO, P.C., WAGNER, J.L., SEARCY, J.A., GANAPATHISUBRAMANI, B., CLEMENS, N.T. & DOLLING, D.S. (2006). Shock/turbulent boundary layer interactions: Review of recent work on sources of unsteadiness. In *44th AIAA Aerospace Sciences Meeting and Exhibit, Reno, Nevada, USA, AIAA-2006-0878*.

BUR, R., CORBEL, B. & DÉLERY, J.M. (1997). Study of passive control in a transonic shock wave/boundary layer interaction. *AIAA paper*.

Bur, R., Benay, R., Galli, A. & Berthouze, P. (2008). Experimental and numerical study of forced shock-wave oscillations in a transonic channel. *Aerospace Science and Technology*, **10**, 265–278.

Bur, R., Coponet, D. & Carpels, Y. (2009). Separation control by vortex generator devices in a transonic channel flow. *Shock Waves*, DOI: 10.1007/s00193-009-0234-6.

Chapman, D.R., Kuehn, D.M. & Larson, H.K. (1957). Investigation of separated flow in supersonic and subsonic streams with emphasis of the effect of transition. Tech. rep.

Cherry, N.J., Hillier, R. & Latour, M.E.M. (1984). Unsteady measurements in a separated and reattaching flow. *Journal of Fluid Mechanics*, **144**, 13–46.

Christensen, K.T. & Adrian, R.J. (2001). Statistical evidence of hairpin vortex packets in wall turbulence. *Journal of Fluid Mechanics*, **431**, 433–443.

Christensen, K.T. & Adrian, R.J. (2002a). Measurement of instantaneous eulerian acceleration fields by particle image accelerometry: method and accuracy. *Experiments in Fluids*, **33**, 759–769.

Christensen, K.T. & Adrian, R.J. (2002b). The velocity and acceleration signatures of small-scale vortices in turbulent channel flow. *Journal of Turbulence*, **3**, 1–28.

Clemens, N.T. & Narayanaswamy, V. (2009). Shock/turbulent boundary layer interactions: Review of recent work on sources of unsteadiness. In *39th Fluid Dynamics Conference and Exhibit, San Antonio, Texas, USA, AIAA-2009-3710*.

Cortelezzi, L. & Karagozian, A.R. (2001). On the formation of the counter-rotating vortex pair in transverse jets. *Journal of Fluid Mechanics*, **446**, 347–373.

Cousteix, J. (1989). *Turbulence et Couche Limite*. CEPADUE-Editions, Toulouse, 1st edn.

Debiève, J.F. (1983). *Etude d'une interaction turbulence- onde de choc*. Thèse d'etat, Université d'Aix-Marseille.

Délery, J.M. (1992). Etude expérimentale de la réflexion d'une onde de choc sur une paroi chauffée en présence d'une couche limite turbulente. *La Recherche Aérospatiale*.

Délery, J.M. (2000). A physical introduction to control techniques applied to turbulent separated flows. *AIAA paper*.

DÉLERY, J.M. & MARVIN, J.G. (1986). Shock wave - boundary layer interactions. Tech. rep.

DI CLEMENTE, M., MARINI, M., DI BENEDETTO, S., SCHETTINO, A. & RANUZZI, G. (2009). Numerical prediction of aerothermodynamic effects on a re-entry vehicle body flap configuration. *Acta Aeronautica*, **65**, 221–239.

DOERFFER, P. (2007). European research on unsteady effects of shock wave induced separation ufast-project. In *Proceedings of the 8th International Symposium on Experimental and Computational Aerothermodynamics of Internal Flows, Lyon, France. ISAIF8-0051*.

DOERFFER, P. & SZLUC, O. (2002). Shock wave strength reduction by passive control using perforated plates. *Journal of Thermal Science*, **16**, 97–104.

DOERFFER, P. & SZWABA, R. (2004). Shock wave- boundary layer interaction control by streamwise vortices. In *11th ICTAM Symposium; Warsaw, Poland*.

DOLLING, D.S. (2001). Fifty years of shock-wave/boundary-layer interaction research: what next. *AIAA Journal*, **39**, 1517–1531.

DOLLING, D.S. & OR, C.T. (1985). Unsteadiness of the shock wave structure in attached and separated compression ramp flows. *Experiments in Fluids*, **3**, 24–32.

DRIVER, D.M., SEEGMILLER, H.L. & MARVIN, J. (1987). Time-dependent behavior of a reattaching shear layer. *AIAA Journal*, **25**, 914–919.

DUPONT, P. & DEBIÈVE, J.F. (1992). A hot wire method for measuring turbulence in transonic or supersonic heated flows. *Experiments in Fluids*, **13**, 84–90.

DUPONT, P., HADDAD, C. & DEBIÈVE, J.F. (2006). Space and time organization in a shock induced boundary layer. *Journal of Fluid Mechanics*, **559**, 255–277.

DUPONT, P., PIPONNIAU, S., SIDORENKO, A. & DEBIÈVE, J.F. (2007). Investigation of an oblique shock reflection with separation by PIV measurements. In *45th AIAA Aerospace Sciences Meeting and Exhibit*.

DUPONT, P., PIPONNIAU, S., SIDORENKO, A. & DEBIÈVE, J.F. (2008). Investigation of an oblique shock reflection with separation by PIV measurements. *AIAA Journal*, **46**, 1365–1370.

DUSSAUGE, J. & PIPONNIAU, S. (2008). Shock/boundary-layer interactions: Possible sources of unsteadiness. *Journal of Fluids and Structures*, **24**.

DUSSAUGE, J.P. & SMITS, A.J. (1995). Characteristic scales for energetic eddies in turbulent supersonic boundary layers. In *Proceedings of the 10th Symposium on Turbulent Shear Flows (Pennsylvania State University)*.

DUSSAUGE, J.P., DUPONT, P. & DEBIÈVE, J.F. (2006). Unsteadiness in shock wave boundary layer interactions with separation. *Aerospace Science and Technology*, **10**, 85–91.

DUSSAUGE, J.P., DEBIÈVE, J.F., DUPONT, P., PIPONNIAU, S. & SOUVEREIN, L.J. (2009). Report on the measurements of shock reflection at M=2.25: Final report. UFAST Deliverable 3.3.5, Institut Universitaire des Systèmes Thermiques Industriels.

EATON, J.K. & JOHNSTON, J.P. (1981). A review of research on subsonic turbulent flow reattachment. *AIAA Journal*, **19**, 1093–1100.

EGGERS, T., NOVELLI, P. & HAUPT, M. (2001). Design studies of the JAPHAR experimental vehicle for dual mode ramjet demonstration. *AIAA paper*.

EHRENSTEIN, U. & GALLAIRE, F. (2008). Two-dimensional global low-frequency oscillations in a separating boundary-layer flow. *Journal of Fluid Mechanics*, **614**, 315–327.

ELENA, M., TEDESCHI, G. & GOUIN, H. (1999). Motion of tracer particles in supersonic flows. *Experiments in Fluids*, **26**, 288–296.

ELSINGA, G.E. (2008). *Tomographic particle image velocimetry and its application to turbulent boundary layers*. Doctoral thesis, Delft University of Technology.

ELSINGA, G.E., VAN OUDHEUSDEN, B.W. & SCARANO, F. (2005a). The effect of particle image blur on the correlation map and velocity measurement in PIV. In *Optical Engineering and Instrumentation, SPIE Annual Meeting, San Diego, USA, Paper 5880-37*.

ELSINGA, G.E., VAN OUDHEUSDEN, B.W. & SCARANO, F. (2005b). Evaluation of optical distortion effects in PIV. *Experiments in Fluids*, **39**, 246–256.

ELSINGA, G.E., SCARANO, F., WIENEKE, B. & VAN OUDHEUSDEN, B.W. (2006). Tomographic particle image velocimetry. *Experiments in Fluids*, **41**, 933–947.

ERENGIL, M.E. & DOLLING, D.S. (1991a). Correlation of separation shock motion with pressure fluctuations in the incoming boundary layer. *AIAA Journal*, **29**, 1868–1877.

ERENGIL, M.E. & DOLLING, D.S. (1991b). Unsteady wave structure near separation in a Mach 5 compression ramp interaction. *AIAA Journal*, **29**, 728–735.

FELEMPIN, F. & SERRE, L. (2006). French contribution to hypersonic air-breathing propulsion technology development, status in 2006. In *42nd AIAA/ASME/SAE/ASEE Joint Propulsion Conference & Exhibit, Sacramento, California, USA*.

FERNHOLZ, H. (1971). Ein halbempirisches Gesetz für die Wandreibung in kompressiblen turbulenten Grenzschichten bei isothermer und adiabater Wand. *Angewandte Mechanik ZAMM*, **51**, 146–147.

FERRI, A. (1940). Experimental results with airfoils tested in the high speed tunnel at Guidonia. Tech. rep.

FREY, M. & HAGEMANN, G. (1998). Status of flow separation prediction in rocket nozzles. *AIAA Paper*.

FREY, M. & HAGEMANN, G. (2000). Restricted shock separation in rocket nozzles. *Journal of Propulsion and Power*, **16**, 478–484.

FRIC, T.F. & ROSHKO, A. (1994). Vortical structure in the wake of a transverse jet. *Journal of Fluid Mechanics*, **279**, 1–47.

GANAPATHISUBRAMANI, B., CLEMENS, N.T. & DOLLING, D.S. (2006a). Large-scale motions in a supersonic turbulent boundary layer. *Journal of Fluid Mechanics*, 271–282.

GANAPATHISUBRAMANI, B., CLEMENS, N.T. & DOLLING, D.S. (2006b). Planar imaging measurements to study the effect of spanwise structure of upstream turbulent boundary layer on shock induced separation. In *44th AIAA Aerospace Sciences Meeting and Exhibit, Reno, Nevada*.

GANAPATHISUBRAMANI, B., CLEMENS, N.T. & DOLLING, D.S. (2007a). Effects of upstream coherent structures on low-frequency motion of shock-induced turbulent separation. In *45th AIAA Aerospace Sciences Meeting and Exhibit, Reno, Nevada*.

GANAPATHISUBRAMANI, B., CLEMENS, N.T. & DOLLING, D.S. (2007b). Effects of upstream on the unsteadiness of shock induced separation. *Journal of Fluid Mechanics*, 369–394.

GARNIER, E. (2009). Stimulated detached eddy simulation of three–dimensional shock / boundary layer interaction. *Shock Waves*, 479–486.

GINOUX, J.J. (1973). Interaction entre ondes de choc et couches limites. In A.L. Jaumotte, ed., *Chocs et ondes de choc, Tome II*, Masson & Cie.

GRAFTIEAUX, L., MICHARD, M. & GROSJEAN, N. (2001). Combining OIV, POD and vortex identification algorithms for the study of unsteady turbulent swirling flows. *Measurement Science and Technology*, **12**, 1422–1429.

GREEN, J. (1970). Reflexion of an oblique shock wave by a turbulent boundary layer. *Journal of Fluid Mechanics*, **40**, 81–95.

GUIBERT, P. & LEMOYNE, L. (2002). Dual particle image velocimetry for transient flow field measurements. *Experiments in Fluids*, **33**, 355–367.

GURTIN, M.E. (1981). *An Introduction to Continuum Mechanics*. Academic Press, San Diego, 1st edn.

HEAD, M.R. & BANDYOPADHYAY, P.R. (1981). New aspects of turbulent boundary layer structure. *Journal of Fluid Mechanics*, **107**, 297–338.

HOLDEN, H. & BABINKSY, H. (2007). Effect of microvortex generators on separated normal shock/boundary layer interactions. *Journal of Aircraft*, **44**, 170–174.

HOU, Y.X. (2003). *Particle Image Velocimetry Study of Shock-Induced Turbulent Boundary Layer Separation*. Doctoral thesis, The University of Texas at Austin.

HUMBLE, R.A. (2009). *Unsteady Flow Organization of a Shock Wave/Boundary Layer Interaction*. Doctoral thesis, Delft University of Technology.

HUMBLE, R.A., ELSINGA, G.E., SCARANO, F. & VAN OUDHEUSDEN, B.W. (2009a). Three-dimensional instantaneous structure of a shock wave/turbulent boundary layer interaction. *Journal of Fluid Mechanics*, **622**, 33–62.

HUMBLE, R.A., SCARANO, F. & VAN OUDHEUSDEN, B.W. (2009b). Unsteady effects in an incident shock wave/turbulent boundary layer interaction. *Journal of Fluid Mechanics*, **635**, 47–74.

JÖBSIS, A.J.P. (2009). *Time–Resolved PIV Analysis of a Shock Wave / Boundary Layer Interaction*. Master of science thesis, Delft University of Technology.

JÖBSIS, A.J.P., VAN OUDHEUSDEN, B.W., SCARANO, F. & SOUVEREIN, L.J. (2010). Investigation of the unsteadiness of a shock wave turbulent boundary layer interaction with time–resolved PIV. In *45th AAAF Symposium of Applied Aerodynamics, 22-24 March 2010, Marseille, France*.

JOVIĆ, S. (1998). Recovery of reattached turbulent shear layers. *Experimental Thermal and Fluid Science*, **17**, 57–62.

KÄHLER, C.J. (2004). Investigation of the spatio-temporal flow structure in the buffer region of a turbulent boundary layer by means of multiplane stereo PIV. *Experiments in Fluids*, **36**, 114–130.

KAMOTANI, Y. & GREBER, I. (1972). Experiments on a turbulent jet in a cross flow. *AIAA Journal*, **10**, 1425–1429.

KIYA, M. & SASAKI, K. (1983). Structure of a turbulent separation bubble. *Journal of Fluid Mechanics*, **137**, 83–113.

KLEBANOFF, P. (1954). Characteristics of turbulence in a boundary layer with zero pressure gradient. Tech. rep., NASA.

KLEBANOFF, P. (1955). Characteristics of turbulence in a boundary layer with zero pressure gradient. Tech. rep., NASA.

KUNTZ, D.W., AMATUCCI, V.A. & ADDY, A.L. (1987). Turbulent boundary-layer properties downstream of the shock-wave / boundary-layer interaction. *AIAA Journal*, **25**, 668–675.

LANG, T. (2008). *Low–order dynamical system for a shock wave boundary layer interaction*. Master of science thesis, Université de Poitiers, Ecole Nationale Supérieure de Mécanique et d'Aérotechnique, Delft University of Technology.

LARCHEVÊQUE, L., DUPONT, P., DE MARTEL, E., GARNIER, E. & DEBIÈVE, J.F. (2009). Experimental and numerical study of unsteadiness in boundary layer / shock wave interaction. In *2nd International Conference on Turbulence and Interaction - TI2009, Sainte-Luce, Martinique, France*.

LAURENT, H. (1996). *Turbulence d'une interaction onde de choc- couche limite sur paroi plane adiabatique ou chauffée*. Thèse de 3ème cycle, Universitéd'Aix-Marseille II.

LEE, S. & LOTH, E. (2009). Supersonic boundary layer interactions with various micro-vortex generator geometries. In *39th Fluid Dynamics Conference and Exhibit, SAn Antonio, Texas, USA, AIAA-2009-3712*.

LEE, S., LOTH, E., GEORGIADIS, N.J. & DEBONIS, J.R. (2009). Effect of mach number on flow past micro-ramps. In *39th Fluid Dynamics Conference and Exhibit, SAn Antonio, Texas, USA, AIAA-2009-4181*.

LEVENBERG, K. (1944). A method for the solution of certain problems in least squares. *Quarterly of Applied Mathematics*, **2**, 164–168.

LIN, C.C. & RUBINOV, S.I. (1948). On the flow behind curved shocks. *Journal of Mathematics and Physics*, **27**, 105–129.

LIN, J.C. (2006). Review of research on low-profile vortexgenerators to control boundary-layer separation. *Progress in Aerospace Sciences*, **38**, 389–420.

LIU, X. & KATZ, J. (2006). Instantaneous pressure and material acceleration measurements using a four-exposure PIV system. *Experiments in Fluids*, **41**, 227–240.

MABEY, D.G. (1972). Analysis and correlation of data on pressure fluctuations in separated flow. *Journal of Aircraft*, **9**, 642–645.

MARQUARDT, D.W. (1963). An algorithm for least-squares estimation of nonlinear parameters. *SIAM Journal on Applied Mathematics*, **11**, 431–441.

OSWATITSCH, K. & ZIEREP, J. (1960). Das Problem des senkrechten Stosses an einer gekrümmten Wand. *Zeitschrift für Angewandte Mathematik und Mechanik (ZAMM)*, **40**, T143–T144, Tagungsheft (special issue).

PAPAMOSCHOU, D. & ROSHKO, A. (1988). The compressible turbulent shear layer: an experimental study. *Journal of Fluid Mechanics*, **197**, 453–477.

PEEBLES, C. (2008). *Road to Mach 10: Lessons Learned from the X-43A Flight Research Program*. AIAA Library of Flight, 1st edn.

PERRET, L., BRAUD, P., FOURMET, C., DAVID, L. & DELVILLE, J. (2006). 3-component acceleration field measurement by dual-time stereoscopic particle image velocimetry. *Experiments in Fluids*, **40**, 813–824.

PIPONNIAU, S. (2009). *Instationnarités dans les décollements compressibles: cas des couches limites soumises à ondes de choc*. Thèse de doctorat, Université de Provence.

PIPONNIAU, S., DUSSAUGE, J.P., DEBIÈVE, J.F. & DUPONT, P. (2009). A simple model for low-frequency unsteadiness in shock-induced separation. *Journal of Fluid Mechanics*, **629**, 87–108.

PIROZZOLI, S. & GRASSO, F. (2006). Direct numerical simulation of impinging shock wave / turbulent boundary layer interaction at M=2.25. *Physics of Fluid*, **18**.

PIROZZOLI, S., BEER, A., BERNARDINI, M. & GRASSO, F. (2009). Computational analysis of impinging shock–wave boundary layer interaction under conditions of incipient separation. *Shock Waves*, 487–497.

PLOTKIN, K. (1975). Shock wave oscillation driven by turbulent boundary layer fluctuations. *AIAA Journal*, **13**, 1036–1040.

POLIVANOV, P., SIDORENKO, A. & MASLOV, A. (2009). Report on the measurement of shock reflection by Mach=2.0: Final report. UFAST Deliverable 3.3.6, Institute of Theoretical and Applied Mechanics.

RAFFEL, M., WILLERT, C.E., WERELEY, S.T. & KOMPENHANS, J. (2007). *Particle Image Velocimetry : A Practical Guide*. Springer, 2nd edn.

RAGNI, D., SCHRIJER, F., VAN OUDHEUSDEN, B.W. & SCARANO, F. (2009). On the determination of PIV particle tracers response time by shock wave tests. In *8th International Symposium on Particle Image Velocimetry - PIV09, Melbourne, Australia*.

REIJASSE, P. & BOCCALETTO, L. (2008). Nozzle flow separation with film cooling. In *38th Fluid Dynamics Conference and Exhibit, Seattle, Washington, USA, AIAA-2008-4150*.

RINGUETTE, M. & SMITS, A. (2007). Wall-pressure measurements in a Mach 3 shock-wave turbulent boundary layer interaction at a DNS-accessible Reynolds number. In *37th AIAA Fluid Dynamics Conference and Exhibit, 25-28 June, Miami, FL*.

RINGUETTE, M., WU, M. & MARTIN, M.P. (2008). Low Reynolds number effects in a Mach 3 shock/turbulent-boundary-layer interaction. *AIAA Journal*, **46**, 1884–1887.

RINGUETTE, M.J., BOOKEY, P., WYCKHAM, C. & SMITS, A.J. (2009). Experimental study of a Mach 3 compression ramp interaction at $re_\theta = 2400$. *AIAA Journal*, **47**, 373–385.

ROBINSON, S.K. (1991). Coherent motions in the turbulent boundary layer. *Annual Review of Fluid Mechanics*, **23**, 601–639.

SCARANO, F. & RIETHMULLER, M.L. (1999). Iterative multigrid approach in PIV image processing with discrete window offset. *Experiments in Fluids*, **26**, 513–523.

SCARANO, F. & VAN OUDHEUSDEN, B.W. (2003). Planar velocity measurements of a two-dimensional compressible wake. *Experiments in Fluids*, **34**, 430–441.

SCHMUCKER, R. (1973). Strömungsvortgänge beim Betrieb überexpandierter Düsen chemischer Raketentriebwerke (Flow Processes in Overexpanded Nozzles of Chemical Rocket Engines). Tech. rep., Technical University Munich.

SCHRIJER, F.F.J. & SCARANO, F. (2007). Particle slip compensation in steady compressible flows. In *7th International Symposium on Particle Image Velocimetry, 11 - 14 September 2007, Rome, Italy*.

SCHRIJER, F.F.J., SCARANO, F. & VAN OUDHEUSDEN, B.W. (2006). Application of PIV in a Mach 7 double-ramp flow. *Experiments in Fluids*, **41**, 353–363.

SELIG, M.S. & SMITS, A.J. (1991). Effect of periodic blowing on attached and separated supersonic turbulent boundary layers. *AIAA Journal*, **29**, 1651–1658.

SELIG, M.S., ANDREOPOULOS, J., MUCK, K.C., DUSSAUGE, J.P. & SMITS, A.J. (1989). Details of a shock - separated turbulent boundary layer at a compression corner. *AIAA Journal*, **27**, 862–869.

SETTLES, G.S. (2006). *Schlieren and Shadowgraph Techniques*. Experimental Fluid Mechanics, Springer, 2nd edn.

SETTLES, G.S., BOGDONOFF, S.M. & VAS, I.E. (1976). Incipient sepatation of a supersonic turbulent boundary layer at high reynolds number. *AIAA Journal*, **14**, 50–56.

SETTLES, G.S., FITZPATRICK, T.J. & BOGDONOFF, S.M. (1979). Detailed study of attached and separated compression corner flowfields in high reynolds number supersonic flow. *AIAA Journal*, **17**, 579–585.

SIMPSON, R.L. (1989). Turbulent boundary-layer separation. *Annual Review of Fluid Mechanics*, **21**, 205–234.

SMITH, S.H. & MUNGAL, M.G. (1998). Mixing, structure and scaling of the jet in crossflow. *Journal of Fluid Mechanics*, **357**, 83–122.

SMITS, A.J. & DUSSAUGE, J.P. (2006). *Turbulent shear layers in supersonic flow*. AIP Press, 2nd edn.

SMITS, A.J. & MUCK, K.C. (1987). Experimental study of three shock wave / turbulent boundary layer interactions. *Journal of Fluid Mechanics*, **182**, 291–314.

SMITS, A.J., HAYAKAWA, K. & MUCK, K.C. (1983). Constant temperature hot-wire anemometer practice in supersonic flows, part I: the normal wire. *Experiments in Fluids*, **1**, 83–92.

SOUVEREIN, L.J. & DEBIÈVE, J.F. (2009). Effects of air jet vortex generators on a shock wave boundary layer interaction. In *3rd EUCASS conference, Versailles, France, EUCASS2009-387*.

SOUVEREIN, L.J. & DEBIÈVE, J.F. (2010). Effects of air jet vortex generators on a shock wave boundary layer interaction. *Experiments in Fluids*, **Accepted**.

SOUVEREIN, L.J. & VAN OUDHEUSDEN, B.W. (2008). Report on measurement of shock reflection at Mach=1.7. UFAST Deliverable 2.3.6, Delft University of Technology.

SOUVEREIN, L.J., VAN OUDHEUSDEN, B.W. & SCARANO, F. (2006). Détermination des forces partir de piv dans des écoulements supersoniques. In *10ième Congrès Francophone de Technique Laser (CFTL), 19-22 September 2006, Toulouse, France*.

SOUVEREIN, L.J., VAN OUDHEUSDEN, B.W. & SCARANO, F. (2007a). Determination of time scales in a shock wave turbulent boundary layer interaction by means of dual PIV. In *7th International Symposium on Particle Image Velocimetry, 1114 September 2007, Rome, Italy*.

SOUVEREIN, L.J., VAN OUDHEUSDEN, B.W. & SCARANO, F. (2007b). Particle image velocimetry based loads determination in supersonic flows. In *45th AIAA Aerospace Sciences Meeting and Exhibit, 811 January 2007, Reno, Nevada, USA, AIAA-2007-0050*.

SOUVEREIN, L.J., DEBIÈVE, J.F., DUPONT, P. & DUSSAUGE, J.P. (2008a). Control of an incident shock wave/ turbulent bl interaction, M=2.3 by means of air jet vortex generators. UFAST Deliverable 3.3.3, IUSTI.

SOUVEREIN, L.J., VAN OUDHEUSDEN, B.W., SCARANO, F. & DUPONT, P. (2008b). Unsteadiness characterisation in a shock wave turbulent boundary layer interaction through dual- PIV. In *38th Fluid Dynamics Conference and Exhibit, Seattle, Washington, USA, AIAA-2008-4169*.

SOUVEREIN, L.J., DUPONT, P., DEBIÈVE, J.F., DUSSAUGE, J.P., VAN OUDHEUSDEN, B.W. & SCARANO, F. (2009a). Effect of interaction strength on shock wave boundary layer interaction: Unsteady behavior. In *39th Fluid Dynamics Conference and Exhibit, San Antonio, Texas, USA, AIAA-2009-3715*.

SOUVEREIN, L.J., VAN OUDHEUSDEN, B.W., SCARANO, F. & DUPONT, P. (2009b). Application of a dual-plane particle image velocimetry (dual-PIV) technique for the unsteadiness characterization of a shock wave turbulent boundary layer interaction. *Measurement Science and Technology*, **20**, 074003 (16pp).

SOUVEREIN, L.J., DUPONT, P., DEBIÈVE, J.F., DUSSAUGE, J.P., VAN OUDHEUSDEN, B.W. & SCARANO, F. (2010). Effect of interaction

strength on shock wave boundary layer interaction: Unsteady behavior. *AIAA Journal*, **Accepted**.

SPAID, F.W. & FRISHETT, J.C. (1972). Incipient separation of a supersonic, turbulent boundary layer, including effect of heat transfer. *AIAA Journal*, **10**, 915–922.

SUMMERFIELD, M., FOSTER, C. & SWAN, W. (1954). Flow separation in overexpanded supersonic exhaust nozzles. Tech. Rep. Vol. 24, Jet Propulsion Laboratory.

THOMAS, F., PUTMAN, C. & CHU, H. (1994). On the mechanism of unsteady shock oscillation in shock wave/turbulent boundary layer interaction. *Experiments in Fluids*, **18**, 69–81.

THOMKE, G.J. & ROSHKO, A. (1969). Incipient separation of a turbulent boundary layer at high reynolds number in two-dimensional supersonic flow over a compression corner. Tech. Rep. DAC-59819, NASA Ames Research Center.

TOUBER, E. & SANDHAM, N. (2008). Oblique shock impinging on a turbulent boundary layer: low-frequency mechanisms. In *38th AIAA Fluid Dynamics Conference, Seattle, Washington, USA*.

TOUBER, E. & SANDHAM, N. (2009). Comparison of three large–eddy simulations of shock–induced turbulent separation bubbles. *Shock Waves*, 469–478.

ÜNALMIS, Ö.H. & DOLLING, D.S. (1996). On the possible relationship between low frequency unsteadiness of shock-induced separated flow and Goertler vortices. In *27th AIAA Fluid Dynamics Conference, New Orleans, Louisiana, USA, AIAA-1996-2002*.

VALDIVIA, A., YUCEIL, K.B., WAGNER, J.L., CLEMENS, N.T. & DOLLING, D.S. (2009). Active control of supersonic inlet unstart using vortex generator jets. In *39th Fluid Dynamics Conference and Exhibit, San Antonio, Texas, USA, AIAA-2009-4022*.

VAN OUDHEUSDEN, B.W. & SCARANO, F. (2008). PIV investigation of supersonic base flow - plume interaction, PIVNET II final workshop, 7-8 sept. 2006, Göttingen, Germany. In A. Schröder & C.E. Willert, eds., *Particle Image Velocimetry, New Developments and Recent Applications; Topics in Applied Physics*, vol. 112, 449–458, Springer Verlag.

VAN OUDHEUSDEN, B.W. & SOUVEREIN, L.J. (2007). Evaluation of the pressure field from PIV in a shock wave boundary layer interaction. In *7th International Symposium on Particle Image Velocimetry, 1114 September 2007, Rome, Italy*.

VAN OUDHEUSDEN, B.W. & SOUVEREIN, L.J. (2009). Report on measurement of shock reflection at Mach=1.7: Final report. UFAST Deliverable 2.3.10, Delft University of Technology.

VAN OUDHEUSDEN, B.W., SCARANO, F., ROOSENBOOM, E.W.M., CASIMIRI, E.W.F. & SOUVEREIN, L.J. (2007). Evaluation of integral forces and pressure fields from planar velocimetry data for incompressible and compressible flows. *Experiments in Fluids*, **43**, 153–162.

WHITE, F.M. (1991). *Viscous Fluid Flow*. McGraw-Hill, New-York, 2nd edn.

WISSE, M.E.N. & BANNINK, W.J. (2001). Half model restrictions for linear plug nozzle testing. *AIAA Journal*, **39**, 2148–2157.

WU, M. & MARTIN, M.P. (2007). Direct numerical simulation of supersonic turbulent boundary layer over a compression ramp. *AIAA Journal*, **45**, 879–889.

WU, M. & MARTIN, M.P. (2008). Analysis of shock motion in shockwave and turbulent boundary layer interaction using direct numerical simulation data. *Journal of Fluid Mechanics*, **594**, 71–83.

YAMAGATA, K., MORIOKA, T., MOTOSUKE, M. & HONAMI, S. (2009). A role of longitudinal vortex on the separating shear layer development over a backward facing step. In *39th Fluid Dynamics Conference and Exhibit, San Antonio, Texas, USA, AIAA-2009-4180*.

YANG, Y.T. & WANG, Y.X. (2005). Three-dimensional numerical simulation of an inclined jet with cross-flow. *International Journal of Heat and Mass Transfer*, **48**, 4019–4027.

ZHOU, J., ADRIAN, R.J., BALACHANDAR, S. & KENDALL, T.M. (1999). Mechanisms for generating coherent packets of hairpin vortices in channel flows. *Journal of Fluid Mechanics*, **387**, 353–396.

ZIEREP, J. (2003). New results for the normal shock in inviscid flow at a curved surface. *Zeitschrift für Angewandte Mathematik und Mechanik (ZAMM)*, **83**, 603–610.

ZUKOSKI, E. (1967). Turbulent boundary-layer separation in front of a forward-facing step. *AIAA Journal*, **5**, 1746–1753.

List of publications

Book chapters

VAN OUDHEUSDEN, B.W. & SOUVEREIN, L.J. (2009). Basic experiments in UFAST: Oblique shock reflection M=1.7 (TUD). In P.P. Doerffer, ed., *Unsteady effects of shock wave induced separation: UFAST Experiments Data Bank (Specific targeted research project AST4-CT-2005012226)*.

DUSSAUGE, J.P., SOUVEREIN, L.J., DEBIÈVE, J.F. & DUPONT, P. (2009). Flow control experiments in UFAST: Oblique shock reflection M=2.25 (IUSTI). In P.P. Doerffer, ed., *Unsteady effects of shock wave induced separation: UFAST Experiments Data Bank (Specific targeted research project AST4-CT-2005012226)*.

VAN OUDHEUSDEN, B.W. & SOUVEREIN, L.J. (2010). Basic experiments: Oblique shock reflection M=1.7. In P.P. Doerffer, ed., *Unsteady Effects of Shock Wave Induced Sepration*, Springer Verlag, ISBN 978-3-642-03003-1.

DUSSAUGE, J.P., SOUVEREIN, L.J., DEBIÈVE, J.F. & DUPONT, P. (2010). Flow control experiments: Oblique shock reflection M=2.25. In P.P. Doerffer, ed., *Unsteady Effects of Shock Wave Induced Sepration.*, Springer Verlag, ISBN 978-3-642-03003-1.

Reports

SOUVEREIN, L.J. & VAN OUDHEUSDEN, B.W. (2008). Report on measurement of shock reflection at M=1.7. UFAST Deliverable 2.3.6, Delft University of Technology.

VAN OUDHEUSDEN, B.W. & SOUVEREIN, L.J. (2008). Data bank input deliverable report. UFAST Deliverable 2.3.9, Delft University of Technology.

SOUVEREIN, L.J., DEBIÈVE, J.F., DUPONT, P. & DUSSAUGE, J.P. (2008). Control of an Incident shock wave/ turbulent BL interaction, M=2.3

by means of Air Jet Vortex Generators. UFAST Deliverable 3.3.3, Institut Universitaire des Systèmes Thermiques Industriels.

VAN OUDHEUSDEN, B.W. & SOUVEREIN, L.J. (2009). TUD Final Report. UFAST Deliverable 2.3.10, Delft University of Technology.

DUSSAUGE, J.P., DEBIÈVE, J.F., DUPONT, P., PIPONNIAU, S. & SOU-VEREIN, L.J. (2009). Report on the measurements of shock reflection at M=2.25: Final Report. UFAST Deliverable 3.3.5, Institut Universitaire des Systèmes Thermiques Industriels.

Journal articles

VAN OUDHEUSDEN, B.W., SCARANO, F., ROOSENBOOM, E.W.M., CASIMIRI, E.W.F. & SOUVEREIN, L.J. (2007). Evaluation of integral forces and pressure fields from planar velocimetry data for incompressible and compressible flows. *Experiments in Fluids*, **43**, 153–162.

SOUVEREIN, L.J., TWIGT, D.J. & ENGELEN, S. (2009). Amateur gas-propelled rocket engine development and advanced rocket design. *Journal of the British Interplanetary Society*, **62**, 9–14.

ENGELEN, S., SOUVEREIN, L.J. & TWIGT, D.J. (2009). DEIMOS Methane / Oxygen Rocket Engine Test Results. *Journal of the British Interplanetary Society*, **62**, 211–218.

SOUVEREIN, L.J., VAN OUDHEUSDEN, B.W., SCARANO, F. & DUPONT, P. (2009). Application of a dual-plane particle image velocimetry (Dual-PIV) technique for the unsteadiness characterization of a shock wave turbulent boundary layer interaction. *Measurement Science and Technology*, **20**, 074003 (16pp).

SOUVEREIN, L.J., DUPONT, P., DEBIÈVE, J.F., DUSSAUGE, J., VAN OUDHEUSDEN, B.W. & SCARANO, F. (2010). Effect of interaction strength on shock wave boundary layer interaction: unsteady behavior. *AIAA Journal*, **Accepted**.

SOUVEREIN, L.J. & DEBIÈVE, J.F. (2010). Effect of air jet vortex generators on a shock wave boundary layer interaction. *Experiments in Fluids*, **Accepted**.

SOUVEREIN, L.J., VAN OUDHEUSDEN, B.W. & SCARANO, F. (2010). PIV Based Loads Determination of an Airfoil in Supersonic Flow. **In preparation**.

SOUVEREIN, L.J. & DUPONT, P. (2010). A scaling analysis of shock wave boundary layer interactions. **In preparation**.

Conference proceedings

SOUVEREIN, L.J., TWIGT, D.J. & ENGELEN, S. (2004). Amateur gas-propelled rocket engine development and advanced rocket design. In *55th International Astronautical Congress, Vancouver, British Columbia, Canada, IAC-04-S.P.05.*

ENGELEN, S., SOUVEREIN, L.J. & TWIGT, D.J. (2005). DEIMOS Methane / Oxygen Rocket Engine Test Results. In *56th International Astronautical Congress, Fukuoka, Japan, IAC-05-C4.3.09.*

VAN OUDHEUSDEN, B.W., SCARANO, F., ROOSENBOOM, E.W.M., CASIMIRI, E.W.F. & SOUVEREIN, L.J. (2006). Evaluation of Integral Forces and Pressure Fields from Planar Velocimetry Data for Incompressible and Compressible Flows. In *14th International Symposium on Applications of Laser Techniques to Fluid Mechanics, Lisbon, Portugal.*

SOUVEREIN, L.J., VAN OUDHEUSDEN, B.W. & SCARANO, F. (2006). Détermination des forces en base de PIV dans des écoulements supersoniques. In *10ème Congrs Francophone de Techniques Laser, Toulouse, France.*

SOUVEREIN L.J. (2006). Aerodynamic loads determination in supersonic and hypersonic flows based on PIV. In *57th International Astronautical Congress, Valencia, Spain, IAC-06-C4.P.5.05.*

SOUVEREIN, L.J., VAN OUDHEUSDEN, B.W. & SCARANO, F. (2007). Particle image velocimetry based loads determination in supersonic flow. In *45th Aerospace Sciences Meeting and Exhibit, Reno, Nevada, USA, AIAA-2007-0050.*

VAN OUDHEUSDEN, B.W. & SOUVEREIN, L.J. (2007). Evaluation of the pressure field from PIV in a shock wave boundary layer interaction. In *7th International Symposium on Particle Image Velocimetry, Rome, Italy.*

SOUVEREIN, L.J., VAN OUDHEUSDEN, B.W. & SCARANO, F. (2007). Determination of time scales in a shock wave turbulent boundary layer interaction by means of dual-PIV. In *7th International Symposium on Particle Image Velocimetry, Rome, Italy.*

VAN OUDHEUSDEN, B.W., HUMBLE, R.A., SOUVEREIN, L.J., SCARANO, F., BEER, A., PIROZZOLI, S. & GRASSO, F. (2007). Experimental and Numerical flow field study of a reflecting shock interaction with a high Reynolds number turbulent boundary layer. In *Proceedings*

of the Joint EWA and UFAST Workshop on Validation of Numerical Methods by Experiments in Aerodynamics, Prague, Czech Republic.

VAN OUDHEUSDEN, B.W., SCARANO, F., ELSINGA, G.E., HUMBLE, R.A. & SOUVEREIN, L.J. (2008). Advanced PIV techniques for the temporal and spatial characterization of turbulent structures in high speed flows. In *Proceedings of the International Workshop on Compressible Turbulent Flow Research for the Next Generation of Air Vehicles, Marseille, France.*

SOUVEREIN, L.J., VAN OUDHEUSDEN, B.W. & SCARANO, F. (2008). Characterization of flow unsteadiness in a shock wave turbulent boundary layer interaction by means of dual-PIV. In *Proceedings of the EWA International Workshop on Advanced Measurement Techniques in Aerodynamics, Delft, the Netherlands.*

SOUVEREIN, L.J., VAN OUDHEUSDEN, B.W., SCARANO, F. & DUPONT, P. (2008). Unsteadiness characterisation in a shock wave turbulent boundary layer interaction through Dual-PIV. In *38th Fluid Dynamics Conference and Exhibit, Seattle, Washington, USA, AIAA-2008-4169.*

DUSSAUGE, J.P., PIPONNIAU, S., SOUVEREIN, L.J., DUPONT, P., & DEBIÈVE, J.F. (2008). Different sorts of unsteadiness in shock induced separation. *Bulletin of the American Physical Society*, **53**(15), 268. In *61st Annual Meeting of the Division of Fluid Dynamics, San Antonio, Texas, USA.*

SOUVEREIN, L.J., DUPONT, P., DEBIÈVE, J.F., DUSSAUGE, J., VAN OUDHEUSDEN, B.W. & SCARANO, F. (2009). Effect of interaction strength on shock wave boundary layer interaction: unsteady behavior. In *39th Fluid Dynamics Conference and Exhibit, San Antonio, Texas, USA, AIAA-2009-3715.*

SOUVEREIN, L.J. & DEBIÈVE, J.F. (2009). Effect of air jet vortex generators on a shock wave boundary layer interaction. In *3rd EUCASS conference, Versailles, France, EUCASS2009-387.*

DUPONT, P., SOUVEREIN, L.J., DUSSAUGE, J.P. (2009). Dependence of unsteady behavior of shock wave boundary layer interactions on the Reynolds number and the state of separation. *Bulletin of the American Physical Society*, **54**(19), 256. In *62nd Annual Meeting of the Division of Fluid Dynamics, Minneapolis, Minnesota, USA.*

JÖBSIS, A.J.P., VAN OUDHEUSDEN, B.W., SCARANO, F. & SOUVEREIN, L.J. (2010). Investigation of the unsteadiness of a shock wave turbulent boundary layer interaction with time-resolved PIV. In *45th AAAF Symposium of Applied Aerodynamics, Marseille, France.*

Curriculum Vitae

Louis Jacques Souverein was born on January 31st in Rotterdam, the Netherlands. He attended secondary school (VWO) at the Regionale Scholengemeenschap Broklede in Breukelen, and graduated in 1999 with honours. In the same year, he started studying Aerospace Engineering at the TU Delft, taking part in the first completely English course programme. He completed his propedeutic year with honours in 2000, and obtained his Bachelor of Science degree in 2003 and his Master of Science degree in 2006, both with honours.

He is one of the founders and honorary member of DARE 'Delft Aerospace Rocket Engineering', a study society aimed at developing and launching amateur rockets. He spent three years as a board member, responsable for the design projects. He also helped to conceive and test a methane / oxygen engine, presenting the results at the IAF conference in Vancouver, Canada in 2004. In addition, he participated in the 2002 ESA student parabolic flight campaign as team leader of the Weightless Weight Watchers, performing a Mass Determination Experiment in Zero–G ('MADE-EZ'). He also took part in the ESA / SNECMA workshop 'Viking Teach Me' in April 2004 in Vernon, France, learning about - and constructing part of - the Viking rocket engine. He later took part in the assembly of the complete Viking engine that still stands in the entrance hall of the Aerospace Engineering faculty. Finally, he participated in a European exchange project of the ATHENS network, following the course 'Europe Utile' (Useful Europe) at the Ecole Nationale Supérieure des Mines de Paris in March 2005.

In his Master phase he did a six month internship at EADS Astrium Space Transportation in Ottobrunn, near Munich, Germany, performing a literature research into green rocket propellant. His Master thesis work was carried out at the Aerodynamics Group of the TU Delft and concerned the determination of loads in supersonic flows by means of particle image velocimetry. In March 2006 he started his Ph.D. research, a 'cotutelle' (double–promotion) between the Delft University of Technology and the Université de Provence - Aix–Marseille I, with as promotors prof. P.G. Bakker, prof. J.P Dussauge, and under direct supervision of dr. B.W van Oudheusden, prof. F. Scarano, dr. P. Dupont and dr. J.F. Debiève. He spent his first year in Delft and the subsequent three years in Marseille, although working for the TU Delft during the last year. The doctoral research was performed in the context of the UFAST "Unsteady Effects of Shock Wave Induced Separation" project, a 6th Framework Programme of the European Commission. Due to his international experiences, he is now fluent in four languages.

During his doctoral research, he traversed the Eurasian continent on the Transsiberien Express and he traveled in China. He also married Irène and he is now the proud father of their son Leen.